

**FORCE-SENSING-BASED MULTI-PLATFORM ROBOTIC
ASSISTANCE FOR VITREORETINAL SURGERY**

by

Berk Gonenc

A dissertation submitted to the Johns Hopkins University in conformity with the
requirements for the degree of Doctor of Philosophy

Baltimore, Maryland

May 2017

© 2017 Berk Gonenc

All Rights Reserved

ABSTRACT

Vitreoretinal surgery aims to treat disorders of the retina, vitreous body, and macula, such as retinal detachment, diabetic retinopathy, macular hole, epiretinal membrane and retinal vein occlusion. Challenged by several technical and human limitations, vitreoretinal practice currently ranks amongst the most demanding fields in ophthalmic surgery. Of vitreoretinal procedures, membrane peeling is the most common to be performed, over 0.5 million times annually, and among the most prone to complications. It requires an extremely delicate tissue manipulation by various micron scale maneuvers near the retina despite the physiological hand tremor of the operator. In addition, to avoid injuries, the applied forces on the retina need to be kept at a very fine level, which is often well below the tactile sensory threshold of the surgeon. Retinal vein cannulation is another demanding procedure where therapeutic agents are injected into occluded retinal veins. The feasibility of this treatment is limited due to challenges in identifying the moment of venous puncture, achieving cannulation and maintaining it throughout the drug delivery period.

Recent advancements in medical robotics have significant potential to address most of the challenges in vitreoretinal practice, and therefore to prevent traumas, lessen complications, minimize intra-operative surgeon effort, maximize surgeon comfort, and promote patient safety. This dissertation presents the development of novel force-sensing tools that can easily be used on various robotic platforms, and robot control methods to produce integrated assistive surgical systems that work in partnership with surgeons against the current limitations in vitreoretinal surgery, specifically focusing on membrane peeling and vein cannulation procedures. Integrating high sensitivity force sensing into

the ophthalmic instruments enables precise quantitative monitoring of applied forces. Auditory feedback based upon the measured forces can inform (and warn) the surgeon quickly during the surgery and help prevent injury due to excessive forces. Using these tools on a robotic platform can attenuate hand tremor of the surgeon, which effectively promotes tool manipulation accuracy. In addition, based upon certain force signatures, the robotic system can precisely identify critical instants, such as the venous puncture in retinal vein cannulation, and actively guide the tool towards clinical targets, compensate any involuntary motion of the surgeon, or generate additional motion that will make the surgical task easier. The experimental results using two distinct robotic platforms, the Steady-Hand Eye Robot and Micron, in combination with the force-sensing ophthalmic instruments, show significant performance improvement in artificial dry phantoms and ex vivo biological tissues.

Dissertation Committee:

Advisor

Iulian Iordachita, Ph.D.

Associate Research Professor, Laboratory of Computational Sensing and Robotics,
Johns Hopkins University

Co-Advisors

Russell H. Taylor, Ph.D.

Johns C. Malone Professor of Computer Science, Johns Hopkins University

Peter L. Gehlbach, M.D., Ph.D.

Associate Professor of Ophthalmology, Wilmer Eye Institute, Johns Hopkins
University School of Medicine

ACKNOWLEDGEMENTS

I truly feel fortunate and honored to be able to work with exceptional colleagues and mentors at Johns Hopkins University. Foremost, I would like to thank my advisor, Dr. Iulian Iordachita, for his continuous support and motivating guidance along the way. I appreciate all his contributions of time, ideas, and funding to make my Ph.D. experience more productive and stimulating. I am also thankful for the excellent example he has provided as a successful engineer, researcher and teacher. I gratefully thank my thesis committee members, Dr. Russell Taylor and Dr. Peter Gehlbach, for their valuable suggestions, constructive comments, and insightful advice. Also, many thanks to the other past and current members of our research team: Dr. James Handa, Dr. Peter Kazanzides, Dr. Jin Kang, Dr. Cameron Riviere, Marcin Balicki, Xingchi He, Ehsan Azimi, Paul Wilkening, Ismail Kuru, Nate Tran, Ellen Feldman, Amrita Gupta, Alireza Chamani, Anzhu Gao, Hao Liu, Meng Li, Gyeong Woo Cheon and Soohyun Lee. This interdisciplinary team has been extremely proficient, creative and productive, which collaboratively led to many of the contributions presented in this dissertation.

Many thanks go to Dr. Ilhan Konukseven from the Middle East Technical University and Dr. Hakan Gurocak from Washington State University Vancouver for establishing the bridge for me to come to the United States and for all their guidance along the way. From start till the end, they created opportunities for me, trusted me, shared their experiences and guided me through very difficult phases while making critical decisions, which enriched me so much, academically, professionally, and personally.

I truly enjoyed being a member of the LCSR and the Mechanical Engineering Department. I was privileged to work in an exceptional robotics research facility with

exceptional professors, excellent staff, and talented students. I would like to thank the faculty members: Dr. Taylor, Dr. Louis Whitcomb, Dr. Noah Cowan, Dr. Marin Kobilarov, Dr. Greg Chirikjian, Dr. David Kraemer, Dr. Steven Marra. Having studied in their classes, and having served as their teaching assistant, I gained invaluable technical knowledge and teaching/mentoring experience. Many thanks to Alison Morrow, Jamie Meehan, Elisa Ahmanson, Julia Ortiz-Foy, Lorrie Dodd, Mike Bernard, Kevin Adams and Niel Leon for their patient support and invaluable help for my activities.

I would also like to thank many dear colleagues and friends. These bright people full of positive energy surrounded me with their friendship, love, expertise, and creativity. In alphabetical order: Alexis, Ali, Alican, Alireza, Am, Amirhossein, Amrita, Amy, Anton, Anzhu, Ayushi, Bahar, Baris, Brian, Cris, Deniz, Ehsan, Ela, Ellen, Erin, Evren, Farshid, Fereshteh, Gang, Giray, Gyeong Woo, Haluk, Hao, Ismail, Jiangzhen, Kai, Kiyong, Mahsan, Meng, Mert, Molly, Min Yang, Nathan, Nhat, Orhan, Ozan, Ozgul, Paul, Preetham, Reza, Robert, Sabine, Sait, Serife, Shahin, Shahriar, Sohrab, Soohyun, Sungmin, Tutkun, Ugur, Xingchi, Yunus, Zihan and the others I failed to recall here.

I would like to acknowledge the financial support I received for my research. The work presented in this dissertation was supported in part by the National Institutes of Health under R01 EB000526, and in part by Johns Hopkins University internal funds as Research to Prevent Blindness, The J. Willard and Alice S. Marriott Foundation, The Gale Trust, Mr. Herb Ehlers and Mr. Bill Wilbur. I also would like to thank the Thomas and Stacey Siebel Foundation for their rewarding support during the final year of my studies.

Finally, I present my sincere appreciation and thanks to my parents, Serap Gonenc and

Sahabettin Gonenc, for their encouragement and continued support. They have always been perfect role models for me and provided great motivation towards reaching my goals. Apart from their emotional support, their experience and expertise in medicine helped me a lot in this study.

Dedication

To my family

TABLE OF CONTENTS

ABSTRACT.....	ii
ACKNOWLEDGEMENTS.....	v
TABLE OF CONTENTS.....	ix
LIST OF TABLES.....	xii
LIST OF FIGURES.....	xiii
Chapter 1 : INTRODUCTION.....	1
1.1 Thesis Statement.....	1
1.2 Vitreoretinal Surgery.....	1
1.2.1 Epiretinal Membrane Peeling.....	3
1.2.2 Retinal Vein Cannulation.....	3
1.3. Challenges in Vitreoretinal Surgery.....	4
1.3.1 Epiretinal Membrane Peeling.....	5
1.3.2 Retinal Vein Cannulation.....	6
1.4 Dissertation Overview.....	8
Chapter 2 : RELATED WORK.....	10
2.1. Force Sensing.....	10
2.2. Robotic Systems for Ophthalmology.....	11
2.3.2 Hand-held Robots.....	12
2.3.3 Cooperatively-Controlled Robots.....	13
Chapter 3 : FORCE-SENSING INSTRUMENTS FOR ASSISTED VITREORETINAL SURGERY.....	15
3.1 Introduction.....	15
3.1.1. Background and Motivation.....	15
3.1.2. Contributions.....	16
3.2 Force-Sensing Micro-Forceps for Membrane Peeling.....	17
3.2.1. 2-DOF Force-Sensing Micro-Forceps.....	18
3.2.2. 3-DOF Force-Sensing Micro-Forceps.....	37
3.3 Force-Sensing Microneedle for Retinal Vein Cannulation.....	82
3.3.1. Actuation Mechanism.....	82
3.3.2. Force Sensor Integration.....	86
3.3.3. Effect of Actuation on Force Sensor Response.....	90
3.4 Integration with Robotic Systems.....	91
3.5 Conclusion.....	94
Publications.....	97
Chapter 4 : FORCE-BASED ROBOTIC ASSISTANCE METHODS FOR EPIRETINAL MEMBRANE PEELING.....	98

4.1	Introduction.....	98
4.1.1.	Background and Motivation	98
4.1.2.	Contributions.....	98
4.2	Auditory Force Feedback.....	99
4.2.1.	Algorithm.....	99
4.2.2.	Experiment 1: Evaluation of the Steady-Hand Eye Robot with a Force-Sensing Micro-Forceps	101
4.2.3.	Experiment 2: Evaluation of Micron with a Force-Sensing Hook	104
4.2.4.	Experiment 3: Performance Comparison Between Micron versus the Steady-Hand Eye Robot.....	111
4.2.5.	Experiment 4: Evaluation of Micron with a Force-Sensing Micro-Forceps..	121
4.3	Micro-Vibratory Modulation	126
4.3.1.	Algorithm.....	126
4.3.2.	Experiment 1: Obtaining a faster peel with the same force	128
4.3.3.	Experiment 2: Obtaining reduced forces at the same peeling rate.....	136
4.4	Automatic Tissue Release.....	145
4.5	Conclusion	149
	Publications	151
	Chapter 5 : FORCE-BASED ROBOTIC ASSISTANCE METHODS FOR RETINAL VEIN CANNULATION.....	153
5.1	Introduction.....	153
5.1.1.	Background and Motivation	153
5.1.2.	Contributions.....	154
5.2	Venous Puncture Detection.....	155
5.2.1	Force-Based Method.....	155
5.2.2.	Force-and-Position-Based Method:	159
5.3	Automatic Position Holding	169
5.3.1	Algorithm.....	169
5.3.2.	Experiment 1: A Multi-User System Evaluation	171
5.3.3.	Experiment 2: A Performance Comparison Between Micron and the Steady-Hand Eye Robot.....	181
5.4	Conclusion	187
	Publications	189
	Chapter 6 : CONCLUSIONS.....	191
6.1	Summary and Recapitulation of Contributions.....	191
6.2	Future Directions	195
	BIBLIOGRAPHY	198
	VITA	210
	APPENDIX.....	211
	Technical Drawings and Software	211
	List of Publications and Presentations	212

Refereed Journal Articles.....	212
Refereed Conference Proceedings	212
Papers in Preparation	215
Patents 215	
Presentations	215

LIST OF TABLES

Table 3.1: Results of the sensitivity analysis.	45
Table 4.1: Membrane Peeling Performance Test Cases	106
Table 4.2: Tested cases for membrane peeling with Micron or the Steady-Hand Eye Robot on the bandage phantom and ISM of fertilized chicken eggs.	113
Table 4.3: Comparison of force and duration of unsafe forces during peeling experiments.	121
Table 4.4: Evaluation of bandage and ISM peeling cases based on the average peeling force and speed measured during each trial.	136
Table 4.5: Mean and standard deviation of the measured average and peak peeling force for each micro-vibration setting.	143
Table 5.1: Variation of tool tip force and position before and at the instant of puncture.	160
Table 5.2: Puncture detection rates with the force-based versus the force-and-position-based methods for two users with differing skill and experience (n=24 trials per user).	169
Table 5.3: Operation mode regulation for Micron and the Steady-Hand Eye Robot (SHER).	171
Table 5.4: Force characteristics associated with the instant of puncture for three different users (n=24 trials/user).	175

LIST OF FIGURES

Figure 1.1: (a) The typical setup in the operating room during vitreoretinal surgery. (b) Tool-retina interaction after pars plana vitrectomy. (Image credit to Mark Erickson and Jireh Design).....	2
Figure 3.1: Standard disposable micro-forceps for membrane peeling in vitreoretinal surgery by (a) Alcon and (b) D.O.R.C. The shafts of the shown instruments fit through a 23 Gauge scleral incision. The jaws can be of various types depending on the operation. (Image credit to Alcon, Inc. and D.O.R.C.).....	18
Figure 3.2: 2-DOF force sensing principle for membrane peeling. The FBG strain sensors are integrated on the tool shaft and located proximal to the tool tip to measure the forces perpendicular to the tool axis (F_x and F_y). The tool shaft is modeled as a cantilever beam; when transverse forces are applied at the tool tip, tool shaft deforms and normal stresses are induced on the attached FBG sensors.	19
Figure 3.3: Fabricated prototype of the manually-actuated 2-DOF force-sensing micro-forceps [101]: (a) jaws open, and (b) jaws closed configurations. Squeezing the handpiece closes the jaws. The jaws and the handle mechanism were taken from a standard 23 Gauge disposable micro-forceps. 3 FBGs were attached onto the 23 Gauge nitinol tube forming the tool shaft. The quick release mechanism enables integration with the Steady-Hand Eye Robot and an easy dismounting for safety in case fast removal of the tool from the eye is needed during the procedure.	21
Figure 3.4: The force sensing module and its fabrication steps [101]. First, three half tubes were located on the nitinol tube (upper). Second, FBGs were inserted through half tubes to achieve axi-symmetric configuration (lower).	22
Figure 3.5: (a) Squeezing the handle slides the actuation tube (green) in distal direction and closes the graspers (blue). (b) The graspers (blue) and the actuation tube (green) can be rotated together in the nitinol tube (red) by rotating the handle.	23
Figure 3.6: Calibration results in x-axis direction (left) and in y-axis direction (right). Linear behavior is observed for all FBGs in both axes.....	24
Figure 3.7: (a) Motorized force-sensing micro-forceps integrated with a handheld micromanipulator (Micron) [102], (b) 2-DOF force-sensing micro-forceps for the Steady-Hand Robot from Section 3.2.1.2, (c) Standard 23 Gauge disposable forceps (Alcon, USA).	26
Figure 3.8: Design of the motorized 2-DOF force-sensing micro-forceps: (a) handle mechanism, (b) motorized force-sensing tip with replaceable jaws. The tool can be inserted through a 20 Gauge trocar into the eye. Squeezing the handle mechanism from the sides drives a sliding potentiometer, which is used to control the linear micro motor in the tip module [102].....	27
Figure 3.9: (a) Motorized force-sensing micro-forceps: an earlier prototype (left) vs. the more compact latest prototype (right) of the tip module. (b) Components of the tip module: The disposable jaws can be easily replaced to accommodate different jaw types for different surgical tasks and prolonged use. (c) The handle mechanism and the tip	

module can be integrated with assistive robotic systems, such as the handheld micromanipulator, Micron [103].	28
Figure 3.10: The linear micro motor in the tip module (Squiggle-RV-1.8) is used to drive the slide assembly back and forth. Moving forward pushes the steel tube carrying the FBGs towards the tip, thus squeezing and closing the jaws. Opposite motion releases and opens back the compliant jaws. During actuation, the position of the slide assembly, carrying a bar magnet attached on its side, and therefore the motor position is detected by a magnetic sensor located on the side of the module [102].	29
Figure 3.11: (a) Calibration results: linear response for all FBGs when the tip is loaded along x and y axes. (b) Computed forces versus the actual forces along x and y axes. (c) The histogram of the residual errors [104].	31
Figure 3.12: Varying nonzero forces are observed due to inner actuation forces as the jaws are opened and closed. The force profile varies depending on the jaw type. Artifact on sensor reading while using jaws for (a) thicker membranes and (b) thinner membranes. The force shift is consistent throughout the open/close cycles, and can be modeled as a function of the motor position [103].	32
Figure 3.13: The implemented correction routine for compensating against the inner actuation forces and maintaining the accuracy of force readings while opening and closing the grasper jaws [103].	34
Figure 3.14: The effect of grasped layer thickness on the force sensing accuracy. A multilayered bandage was grasped from 3 different segments to compare the measured forces with the actual loading on the tool tip. Measured forces normally deviate from the ideal line more if thicker layers are grasped. The correction routine ensures that the measured tip forces remain accurate regardless of the thickness of the grasped material [103].	35
Figure 3.15: Transient response characteristics of the force sensor: (a) setup, (b) step response of the sensor. Simulated response of a first order system with a time constant of 0.005 seconds matched the measured force profile [104].	36
Figure 3.16: Manually-actuated 3-DOF force-sensing micro-forceps for membrane peeling: Basic components and actuation principle [105].	38
Figure 3.17: Topology optimization: (a) Design domain and boundary conditions; (b) final concept output; (c) simplified design and associated parameters; (d) levels used in the optimal value search [106].	39
Figure 3.18: The effect of design parameters on the opening compliance and grasping stiffness. The optimization goal is to maximize both functions while satisfying the limiting factors [106].	41
Figure 3.19: Optimal jaw design: (a) Dimensions (b) Stress distribution while opening the jaws with 1N of actuation force, (b) Fatigue life under 1 N cyclic loading: more than 60,000 cycles of actuation cycles before failure based on nitinol use ($E=41$ GPa, $\nu=0.33$) [106].	42

Figure 3.20: Induced normal strain on each FBG sensor under principle loading conditions. Linear rise in strain with increasing tip load, and success in decoupling lateral-axial forces [106].	44
Figure 3.21: Force-sensing micro-forceps conceptual overview. (a) Epiretinal membrane peeling. (b) Axial FBG in the center: actuation force (F^{act}) degrades the sensor reading. (c) Axial FBG attached on the flattened arm of the jaw: bypassed F^{act} and direct exposure to tool tip forces (F^{ax} and F^{tr}) [108].	46
Figure 3.22: (a) Fabricated prototype and experimental setup. (b) Thermal drift in lateral (FBGs 1-3) and axial (FBG 4) sensor readings. (c) Linear correlation between the common mode of lateral FBGs and the axial FBG [108].	51
Figure 3.23: Lateral (FBGs 1-3) and axial (FBG 4) sensor response to loading (0-25 mN) at the tool tip for three different orientations ($\theta = 0^\circ, 45^\circ, 90^\circ$) [108].	53
Figure 3.24: Computed transverse and axial forces vs. the actual values. Similar accuracy for both methods in estimating the transverse load, better performance with the polynomial method for estimating the axial load [108].	54
Figure 3.25: (a) Epiretinal membrane peeling using our motorized force-sensing micro-forceps with the force-sensitive region of the tool inserted into the eye through a 20 Gauge sclerotomy. (b) Components of the design (c) Motorized actuation mechanism driving the guide tube up/down for opening/closing the jaws. (c) The tool coordinate frame and FBG sensor configuration. The axial FBG sensor (FBG 4) at the center inside the guide tube and three lateral FBG sensors integrated on the guide tube (FBGs 1-3) measure axial (F_z) and transverse forces (F_x and F_y) at the tool tip, respectively [110].	55
Figure 3.26. (a) The standard 23 Gauge disposable micro-forceps by Alcon Inc. vs. the manufactured prototype of our motorized force-sensing micro-forceps. (b) Close-up view of the distal force-sensing segment. A fine-polished filleted stainless steel piece (23 Gauge trocar) was bonded at the distal end of guide tube, to modify the jaw/guide tube interface so that the reaction force during tool actuation is consistently smaller and its adverse influence on axial FBG sensor is minimal [110].	56
Figure 3.27: (a) Geometric parameters of the jaw model, guide tube and the trocar attachment used in finite element simulations, (b) The micro-forceps kinematics with and without the trocar attachment. While fully open, the jaw tips are 0.7 mm apart; full closure requires driving the motor about 1240 μm without the trocar and 1400 μm with the trocar. An almost linear response is obtained with the trocar [110].	58
Figure 3.28: Finite element simulation results showing the axial FBG response to tool actuation for various levels of friction coefficient (C_f) at the jaw/guide tube interface (a) without the trocar and (b) with the trocar attachment at the guide tube's tip. Larger friction coefficients produce more strain. Lower strain levels are observed with the trocar. (c) The force-induced strain on the axial FBG vs. the applied axial load when the trocar attachment is used: the strain is linearly correlated with the axial load, and the sensitivity is almost identical for all levels of jaw opening (JO) [110].	61
Figure 3.29: Force computation algorithm using an experimentally identified model to cancel the actuation-induced drift in FBG sensor readings based on the motor position	

and two distinct (linear and nonlinear) methods for transforming the corrected sensor readings into transverse (F_x and F_y) and axial (F_z) force information [110]..... 63

Figure 3.30: Experimental setup. (a) The 3-DOF force-sensing micro-forceps was mounted on two rotary stages to control the roll (α) and pitch (β) angles of the tool. (b) By hanging washers onto the grasped hook, the magnitude of the applied force was changed. (c) Modulating the tool orientation (α and β), thus the direction of the applied force, various combinations of F_x , F_y and F_z were applied at the tool tip [110]..... 65

Figure 3.31: The effect of opening/closing the forceps on the lateral (FBG 1,2,3) and axial (FBG 4) sensors while operating (a) in air and (b) in water. The actuation induces high levels of wavelength shift on the axial sensor (up to 167 pm in air and up to 222 pm in water), which exhibit a consistent variation among repeated trials, and hence can be modeled as a function of motor position for each environment [110]..... 67

Figure 3.32: Response of (FBG 1,2,3) and axial (FBG 4) sensors during two sample loading conditions: (a) pure transverse loading and (b) pure axial loading. Probability distribution of Bragg wavelength shift errors for lateral (c-e) and axial (f) FBG sensors under 168 different combinations of transverse and axial forces. The standard deviations are less than 0.6 pm for the lateral FBGs and is about 1.96 pm for the axial FBG, indicating a highly repeatable response [110]. 69

Figure 3.33: Thermal drift in lateral (a) and axial (b) FBG sensor readings during 4 test sessions each spanning a period of 225 minutes. (c) The Bragg wavelength shift in the axial FBG sensor shows a linear correlation with the common mode (average Bragg wavelength shift) of lateral FBG sensors with a proportionality constant of $\kappa=0.92$ [110]. 71

Figure 3.34: Global linear calibration results for transverse forces: (a,b) Calculated F_x and F_y versus the actual values. (c,d) residual errors versus the actual forces, (e,f) probability distribution of residuals (bin size = 0.1 mN). The global linear fitting can predict the applied forces with an rms error of 0.25 mN and 0.52 mN for F_x and F_y , respectively [110]..... 73

Figure 3.35: Axial force (F_z) computation error versus the concurrent transverse load along (a) x-axis and (b) y-axis based on the global linear calibration. The magnitude of errors rapidly grows when larger transverse forces are applied, deteriorating the linearity of the axial FBG [110]. 74

Figure 3.36: Axial force computation results for local linear calibration using samples with limited roll ($\alpha \leq 30^\circ$) and pitch ($\beta \leq 15^\circ$) angles (black), and for global nonlinear calibration (blue): (a,b) The comparison of computed values to the actual force level, (c,d) variation of error with respect to the axial force magnitude, (e,f) probability distribution of residuals (bin size = 0.1 mN). The latter provides almost the same sensing accuracy as the local fitting, but for the entire range of force directions [110]..... 75

Figure 3.37: Results of local nonlinear calibration using samples with limited roll ($\alpha \leq 30^\circ$) angles for computing F_x (red), F_y (green) and F_z (blue): (a-c) The comparison of computed values to the actual force level, (d-f) variation of residuals with respect to the force magnitude, (g-i) probability distribution of residuals (bin size = 0.1 mN). By limiting the roll angle ($\alpha \leq 30^\circ$), samples with excessive F_y (>11.7 mN), which are not very

likely in an actual membrane peeling operation, were excluded from calibration. The rms errors in estimating F_x , F_y and F_z are 0.12, 0.07 and 1.76 mN respectively [110]..... 77

Figure 3.38: Results of the validation experiment for computing F_x (red), F_y (green) and F_z (blue): (a-c) The comparison of computed values to the actual force level, (d-f) variation of residuals with respect to the force magnitude, (g-i) probability distribution of residuals (bin size = 0.1 mN). Tested data consists of loading conditions that were not involved during calibration. The identified local nonlinear regression can still accurately predict the applied forces with rms errors of 0.16, 0.07 and 1.68 mN for F_x , F_y and F_z , respectively [110]..... 78

Figure 3.39: Conceptual design of our motorized force-sensing microneedle for retinal vein cannulation. The needle has a modular design that allows an easy integration with robotic devices, such as the handheld micromanipulator: Micron. 82

Figure 3.40: (a) Components of the design: force sensitive motorized unit, and the disposable prebent needle (b) Assembled prototype (c) Tool actuation: the microneedle is exposed by retracting the guide tube as much as 2.4 mm..... 83

Figure 3.41: Sample integration of the motorized force-sensing microneedle with a handheld micromanipulator, Micron. (a) The controller board for the tool’s motor was located on Micron’s handle inside the two hand pieces. (b) A force-sensing resistor was mounted on one of the hand pieces, under the operator’s thumb, to control the microneedle’s actuation by squeezing or releasing the hand piece. The injection line passes through the center of the instrument and is connected to a syringe via polyethylene tubing to deliver fluid to the microneedle..... 86

Figure 3.42: Motorized actuation of the tool for retracting the guide tube back and exposing the prebent microneedle. The inner tube of the tool shaft delivers the injection fluid, while 3 FBG sensors on the outer tube sense transverse forces on the microneedle. 87

Figure 3.43: (a) Setup for calibration experiments: The force-sensing micro-needle was held horizontal and mounted on a rotary stage to modulate its axial orientation (θ). (b) The microneedle tip was inserted into a soft plastic piece carrying a wire hook. Forces were applied at the needle tip by hanging washers of known weight on the hook..... 88

Figure 3.44: (a) Calibration results: linear response for all FBGs when the needle is loaded along x and y axes. (b) The force-sensing coordinates relative to the target vein and the histogram of residual errors in each direction. (c) Computed forces vs. the actual forces along the x and y axes. 89

Figure 3.45: Effect of actuation on the sensed forces during 3 cycles of cover/expose cycles. Although the microneedle is not contacting any tissue, covering and exposing the microneedle shifts the force readings by about 2 mN in F_x and 6 mN in F_y with a consistent behavior. In practice, these undesired components due to actuation can be eliminated from the force readings by automatically rebiasing the FBG readouts once the motor position reaches the fully exposed position (2400 μm)..... 91

Figure 3.46: (a) Coordinate systems associated with the robotic systems and force-sensing tools. (b) Setup for finding the transformation from the robot’s tool mount frame to the force-sensing tool’s coordinate system for their integrated use..... 92

Figure 4.1: (a) Setup for membrane peeling experiments on 12-day fertilized chicken eggs using the Steady-Hand Eye Robot and a force-sensing micro-forceps.	102
Figure 4.2: Membrane peeling forces on chicken embryo from a test sample: (a) completely unaided, (b) robot assisted with only auditory force feedback, (c) robot assisted with only force scaling, (d) robot assisted with auditory force feedback and force scaling. High frequency oscillations in delaminating forces are reduced by steady-hand robot. Force scaling provides smoother force variations. Auditory feedback (yellow line is the threshold for the caution signal and red line indicates the threshold for the danger warning) is beneficial for keeping the forces within the safe operation zone (below the red line).	104
Figure 4.3: Setup for membrane peeling experiments using the Micron system with a force-sensing hook [128].	105
Figure 4.4: Experiments were done on two types of phantoms: (a) bandage phantom and (b) inner shell membrane of raw chicken eggs [128].	105
Figure 4.5: Force sensing Micron control scheme. The measured forces on the tool tip are translated into auditory signals to guide the surgeon while Micron suppresses hand-tremor in another loop [128].	107
Figure 4.6: Measured membrane peeling force samples for four different cases using bandage phantom. Maximum allowable operation zone (3.5 mN - 7mN) is between the green dashed and red solid lines. High frequency oscillations in the force and speed due to hand tremor (left) are eliminated when Micron is activated (right). Without the auditory sensory substitution, the exerted forces may exceed the safety threshold shown in red (upper), whereas with the auditory feedback they are mostly maintained at a safe level (lower).	108
Figure 4.7: Frequency analysis of recorded forces for all 4 cases on bandage phantom: with auditory feedback (left), without auditory feedback (right), with tremor suppression (blue), and without tremor suppression (red).	108
Figure 4.8: Micron aided to free-hand force magnitude ratio with respect to frequencies. Significant reduction in 2-20 Hz forces: (a) 60%-90% with auditory feedback, (b) 70%-90% without auditory feedback.	109
Figure 4.9: Membrane peeling forces on raw chicken eggs:(a) completely unaided, (b) only Micron aided, (c) only with auditory feedback, (d) Micron aided with auditory feedback. Oscillations in delaminating forces are highly reduced by Micron while auditory feedback could prevent application of forces above 7 mN.	110
Figure 4.10: Frequency analysis of recorded forces on raw chicken eggs: with tremor suppression (blue), and without tremor suppression (red).	111
Figure 4.11: Setup for membrane peeling experiments using (a) the Steady-Hand Eye Robot with a force-sensing micro-forceps, and (b) Micron with a force-sensing hook. [129].	112
Figure 4.12: Membrane peeling procedure using bandage phantom (left) and inner shell membrane in chicken embryo (right) [129].	112

Figure 4.13: System overview with robotic assistance and integrated force sensing. Auditory feedback is provided to the user based on sensed forces at the tool tip.	114
Figure 4.14: Measured peeling forces (blue) using bandage phantom for all trials (10 trials/case). Auditory feedback helps in keeping forces below the safety threshold (red horizontal line). Robotic assistance helps in eliminating oscillations. Additional effort and longer duration in grasping the bandage while using micro-forceps with the Steady-Hand Robot due to additional system inertia.....	116
Figure 4.15: Frequency analysis on forces applied in all trials on bandage phantom. 60-80% reduction in 2-15 Hz oscillations by using Micron (left), Steady-Hand Eye Robot (right) [129].....	117
Figure 4.16: Measured peeling forces (dark blue) using ISM of chicken embryo for all trials (2 trials/case). Shorter multiple peeling periods (light blue rectangles) as opposed to bandage phantom trials [129].....	119
Figure 4.17: Frequency analysis on forces applied in all trials on ISM of chicken embryo. Reduction in 2-15 Hz oscillations: 40-50% by Micron (left), 50-60% by the Steady-Hand Eye Robot (right). 10 Hz peak corresponding to physiological hand tremor is not visible while using hook (upper) due to the inability to grasp, hence the tissue slippage [129].	120
Figure 4.18: Setup for membrane peeling experiments in an artificial eye model with bandages using Micron with a force-sensing micro-forceps [102].....	122
Figure 4.19: Measured peeling forces using bandage phantom for all trials (5 trials/case). One of the trials was shown in darker color to highlight the important characteristics. Auditory feedback helps in keeping forces below the safety threshold (7.5 mN). The peeling speed is kept below 0.5 mm/s successfully in all cases, but with much difficulty when Micron is off. The tremor canceling feature of Micron helps in reducing high frequency oscillations in both tip force and tip velocity [102].	124
Figure 4.20: Tool tip trajectory during the delaminating period. The arrow indicates the peeling direction. Higher positioning accuracy and smoother paths are observed with Micron use. [102].....	125
Figure 4.21: Frequency analysis on tip position and peeling forces. Highly correlated spectral density traits due to strong grasping provided by forceps use: a peak at 9 Hz due to physiological hand tremor and a 60-95% reduction in 2-20 Hz oscillations in both tip force and position spectra [102].....	126
Figure 4.22: System overview. A handheld micromanipulator (Micron) was combined with a force-sensing micro-forceps to assist membrane peeling previously. A novel feature, vibrating the tool tip along the peeling direction, is added to the system to facilitate membrane delamination (shown in orange) [103].	127
Figure 4.23: Setup for membrane peeling experiments on bandage phantom and inner shell membrane of raw chicken eggs [103].	129
Figure 4.24: Sample force measurements while peeling off bandages with a force-sensing micro-forceps under five different conditions with varying micro-vibration frequency.	131

Figure 4.25: Power spectra of tip position and tip forces measured while peeling bandages (3 arbitrary trials per set are shown). Freehand trials exhibit a peak at 10 Hz due to physiological hand tremor. 80-90% reduction in 2-20 Hz oscillations and visible peaks at 10, 30, and 50 Hz at both spectra reveal success in tremor canceling, strong grasping, and accurate fast tip vibrations [103]...... 132

Figure 4.26: Sample force measurements while peeling off the ISM of raw chicken eggs with a force-sensing micro-forceps under five different conditions with varying micro-vibration frequency. 133

Figure 4.27: Power spectra of tip position and tip forces measured while peeling inner shell membrane of raw chicken eggs (3 arbitrary trials per set are shown). More deviation between trials as compared with bandage phantom, but the main traits were preserved: 45-90% and 5-85% reduction in 2-20 Hz band of tip position and force spectra respectively with tremor cancellation; visible peaks at 10, 30, and 50 Hz at both spectra [103]...... 134

Figure 4.28: Experimental setup: (a) To ensure constant peeling speed, the phantoms were moved on a linear stage. (b) Peeling inner shell membrane of raw eggs produces triangular shaped strips, and requires both tearing and delaminating forces. Using sliced egg shell membranes (c) and bandages (d), the effect of tearing forces and varying membrane width throughout delamination were avoided [104]. 137

Figure 4.29: (a) A single bandage strip was peeled at constant speed (0.15 mm/s) and brushed back on several times. The required delamination force leveled off after approximately the 10th peel. (b) Sample recordings for 3 different micro-vibratory settings: Increasing the micro-vibration amplitude causes larger oscillations in force, the micro-vibration frequency correlates with the frequency of oscillations in the peeling force. 140

Figure 4.30: Variation of average peeling force (F_{average}) with respect to the (a) frequency and (b) amplitude of micro-vibrations. Dotted lines represent the mean, and the shaded region is ± 1 standard deviation. Inducing micro-vibrations at an "optimal" frequency among the tested cases—at 30 Hz for bandages, and at 50 Hz for the egg shell membranes within the tested frequency interval—minimized F_{average} . The force-frequency trend varied depending upon the peeling speed (0.15 mm/s in blue vs. 0.30 mm/s in striped grey) as seen from bandage peeling with 100 μm vibrations. Increasing the amplitude of micro-vibrations lowered F_{average} in most cases, except for bandage peeling with 50 and 100 μm vibrations at 10 Hz..... 142

Figure 4.31: Variation of maximum peeling force (F_{peak}) with respect to micro-vibration amplitude at different frequencies while peeling bandages with 0.15 mm/s speed. Solid lines represent the mean, and the shaded region is ± 1 standard deviation. Above 10 Hz, the peak force increased with greater micro-vibration amplitude due to larger fluctuations in force. 144

Figure 4.32: Experimental setup for testing the automatic tissue release feature. (a) Micron with the motorized force-sensing micro-forceps was held fixed in a vise while the phantom platform with attached bandages was mounted on a linear stage. (b) A bandage strip on the phantom was grasped using the micro-forceps, and the phantom was driven

relative to the tool by actuating the linear stage to perform the peel at constant speed. To simulate nonuniform tissue properties, a second layer (shown in orange) was attached onto the bandage strip after about the 5th mm..... 146

Figure 4.33: Sensed forces while peeling off a bandage strip at a constant rate (a) without and (b) with the automatic tissue release feature. With the automatic tissue release, after reaching the double layered segment of the phantom, when the force reaches a critical level (dashed red line at 7.5 mN), the forceps jaws are quickly opened (motor position=800 μ m) to release the tissue and prevent excessive forces..... 147

Figure 4.34: Forces measured while peeling the bandage (a) with auditory force feedback and (b) with the automatic tissue release feature. With the auditory feedback, it's challenging to adapt to the changing phantom properties and peel off the double layered segment of the bandage while keeping the applied force below the safety threshold (dashed red line at 7.5 mN). The automatic tissue release mode prevents forces above the threshold, but may lead to longer task completion time since the tissue may need to be regrasped multiple times. In this sample trial, 8 releases were recorded during the peel, which are marked as red dots (micro-forceps' motor position=800 μ m). 149

Figure 5.1: (a) Setup for vein cannulation experiments on CAM of 12-day fertilized chicken eggs. (b) Using a linear stage, the force-sensing microneedle was driven into the target vein on CAM at constant speed while its position was recorded by the ASAP tracker. (c) After vein puncture is detected, air injection was started. The success of cannulation was assessed based on the observation of air bubbles inside the vein. 157

Figure 5.2: (a) A representative cannulation trial from each speed setting. The sharp drop in force signifies vessel puncture and generates an alarm to warn the operator. (b,c) Force statistics for 8 trials per speed setting. 158

Figure 5.3: Experimental setup for cannulation experiments using an artificial phantom. (a) Stretched vinyl membranes simulating the vein walls were punctured using the force-sensing micro-needle under an ophthalmic microscope. (b) An acrylic insert with channels (1mm wide) was used to tension the vinyl layer. The phantom was placed inside a container filled with balanced salt solution (BSS). To approach the channels on the phantom, the needle was inserted through the trocar on the movable (as shown with red arrows) sclerotomy port. A digital microscope was used to monitor the operational area from the side and assess the moment of puncture: (c) before puncture, (d) after puncture. 162

Figure 5.4: Measured forces during 20 consecutive punctures on the stretched vinyl membrane phantom. Grey zones correspond to the needle insertion phase while the white regions are for the retraction of the needle after puncture. During the insertion phase, most of the forces are along the needle axis (y-axis of the tool), with minor side load ($F_x < 5$ mN). The peak force before puncture ranges from 7.72 mN to 13.48 mN as the stretch of the phantom was adjusted targeting a range of 8-15 mN. The rate of force drop at the instant of piercing the membrane (marked with red dots in the lower plot) vary with a minimum of -35.21 mN/s and maximum of -8.73 mN/s for this set of trials. 163

Figure 5.5: Measurements from a sample trial for each user: needle tip force (F_x in grey, F_y in red), needle tip position (x in grey, y in red, z in black), the variation of force

($dF_{needle}dt$) and the inner product of tool velocity and variation of force ($dF_{needle}dt \cdot dp_{needle}dt$). The timing of the actual puncture in each trial is marked with a green dashed line. (a) Data for the first user: The elevated threshold (the dashed blue line at $dF_{needle}dt = -19.67$ mN/s) may intersect the time derivative of force multiple times, and may trigger faulty detections after the actual puncture. (b) Data for the second user: The low threshold (the dashed black line at $dF_{needle}dt = -49.63$ mN/s) fails to intersect the force variation curve while the elevated threshold intersects it twice, leading to a faulty detection before the actual puncture using the force-based method. In both trials, the inner product of the force variation and tool velocity clearly displays the instant of actual puncture with a prominent positive peak. The force-and-position-based method, relying on the inner product value, is able to distinguish the event of puncture. 168

Figure 5.6: The control scheme of the integrated system for Micron. The time derivative of needle position and force are computed and filtered. The inner product of the two turns positive at the event of vein puncture. When puncture is detected (1) the operator is informed with an alarm sound, and (2) Micron operation mode is switched from default "only tremor canceling" to "active position holding". 171

Figure 5.7: Experimental setup. (a) An ophthalmic microscope was used to monitor the operation site, and the optical sensing interrogator acquired the readings from the force-sensing microneedle. (b) Trials were done on the vinyl phantom submerged in BSS. (c) The experimental task was to approach the vinyl membrane inserting the force-sensing micro-needle through the sclerotomy port, puncture it which is detected by the force-and position-based method, and maintain it fixed during the following 45 seconds. 172

Figure 5.8: Typical measurements taken during trials of the first user using the tremor canceling (blue) and automatic position holding (red) features of the system. (a) Forces on the needle: mostly along the y-axis with a gradual rise during insertion and a sharp drop at the instant of puncture. (b) Position of the needle remains fixed with the position holding mode in contrast to the fluctuations with only tremor canceling. (c) The event of puncture: a positive peak in the inner product of needle velocity and force variation vectors. (d) Recorded needle tip trajectories for 3 representative trials of each mode. Position holding mode significantly reduced tool tip deviation from the puncture point. 174

Figure 5.9: The total time that the needle tip was maintained inside various sizes of zones around the puncture point using the TCM (in blue) versus the PHM (in orange) features. The solid bars show the mean, and the error bars represent the maximum values. The active position holding helps in maintaining the needle tip inside the vein for a significantly longer time, especially for veins smaller than 300 μ m. 177

Figure 5.10: The performance of each user in maintaining the needle around the point of puncture (zone size=distance from the puncture point). User 1 is a non-surgeon with extensive experience on the robotic system. Users 2 and 3 are, respectively, an ophthalmology fellow and an expert vitreoretinal surgeon with some training on the robotic system. The solid bars show the mean, and the error bars represent the maximum and minimum values. The automatic position holding mode aids in maintaining the needle close to the puncture point for a longer period for all users. 178

Figure 5.11: The variation of time that the needle is maintained in different zones as a function of the hold duration for each user using the TCM (blue) vs. the PHM (orange). The ideal line (dashed grey) corresponds to keeping the needle inside the zone throughout the entire hold period. The performance of each user is closer to the ideal line when the PHM is used..... 180

Figure 5.12: Deviation from the puncture point vs. the hold time for each user. The solid bars show the mean distance from the puncture point, and the error bars represent the maximum values. A longer hold time causes the needle to move away from the puncture point more. The automatic position holding mode significantly helps in keeping the needle tip proximal to the puncture point. 181

Figure 5.13: The experimental setup for evaluating the performance of (a) Micron and (b) SHER on an artificial phantom. Stretched vinyl membranes, simulating the vein walls, were punctured open-sky using the force-sensing microneedle. 182

Figure 5.14: Sample measurements from the trials using the default modes of two robotic platforms: Active tremor canceling mode of Micron (blue), and cooperative control of SHER (red). Large deviations from the puncture point are observed in both systems. Modulating the controller gains on the SHER system does not lead to a significant improvement in terms of reducing the needle movement after the puncture. 184

Figure 5.15: Sample measurements from the trials using the automatic position holding modes of two robotic platforms: Micron (blue) and SHER (red). Deviations from the puncture point are significantly reduced with Micron, and almost eliminated with SHER. Modulating the controller gains on the SHER system does not change the performance. 186

Figure 5.16: Experimental results: Average deviation from the puncture point during the initial 15, 30 and 45 seconds after the puncture. The solid bars represent the mean, and the error bars show ± 1 standard deviation. (a) Changing the controller admittance gain of SHER does not create a statistically significant difference. (b) Activating the force-based puncture detection and PHM significantly reduces the deviation. (c) When Micron and SHER are used in their normal operating modes, TCM and CCM respectively, slightly larger deviation is observed in SHER trials. (d) When Micron and SHER are used with puncture detection and PHM, SHER system fixates the needle position better since Micron has a smaller workspace and its actuators may saturate. 187

CHAPTER 1 : INTRODUCTION

1.1 Thesis Statement

Continual monitoring of tool-tissue interaction forces combined with augmented control methods of robotic assistance provides a safer and easier operation during existing common procedures in vitreoretinal surgery, and can promote new and more effective treatment methods that cannot be performed due to their high risks in conventional manual microsurgery today.

The elements comprising the argument:

- Force sensing mechanisms that can precisely detect the very fine forces between the surgical instrument and the retina during microsurgery.
- Tool architectures with integrated force sensing mechanisms that preserve the functions of standard retinal surgery tools and that can operate in combination with multiple robotic platforms.
- Methods of robotic control based upon the acquired tool-tissue interaction force information to promote safety and surgeon comfort during routine procedures, reduce complications, diminish surgical risks, and potentially enable novel and more effective treatment methods.

1.2 Vitreoretinal Surgery

Vitreoretinal surgery refers to the subset of intraocular surgical procedures that treat retina related disorders, including but not limited to retinal detachment, macular pucker, and macular holes. The typical setup in the operating room during vitreoretinal surgery is shown in Fig. 1.1. The lead surgeon generally sits above the head of the patient while an ophthalmic operating microscope provides a magnified view of the interior of the eye. To

bring current surgical tools into the eye, typically a three-port approach is followed where three incisions are made in the pars plana, avoiding the lens, the retina, and bleeding. Then inserting tools through these ports, the surgeons begin to operate. The diameter of the ophthalmic tools range from 27 Gauge ($\text{\O} 0.41\text{mm}$) to 20 Gauge ($\text{\O} 0.91\text{mm}$). In order to provide tool access to the posterior of the eye, the vitreous is removed via vitrectomy. The first incision in the three-port approach is the infusion sclerotomy (port 1 in Fig. 1.1.b), typically in the inferotemporal (lower lateral) quadrant. The infusion line is secured with cannula/trocar or with suture. This infusion supplies saline liquid to maintain the intraocular pressure. The other two incisions (ports 2 and 3 in Fig. 1.1.b) are for inserting an endoilluminator and the surgical instruments such as a vitreous cutter, pick, forceps, scissors or a laser probe. After vitrectomy, the surgeon can proceed with additional surgical treatments, such as membrane peeling, laser, air-fluid exchanges or even retinal vein cannulation.

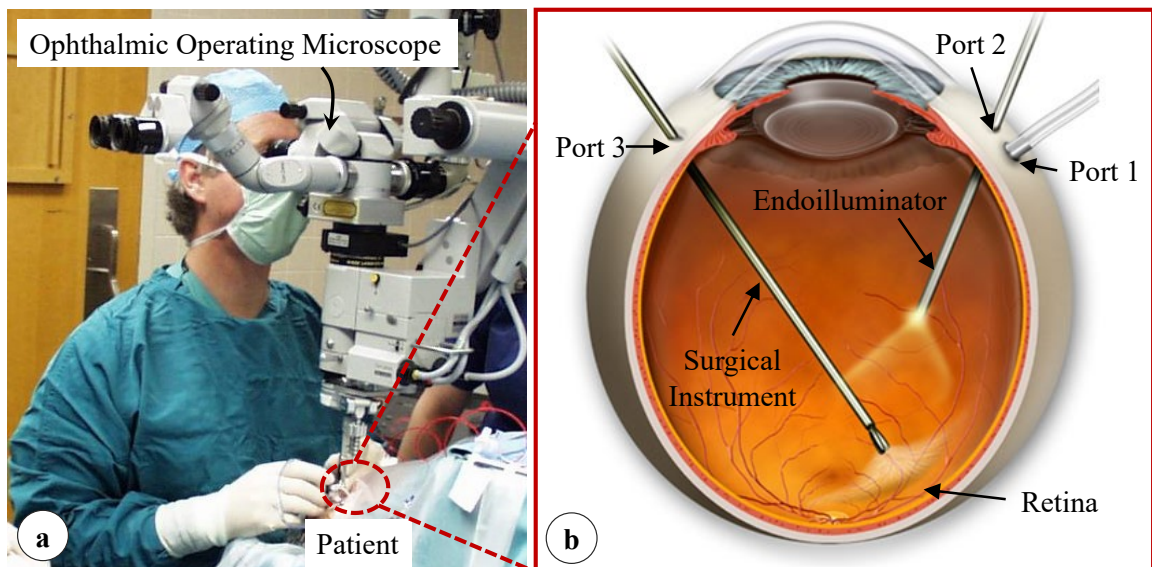


Figure 1.1: (a) The typical setup in the operating room during vitreoretinal surgery. (b) Tool-retina interaction after pars plana vitrectomy. (Image credit to Mark Erickson and Jireh Design)

1.2.1 Epiretinal Membrane Peeling

Vision-threatening diabetic retinopathy afflicts 8.2% of diabetic adults over 40 in the US [1], or 0.6% of the overall population within this age range [2]. By 2050 the number of Americans with vision-threatening diabetic retinopathy within this age range is estimated to triple to 3.4 million [3]. Membrane peeling is an essential and challenging component of the surgical treatment of advanced diabetic retinopathy [4]. It also plays an important role in treating macular pucker [5], prevalent in 3.8% of the population aged 45-84 [6], as well as macular holes [7], affecting approximately 0.3% of Americans over 50 [8]. Epiretinal membrane surgery is the most common vitreoretinal surgery performed, over 0.5 million times annually, as reported by the Centers of Medicare and Medicaid Services [9]. The procedure involves the dissection of a thin (micron-scale) fibrocellular tissue adherent to the inner surface of the retina, which requires first inserting the surgical tool tip to a desired depth for lifting the membrane edge without harming the underlying retina. After grasping the membrane edge using mostly a micro-forceps tool, the surgeon pulls the membrane away from the retinal surface very slowly trying to avoid deleterious force transfer to the retina.

1.2.2 Retinal Vein Cannulation

Retinal vein occlusion (RVO) is one of the most common retinovascular diseases, affecting approximately 16.4 million people worldwide [10] and has a prevalence of 1.8% and 0.5% for central and branch retinal veins, respectively [11]. RVO typically occurs when there is thickening of the crossing artery, low flow, hyper-coagulability, or thrombosis in the central or the branched retinal veins of the eye. This results in the affected retinal vein becoming dilated, tortuous and hemorrhaging into the retinal tissue.

In many cases, the resulting ischemia leads to macular edema and even death of retinal cells. Other serious complications of RVO include neovascularization, vitreous hemorrhage, and retinal detachment [12,13]. Patients with RVO are reported to experience blurred or distorted vision, and in severe cases blindness results [14].

The available treatments for RVO – including photocoagulation, hemodilution, radial optic neurotomy, vitrectomy and intra-vitreous injections – currently are focused on limiting the damage induced by the occlusion, rather than directly resolving the occlusion [15-19]. Retinal vein cannulation (RVC) is an experimental surgical procedure proposed to treat RVO by direct therapeutic agent delivery methods to the site of occlusion. The procedure involves three main steps: (1) accurately bringing a sharp tipped cannula onto the occluded retinal vein, (2) puncturing through the vein wall and precisely halting the cannula tip at the right depth, and (3) maintaining the cannula inside the vein for several minutes, during which time the therapeutic agent – presently tissue plasminogen activator (t-PA) [20] or ocriplasmin [21] – is delivered to dissolve the obstructing thrombus. This is a very demanding and risky procedure because of the small size and fragility of retinal veins – especially if the occlusion is at a branch retinal vein (typically $\text{Ø} < 200 \mu\text{m}$) rather than the central vein [22].

1.3. Challenges in Vitreoretinal Surgery

Arguably the most technically demanding field of ophthalmic surgery, vitreoretinal practice has faced significant challenges due to present technical and human limitations. This section presents a summary of the main difficulties associated with the two targeted applications in this domain: epiretinal membrane peeling, and retinal vein cannulation.

1.3.1 Epiretinal Membrane Peeling

Membrane peeling procedures consist broadly of two main phases. The first phase is approaching the membrane-retina interface, creating an edge, and grasping/lifting the membrane edge using either a hook or a micro-forceps tool. To then dissect the membrane off the retina, very precise tool manipulation and careful monitoring of interaction between the tool and the tissue, as well as the effect of applied forces on the tissue. Applied forces may injure the retina at the point of tool contact and also remote from the point of tool contact, if the forces applied result in traction and tearing. Therefore, the second phase is membrane delamination from the retina by moving the membrane grasping tool strategically and slowly in order to limit the forces exerted on the retina. Excessive peeling forces can damage retinal tissue and its blood supply [23] and cause serious complications such as iatrogenic retinal breaks [24], vitreous hemorrhage [25] and subretinal hemorrhage [26], leading to potentially irreversible damage and loss of vision. Prior work has found that iatrogenic retinal breaks, not related to the sclerotomy, occur in as many as 9.6%-10.7% of cases, and may result in retinal detachments in 1.7%-1.8% of cases [27,28]. The problem is exacerbated by the fact that the forces involved are below the tactile perception threshold of the surgeon in the majority of instrument-to-tissue contact events in retinal microsurgery. Among these forces, 75% were shown to be less than 7.5 mN in porcine cadaver eyes and only 19% of events with this force magnitude can be felt by surgeons [29]. Currently, the knowledge, and hence skill, to apply appropriate peeling forces is acquired mostly through visual substitution and is qualitatively conveyed from expert surgeons to trainees through years of training and many hundreds of case observations. Continual quantitative monitoring of

tool-tissue interaction forces via a sensitized instrument is becoming appreciated to be essential to inform the operator and limit applied forces to a safe level either manually through auditory feedback or via robotic assistance [30].

1.3.2 Retinal Vein Cannulation

Cannulation of retinal vessels has been previously explored using a variety of *in vivo* models. Prior work shows that puncturing larger vessels in porcine eyes is technically easier than piercing the distal smaller veins [31]. Nevertheless, when a small branch vein is occluded, cannulation of a nearby larger vessel may diminish the effectiveness of the treatment [32]. To easily pierce the retinal vasculature and enable injection directly into such small branch veins, glass micropipettes with very fine sharp tips have been used [33-42]. However, the transparent small tips are hard to visualize under the microscope and the fragile glass structure raises safety concerns for real time intraocular use. As alternatives, stainless steel microneedles ($\text{\O} 50 \mu\text{m}$) have been used to inject balanced saline solution to disrupt the clot [43], or soft thin ($\text{\O} 100 \mu\text{m}$) wires have been used to advance through the lumen of a 37-Gauge needle and mechanically fragment the thrombi [44]. Tests on porcine eyes showed feasibility, and this was further supported by successful clinical demonstrations on human retinal veins with few intraoperative and postoperative complications [45]. In these approaches, using a curved cannula or an angulated tip was found to enable a more gradual and therefore safer approach into the vein, as well as to allow easier venous puncture, and improve safety by reducing the likelihood of double puncturing through the vein. However, there were challenges in introducing the bent tip into the eye through the sclera, requiring a larger incision and introduction of a trocar through the sclera. In order to enhance the intraocular distal dexterity, a stent deployment

unit with an adjustable approach angle via concentric tubes was devised, and the optimal approach angle while cannulating vasculature on the chorioallantoic membrane (CAM) of fertilized chicken eggs – an accepted *in vivo* model for RVC studies [46] – was explored, revealing a range of 25°-35°, which is not easy to achieve via typically straight instruments [47]. Flexible pre-bent stainless steel microneedles, which are normally held straight inside a protective shaft to be more easily introduced into the eye through the sclerotomy, have been developed so that, when fully deployed, the angle between the needle tip and vein surface falls within the identified optimal range [48,49].

Despite the aforementioned progress in improving the available instruments and realizing effective RVC, the procedure still remains at the limit of human performance. There are three main challenges that hinder the success of cannulation. First, a proper cannula is required that is not only thin enough to be inserted into the retinal vein ($\varnothing < 100 \mu\text{m}$) but can also withstand the forces while puncturing the vein and can easily be seen under the microscope. This challenge has partially been resolved by using stainless steel microneedles in replacement of the transparent and fragile glass micropipettes. The second challenge is the physiological hand tremor of the vitreoretinal surgeon, which is comparable in amplitude to the size of retinal veins [50]. Due to tremulous tool tip motion, it is hard to accurately aim at the thin branch retinal veins and to maintain the cannula within the lumen after piercing the vein throughout the drug delivery which can take several minutes [20]. The third challenge in RVC stems from the fact that cannulating retinal veins occurs at forces that are almost imperceptible to humans, which makes it very hard to identify the instant of venous puncture, halt needle advancement and appropriately begin the injection of agents (t-PA or balanced saline solution) at the

correct depth. Unlike cannulating retinal veins, conventional venipuncture occurs on larger structures and the resulting tactile forces are both perceptible and familiar to experienced phlebotomists. Specifically, the clinician can feel the moment of vessel puncture [51]. Tests on the CAM model [46] have confirmed that most RVC forces lie below the human perception threshold, yet there is still a sharp force drop upon venous puncture, as observed in a conventional venipuncture [52]. Continual monitoring of these very fine tool-tissue interactions via a very sensitive force sensor therefore has the potential to inform the operator of the moment of venous puncture during RVC. Combining a force-sensing cannulation tool with a robotic assistant is a powerful potential solution to overcome the challenges in RVC. Precisely identifying the moment of venous puncture and fixating the cannula to attain an extended period of intravenous cannula stability during delivery of the drug are each important to success.

1.4 Dissertation Overview

This dissertation presents novel sensitized tools for vitreoretinal surgery which can collect accurate tool-tissue force information, and which can be used on various robotic platforms to provide useful force feedback and motion guidance to surgeons during the procedure, and hence enable safer interaction with patients. The developed control methods fuse position and force information during the surgery and produce integrated assistive surgical systems that work in partnership with surgeons against the current limitations in vitreoretinal surgery, specifically focusing on membrane peeling and vein cannulation procedures.

Chapter 2 presents a review on the state of the art in force sensing and robotic systems that were motivated by ophthalmic applications.

Chapter 3 presents the developed surgical instruments that are sensitized to detect the very fine tool-to-tissue interaction forces during membrane peeling and retinal vein cannulation procedures.

Chapter 4 describes how the acquired force information from the sensitized instruments can be fused with the aid of robotic platforms for assisting the membrane peeling procedure, and evaluates the developed methods on two robotic platforms (Micron and the Steady-Hand Eye Robot) via phantom experiments.

In combination with the same robotic systems, Chapter 5 demonstrates methods of using the force information from the sensitized microneedle for better performance during retinal vein cannulation. Chapter 6 summarizes the contributions of this dissertation and proposes future research directions.

CHAPTER 2 : RELATED WORK

2.1. Force Sensing

There have been numerous studies proposing various techniques for quantifying tool-tissue interaction forces in microsurgery and minimal invasive surgery (MIS). Semiconductor strain gauges were used as force sensors on robotic microgrippers [53], though the resulting geometry had an overall length of 17 mm, width of 7.5 mm and thickness of 0.4 mm. Using microelectromechanical-systems-based diffractive optical encoders, a silicon-nitride cell manipulation probe was built providing a micronewton level force sensing [54]. For laparoscopic instruments in MIS, a tri-axial force sensor was developed based on intensity-modulated fiber optic sensing [55]. This sensor had a diameter of 5 mm and provided a force sensing resolution of 0.01 N. Another tri-axial fiber optics based sensor was developed for capturing forces during tissue palpation in MIS with a resolution of 0.02 N [56]. Again, for MIS, a 6-degree of freedom (DOF) force-sensing forceps was designed using 6 strain gauges mounted on a Stewart platform producing a force resolution of 0.05 N for transverse loads and 0.25 N for axial loads [57]. For stapedotomy, a force-sensing micro-forceps was developed using fiber Bragg grating (FBG) strain sensors, and was used in combination with a robot to quantify the forces involved in crimping a stapes prosthesis, ranging from 2.4 N to 5.2 N [58]. Based on a monolithic structure flexure and photo-sensors, a compact axial force sensor was developed providing a force resolution of 0.48 N [59], and was shown to properly work with a handheld robotic device to maintain a fixed contact force (200 and 400 mN) at the tool tip [60]. Recently, by integrating two sets of strain gauges in two orthogonal directions a force-sensing bipolar forceps was developed to quantify axial and planar

forces ranging up to 1.20 N during neurosurgical tasks in cadaveric brain experiments [61].

The force sensing methods in the above studies have several limitations that impede their application to vitreoretinal surgery. In order to measure the very fine forces (typically less than 10 mN with gradual changes, i.e. small pace of generation, to prevent retinal injuries based upon studies using animal models [62]), sensing instruments with millinewton resolution and accuracy are required. A miniature tri-axial force sensor with sub-millinewton resolution was developed based on strain gauges, which was designed to be mounted on the handle of a microsurgical instrument [63]. However, in retinal microsurgery, the tools are inserted through an incision on the sclera, and the contact forces at the insertion port are considerably larger than the tissue manipulation forces at the tool's tip. Therefore, a handle mounted force sensor is not practical for vitreoretinal surgery, as the measurements would involve not only the tool-tissue interaction forces but also the adverse effect of frictional and displacement forces at the insertion port [64]. This necessitates positioning the force sensor proximal to the tool tip inside the eye, which imposes strict dimension constraints as well as biocompatibility, sensitivity and safety requirements, and hence limits the available sensors for this use.

2.2. Robotic Systems for Ophthalmology

Robotic systems to enhance microsurgical accuracy have been a topic of extensive research during the past 20 years [65]. During this time, various teleoperated [66-69], cooperatively-controlled [70,71] and handheld [72-78,81,82] robotic devices have been proposed with the common goal of suppressing involuntary motion components, such as physiological hand tremor in surgeons. These systems were shown to improve the tool

manipulation accuracy in studies using artificial phantoms and animal models, and therefore posed the potential to facilitate the safety and performance of the surgery. However, it wasn't until recently that any of these systems appeared in an actual retinal microsurgery. In September 2016, using the Preceyes Surgical System, a motion-scaling tremor-suppressing teleoperated robot [69], surgeons at Oxford's John Radcliffe Hospital performed the world's first robot-assisted vitreoretinal surgery for a membrane peeling operation in a human [79]. In January 2017, eye surgeons at University Hospitals Leuven were the first to demonstrate robot-assisted RVC using another system to inject t-PA into the patient's occluded retinal vein [80]. These are two of the more recent major steps forward for showing the benefits and feasibility of robot-assisted tool manipulation during vitreoretinal surgery.

2.3.2 *Hand-held Robots*

Handheld robotic devices are ungrounded and used in a very similar way to conventional manual tools. They are often relatively compact, low-cost, and easily integrated into a clinical workflow. Riviere *et al.* have developed a 6-DOF handheld active tremor canceling microsurgical tool called Micron [81,82]. Its optical tracking system, Apparatus to Sense Accuracy of Position (ASAP), measures the tool movement. Its control system distinguishes between desired and undesired user motions, and then actively cancels the involuntary motions by actuation of the tool tip. Micron can provide useful assistive behaviors using computer vision [83,84] and optical coherence tomography (OCT) [85]. Micron offers the surgeon a very intuitive interface to enhance manipulation precision, but Micron preserves a 1:1 force feedback ratio and cannot provide scaled force feedback. This is mostly likely to be seen as unfavorable in

vitreoretinal surgery. Another drawback of Micron is the exceedingly small workspace constrained by its external tracking system. Several hand-held robotic tools were developed to provide scaled force feedback to users. Setten *et al.* [86] designed force magnifying surgical tools that can apply a magnified force at the back of the users' hands. Payne *et al.* [74,87] investigated another possibility in which the scaled force feedback was exerted as a linear push on the index finger. While preliminary experimental results have shown the effectiveness of scaled force feedback, these devices only provide force feedback in one direction, i.e., along the tool axis. Song *et al.* [88] developed a microsurgical forceps tool that can actively stabilize tool tip motion along the tool axis. This tool uses a fiber-optic OCT to measure the distance between tool tip and the target tissue. A piezoelectric motor servos the tool tip to the desired distance for safe tissue manipulation. This positioning can be particularly useful for 1-DOF motion stabilization when a target tissue and an environment is delicate, and undesired collision need to be avoided.

2.3.3 *Cooperatively-Controlled Robots*

Cooperative control is a shared control scheme between the operator and the robot, where they both hold the surgical instrument [89-94]. The force exerted by the operator guides the robot to comply with the operator's movements. Using various control modes, the robot can provide precise, tremor-free, smooth, and steady manipulation. The result is a manipulation system with the precision and sensitivity of a machine, but with the manipulative transparency and immediacy of hand-held instruments that surgeons can comfortably every day. Compared to other robotic systems, the advantages of our approach for micromanipulation include the following: simplicity, a potentially lower

implementation cost, more direct coupling to natural kinesthetic human senses, a straightforward integration into existing application environments, and greater “immediacy” for the human operators. Two generations of the Steady-Hand Eye Robot were designed and extensively used in phantom and in vivo experiments [91-93]. The newest generation is the Eye Robot 2.1 (ER2.1). In contrast to Eye Robot 2 (ER2), ER2.1 has a new robot wrist design that addresses the limitations found with the previous versions of the Eye Robot and provides new safety and ergonomics features. These features make the Steady-Hand Eye Robot well suited for the clinical environment.

CHAPTER 3 : FORCE-SENSING INSTRUMENTS FOR ASSISTED VITREORETINAL SURGERY

3.1 Introduction

3.1.1. Background and Motivation

The forces associated with vitreoretinal microsurgery are routinely less than 7.5 mN [29]. Measuring these very tiny forces demands a sensing instrument with sub-mN accuracy. In design, the size and weight of the sensing instrument are important factors since the sensitized tool may be used handheld in a manual operation or mounted on a handheld manipulator for robot-assisted surgery. In addition, the sensitized instrument should have a slender shaft that can pass through a maximum of 20 Gauge scleral opening (\varnothing 0.91 mm) so that the sensor can be introduced into the eye and be located close to the tool tip. Only in this way, can force measurements pertain solely to the instrument's tip, with no adverse contribution from the frictional forces at the sclera.

Fiber Bragg grating (FBG) sensors are optical strain gauges with periodically inscribed refractors, called gratings, in the core of the fiber [95]. The gratings are created using ultraviolet light and work as a wavelength specific reflector or filter. Depending on the distance between gratings, a narrow spectral component at a particular wavelength, termed the Bragg wavelength, is reflected, while the spectrum without this component is transmitted through the optical fiber. Therefore, if the sensitive segment of the fiber experiences strain, due to factors such as external forcing or ambient temperature variation, the distance between the gratings change inducing a shift in the Bragg wavelength given by the following linear correlation:

$$\lambda_B = 2n_e\Lambda \quad (3.1)$$

where λ_B denotes the Bragg wavelength, n_e is the effective refractive index of the grating, and Λ denotes the grating period.

FBG sensors can detect fine changes in strain (less than $1\mu\epsilon$) in real time, have generated increased interest in various medical applications for shape [96], force [97] and temperature [98] sensing purposes. They are very small (\varnothing 60-200 μm) and hence can fit through narrow openings, inherently safe, biocompatible, sterilizable, relatively inexpensive, and highly sensitive; furthermore, their output is immune from electrostatic and electromagnetic noise. To provide the surgeon with real-time physiological information and assist maneuvers during vitreoretinal practice, this chapter aims at transforming the current ophthalmic instruments into “smart” tools that are compatible with robotic assistance platforms and introduces various force-sensing instruments based on FBG sensors. The tool architecture and force computation methods extend from earlier static tools for membrane peeling [99].

3.1.2. Contributions

Main contributions reported in this chapter are as follows:

Force-sensing micro-forceps for membrane peeling: These tools were developed in two groups. The first group senses tool tip forces only perpendicular to the tool shaft in 2 dimensions [101-104]. The novelty is the extension of this method to actuated tools by developing both manually actuated and motorized designs, and modeling/eliminating the artifact induced by tool actuation in sensor readings as a function of forceps opening. The second group has axial force sensing capability in addition to transverse forces [105,106,108,110]. These are the first micro-forceps tools that can sense 3-DOF forces at the tool tip and be potentially used in retinal microsurgery. The main contribution lies in

the calibration procedure and force computation methodology based on FBG sensor readings.

Credit: The 2-DOF manually actuated micro-forceps tool (Section 3.2.1.2) was designed and assembled by Ismail Kuru. Other tools were assembled by Berk Gonenc with help from Iulian Iordachita. Tool design in Section 3.2.1.3 and its functional evaluation was completed with contributions from Ellen Feldman. Finite element simulations in Section 3.2.2.2 were performed with the help of Alireza Chamani. Calibration experiments and software development for Micron system were carried out by Berk Gonenc and Nate Tran.

Force-sensing microneedle for retinal vein cannulation: This tool extends the transverse force-sensing principle to a microneedle for detecting venous puncture, and makes use of a motorized mechanism to retract/expose the pre-bent tip [49]. This is the first actuated force-sensing microneedle that can be introduced through an opening under 1 mm, and that has a small enough tip ($\text{\O} 70 \mu\text{m}$) for injections into retinal veins.

Credit: Tool assembly and calibration was completed by Berk Gonenc with help from Iulian Iordachita.

3.2 Force-Sensing Micro-Forceps for Membrane Peeling

Membrane peeling is often performed either by using a hook or a micro-forceps. Due to the inherent grasping capability, the latter is usually considered safer and preferred by surgeons. It enables easier and more controlled removal of the membrane from the eye with less slippage of the tissue and reduced number of grasping attempts close to the retina surface [100]. The available disposable instruments today range from 27 Gauge to 20 Gauge in tool diameter ($\text{\O} 0.41\text{-}0.91 \text{ mm}$), and come with several types of jaws for grasping various structures as shown in Fig. 3.1. Preserving the firm grasping

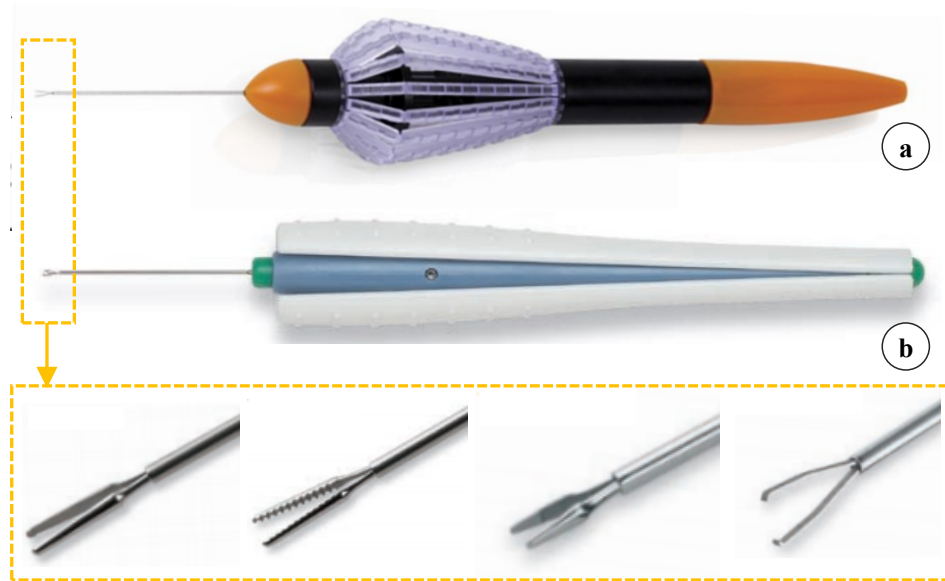


Figure 3.1: Standard disposable micro-forceps for membrane peeling in vitreoretinal surgery by (a) Alcon and (b) D.O.R.C. The shafts of the shown instruments fit through a 23 Gauge scleral incision. The jaws can be of various types depending on the operation. (Image credit to Alcon, Inc. and D.O.R.C.)

functionality and tool diameter constraints, in the following sections we build force sensing capabilities into micro-forceps instruments in a form that enables integrated use with robotic assistance platforms for safer and easier vitreoretinal surgery.

3.2.1. 2-DOF Force-Sensing Micro-Forceps

This section introduces micro-forceps tools which can sense the transverse forces at the tool tip, i.e. the 2 dimensional forces perpendicular to the tool shaft (F_{xy}) as shown in Fig. 3.2.

3.2.1.1. Force Computation Algorithm

When a transverse force is applied at the tool tip, the tool shaft will deform, which can be modeled as a cantilever beam. The resulting strain will be linearly dependent on the moment and thus proportional to the transverse forces applied at the tool tip:

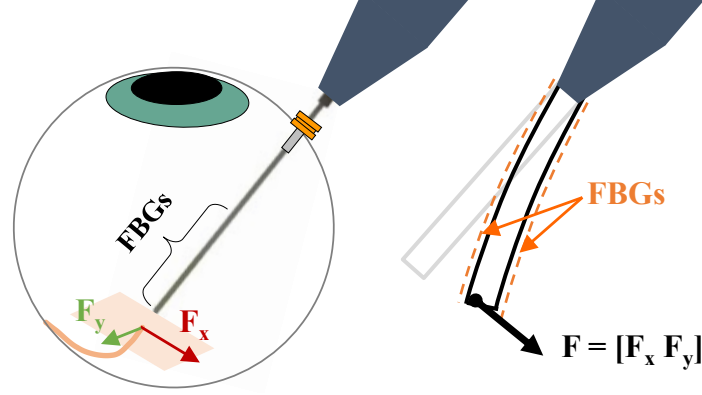


Figure 3.2: 2-DOF force sensing principle for membrane peeling. The FBG strain sensors are integrated on the tool shaft and located proximal to the tool tip to measure the forces perpendicular to the tool axis (F_x and F_y). The tool shaft is modeled as a cantilever beam; when transverse forces are applied at the tool tip, tool shaft deforms and normal stresses are induced on the attached FBG sensors.

$$\varepsilon = \frac{M r}{E I} = \frac{F_{xy} d r}{E I} \quad (3.2)$$

where ε is the local strain at the FBG sensor, M is the bending moment due to the transverse forces F_{xy} at the tool tip, d is the distance between the tool tip and the FBG sensor, E is the Young's modulus, I is the moment of inertia, and r is the radial distance between the bending neutral axis and the FBG sensor. Linearly dependent on both the local strain due to external forcing (ε) and the ambient temperature change (ΔT), the Bragg wavelength of the sensor will shift by $\Delta \lambda$ which can be formulated as:

$$\Delta \lambda = k_{\varepsilon} \varepsilon + k_{\Delta T} \Delta T \quad (3.3)$$

where k_{ε} and $k_{\Delta T}$ are constants associated with the strain due to forcing and temperature, respectively. Although the temperature in patients' eyeball is fairly constant, FBG sensors are typically very sensitive to temperature changes (approximately $10 \text{ pm}/^{\circ}\text{C}$). Hence, force sensing robustness against small thermal fluctuations is a desired feature. Combining equations 3.2 and 3.3, the following is obtained:

$$\Delta\lambda = k_\varepsilon \frac{F_{xy} d r}{E I} + k_{\Delta T} \Delta T = k_x F_x + k_y F_y + k_{\Delta T} \Delta T \quad (3.4)$$

When multiple FBG sensors ($n=3$ for the tools presented in this section) are attached along the tool shaft, the common mode of the sensors will be due to axial forcing (if any) and temperature changes only. To detect transverse forces only, the common mode ($\Delta\lambda^{\text{mean}}$) can be removed by subtracting the mean of the Bragg wavelength shifts of all three FBG sensors.

$$\Delta\lambda_i^{\text{diff}} = \Delta\lambda_i - \Delta\lambda^{\text{mean}} = k_{xi} F_x + k_{yi} F_y - \frac{1}{n} \sum_{j=1}^n (k_{xj} F_x + k_{yj} F_y) \quad (3.5)$$

The remaining differential mode of each sensor ($\Delta\lambda_i^{\text{diff}}$) can be transformed into force information using a calibration matrix (K). Using 3 sensors around the tool shaft, F_x and F_y can be computed as:

$$[F_x \quad F_y]^T = K [\Delta\lambda_1^{\text{diff}} \quad \Delta\lambda_2^{\text{diff}} \quad \Delta\lambda_3^{\text{diff}}]^T \quad (3.6)$$

The coefficients forming the calibration matrix are found via an experimental calibration procedure which will be detailed for each tool separately in the following sections.

3.2.1.2. Concept 1: Manual Actuation

3.2.1.2.1. Design and Fabrication

Reusable forceps must be cleaned and sterilized after every operation. As the tool goes through many cycles of surgery, cleaning and sterilization, material fatigue may occur and surface properties may change. Consequently, forceps cannot grasp the membrane as required and in a worst case they break during the surgery. In order to avoid such problems and reduce the associated cost, the current trend in vitreoretinal surgery is to

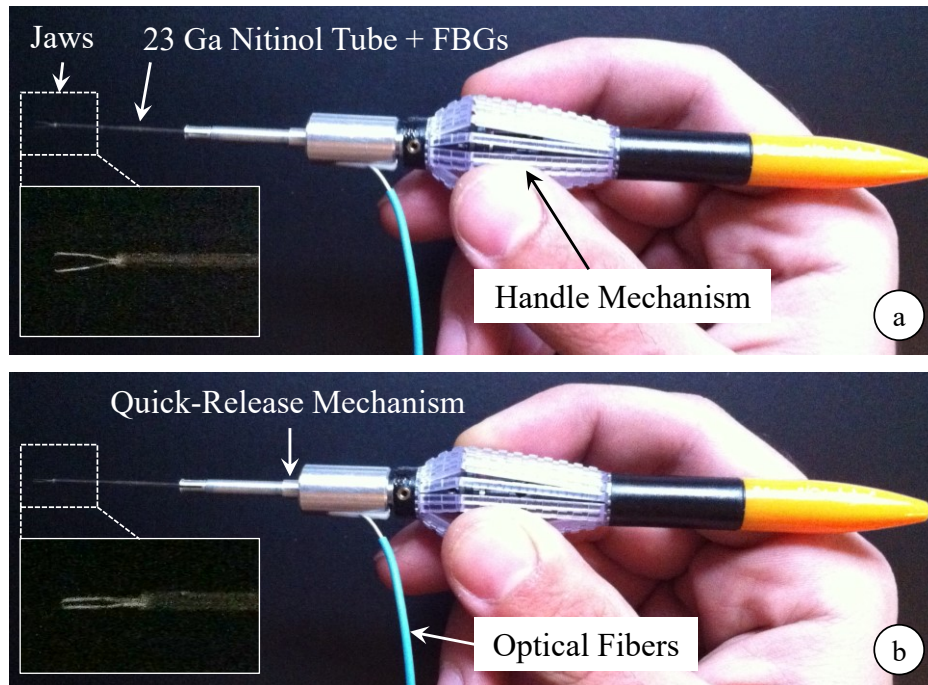


Figure 3.3: Fabricated prototype of the manually-actuated 2-DOF force-sensing micro-forceps [101]: (a) jaws open, and (b) jaws closed configurations. Squeezing the handpiece closes the jaws. The jaws and the handle mechanism were taken from a standard 23 Gauge disposable micro-forceps. 3 FBGs were attached onto the 23 Gauge nitinol tube forming the tool shaft. The quick release mechanism enables integration with the Steady-Hand Eye Robot and an easy dismounting for safety in case fast removal of the tool from the eye is needed during the procedure.

use disposable forceps. Another important advantage of disposable forceps is the axially symmetric handle which is very convenient for rotating the tool around the tool shaft, since rotation is crucial for membrane peeling surgery to grasp the membrane at the right angle.

The idea of integrating force sensing into disposable forceps is a challenging design task since using new sensors for every operation would not be a cost-effective solution. Another challenge is maintaining the present rotation functionality: FBG sensors could easily be damaged or could block a surgeon's maneuvers during rotation. We have solved these problems by building two mechanically decoupled functional parts: the force sensing module and the forceps mechanism.

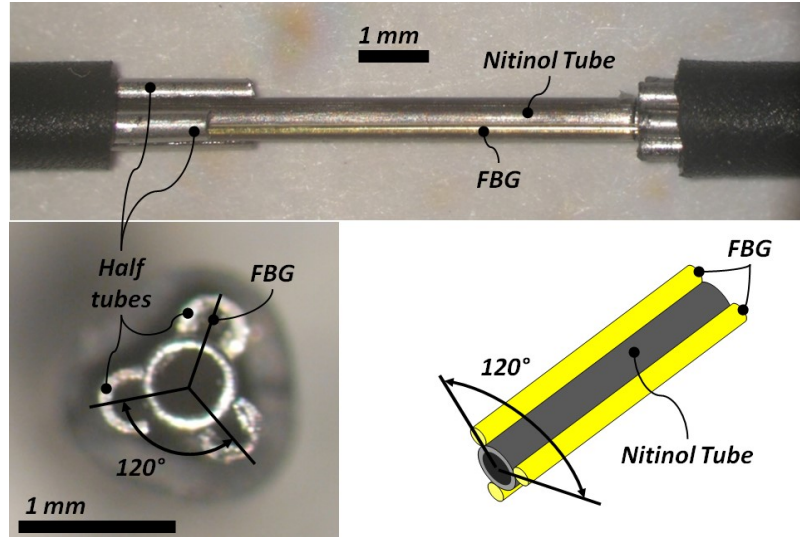


Figure 3.4: The force sensing module and its fabrication steps [101]. First, three half tubes were located on the nitinol tube (upper). Second, FBGs were inserted through half tubes to achieve axi-symmetric configuration (lower).

The force sensing module, shown in Fig. 3.4, is a 23 Gauge nitinol tube with three embedded FBG strain sensors. FBG strain sensors (Smart Fibers, UK) are preferred mainly due to their small dimension, high sensitivity, biocompatibility, sterilizability and immunity from electro-static and electromagnetic noise. For axially symmetric FBG positioning around the nitinol tube, first we built a small apparatus that could place three half tubes on the nitinol tube. Then we inserted the FBGs through these half tubes. After the FBGs were glued the half tubes were removed. The nitinol tube with force sensors was mounted into a custom quick-release mechanism that connected the steady-hand robot tool holder. In order to monitor the FBG strain sensors, an optical sensing interrogator, sm130-700 from Micron Optics Inc. (Atlanta GA), was used.

Our forceps mechanism consists of an actuating tube and graspers. For this mechanism, we have customized disposable forceps from Alcon, Inc. (Fort Worth, TX) as shown in Fig. 3.3. The graspers were taken off from a 23 Gauge disposable forceps and actuation tube was built with a 27 Gauge stainless steel hypodermic needle. The handle of a

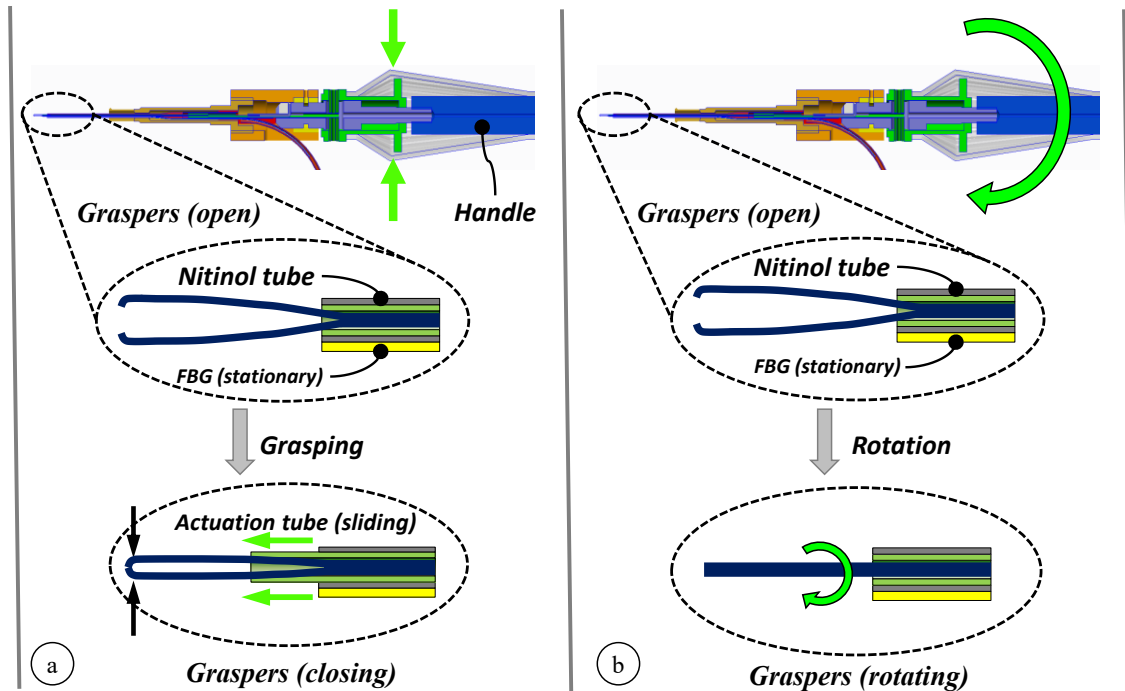


Figure 3.5: (a) Squeezing the handle slides the actuation tube (green) in distal direction and closes the graspers (blue). (b) The graspers (blue) and the actuation tube (green) can be rotated together in the Nitinol tube (red) by rotating the handle.

disposable forceps tool was customized, so that the graspers and the actuation tube could easily be replaced after each operation. As shown in Figs. 3.3 and 3.5.a, the mechanism can be actuated by squeezing the tool handle. The squeezing motion causes the actuation tube to slide in the distal direction so that the graspers are closed. The graspers open again if the handle is released. Fig. 3.5.b shows the rotation functionality, where the tool tip can be rotated by rotating the tool handle. In either case, the force sensing module remains stationary relative to the easy-release mechanism.

Finally, the customized forceps mechanism was inserted through the force sensing module. In this design, the optical fibers leave the tool right after the easy-release mechanism as shown in Fig. 3.3. This inhibits any interference with the surgeon's hand at the handle during the operation. Furthermore, the fibers never get twisted or bent since

they are separated from all of the rotating components. The complete design can be actuated and rotated just like the original tool.

3.2.1.2.2. Calibration

The calibration setup, calibration protocol, and the force computation steps follow [99]. Due to the interaction between the actuation tube and the nitinol tube with FBGs, a constant offset in force measurement exists when the micro-forceps is open. Since measuring the tool-to-tissue interaction forces after grasping the membrane is critical, the micro-forceps was kept closed during the calibration. A linear reproducible behavior was observed for all FBGs during both x and y axis calibration procedure as shown in Fig 3.6. The following calibration matrix was determined:

$$K = \begin{bmatrix} 0.0213 & -0.1525 & 0.1311 \\ -0.1523 & 0.0686 & 0.0836 \end{bmatrix} \text{ mN/pm}$$

To verify our calibration results, we rotated the forceps mechanism and the tool shaft relative to the force sensing module while monitoring the change in measured forces under constant loading on tool tip. The rotation caused a shift in the force measurement,

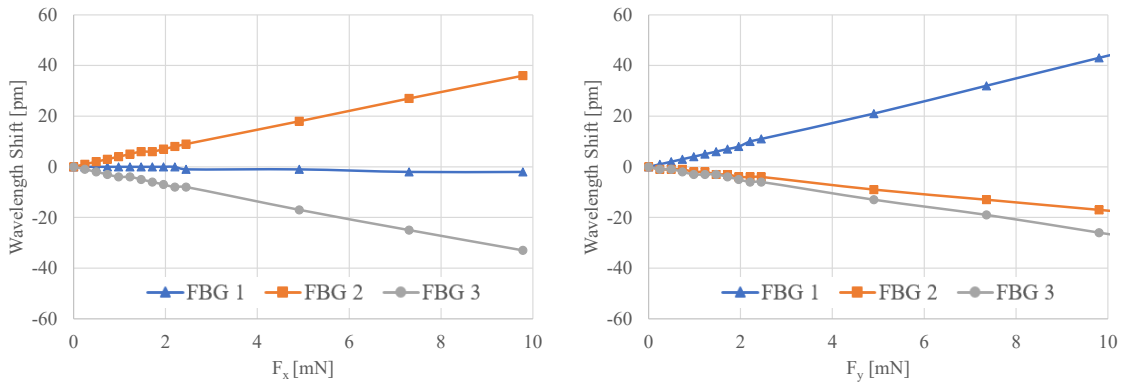


Figure 3.6: Calibration results in x-axis direction (left) and in y-axis direction (right). Linear behavior is observed for all FBGs in both axes.

but did not affect the linear trend of the calibration functions except for the starting points. Since the initial linear trend is preserved, recalibration is not required during the operation. The shift in the starting points can easily be eliminated by rebiasing the system during use. After the system rebias, the errors in our tests were less than 0.3 mN in the relevant force range of 0-10 mN. This shows that our tool is able to measure the forces in any direction in the xy-plane and in any orientation of the graspers relative to the tool, with an accuracy of 0.3 mN and precision of 0.25 mN.

3.2.1.3. Concept 2: Motorized Actuation

Currently a standard tool for membrane peeling is the disposable micro-forceps by Alcon Inc. (Fort Worth, TX), which is shown in Fig. 3.7.c. This tool operates based on a squeezing mechanism [101]: when the tool handle is compressed, the tubular tool shaft is pushed forward, and squeezes the flexible jaws anchored to the back of the tool handle; when the tool handle is released the spring-loaded mechanism pulls the tubular tool shaft back opening the jaws. Due to the moving parts within the mechanism during this actuation, studies have shown significant motion artifact at the tool tip [78], which limits tool tip positioning accuracy while trying to catch the membrane edge to begin delamination. Furthermore, such mechanical coupling between the tool handle and tip for actuation challenges the integration of the tool with many of the available systems for robot-assisted surgery as it can easily interfere with the operation of the attached robotic system. To address these issues, the design goal in our work has been devising a compact, lightweight and modular unit that can be controlled independently and remotely when necessary regardless of its site of attachment (such as a manual tool handle, a handheld micromanipulator [72-78,81,82] or a teleoperated/cooperatively-controlled robot [66-

71]), resulting in the motorized micro-forceps shown in Fig. 3.7.b.

3.2.1.3.1. Design and Fabrication

Our motorized micro-forceps tool consists of two mechanically decoupled pieces: the handle mechanism, and the motorized force-sensing tip. The handle mechanism, shown in Fig. 3.8.a, was designed to clamp around any cylindrical micromanipulator body up to 25 mm in diameter with the help of set screws, transforming it into a micro-forceps handle. It preserves the intuitive actuation principle on the standard disposable micro-forceps tools, and does not interfere with the operation of the micromanipulator. The disposable Alcon forceps is actuated simply by squeezing the sides of the instrument handle, which causes the tube forming the tool shaft to slide in the distal direction so that the graspers are closed [101]. In our case, however, such rigid coupling between handle

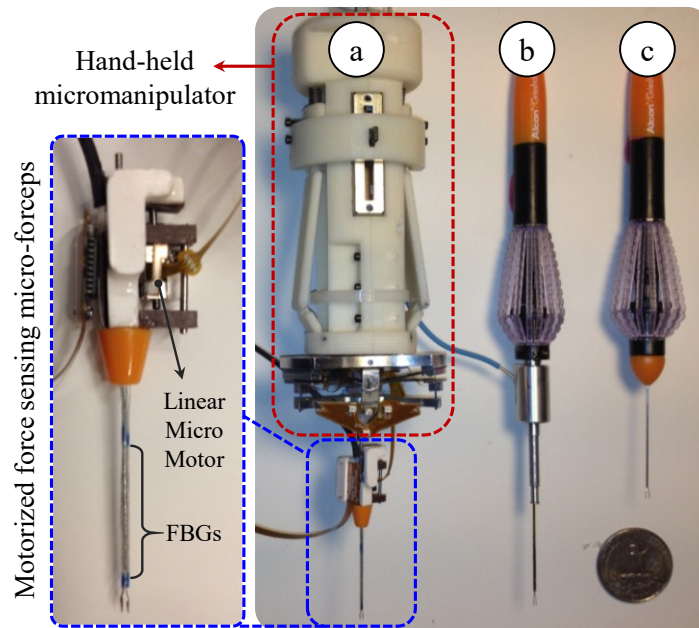


Figure 3.7: (a) Motorized force-sensing micro-forceps integrated with a handheld micromanipulator (Micron) [102], (b) 2-DOF force-sensing micro-forceps for the Steady-Hand Robot from Section 3.2.1.2, (c) Standard 23 Gauge disposable forceps (Alcon, USA).

motion and tip actuation is not possible since it would significantly interfere with the actuators of the micromanipulator. Instead of such a mechanical coupling, we used a sliding potentiometer on the handle to assess forceps closure. The sides of the handle mechanism are normally kept propped open by two springs. Compressing the sides causes the sliders to move up along the tool handle, inducing a voltage change in the potentiometer output, and driving the motor of the tip forward to close the graspers.

To design a clinically feasible micro-forceps tip that is compatible with various micromanipulators, there are four main challenges that need to be resolved: (1) integrating accurate force sensing capabilities while preserving the grasping motion of the forceps, (2) avoiding interference between the micromanipulator's own actuation and the opening/closing action of the forceps, (3) generating a self-standing universal module for compatibility with various handheld manipulators, and (4) enabling easy replacement of the grasper jaws for accommodating different jaw types for different surgical tasks,

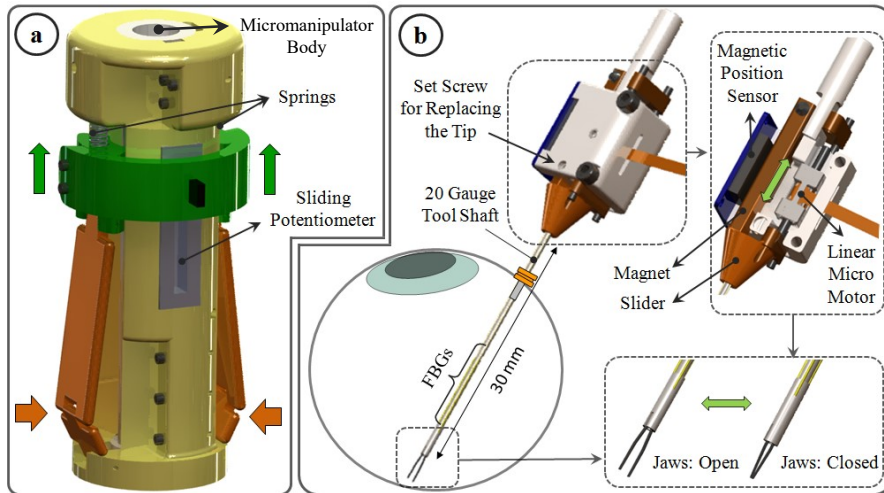


Figure 3.8: Design of the motorized 2-DOF force-sensing micro-forceps: (a) handle mechanism, (b) motorized force-sensing tip with replaceable jaws. The tool can be inserted through a 20 Gauge trocar into the eye. Squeezing the handle mechanism from the sides drives a sliding potentiometer, which is used to control the linear micro motor in the tip module [102].

and for disposable use. This requires a very compact and lightweight micro-forceps module that is motorized so that it can be actuated independently regardless of the micromanipulator motion, and that carries all of the force-sensing elements on it. Under these constraints, we designed our “drop-in” micro-forceps as shown in Fig. 3.8.b. Reusable forceps require cleaning and sterilization after every operation. As the tool goes through many cycles of operation, the resulting material fatigue and change in surface properties diminish the grasping quality. Consequently, the forceps jaws cannot grasp the membrane as required and in the worst case they may break during the surgery. In addition, depending on the thickness and type of the targeted tissue, surgeons may need to use micro-forceps with varying grasper jaw profiles as shown earlier in Fig. 3.1. To enable the easy change of disposable jaws and switch between differing types of jaws (Fig. 3.1) preserving the force-sensing motorized unit, the design of the tip module was modified as shown in Fig. 3.9.a.

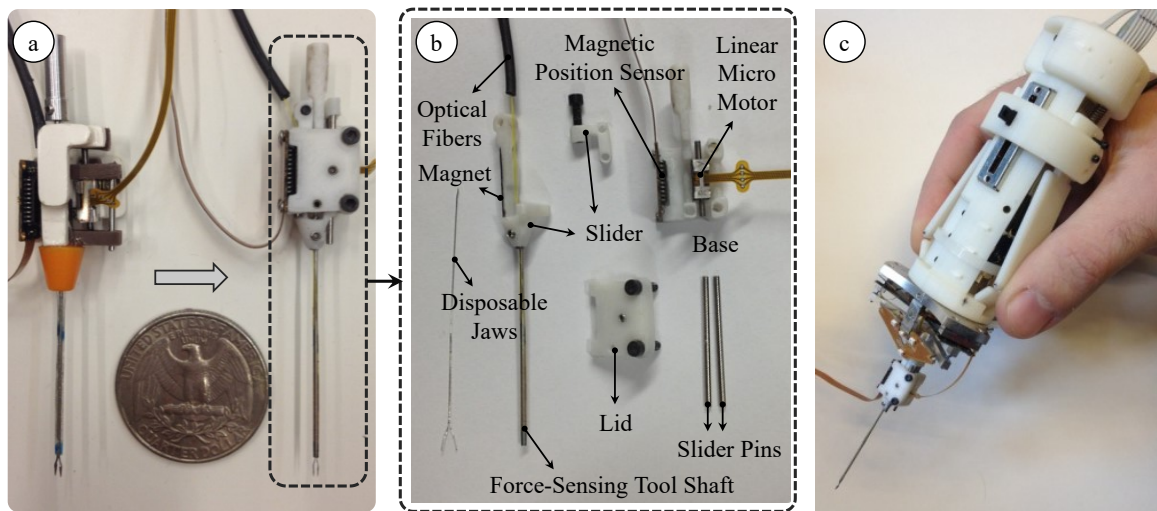


Figure 3.9: (a) Motorized force-sensing micro-forceps: an earlier prototype (left) vs. the more compact latest prototype (right) of the tip module. (b) Components of the tip module: The disposable jaws can be easily replaced to accommodate different jaw types for different surgical tasks and prolonged use. (c) The handle mechanism and the tip module can be integrated with assistive robotic systems, such as the handheld micromanipulator, Micron [103].

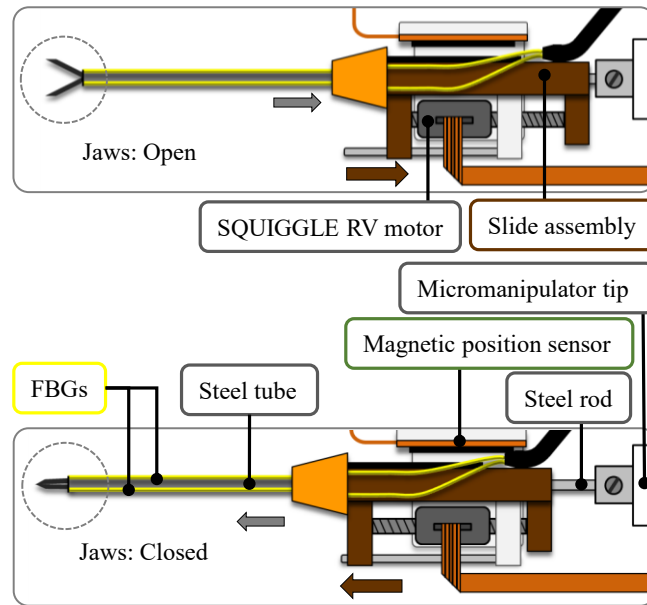


Figure 3.10: The linear micro motor in the tip module (Squiggle-RV-1.8) is used to drive the slide assembly back and forth. Moving forward pushes the steel tube carrying the FBGs towards the tip, thus squeezing and closing the jaws. Opposite motion releases and opens back the compliant jaws. During actuation, the position of the slide assembly, carrying a bar magnet attached on its side, and therefore the motor position is detected by a magnetic sensor located on the side of the module [102].

Components of the current design are presented in Fig. 3.9.b. The disposable jaws are at this time taken from the standard 23 Gauge Alcon micro-forceps. The normally open jaws are fixed to the base via a set screw located on the lid. By releasing the set screw, the jaws can easily be replaced and switched between different types, such as the thicker profile in Fig. 3.12.a for peeling dense epiretinal membranes and the slimmer profile in Fig. 3.12.b for delamination of finer internal limiting membranes. The lid, base and slider shown in Fig. 3.9.b are polycarbonate parts. The tool shaft is a 23 Gauge stainless steel tube. It is attached to a slider, which is moved back and forth along the pins of the base by a linear micro motor, Squiggle-RV-1.8 by New Scale Technologies Inc. Driving the slider forward pushes the tool shaft towards the tip, thus squeezing and closing the forceps jaws. The selected micro motor supplies enough force for this task in a very small

(2.8x2.8x6 mm), and light weight (0.16 grams) package. Fully opening and closing the jaws requires a travel distance of 0.8 mm, which is well below the motor's limit (6mm). A bar magnet is attached on the side of the slider. The position of the slider, and thus of the micro motor, is tracked via the magnetic position sensor fixed on the side of the base. To integrate force sensing capabilities, FBG strain sensors (Smart Fibers, UK) were preferred mainly due to their small dimension, high sensitivity, biocompatibility, sterilizability, and immunity from electrostatic and electromagnetic noise. Following the fabrication method presented in [99], 3 FBGs were fixed evenly around the 23 Gauge tubular tool shaft using medical epoxy adhesive. The outer diameter of the finalized tool shaft is approximately 0.9 mm, and is small enough to fit through a 20 Gauge trocar. The module weighs about 1.9 grams.

3.2.1.3.2. Calibration

The micro-forceps module is capable of sensing the transverse forces exerted at its tip via the 3 FBG strain sensors attached evenly around the tool shaft. To find the calibration constants required by equation 3.5, we took measurements using the setup in Fig. 3.11.a. The tip module was mounted on a rotary stage and held horizontal while transverse forces were applied by hanging washers of known weight at the tool tip. The varying loading at the tool tip induced changes in the Bragg wavelength of each FBG sensor, which normally depends linearly on both the local strain and the temperature variation. During calibration, the effect of temperature change was removed by subtracting the mean wavelength shift from each sensor measurement. Resulting temperature-compensated sensor readings exhibit a linear reproducible behavior during both the x- and y-axis

calibration procedures, as shown in Fig. 3.11.a. The slopes of the response curves form the calibration matrix (K):

$$K = \begin{bmatrix} 0.2127 & -0.1283 & -0.0843 \\ 0.0183 & 0.1613 & -0.1797 \end{bmatrix} \text{ mN/pm}$$

The shaft of the disposable jaws in comparison to the actuation tube is very thin, and thus has no significant effect on the overall stiffness of the tool shaft. Thus, even if the tip is replaced, the calibration matrix remains the same.

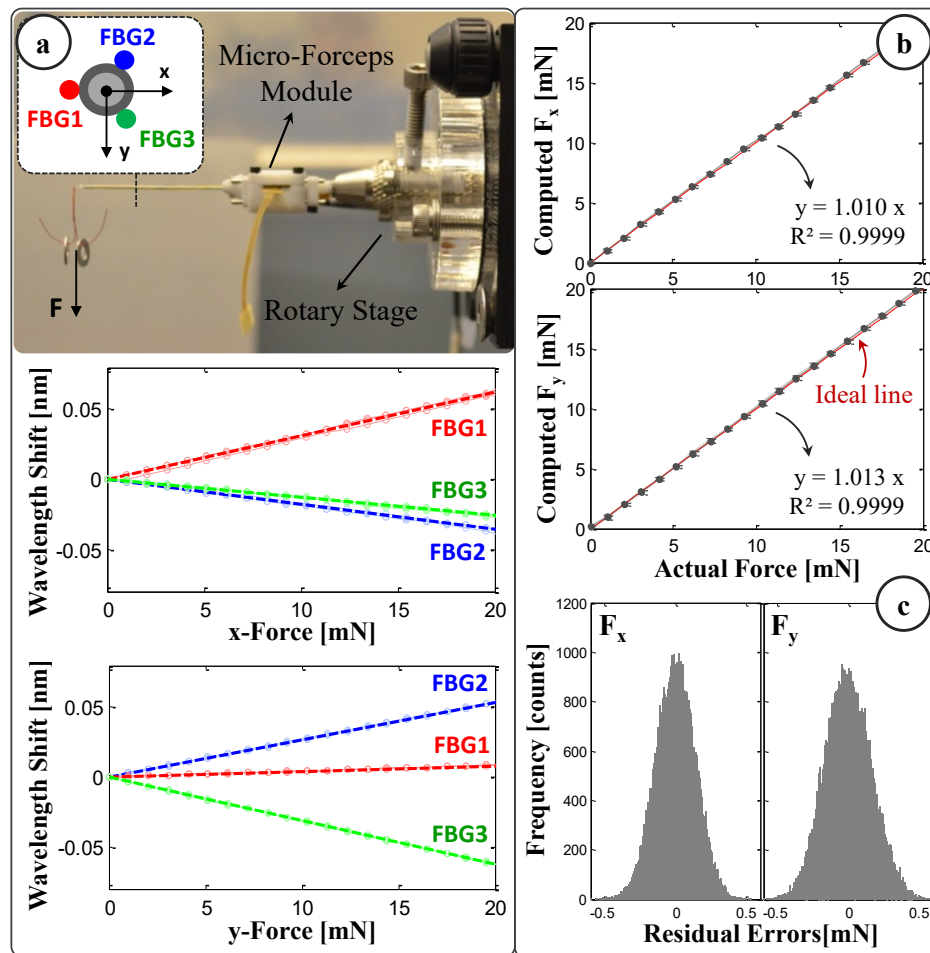


Figure 3.11: (a) Calibration results: linear response for all FBGs when the tip is loaded along x and y axes. (b) Computed forces versus the actual forces along x and y axes. (c) The histogram of the residual errors [104].

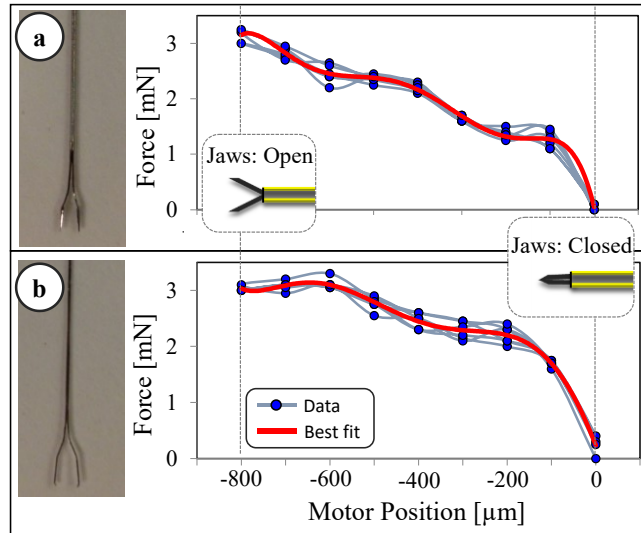


Figure 3.12: Varying nonzero forces are observed due to inner actuation forces as the jaws are opened and closed. The force profile varies depending on the jaw type. Artifact on sensor reading while using jaws for (a) thicker membranes and (b) thinner membranes. The force shift is consistent throughout the open/close cycles, and can be modeled as a function of the motor position [103].

In order to monitor the FBGs, we use an optical sensing interrogator (sm130-700 from Micron Optics Inc., Atlanta, GA). The wavelength resolution of the interrogator is 1 pm. Based upon the obtained calibration matrix, this corresponds to a transverse force resolution of about 0.21 mN. To verify sensor operation, the tool tip was loaded and unloaded repeatedly (3 times) in different angles (0° , 45° and 90°), and the computed forces were compared with the actual tip loading. Results showed consistency with the actual values for both F_x and F_y , and a close fit to the ideal straight line (slope=1) passing through the origin (Fig. 3.11.b). The root mean square error was 0.14 mN and 0.17 mN respectively for F_x and F_y . The histogram of the residual errors in Fig. 3.11.c show that the probability of errors beyond 0.5 mN is very low.

The grasping action in this design is provided by squeezing the forceps jaws by sliding the tubular tool shaft forward. During this motion, various external loads and friction

forces are exerted on this tube, which is also carrying the force-sensing FBGs. As the forceps is closed and opened, FBGs are influenced by these inner actuation forces resulting in a shift in force readings even when there is no external loading on the tip. The force variation due to actuation depends on (1) the type of the attached forceps jaws, and (2) the jaw orientation relative to the base. The sensed actuation forces are usually comparable (up to 3 mN as in Fig. 3.12.b and 3.12.c) with the amplitude of most forces during vitreoretinal practice (routinely below 7.5 mN). Due to various structural factors, such as the grasper jaw geometry, friction forces and material properties, the effect of inner actuation forces is usually complex, and thus normally hard to predict. However, because the actuation is provided by a motorized system, the force shift exhibits a very consistent trend during repeated open/close cycles, and can be modeled as a function of motor position. In order to cancel this systematic error, we implemented a correction routine that is performed after each jaw replacement (Fig. 3.13).

Before the operation, the desired jaws are mounted using the set screw on the lid (Fig. 3.8.b). Then, with no external loading on the tip, the grasper jaws are opened and closed three times while the variation in sensed forces is recorded. This results in a mapping between the micro motor position and force error specific to that particular jaw type and mounting orientation. Then a polynomial is fit to the acquired data. Based on the best fit and sensed motor position, the induced forces due to actuation can be estimated (within a ± 0.15 mN envelope) and subtracted from the measured values to obtain a corrected force reading. This provides a significant reduction in force variation as the forceps is closed and opened repeatedly. As shown in Fig. 3.13, without such correction, opening the forceps jaws induces an error that is slightly larger than 3 mN. The correction routine

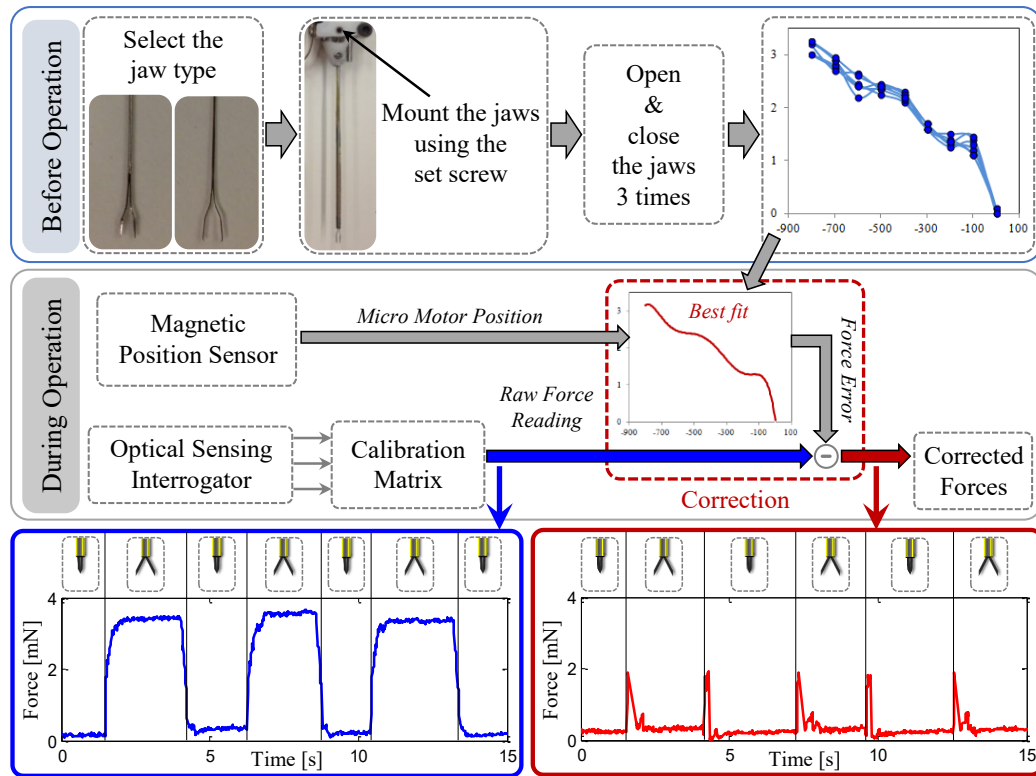


Figure 3.13: The implemented correction routine for compensating against the inner actuation forces and maintaining the accuracy of force readings while opening and closing the grasper jaws [103].

lowers the error down to 0.3 mN. This indicates that our tool is able to sense transverse forces within an accuracy of 0.3 mN after correction. The jumps on the corrected data correspond to the instant when the actuation tube starts and stops moving, and are mainly due to inertial effects. These jumps can further be reduced by integrating the acceleration term in the correction routine, but has no significance for practical use since the forces while grasping the tissue (while the jaws are stationary) are of interest.

In vitreoretinal practice, surgeons may need to manipulate tissues with varying thickness. Depending on the grasped layer thickness, the jaw opening and the final motor position would change, resulting in different offsets in the raw force reading. The force correction routine based on motor position ensures that the computed tip forces remain accurate

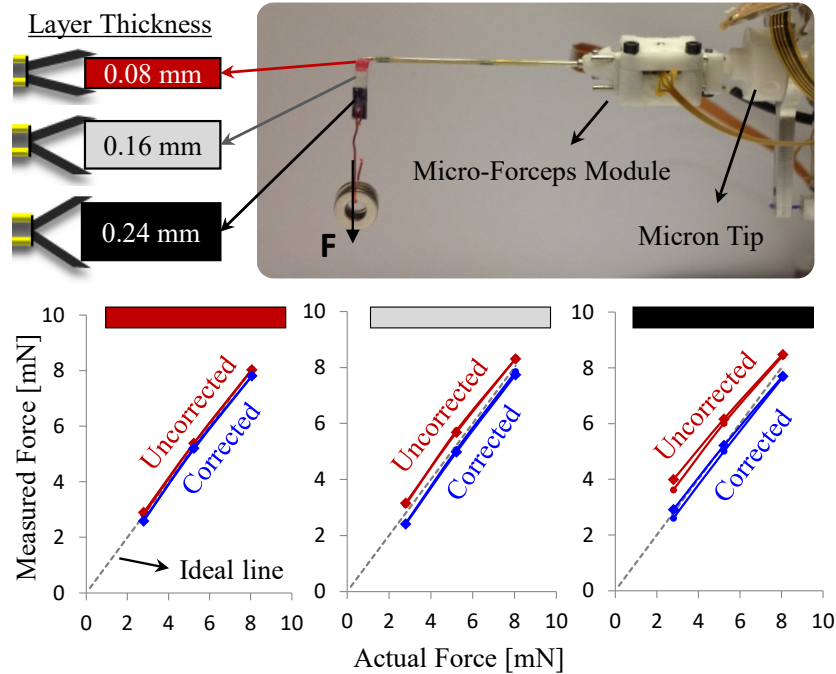


Figure 3.14: The effect of grasped layer thickness on the force sensing accuracy. A multilayered bandage was grasped from 3 different segments to compare the measured forces with the actual loading on the tool tip. Measured forces normally deviate from the ideal line more if thicker layers are grasped. The correction routine ensures that the measured tip forces remain accurate regardless of the thickness of the grasped material [103].

regardless of the thickness of the grasped material. To validate this, we did experiments for 3 different layer thicknesses, and 3 different tip load levels on the setup shown in Fig. 3.14. The colored grasping tab carrying the loads is made of bandages and has a non-uniform cross section. The red segment consists of a single layer bandage, while adjacent white and black segments have layers stacked on top of each other, resulting in 0.08mm, 0.16mm and 0.24mm thick material respectively.

During the test, the strip was grasped from one of these segments, and washers were hung to increase the forces on the tool tip gradually. The force readings were recorded with and without the proposed correction routine while loading and removing washers. The test was repeated for each segment on the strip. When grasped from the thinnest segment, the

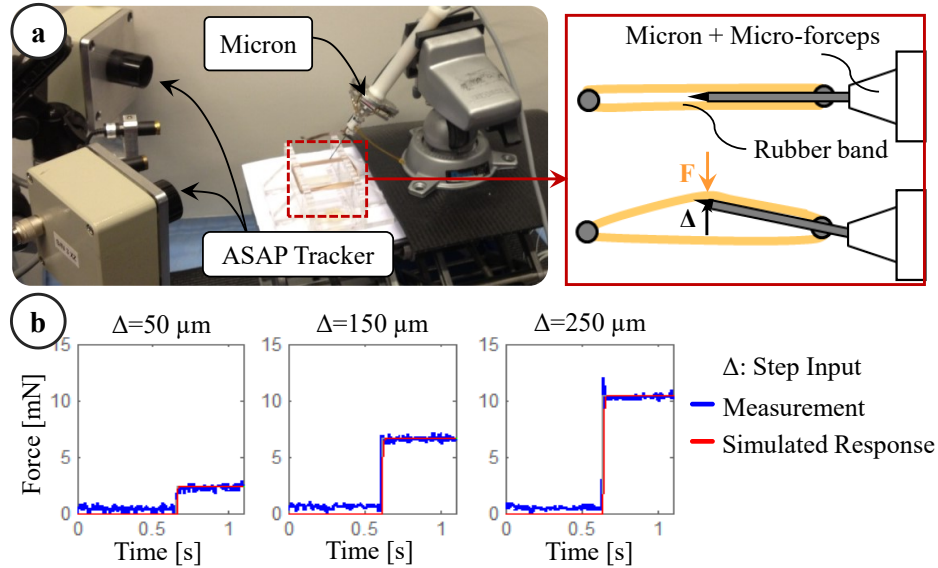


Figure 3.15: Transient response characteristics of the force sensor: (a) setup, (b) step response of the sensor. Simulated response of a first order system with a time constant of 0.005 seconds matched the measured force profile [104].

measured forces were observed to be very close to the actual values, even without the correction routine. However, as the grasped layer got thicker, the measured values deviated from the ideal line, and thus the correct force value, more if the proposed correction routine was not applied. With the correction routine, the measured forces always remained accurate, regardless of the thickness of the grasped segment.

Accurate measurement of membrane peeling forces in the presence of fast variations, such as while using micro-vibrations which will be detailed in Section 4.4, requires not only sub-mN force-sensing resolution but also a very fast responding force sensor. In order to characterize the transient response of our force-sensing micro-forceps we used the setup shown in Fig. 3.15.a. The micro-forceps module was mounted onto a micromanipulator, Micron, fixed in a vise. The forceps jaws were put between two elastic rubber bands. Then, Micron was given a step input to move the tool tip towards one side laterally while the resulting reaction force was recorded. Measurements were taken for 3

levels of step amplitude (50, 150 and 250 μm). In all cases, the force output of the micro-forceps matched a first order system response with 0.005 s time constant as shown in Fig. 3.15.b, proving a fast-enough response to track rapid force variations even in the presence of high frequency micro-vibrations (up to 50 Hz).

3.2.2. 3-DOF Force-Sensing Micro-Forceps

In this section, force-sensing micro-forceps that can firmly grasp layers and detect not only the transverse forces (F_x , F_y) but also the axial tension (F_z) during membrane peeling via their integrated FBG sensors are presented. To the best of our knowledge, these are the only micro-forceps at this scale (tool shaft diameter < 0.9 mm) that can sense 3-DOF forces at the tool tip and be potentially used in retinal microsurgery. The main contribution of our study is the calibration procedure and force computation methodology based on FBG sensor readings. In the following sections, for each design concept, we first discuss how a set of FBG sensors can be configured to accurately capture tool-tissue forces while preserving the grasping functionality of the micro-forceps. This will be followed by methods to transform the optical information from the FBG sensors into force values, and calibration experiments and verification of the sensor readings.

3.2.2.1. Concept 1: Manual Actuation

3.2.2.1.1. Design of the Actuation Mechanism

In this design, shown in Fig. 3.16, we modified the handle of disposable forceps by Alcon such that squeezing the tool handle retracts the tool shaft instead of pushing it forward, but still leads to opening of compliant jaws, which are custom built and normally closed as will be detailed in the next section. The tool shaft is composed of two concentric tubes

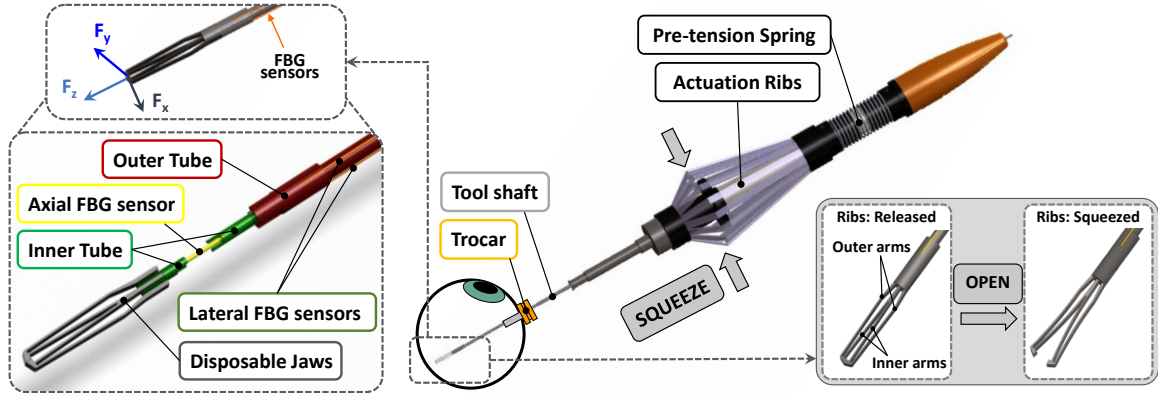


Figure 3.16: Manually-actuated 3-DOF force-sensing micro-forceps for membrane peeling: Basic components and actuation principle [105].

which are connected to the inner and outer arms of the grasper jaws. Besides this flexible coupling at the distal end, the proximal end of each tube is also held rigidly by different parts of the actuation mechanism. The inner tube is fixed to the handle body while the outer tube is grasped by the ribs of the handle. When the user squeezes the hand piece, the outer tube is retracted into the handle body while the inner tube is held stationary. In this way, the outer arms of the jaws are pulled up to open the forceps. In contrast to the existing Alcon tool design, in our concept, the adjustable pre-tension spring on the handle keep the jaws normally closed. Upon releasing the ribs, the jaws close under the force applied by this pre-tension spring and the jaws' own stiffness.

3.2.2.1.2. Design of the Forceps Jaws

There are two main approaches in designing forceps depending on the neutral position of the grasper jaws: a normally closed design vs. a normally open configuration. In our design, the grasper jaws function as a flexible coupling between the outer and the inner tubes. Thus, this part has a significant effect on the required actuation forces, and the resulting inner stresses. Apart from providing actuation, the inner and outer tubes also carry the force sensing elements. In vitreoretinal practice, it is desired to sense the forces

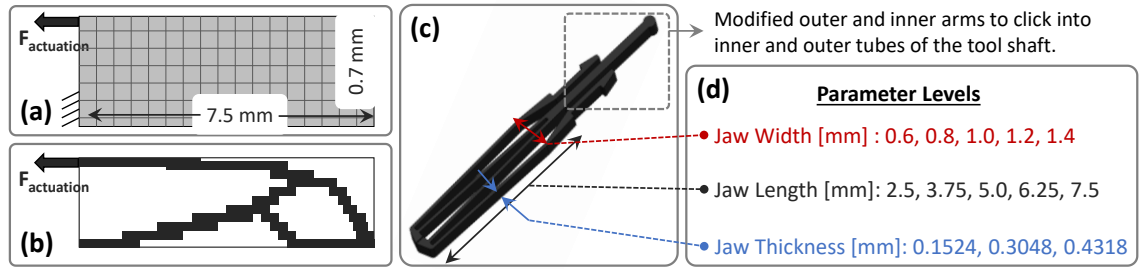


Figure 3.17: Topology optimization: (a) Design domain and boundary conditions; (b) final concept output; (c) simplified design and associated parameters; (d) levels used in the optimal value search [106].

at the tool tip mostly after the tissue is grasped. Thus, the influence on the sensing elements from inner actuation forces must be minimized when the jaws are closed, which necessitates normally closed configuration. Furthermore, due to the limited strain that each FBG can take (9000 μ strain), the pulling force on the outer tube while opening the jaws need to be minimized. However, reducing this force too much would also result in very flexible jaws and poor grasping force. Therefore, the actuation force should be minimized while satisfying the minimum grasping force requirement (20 mN). We solved this optimization problem in two steps: (1) topology optimization, (2) linear search. During these steps, the material was specified as nitinol (SE508 from Nitinol Devices & Components, Inc.) for its super-elastic properties.

Topology optimization is a finite-element-based approach which provides the optimum structural layout to satisfy a target design requirement in a well-defined design domain [107]. In our case, it is important to find a concept that will provide minimal actuation force. Utilizing symmetry, the design domain for half of the graspers is set to be within a 0.7mm x 7.5mm rectangular region. The domain is divided into 50 μ m x 50 μ m squares to get a total of 2100 elements as schematized in Fig. 3.17.a. Then the conceptual design generated by topology optimization (Fig. 3.17.b) was simplified considering

manufacturability. Also, in order to make this part replaceable, the outer and inner arm ends were slightly modified so that the grasper jaws click into the slots on the outer and inner tubes of the tool shaft, and can be taken out by squeezing and pulling them out.

The optimal values for the dimensions of this concept were found via linear search, by static analyses on 75 different designs in SolidWorks. The design parameters and the explored values for each are shown in Fig. 3.17.c and Fig. 3.17.d, respectively. Analyses showed that increasing the jaw length, the jaw width and decreasing the arm thickness provide smaller actuation force. The effect of jaw length on the actuation force is most significant when greater arm thicknesses are considered while the jaw width is not critical especially for longer jaws. On the other hand, tuning all these parameters so as to minimize actuation force reduces the grasping force. For this reason, the minimum grasping force criterion defines a bound on these variables. In addition to functional requirements, the design variables are also limited by application based facts and manufacturing capabilities. The jaw length cannot be greater than 14 mm since the adult human eye ball is typically below 24 mm in diameter, 10 mm of which is already occupied by the active segment of FBGs. The jaw width cannot be increased too much since the instrument has to pass through a 20 Gauge trocar (0.9 mm ID). However, this limit can be slightly exceeded as long as the tool can be squeezed to pass through the trocar without breaking. Finally, the links on the jaws cannot be thinner than 50 microns as smaller values would make laser cutting really challenging, or in some cases even impossible depending on the equipment available. Under these constraints, our linear search aimed to maximize two objective functions simultaneously: (1) opening

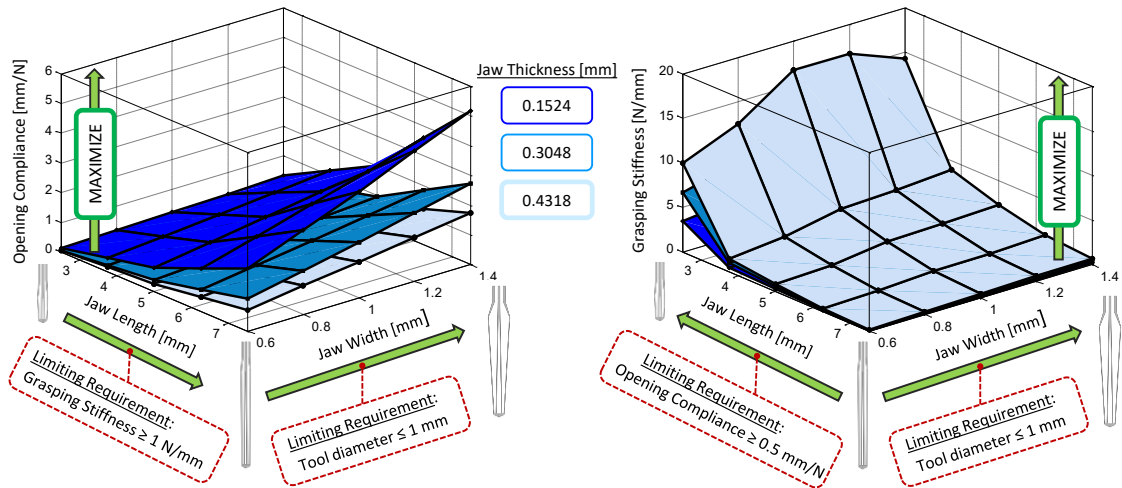


Figure 3.18: The effect of design parameters on the opening compliance and grasping stiffness. The optimization goal is to maximize both functions while satisfying the limiting factors [106].

compliance (jaw opening/actuation force) for smaller actuation force, and (2) grasping stiffness (grasping force/jaw deformation) for better grasping.

The effect of design parameters on the objective functions and associated limits are shown in Fig. 3.18. In order to maximize both functions, it is desirable to increase the jaw width. However, the tool tip needs to fit through at least a 20 Gauge trocar (I.D. \approx 0.9mm). On the other hand, the jaw length, and the jaw thickness both have opposite effects on the objective functions. Therefore, it is not possible to maximize both grasping stiffness and opening compliance at a single value of jaw length or width. The optimum values of these parameters (3.19.a) were selected considering the target performance limits, which are set as 1N/mm for the minimum grasping stiffness (K_{grasp}), and 0.5 mm/N for the minimum opening compliance (C_{open}) considering tissue properties (for grasping), and maximum allowable strain on the FBGs during actuation.

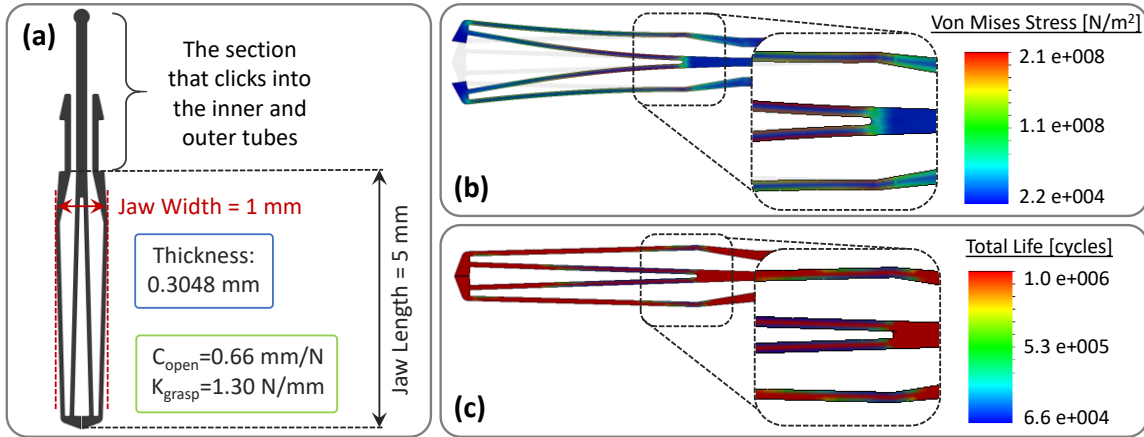


Figure 3.19: Optimal jaw design: (a) Dimensions (b) Stress distribution while opening the jaws with 1N of actuation force, (b) Fatigue life under 1 N cyclic loading: more than 60,000 cycles of actuation cycles before failure based on nitinol use ($E=41$ GPa, $\nu=0.33$) [106].

The true scale deformation under 0.7 N of actuation force and the corresponding stress distribution of the optimal design are shown in Fig. 3.19.b. The opening between the jaws ranges between 0-0.8 mm for forces between 0-0.7 N, which should be sufficient for grasping and peeling thin membranous layers inside the eye. Another concern in forceps design is the life-time of the jaws. Being subject to cyclic loading during use, the jaws will eventually break due to fatigue. Both the magnitude and frequency of applied actuation forces is important in determining the life time of the instrument. Since most of the tool tip-to-tissue forces normally range between 0 and 10 mN [29], small damage is caused during tissue manipulation. The life limiting damage mainly stems from the opening and closing motion of the jaws. Shown in Fig. 3.19.c is the total life of the optimal design considering an average actuation force of 1N. Accordingly, the instrument is expected to function for over 60,000 opening-closing cycles before failure. This approximate value will be lower with greater applied forcing and because of the wear and tear caused by sterilization. Nevertheless, the estimated lifetime is more than sufficient for a disposable tip.

3.2.2.1.3. Integration of Force Sensing

Due to both form factor constraints and measurement resolution requirements, accurate sensing of tool to tissue interactions in vitreoretinal surgery is a significantly challenging task. In order to measure forces applied solely at the instrument tip without any contribution from the sclerotomy site, the force sensor has to be functioning inside the eye close to the tool tip. This requirement implies several limitations in terms of availability of force sensing technologies: (1) the sensing part should be thin so that it can be introduced into the eye through at least a 20 Gauge trocar; (2) it has to be either inexpensive for a disposable design or sterilizable for multiple uses; (3) the sensor itself has to be biocompatible as it will be introduced into the eye during the surgery; (4) the measurements should have sub-mN resolution since the forces associated with vitreoretinal microsurgery are routinely less than 7.5 mN. Under these limitations, using FBG strain sensors is a possible good option.

Using FBGs has revealed promising results in 2-D force sensing instruments in previous sections. In these designs, 3 FBGs were mounted around the tool shaft to sense transverse loading at the tool tip. In designing 3-DOF forceps we followed a similar approach. The transverse loading is still measured via the 3 lateral FBGs on the outer tube of the forceps. However, additionally, a 4th axial FBG is located in the central tube for measuring the axial forces (Fig. 3.16). The tubes carrying the lateral and axial FBGs are connected to each other via the arms of the grasper jaws, which function as a flexure besides grasping. This flexure provides the decoupling of axial and transverse forces so that the axial FBG remains insensitive to transverse loading. Similarly, due to design of the grasper jaws and the coupling with tubes, the strain on lateral FBGs is minimal in the

presence of axial forces. The axial-transverse force decoupling is verified through sensitivity analyses in the next section.

3.2.2.1.4. Sensitivity Analysis

In order to determine the strain induced on each FBG under various loading cases, simulations were done using SolidWorks. The axis directions, applied loads and resulting strains in these simulations are shown in Fig. 3.20. When the loading was increased gradually, linearly increasing strain response was obtained, as expected. The slope of each line in this figure denotes the relative sensitivity of the associated FBG with regard to the related loading case. When there is pure axial loading on the tool tip, almost no strain is induced on the lateral FBGs. Similarly, application of only transverse forces does not cause a significant variation in axial FBG strain. The strain curves in Fig.3.20 and the associated slope values in Table 3.1 indicate that successful transverse-axial force decoupling has been accomplished.

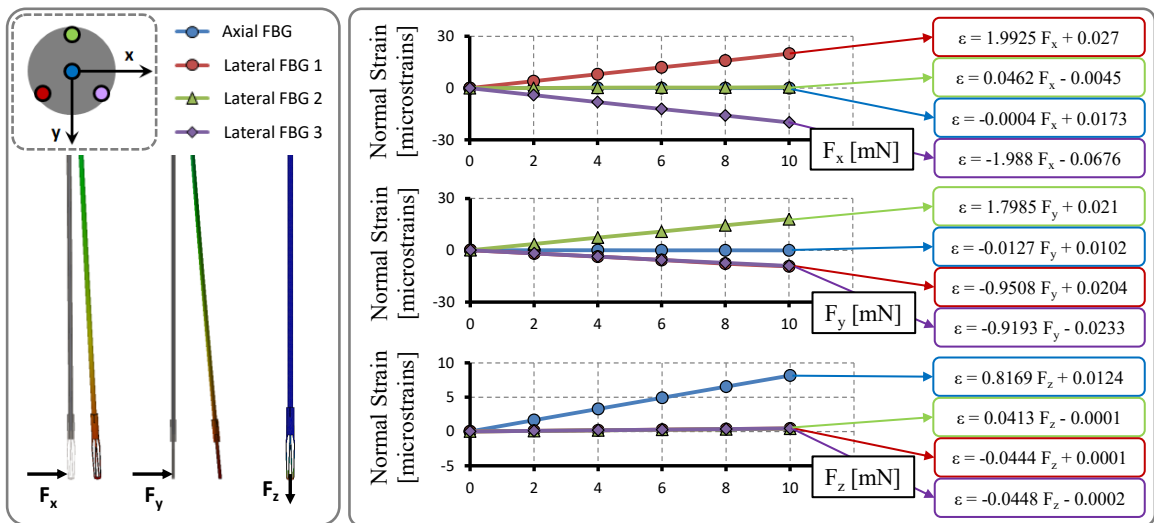


Figure 3.20: Induced normal strain on each FBG sensor under principle loading conditions. Linear rise in strain with increasing tip load, and success in decoupling lateral-axial forces [106].

Table 3.1: Results of the sensitivity analysis.

Forces	Sensitivities [microstrain/mN]			
	Axial FBG	Lateral FBG 1	Lateral FBG 2	Lateral FBG 3
F_x	0.0004	1.9925	0.0462	-1.988
F_y	-0.0127	-0.9508	1.7985	-0.9193
F_z	0.8169	-0.0444	0.0413	-0.0448

3.2.2.1.5. Force Computation:

The measured wavelength shift for each FBG channel (λ) is related to the force induced normal strain (ϵ_F) and the temperature induced strain (ϵ_T) via equation (3.7):

$$\lambda = c_F \epsilon_F + c_T \epsilon_T \quad (3.7)$$

The contribution from the ambient temperature variation can be eliminated by taking the average of all measurements and subtracting this mean value from the actual readings to form a new data set ($\Delta\lambda$). The linear relationship (3.8) gives the tip forces based on the force induced strain, where S is the sensitivity matrix and S^+ denotes its pseudoinverse:

$$\begin{bmatrix} F_x \\ F_y \\ F_z \end{bmatrix} = S^+ \epsilon_F = \frac{1}{c_F} S^+ \begin{bmatrix} \Delta\lambda_{\text{axial}} \\ \Delta\lambda_{\text{lateral}_1} \\ \Delta\lambda_{\text{lateral}_2} \\ \Delta\lambda_{\text{lateral}_3} \end{bmatrix} \quad (3.8)$$

$$\text{where } S = \begin{bmatrix} 0.0004 & 1.9925 & 0.0462 & -1.988 \\ -0.0127 & -0.9508 & 1.7985 & -0.9193 \\ 0.8169 & -0.0444 & 0.0413 & 0.0448 \end{bmatrix} \mu\text{strain/mN}$$

3.2.2.2. Concept 2: Motorized Actuation with Asymmetric Jaws

For easy integration with robotic platforms, in this section we focused on a modular micro-forceps that is motorized similar to previously introduced 2-DOF force-sensing tool in Section 3.2.1.3, but with a modified design to add axial force sensing capability.

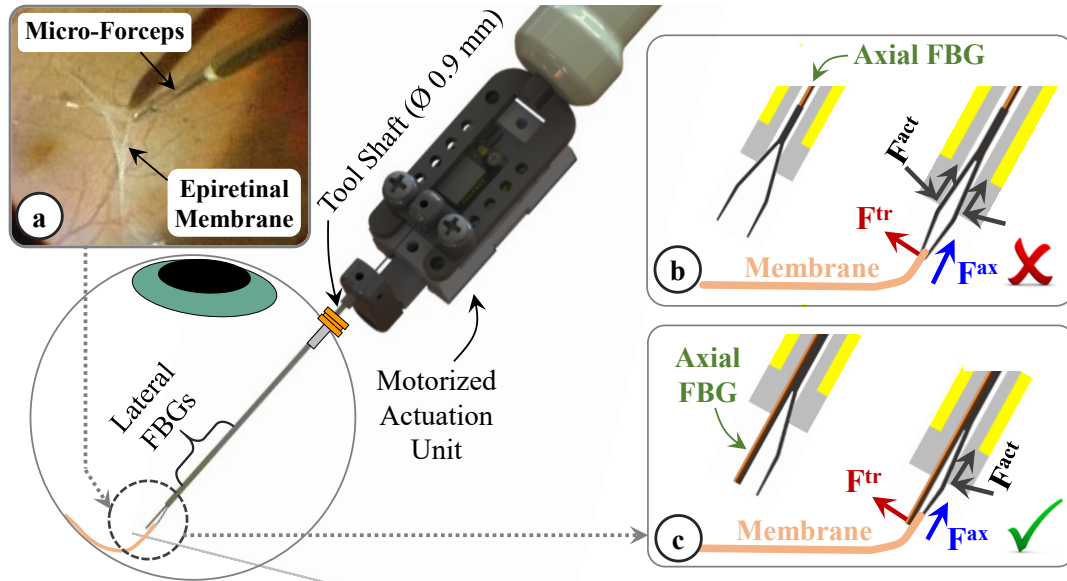


Figure 3.21: Force-sensing micro-forceps conceptual overview. (a) Epiretinal membrane peeling. (b) Axial FBG in the center: actuation force (F^{act}) degrades the sensor reading. (c) Axial FBG attached on the flattened arm of the jaw: bypassed F^{act} and direct exposure to tool tip forces (F^{ax} and F^{tr}) [108].

3.2.2.2.1. Design and Fabrication

The tool consists of a grasping mechanism and force-sensitive elements as shown in Fig. 3.21. The actuation unit houses a compact (28 x 13.2 x 7.5 mm) and lightweight (4.5 g) piezoelectric linear motor (M3-L, New Scale Technologies Inc., Victor, NY) with its embedded driver and encoder providing precise position control, which is used for opening and closing the forceps jaws. The normally-open compliant jaws are passed through a 23 Gauge guide tube and firmly anchored to the actuation unit via a set screw. The guide tube is attached to the shaft of the linear motor, so that when the motor is actuated, the guide tube is moved up and down along the tool axis, releasing or squeezing the forceps jaws.

In order to sense the applied forces after the membrane is grasped, the design employs 4 FBGs ($\text{\O}80 \mu\text{m}$ by Technica, GA, USA). Following a similar strategy as in our previous

2-DOF force-sensing micro-forceps, 3 lateral FBGs are fixed evenly around the guide tube to capture the transverse forces at the tool tip. This results in a sufficiently small tool shaft diameter of 0.9 mm. New in this work is the fourth FBG responsible for detecting the tensile axial forces while the membrane is pulled away from the retina. The location of this sensor is critical to maximize accuracy. Our initial concept hypothesized that centrally locating this sensor inside the guide tube at the distal end of jaws (Fig. 3.21.b) could provide the best decoupling between transverse and axial forces. In this configuration, although the sensor is positioned along the neutral axis for transverse loads and thus should sense only the axial loads, our preliminary experiments have shown that the frictional and elastic deformation forces generated at the guide tube/jaw interface during tool actuation significantly degrades the response of the sensor. As a remedy, we studied an alternative concept, where the forceps jaws are modified by flattening one arm (Fig. 3.21.c). When the guide tube is moved up and down, the flat arm is kept straight always while the other bent arm in contact with the guide tube elastically deforms to open/close the jaws. The central FBG is fixed on the flat arm of the jaws, where the sensitive region of the fiber is maintained close to the jaw tip outside the guide tube, bypassing the undesired actuation forces at the guide tube/jaw interface.

3.2.2.2.2. Force Computation Algorithm

A. Linear Method

Due to the asymmetry of the jaws, to grasp the membrane, this tool needs to be held at a certain orientation, which will induce transverse forces mostly along the open/close axis of the jaws as illustrated in Figs 3.21.b and 3.21.c. Hence in this study, instead of defining x and y components separately, we focused on this particular direction of the

transverse force, and modeled the elastic deformation of the guide tube as an Euler-Bernoulli beam under the transverse (F^{tr}) and axial (F^{ax}) loading at the tool tip, inducing a linearly proportional local elastic strain on each of the attached lateral FBGs and thus a linearly proportional shift in the Bragg wavelength of each sensor. In addition, even slight variations in ambient temperature (ΔT) may cause a drift in the Bragg wavelength. Then, the combined Bragg wavelength shift ($\Delta\lambda_i$) for each lateral FBG (FBGs 1, 2 and 3) can be expressed as

$$\Delta\lambda_i = C_i^{F_{-tr}} F^{tr} + C^{F_{-ax}} F^{ax} + C^{\Delta T} \Delta T, \text{ where } i = 1,2,3 \quad (3.9)$$

where $C_i^{F_{-tr}}$, $C^{F_{-ax}}$ and $C^{\Delta T}$ are constants associated with the transverse force, the axial force and the temperature change, respectively. Since the lateral FBGs are closely located within the same ambient, ideally, they are equally affected from the axial load ($C_1^{F_{-ax}} = C_2^{F_{-ax}} = C_3^{F_{-ax}} = C^{F_{-ax}}$) and the temperature variation ($C_1^{\Delta T} = C_2^{\Delta T} = C_3^{\Delta T} = C^{\Delta T}$). When the mean Bragg wavelength shift in all three lateral sensors is computed, due to axisymmetric distribution of lateral FBGs around the guide tube (120° apart from each other), the terms related to the transverse forces cancel each other, resulting in the common mode ($\Delta\lambda^{mean}$) which is a function of the axial force and the temperature change only.

$$\Delta\lambda^{mean} = C^{F_{-ax}} F^{ax} + C^{\Delta T} \Delta T \quad (3.10)$$

The effect of temperature change and axial force in sensor readings can be eliminated by subtracting the common mode from Bragg wavelength shift of each sensor.

$$\Delta\lambda_i^{diff} = \Delta\lambda_i - \Delta\lambda^{mean} = C_i^{F_{tr}} F_{tr}, \quad i = 1,2,3 \quad (3.11)$$

The remaining differential mode of each sensor ($\Delta\lambda_1^{\text{diff}}$) can then be used in the following equation to compute the transverse forces:

$$\mathbf{F}^{\text{tr}} = \mathbf{C}^{\text{tr}} [\Delta\lambda_1^{\text{diff}} \quad \Delta\lambda_2^{\text{diff}} \quad \Delta\lambda_3^{\text{diff}}]^{\text{T}} \quad (3.12)$$

where \mathbf{C}^{tr} is a 1x3 coefficient matrix that represents the linear mapping from optical sensor readings to the force domain, and will be found via a calibration procedure.

In addition to the elastic strain due to axial load, the axial FBG (FBG 4) experiences also a bending moment induced by the transverse force at the tool tip. Furthermore, changes in ambient temperature will induce a drift in the measured Bragg wavelength. Since the axial and transverse FBGs share the same environment, we hypothesize that the thermal drift of the axial FBG and that of the common mode of the three lateral FBGs are linearly correlated. Based upon this hypothesis, multiplying the common mode of lateral FBGs ($\Delta\lambda^{\text{mean}}$) with a proper coefficient (κ) and subtracting it from $\Delta\lambda_4$, the effect of temperature change can be eliminated.

$$\Delta\lambda_4^{\text{diff}} = \Delta\lambda_4 - \kappa \Delta\lambda^{\text{mean}} = \mathbf{C}^{\text{ax}} \mathbf{F}^{\text{ax}} + \mathbf{C}_4^{\text{F-tr}} \mathbf{F}^{\text{tr}} \quad (3.13)$$

Since \mathbf{F}^{tr} is already found based upon lateral FBGs, the axial load can be computed after \mathbf{C}^{ax} and $\mathbf{C}_4^{\text{F-tr}}$ constants are identified via calibration.

$$\mathbf{F}^{\text{ax}} = (\Delta\lambda_4^{\text{diff}} - \mathbf{C}_4^{\text{F-tr}} \mathbf{F}^{\text{tr}}) / \mathbf{C}^{\text{ax}} \quad (3.14)$$

B. Nonlinear Method

Due to the very small dimensions and imperfections in tool fabrication, it may not be possible to accurately decouple the effect of axial and lateral loads using a linear model, especially on the axial FBG. We hypothesize that such a linear fitting may perform well

only locally, when the transverse forces are much smaller than the axial load. In order to obtain a global estimate of force, a nonlinear fitting method based on second order Bernstein polynomials can be used as

$$F = \sum_{i=0}^n \sum_{j=0}^n \sum_{k=0}^n \sum_{l=0}^n c_{ijkl} b_{i,n}(\Delta\lambda_1^*) b_{j,n}(\Delta\lambda_2^*) b_{k,n}(\Delta\lambda_3^*) b_{l,n}(\Delta\lambda_4^*) \quad (3.15)$$

where c_{ijkl} denotes constant coefficients and $\Delta\lambda_i^*$ denotes the differential mode (thermal drift eliminated response as described by equations (3.11) and (3.13)) of each FBG scaled down to [0,1] interval – since Bernstein polynomials exhibit good numerical stability within this range [109] – using the following equation:

$$\Delta\lambda_i^* = \frac{\Delta\lambda_i^{\text{diff}} - \Delta\lambda_{i,\text{min}}^{\text{diff}}}{\Delta\lambda_{i,\text{max}}^{\text{diff}} - \Delta\lambda_{i,\text{min}}^{\text{diff}}} \text{ for } i = 1,2,3,4 \quad (3.16)$$

$b_{v,n}(\Delta\lambda_i^*)$ terms in equation (3.15) are the Bernstein basis polynomials of order n defined as follows:

$$b_{v,n}(\Delta\lambda_i^*) = \binom{n}{v} \Delta\lambda_i^{*v} (1 - \Delta\lambda_i^*)^{n-v} \text{ for } v = 0 \dots n \text{ and } i = 1,2,3,4 \quad (3.17)$$

In our approach, in order to avoid overfitting with a reasonable sample size, we use a 2nd order regression by setting n=2 and defining

$$B_{ijklm} = b_{j,2}(\Delta\lambda_1^*) b_{k,2}(\Delta\lambda_2^*) b_{l,2}(\Delta\lambda_3^*) b_{m,2}(\Delta\lambda_4^*) \quad (3.18)$$

Then, equation (3.15) can be rearranged as

$$[F^{\text{tr}} \quad F^{\text{ax}}] = \sum_{i=0}^2 \sum_{j=0}^2 \sum_{k=0}^2 \sum_{l=0}^2 B_{ijkl} c_{ijkl} = B C^{\text{Bernstein}} \quad (3.19)$$

where B is a 1x81 row vector formed by the product of Bernstein basis polynomials and $C^{\text{Bernstein}}$ is a 81x2 constant matrix. The coefficients in $C^{\text{Bernstein}}$ can be found by

applying known forces (F^{tr} and F^{ax}) in various directions at the tool tip and monitoring the corresponding FBG data ($\Delta\lambda_i^*$).

3.2.2.2.3. Calibration Experiments

In order to identify the constants used in our force computation algorithm, we performed a set of calibration experiments. The goal in our first experiment was to test the hypothesis of linear correlation between the temperature drift in common mode of lateral FBGs and the axial FBG. Using an optical sensing interrogator (sm130-700 from Micron Optics Inc., Atlanta, GA), we recorded the Bragg wavelength of all FBGs during a 180 minute period with 15 minute intervals while exposing the tool to routine changes in room temperature. The wavelength shift of the lateral FBGs were observed to be almost identical (Fig. 3.22.b). The change in the common mode of lateral FBGs and the shift in

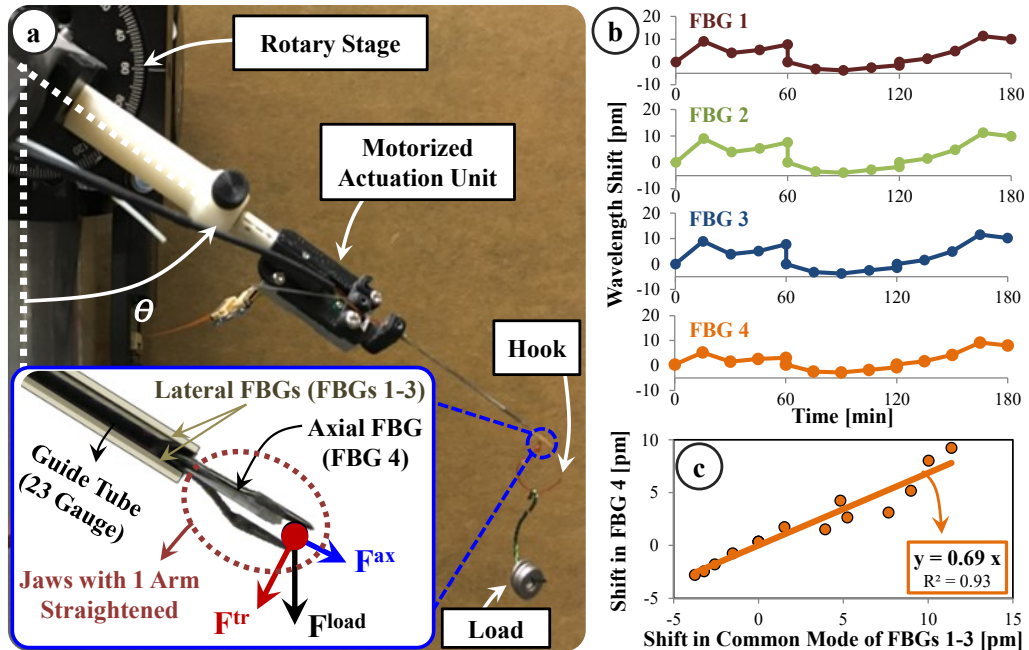


Figure 3.22: (a) Fabricated prototype and experimental setup. (b) Thermal drift in lateral (FBGs 1-3) and axial (FBG 4) sensor readings. (c) Linear correlation between the common mode of lateral FBGs and the axial FBG [108].

the axial FBG could be linearly correlated as shown in Fig. 3.22.c ($R^2=0.93$). The corresponding proportionality constant was found to be $\kappa=0.69$.

Our second experiment was for modeling the lateral and axial FBG response under various forces. For this, we mounted our forceps on a rotary stage and used the jaws to grasp a wire hook (Fig. 3.22.a). By hanging various loads on the hook and modulating the tool orientation (θ) the axial and transverse forces at the tool tip were changed. Measurements were taken for loads ranging from 0 to 25 mN with 5 mN intervals and at angles from $\theta=0^\circ$ (entirely axial loading) to $\theta=90^\circ$ (entirely transverse loading) with 15° intervals. This produced 42 distinct loading cases; and at each orientation, the tool tip was repeatedly loaded/unloaded 3 times. The obtained response for 3 illustrative orientations is shown in Fig. 3.23. When the tool was held at $\theta=0^\circ$, the entire loading was axial, therefore affecting only the axial FBG linearly with a slope of 0.78. This suggests $C^{\text{ax}}=0.78$ pm/mN in eqn. (3.14). At $\theta=90^\circ$, the induced force was purely transverse which caused a linear response in all FBGs. The sensitivity of the axial FBG in this orientation revealed $C_4^{\text{F.tr}} = 2.32$ pm/mN. Based upon the slope of lateral FBG response curves, the coefficient matrix in eqn. (3.12) was found as $C^{\text{tr}}=[-0.0342 \ 0.089 \ -0.0548]$ mN/pm. The wavelength resolution of our interrogator is 1 pm, which propagates to a transverse force resolution of 0.17 mN and an axial force resolution of 1.8 mN considering the identified coefficients for the linear method. Finally, using the entire data set of 252 measurements, the least squares problem formulated in eqn. (3.19) was solved to find $C^{\text{Bernstein}}$. The identified coefficient provided a transverse force resolution of 0.08 mN and an axial force resolution of about 1.08 mN. The fit polynomial could estimate the

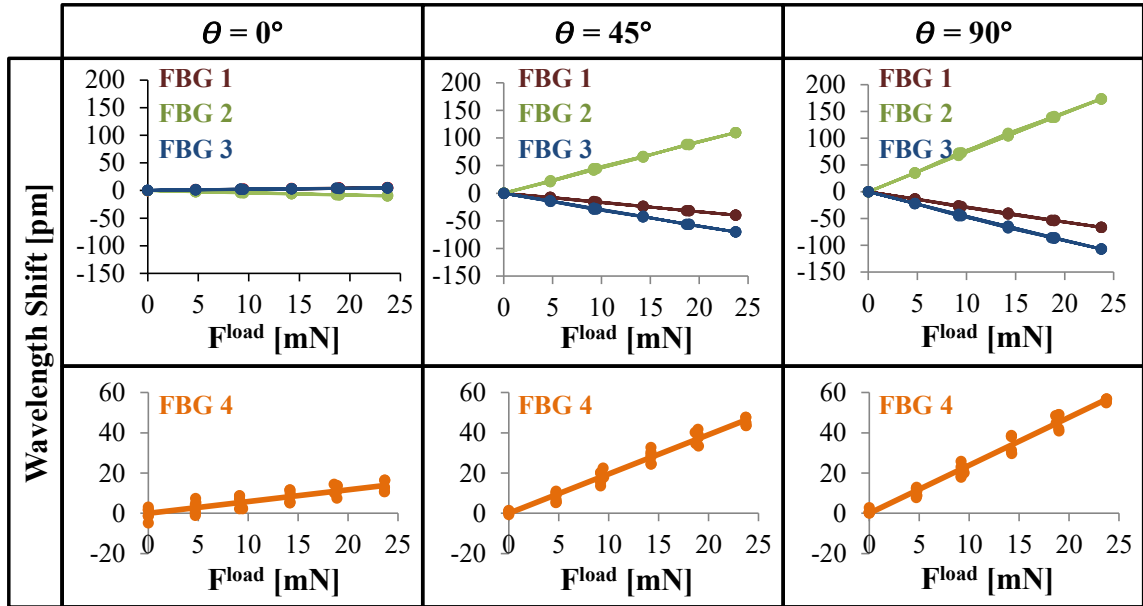


Figure 3.23: Lateral (FBGs 1-3) and axial (FBG 4) sensor response to loading (0-25 mN) at the tool tip for three different orientations ($\theta = 0^\circ, 45^\circ, 90^\circ$) [108].

transverse and axial forces in the calibration data set with mean absolute residual errors of 0.11 mN and 1.23 mN and RMS errors of 0.15 mN and 1.69 mN, respectively.

3.2.2.2.4. Validation Experiments

Forces ranging from 0 mN to 25 mN were applied on the tool with 5 mN intervals at 20° , 40° and 70° orientations; each test was repeated 6 times, producing 108 measurements. The data set was extended by adding 15 more measurements at randomized angles (0° - 90°) and forces (0-25 mN). Our first attempt to estimate applied force using a linear model performed well for the transverse load with an RMS error of 0.13 mN (Fig. 3.24.a), though did not provide an adequate accuracy in finding the axial force (Fig. 3.24.b). The linear method produced an RMS error of 2.05 mN for cases with a transverse force less than 5 mN, but when larger (up to 25 mN) transverse loads were involved, the RMS error in the computed axial force rose up to 5.14 mN. This indicates that the linearity of sensor response is lost when large transverse forces are applied at the

tool tip in addition to axial loads. Our second approach, the Bernstein polynomial method, showed similar success in estimating the transverse force with an RMS error of 0.22 mN (Fig. 3.24.c). More importantly, the accuracy in axial force estimation was significantly improved with a much smaller RMS error of 1.99 mN (Fig. 3.24.d) for the entire force range (0-25 mN), which is closer to the required accuracy for feasibility in membrane peeling. Our future work aims at investigating other tool architectures preserving the axial symmetry of the tool and providing better axial force sensing accuracy.

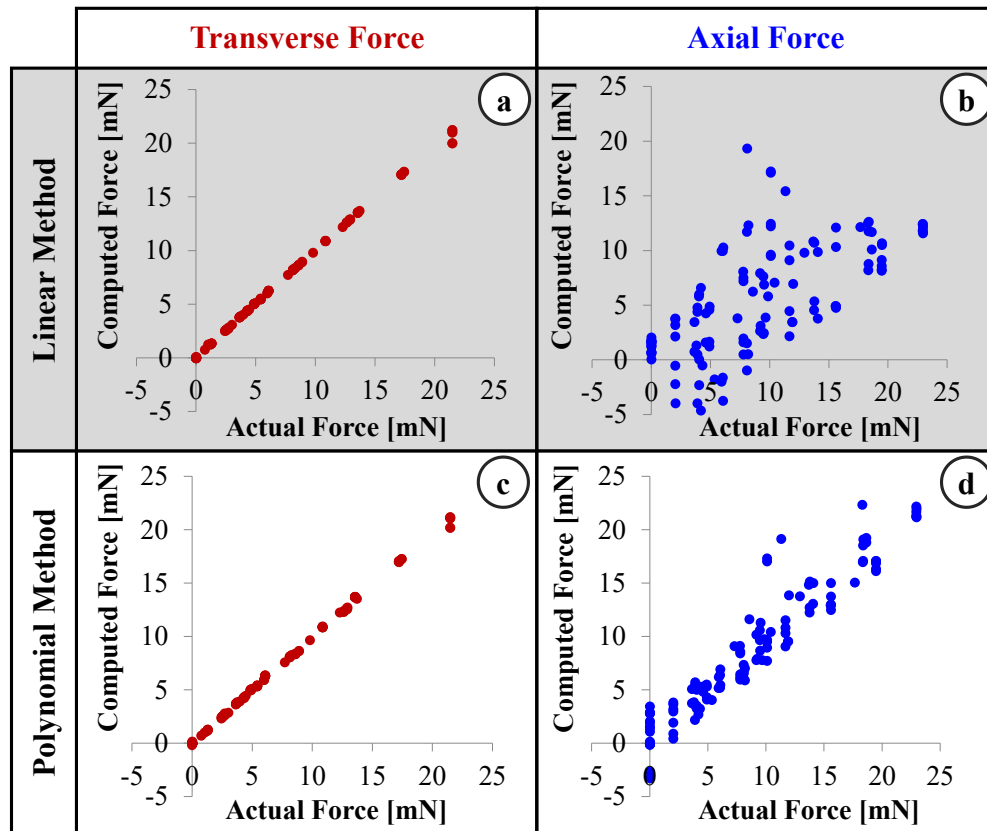


Figure 3.24: Computed transverse and axial forces vs. the actual values. Similar accuracy for both methods in estimating the transverse load, better performance with the polynomial method for estimating the axial load [108].

3.2.2.3. Concept 3: Motorized Actuation with Symmetric Jaws

Unlike in the previous section, this design concept uses symmetric jaws, and is intended to measure tool tip forces about the x, y and z axes of the tool separately. The assigned coordinate system of the forceps is shown in Fig. 3.25. The x and y axes form the transverse plane while the z-axis lies along the tool axis. During the grasping action, the jaws elastically deform to move toward each other along the x-axis. After grasping the membrane edge, the tool is moved mostly along its z-axis and x-axis to respectively pull and peel the membrane away from the adherent inner retina surface.

3.2.2.3.1. Design and Fabrication

Similar to the previous concept, the grasping functionality is provided by a piezoelectric linear motor (M3-L, New Scale Technologies Inc., Victor, NY) with its embedded driver and encoder providing precise position control. The normally-open compliant jaws are

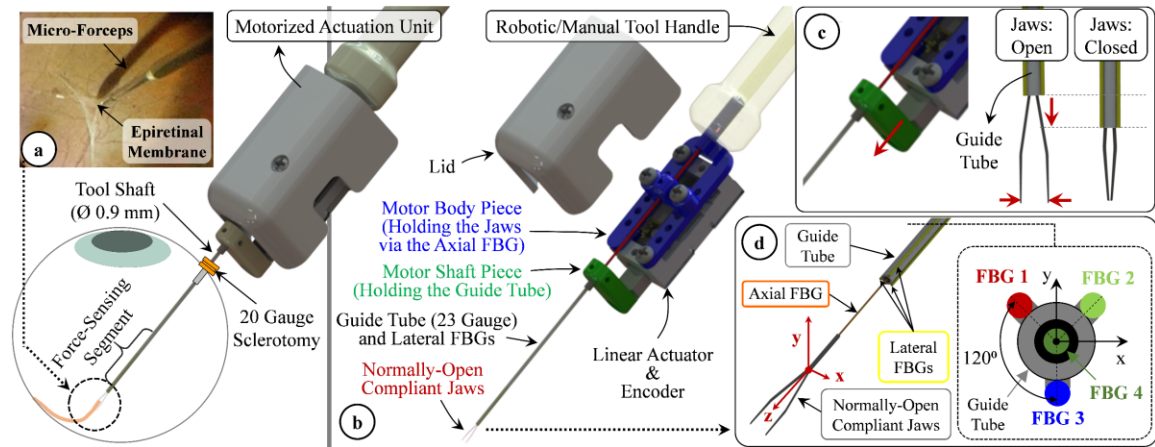


Figure 3.25: (a) Epiretinal membrane peeling using our motorized force-sensing micro-forceps with the force-sensitive region of the tool inserted into the eye through a 20 Gauge sclerotomy. (b) Components of the design (c) Motorized actuation mechanism driving the guide tube up/down for opening/closing the jaws. (d) The tool coordinate frame and FBG sensor configuration. The axial FBG sensor (FBG 4) at the center inside the guide tube and three lateral FBG sensors integrated on the guide tube (FBGs 1-3) measure axial (F_z) and transverse forces (F_x and F_y) at the tool tip, respectively [110].

taken out from a standard disposable 23 Gauge micro-forceps (Alcon Inc., Fort Worth, TX). They are passed through a 23 Gauge stainless steel guide tube and firmly anchored to the motor body. The guide tube is attached to the shaft of the linear motor, so that when the motor is actuated, it drives the guide tube up and down along the z-axis, releasing or squeezing (thus opening or closing) the forceps jaws (Fig. 3.25.c). The parts connecting the guide tube to the motor shaft, housing the motor, anchoring the jaws to the motor body and the lid shielding the mechanism were built using 3D printed Acrylonitrile Butadiene Styrene (ABS). The assembled actuation (Fig. 3.26.b) unit occupies a space of 1.8 x 1.8 x 3.5 mm and weighs approximately 8.9 grams, which is close to the weight of Alcon's 23 Gauge disposable micro-forceps (about 7.9 grams).

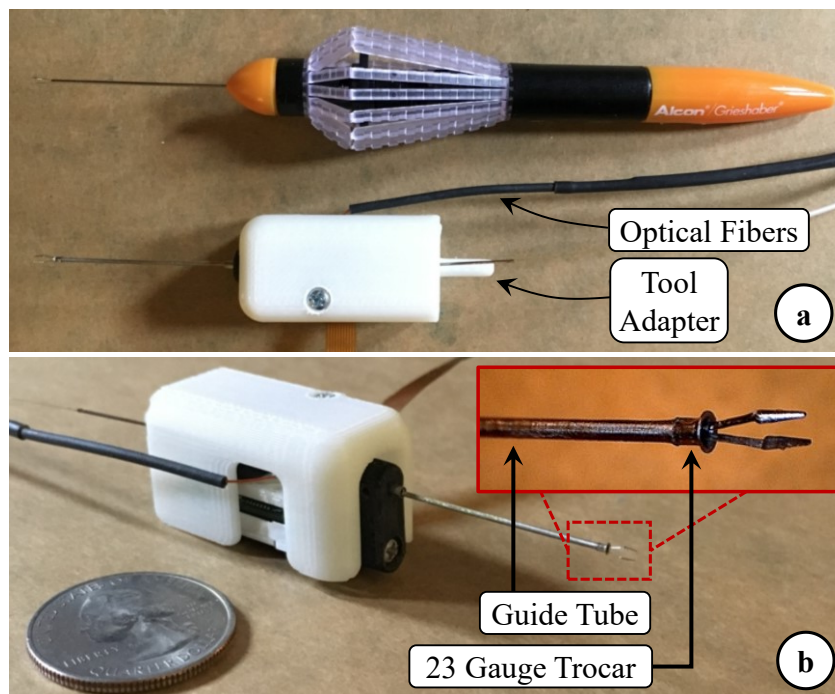


Figure 3.26. (a) The standard 23 Gauge disposable micro-forceps by Alcon Inc. vs. the manufactured prototype of our motorized force-sensing micro-forceps. (b) Close-up view of the distal force-sensing segment. A fine-polished filleted stainless steel piece (23 Gauge trocar) was bonded at the distal end of guide tube, to modify the jaw/guide tube interface so that the reaction force during tool actuation is consistently smaller and its adverse influence on axial FBG sensor is minimal [110].

The exerted forces in membrane peeling are typically along the x-axis of the instrument during delamination and mostly tensile in the z-axis while pulling the membrane away from the retina. Experiments in porcine cadaver eyes demonstrate that the forces utilized in peeling are generally less than 7.5 mN [29]. Measuring these very fine forces without adverse contribution from contact at the sclerotomy requires locating the sensor inside the eye, hence a sensor that (1) can fit through a small incision ($\text{Ø} \leq 0.9\text{mm}$) on the sclera, (2) is sterilizable and biocompatible, and (3) can provide sub-mN accuracy for transverse force measurements and predict the axial load within an accuracy less than 2 mN. Based upon these constraints, our design employs 4 FBG sensors which all have one 3 mm FBG segment with center wavelength of 1545 nm (Technica S.A., Beijing, China).

Following a similar strategy to the previously described tools, we fixed 3 lateral FBGs ($\text{Ø} = 80 \mu\text{m}$) evenly around the 23 Gauge guide tube using medical epoxy adhesive (Loctite 4013, Henkel, CT) to capture the transverse forces (F_x and F_y) at the tool tip (Fig. 3.25.d). Although the previous motorized 3-DOF micro-forceps architecture (in section 3.2.2.2) ensured that the axial sensor response is not affected from tool actuation, the asymmetric design complicated the calibration procedure as well as the force decoupling and computation steps. In our new concept, instead of customizing the jaws, we maintained the axial FBG in the tool center inside the guide tube preserving the axial symmetry of the tool and modified the jaw/guide tube interface by attaching a fine-polished and filleted piece, the introduction section of a standard 23 Gauge trocar with the cannula section trimmed off [111] at the distal end of the guide tube as shown in Fig. 3.26.b. The inner diameter of the trocar fit onto the guide tube, and the flange member at its proximal end was trimmed to fit through a 20 Gauge opening ($\text{Ø} = 0.9 \text{ mm}$). Using

medical epoxy adhesive (Loctite 4013, Henkel, CT), it was bonded onto the guide tube such that the flange member of the trocar is at the distal end of the tool and the filleted end of the trocar's hollow bore contacts the jaws for squeezing and closing them. This modification aimed at lowering the frictional forces during the actuation of the tool, preventing the jaws from getting stuck, enabling the applied axial forces to generate sensible strain on the axial FBG with the same sensitivity regardless of the opening state of the jaws. This functionality will be verified through finite element simulations in the next section, and the effect of actuation on the axial FBG response will be experimentally characterized in the following section.

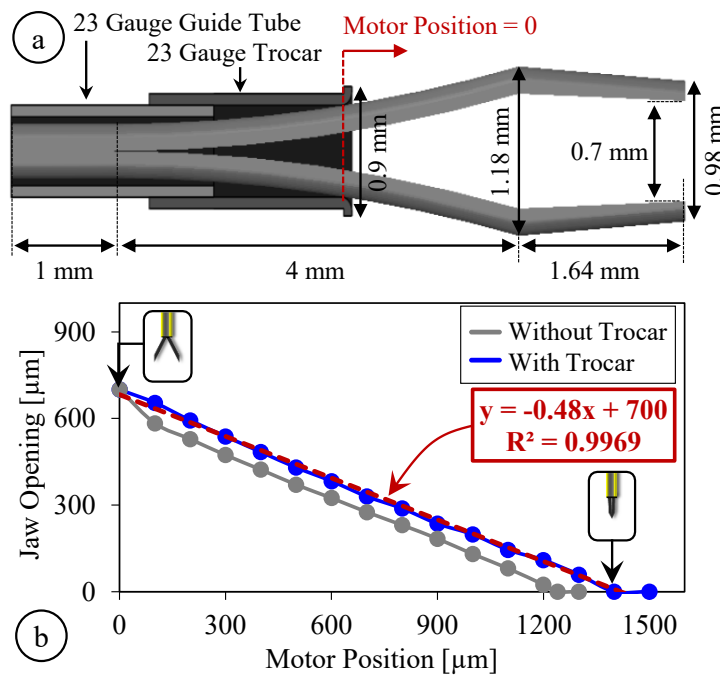


Figure 3.27: (a) Geometric parameters of the jaw model, guide tube and the trocar attachment used in finite element simulations, (b) The micro-forceps kinematics with and without the trocar attachment. While fully open, the jaw tips are 0.7 mm apart; full closure requires driving the motor about 1240 μm without the trocar and 1400 μm with the trocar. An almost linear response is obtained with the trocar [110].

3.2.2.3.2. *Finite Element Analyses*

The motorized and encoded actuation provides a highly repeatable response, which enables a consistent correlation between the motor position and the opening between the jaws. In order to identify the kinematics of our tool, we first found the geometric parameters of the jaws taken out from Alcon's disposable 23 Gauge micro-forceps. We used a digital microscope to capture projection images of the jaws, and then used Digimizer (MedCalc Software, Belgium) software to process these images. Resulting geometric parameters are shown in Fig. 3.27.a. Next, we implemented the identified jaw model and the 23 Gauge guide tube in ABAQUS 6.13 (Dassault Systems, USA) software to simulate the opening/closing action of jaws both with and without the trocar at the distal end of the guide tube. The material of jaws and the guide tube were both set as stainless steel, SS316 (Young's modulus=193 GPa and Poisson ratio=0.3). The jaws were maintained fixed while an increasing displacement was applied to the proximal end of the guide tube to gradually close the jaws, generating the plots shown in Fig. 3.27.b. According to simulation results, when the jaws are fully open, the forcep tips are about 0.7 mm apart. As the guide tube is driven forward, the jaw opening decays nonlinearly at a decreasing rate without the trocar attachment. When the trocar is used, the jaws close with an almost linear response, at a rate of about 0.48 $\mu\text{m}/\mu\text{m}$. For full closure, using the trocar requires slightly larger translation of the guide tube, approximately 1400 μm in comparison to the 1240 μm without the trocar; however, this is still within the travel range of the linear actuator (6 mm) and does not correspond to a significant difference in the time it takes to fully close the jaws thanks to the fast response of the actuator (>5mm/s).

Next, we simulated the variation of the strain induced on the axial FBG during the actuation of the forceps. Since the exact value of the friction coefficient at the jaw/guide tube interface is not known, we analyzed the behavior for three different coefficients ($C_f = 0.4, 0.5$ and 0.6) considering typical steel-steel dry contact properties. Results in Fig. 3.28.a show that using the bare guide tube, the strain rises very rapidly initially at a decreasing rate during the first $300 \mu\text{m}$ of motor actuation. The trocar attachment leads to a more gradual increase in strain. After the jaws are fully closed (motor position reaches $1240 \mu\text{m}$ without the trocar and $1400 \mu\text{m}$ with the trocar), driving the motor forward further does not change the jaw opening but squeezes the jaws more, producing higher grasping force, and leading to a rapid rise in strain in all cases. Higher friction coefficients generate greater strain during actuation regardless of the trocar. However, for each value of friction coefficient, the use of trocar clearly lowers the strain level. For instance, for $C_f = 0.5$, without the trocar, full closure of the forceps generates of about $140 \mu\text{strains}$ as compared to $98.5 \mu\text{strains}$ with the trocar. The actual effect in the Bragg wavelength of the axial sensor will be characterized experimentally in Section 3.2.2.3.4.

In order to monitor the influence of axial forces at the tool tip, we ran additional simulations for the configuration with the trocar attachment. We applied forces at the tip of jaws along the z-axis for various levels of jaw opening. Simulations involved forces ranging from 0 to 25 mN in increments of 5 mN . For each load condition, the motor was moved from 0 (fully open state) to $1400 \mu\text{m}$ (fully closed state), and the strain on the axial FBG sensor was recorded at each $100 \mu\text{m}$ step. After subtracting the previously identified actuation-induced strain component for each motor position (Fig. 3.28.b), we computed and plotted the strain purely due to the applied axial load for each jaw opening.

Results in Fig. 3.28.c show that with the modified jaw/guide tube interface, the variation of force-induced strain on the axial FBG is linear for all jaw states (from fully closed to fully open); and the slope of the response remains almost the same regardless of the opening between the forceps jaws.

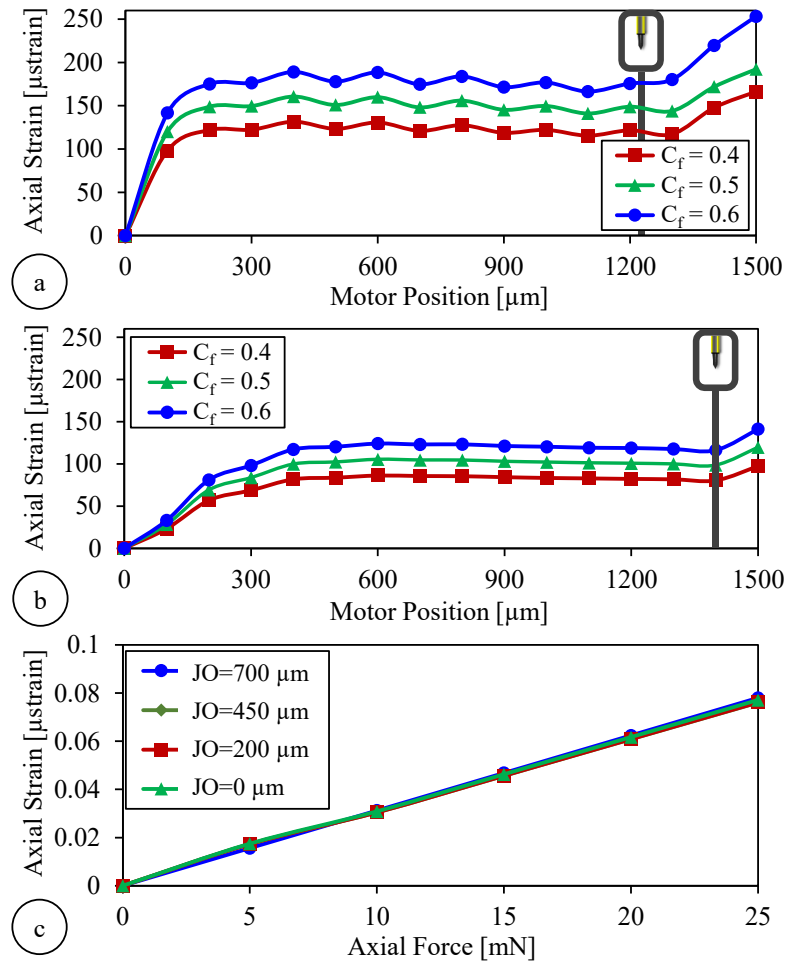


Figure 3.28: Finite element simulation results showing the axial FBG response to tool actuation for various levels of friction coefficient (C_f) at the jaw/guide tube interface (a) without the trocar and (b) with the trocar attachment at the guide tube's tip. Larger friction coefficients produce more strain. Lower strain levels are observed with the trocar. (c) The force-induced strain on the axial FBG vs. the applied axial load when the trocar attachment is used: the strain is linearly correlated with the axial load, and the sensitivity is almost identical for all levels of jaw opening (JO) [110].

3.2.2.3.3. Force Computation Algorithm

In order to transform the optical wavelength information from each embedded sensor to x-y-z force values, we use the force computation algorithm summarized in Fig. 3.29. The FBG sensors in our design are bonded to parts that move during the actuation of the forceps, i.e. opening/closing the jaws induces undesired drift in sensor readings. Since the actuation is performed by a precision motor with an integrated encoder, the deformation and resulting reaction forces during actuation are highly repeatable, and the influence on each FBG sensor can be modeled as a function of the motor position. This model accounts for the frictional and elastic deformation forces at the jaw/guide tube interface inducing strain especially on the axial FBG. The effect of actuation on lateral FBGs are presumably minor since the lateral FBGs are mostly sensitive to the transverse deformations, which ideally do not take place assuming perfectly aligned parts and purely linear translation of the guide tube. Furthermore, apart from the material and dimensions of the forceps structure, the model may vary depending upon the medium in which the forceps tool is operated (air, water, etc) as the coefficient of friction at the jaw/guide tube interface may change. We will verify these assumptions and identify the actuation influence through experiments in Section 3.2.2.3.4.

During the actual use of the micro-forceps, based on the identified actuation model and sensed motor position, the readings from each FBG sensor are corrected, simply by subtracting the estimated Bragg wavelength shift due to actuation. After the actuation effect correction, we cancel out the drift due to thermal changes based on the common mode of lateral FBGs.

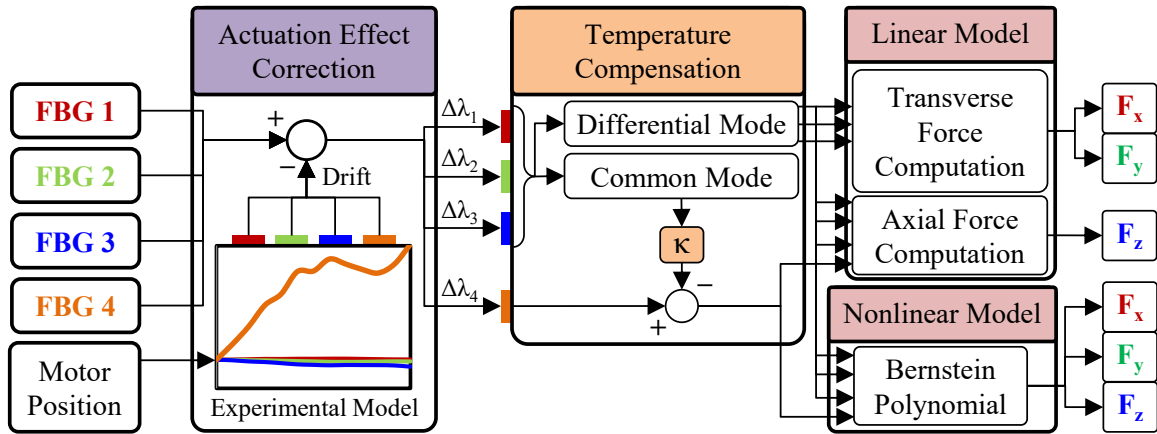


Figure 3.29: Force computation algorithm using an experimentally identified model to cancel the actuation-induced drift in FBG sensor readings based on the motor position and two distinct (linear and nonlinear) methods for transforming the corrected sensor readings into transverse (F_x and F_y) and axial (F_z) force information [110].

Different than the previous concept, the axial FBG (FBG 4) in this design lies along the tool axis ideally centered inside the guide tube, which would result in an ideal decoupling of transverse and axial loads, i.e. an axial FBG response immune to F_x and F_y , sensing purely F_z . However, due to the very small dimensions and imperfections resulting from tool assembly, this condition is very hard to achieve. Even if the axial FBG is slightly off-centered, besides the elastic strain due to F_z , the axial FBG will experience a bending moment due to F_x and F_y . In addition, excessive off-centered loading at the tool tip may also induce torsion on the axial fiber and deteriorate the FBG response, which we assume will be negligible considering the targeted force range (0-25 mN) and the small tool diameter (0.9 mm).

To compute tool tip forces from the corrected and temperature compensated sensor readings, we explored the use of two distinct methods which were previously introduced in Section 3.2.2.2.2: (1) a linear method based on ideal decoupling of transverse and axial forces, and (2) a nonlinear regression based on second order Bernstein polynomials. In

the derived equations for both methods (eqns. 3.8-3.18), the transverse force terms (F^{tr}) were replaced by F_x and F_y to detect forces in 3 dimensions separately. For the linear method, the forces are computed as follows:

$$[F_x \quad F_y]^T = C^{\text{tr}} [\Delta\lambda_1^{\text{diff}} \quad \Delta\lambda_2^{\text{diff}} \quad \Delta\lambda_3^{\text{diff}}]^T \quad (3.19)$$

$$F_z = C^{\text{ax}} [\Delta\lambda_1^{\text{diff}} \quad \Delta\lambda_2^{\text{diff}} \quad \Delta\lambda_3^{\text{diff}} \quad \Delta\lambda_4^{\text{diff}}]^T \quad (3.20)$$

C^{tr} is a 2x3 coefficient matrix, and C^{ax} is a 1x4 coefficient vector, which are found via calibration experiments. The nonlinear method computes the forces based on:

$$[F_x \quad F_y \quad F_z] = \sum_{i=0}^2 \sum_{j=0}^2 \sum_{k=0}^2 \sum_{l=0}^2 B_{ijkl} c_{ijkl} = B C^{\text{Bernstein}} \quad (3.21)$$

where B is a 1x81 row vector formed by the product of Bernstein basis polynomials and $C^{\text{Bernstein}}$ is a 81x3 constant matrix. The coefficients in $C^{\text{Bernstein}}$ can be found by applying known forces (F_x , F_y and F_z) in various directions at the tool tip, acquiring FBG wavelength data and forming a B vector for each recorded sample, and finding the best fit in the least-squares sense.

3.2.2.3.4. Tool Calibration

A. Setup

Using the setup shown in Fig. 3.30, we performed a series of experiments to model the effect of forceps actuation on force sensor readings, examine the repeatability of sensor outputs, identify calibration constants and validate our linear and nonlinear force computation methods. In order to acquire the Bragg wavelength of each FBG sensor, the setup employed an optical sensing interrogator (sm130-700 from Micron Optics Inc., Atlanta, GA). The force-sensing micro-forceps was mounted on a rotary stage to adjust

the axial orientation (roll angle, α) of the tool. The stage was attached onto a second rotary stage to modify the pitch angle (β) and tilt the tool in the vertical plane. The jaws of the forceps were closed to grasp a thin ($\sim 80 \mu\text{m}$ thick) layer of tape carrying a wire hook. The wire hook was used to hang aluminum washers and apply varying forces at the tool tip (Fig. 3.30.b).

The washers were weighed by using a precision scale (Sartorius GC2502, Germany) which has a resolution of 1 mg and a repeatability of ± 2 mg. The maximum test load was 23.35 mN, and each washer weighed about 4.67 mN. By changing the tool orientation (α

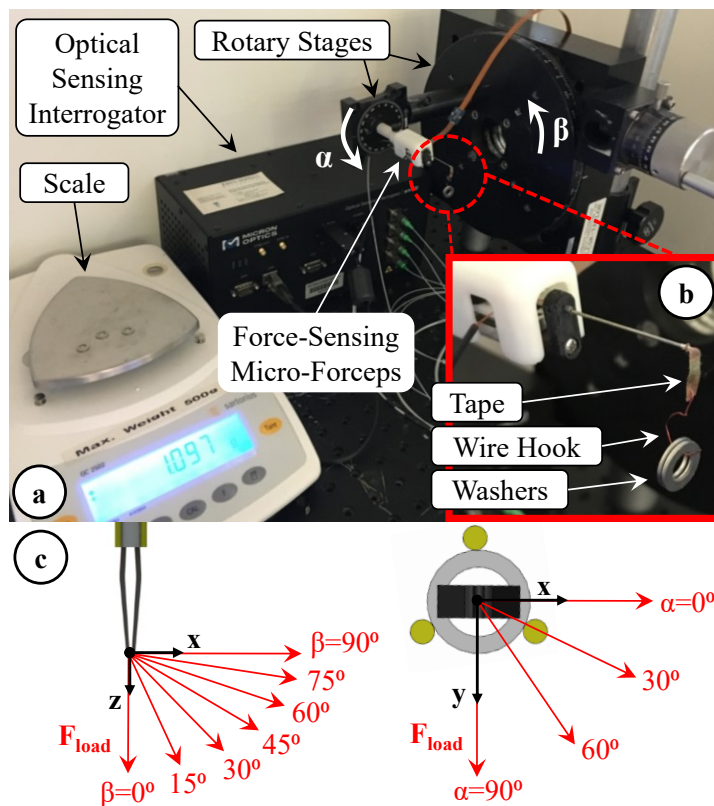


Figure 3.30: Experimental setup. (a) The 3-DOF force-sensing micro-forceps was mounted on two rotary stages to control the roll (α) and pitch (β) angles of the tool. (b) By hanging washers onto the grasped hook, the magnitude of the applied force was changed. (c) Modulating the tool orientation (α and β), thus the direction of the applied force, various combinations of F_x , F_y and F_z were applied at the tool tip [110].

and β) and the load hanging at the tip (F_{load}), various combinations of F_x , F_y and F_z were generated as shown in Fig 3.30.c. The resulting forces at the tool tip can be resolved into their x, y and z components using the following formulae:

$$F_x = \|F_{load}\| \cos \alpha \sin \beta \quad (3.22)$$

$$F_y = \|F_{load}\| \sin \alpha \sin \beta \quad (3.23)$$

$$F_z = \|F_{load}\| \cos \beta \quad (3.24)$$

B. Effect of Actuation

The goal of this experiment was to generate a model for compensating the detrimental effect of grasping motion on the FBG sensors. For this, the linear motor of the micro-forceps was actuated back and forth in discrete steps of 100 μm , and gradually opening/closing the forceps jaws. The jaws were fully closed after the motor was driven about 1400 μm forward from the fully open state, which is consistent with the simulation results previously presented in Fig. 3.27.b. After each 100 μm step, the motor was stopped and the wavelength shifts of the FBG sensors were recorded. The open/close cycle was repeated 3 times, leading to 6 measurements for each sensor at each motor position. Following the identical procedure, the experiment was repeated whilst the tool tip was immersed in water.

Results in Fig. 3.31 show that the motorized actuation does not induce a detectable change in the output of lateral sensors (FBGs 1, 2 and 3). However, the Bragg wavelength of the axial sensor (FBG 4) significantly varies depending on the motor position and therefore the opening state of forceps jaws in air and water. The wavelength shift profiles closely follow the axial strain variation trend that was predicted through

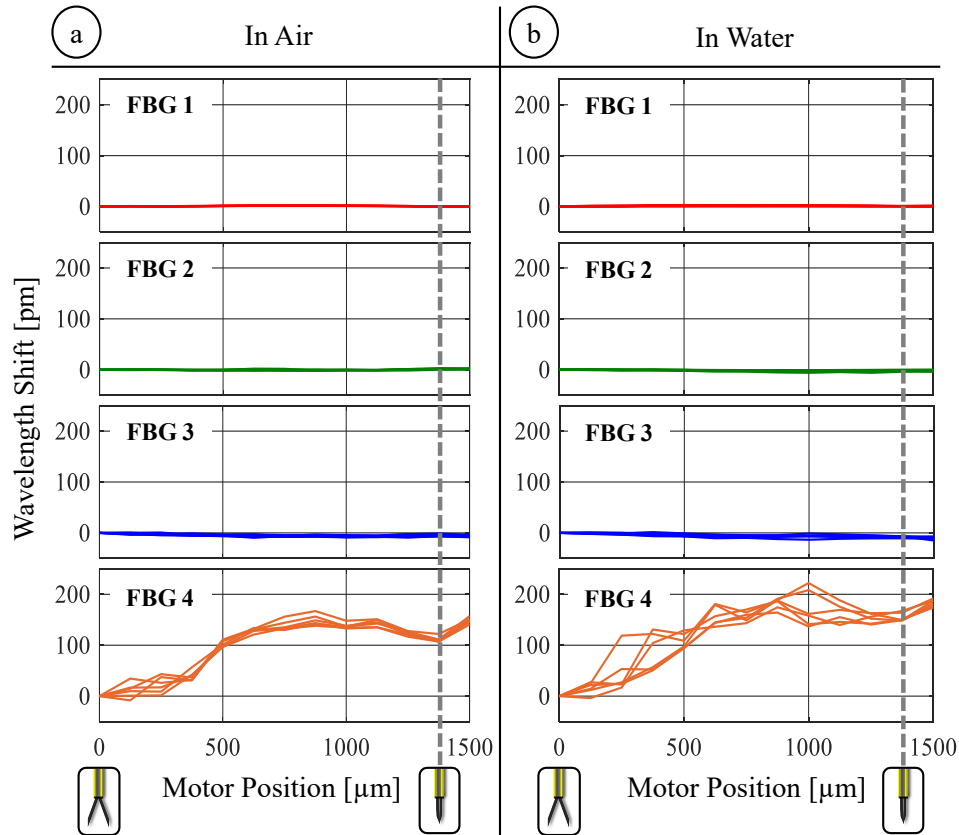


Figure 3.31: The effect of opening/closing the forceps on the lateral (FBG 1,2,3) and axial (FBG 4) sensors while operating (a) in air and (b) in water. The actuation induces high levels of wavelength shift on the axial sensor (up to 167 pm in air and up to 222 pm in water), which exhibit a consistent variation among repeated trials, and hence can be modeled as a function of motor position for each environment [110].

simulations in Fig. 3.28.b. While operating in air, wavelength shifts up to 167 pm are recorded. These recordings show much better consistency among the 6 measurements taken per each motor position in comparison to our earlier prototype without the trocar attachment [112]. When the test is repeated in water, slightly larger shifts up to 222 pm are observed in the axial FBG output, and the consistency of readings at each motor position is relatively deteriorated. The small change can be attributed to the floating impurities inside water which can get stuck between the jaws and guide tube, and lead to larger reaction forces during actuation. Hence, the model relating wavelength shift to motor encoder readings is dependent also on the properties of the surrounding medium

and needs to be experimentally tuned before each operation by opening/closing the forceps several times.

C. Repeatability

This experiment explored the consistency of the FBG sensor readings in response to axial and transverse loads. Forces were applied at the tool tip in 28 different directions by orienting the tool at 4 roll (α) and 7 pitch (β) angles. The roll angle ranged from 0° to 90° with 30° increments while the pitch angle was altered from 0° to 90° in steps of 15° . The magnitude of applied forces varied evenly at 6 levels within 0-23.35 mN. For each direction, the forcing was gradually increased up to 23.35 mN and then decremented back to zero by unloading the washers at the tool tip. The wavelength information from all four FBGs was acquired after the oscillations due to loading/unloading were fully damped out. This cycle was repeated 3 times, generating 6 measurements for each load case. For each measurement, 500 samples were recorded. As an example, Fig. 3.32.a and 3.32.b show the recorded sensor response for purely transverse and axial loading conditions.

The log data involved a total of 168 distinct loading conditions, 1008 measurements and 504,000 samples. To examine the repeatability of each sensor's response, the recorded samples were grouped into 168 subsets so that each subset contained 3000 samples associated with the same loading condition. Within each subset, after identifying the mean Bragg wavelength shift for each FBG sensor, the deviations from the mean value (residuals) were computed. The residuals of all subsets were then combined to obtain the standard deviation for each FBG sensor as a measure of repeatability.

Figs. 3.32.c-e show the probability distribution of the residuals for each FBG sensor. The standard deviations for the lateral FBG sensors (FBG 1, 2 and 3) are 0.47, 0.58 and 0.59

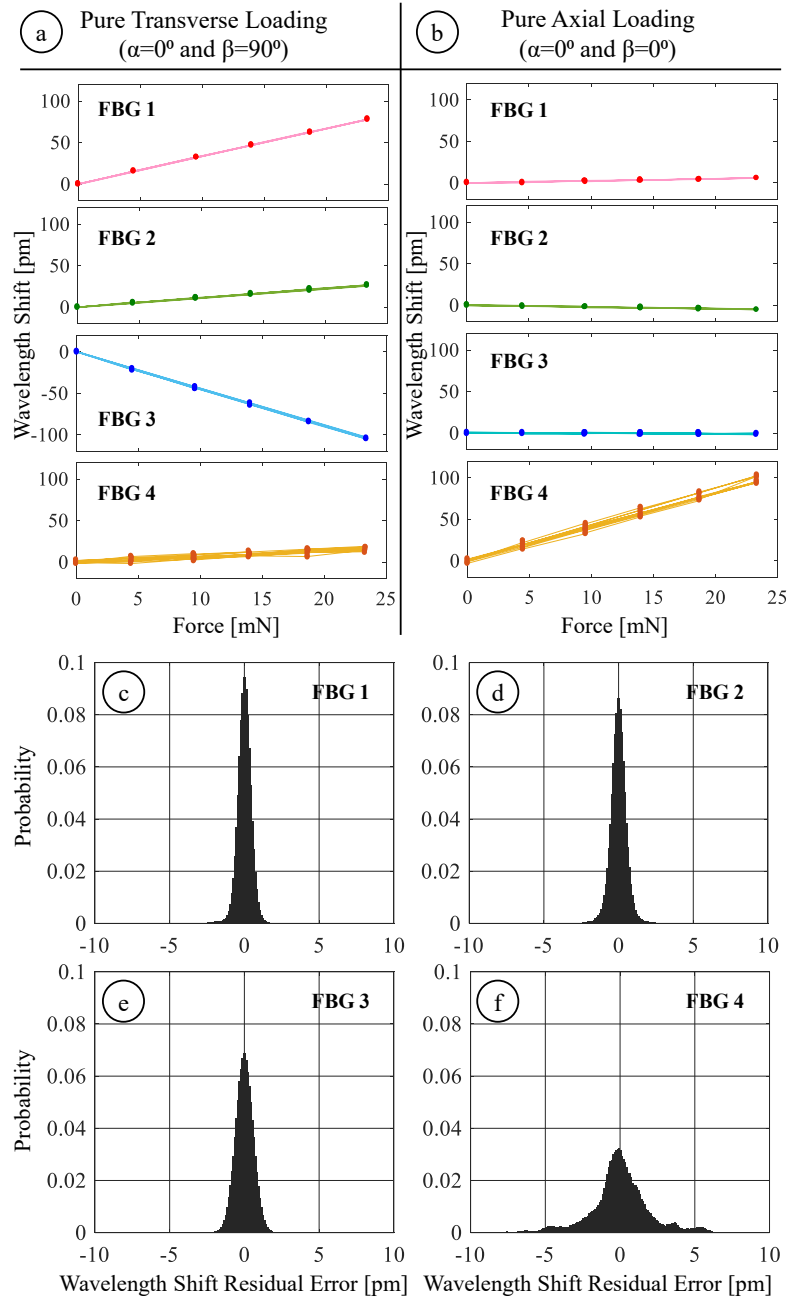


Figure 3.32: Response of (FBG 1,2,3) and axial (FBG 4) sensors during two sample loading conditions: (a) pure transverse loading and (b) pure axial loading. Probability distribution of Bragg wavelength shift errors for lateral (c-e) and axial (f) FBG sensors under 168 different combinations of transverse and axial forces. The standard deviations are less than 0.6 pm for the lateral FBGs and is about 1.96 pm for the axial FBG, indicating a highly repeatable response [110].

pm, respectively. The axial FBG sensor (FBG 4) exhibits slightly a more variable response with a standard deviation of 1.96 pm. Our optical sensing interrogator has a

wavelength repeatability of 1 pm; its wavelength stability is 2 pm typically and 5 pm at maximum. Considering these values, we can conclude that the FBG sensors on our tool provide reliable repeatability that is consistent with the intrinsic properties of our optical sensing interrogator.

D. Calibration Experiments

In order to identify the coefficients used in our force computation algorithm, we performed a set of calibration experiments. The goal in our first calibration experiment was to test the hypothesis of linear correlation between the temperature drift in common mode of lateral FBGs and the axial FBG. We recorded the Bragg wavelength variation in each FBG sensor while the tool was exposed to routine changes in room temperature, which involved gradual changes within $\pm 2.5^\circ\text{C}$. In order to avoid disturbances due to air flow in the room, the setup was maintained inside a plastic box while acquiring data. The test was completed in 4 sessions; each session spanned a 225 minute period during which a measurement was taken in every 15 minutes. In between the sessions, we altered the roll and pitch angles to capture the effect of tool orientation on the thermal drift coefficient, if any.

The results are shown in Fig. 3.33, which display the changes in Bragg wavelength of each sensor due to 2 main sources. The larger jumps while moving to the next set of measurements are due to the modified tool orientation, thus the new loading at the tool tip. The rest of the variations within each session are purely due to thermal effects. We observe from Fig. 9a that the lateral FBGs exhibit almost identical sensitivity to thermal changes, whereas the drift in the axial FBG was slightly smaller (Fig. 3.33.b). For a quantitative comparison of thermal effects, we evaluated the wavelength shift of all four

sensors within each session, and computed the common mode of lateral FBGs. The wavelength shift in the axial FBG and the common mode of the lateral FBG sensors revealed a linear correlation with a covariance of 0.94. The corresponding proportionality constant was found to be $\kappa=0.92$ (Fig. 3.33.c).

Our second calibration experiment was aimed at monitoring the FBG response under various combinations of transverse and axial forces. In order to collect sufficient data

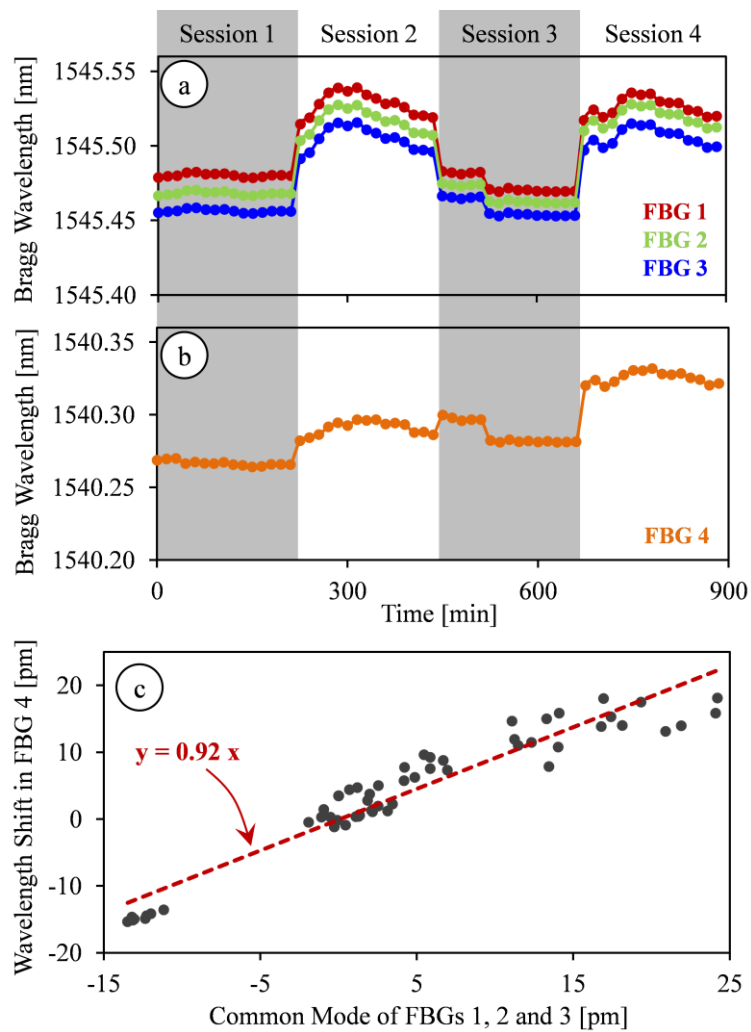


Figure 3.33: Thermal drift in lateral (a) and axial (b) FBG sensor readings during 4 test sessions each spanning a period of 225 minutes. (c) The Bragg wavelength shift in the axial FBG sensor shows a linear correlation with the common mode (average Bragg wavelength shift) of lateral FBG sensors with a proportionality constant of $\kappa=0.92$ [110].

with a fine enough sampling grid, we took the measurements recorded for repeatability tests (504,000 samples of log data with 6 levels of forcing in 28 different directions) and performed 4 additional analyses: global linear calibration, local linear calibration, global nonlinear calibration, and local nonlinear calibration.

Global Linear Calibration

After computing the differential mode of each sensor, the linear system of equations described in Section 3.2.2.3.3 was formed and solved by using the method of least squares. The resulting coefficient matrix for the transverse forces in equation (3.19) was

$$C^{\text{tr}} = \begin{bmatrix} 0.0992 & 0.0400 & -0.1392 \\ -0.1007 & 0.1435 & -0.0428 \end{bmatrix} \text{mN/pm}$$

Considering the wavelength resolution of the optical sensing interrogator (1 pm) and the identified coefficient matrix, the linear method produces a transverse force resolution of about 0.14 mN, which is within the initial design target of 0.25 mN. The linear fitting results are shown in Fig. 3.34.a and 3.34.b for F_x and F_y , respectively. The estimated F_x values closely follow the actual forces with a root mean square (rms) error of 0.25 mN and a mean absolute error of 0.18 mN. A similarly accurate estimation is observed for F_y up to about 10 mN. However, beyond this level, slight deviations from the actual value are observed, leading to an overall rms error of 0.52 mN and a mean absolute error of 0.36 mN. The sliding contact between the jaws and the guide tube provides firm support along the x-axis of the tool, but not along the y-axis as shown in Fig. 3.30.c. Therefore, large F_y forces can deform and dislocate the jaws inside the guide tube, which may change the overall geometry and deteriorate the linearity of the force sensor response. Nevertheless, this is not a major concern in membrane peeling since most of the applied

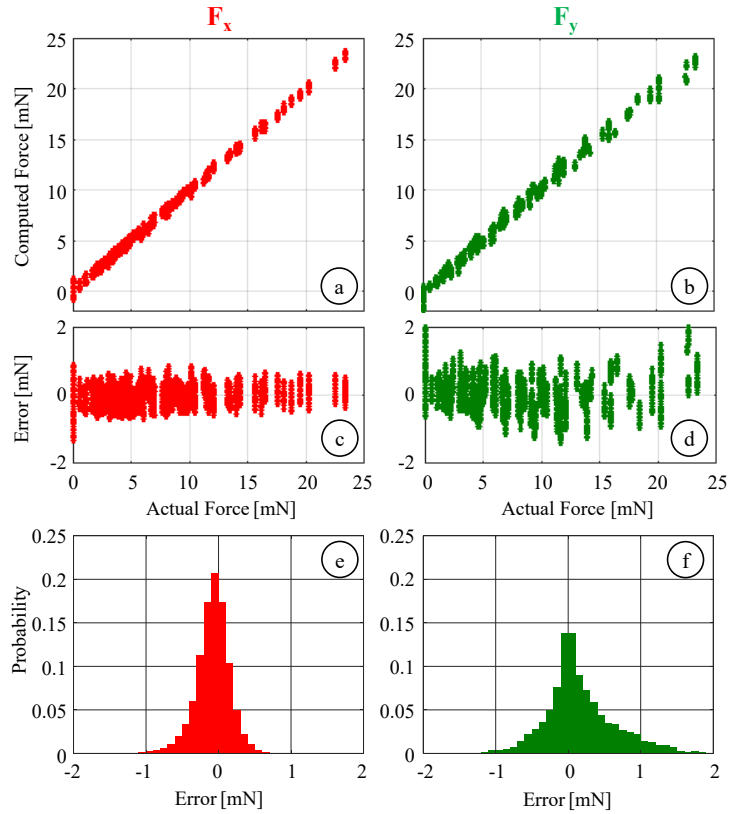


Figure 3.34: Global linear calibration results for transverse forces: (a,b) Calculated F_x and F_y versus the actual values. (c,d) residual errors versus the actual forces, (e,f) probability distribution of residuals (bin size = 0.1 mN). The global linear fitting can predict the applied forces with an rms error of 0.25 mN and 0.52 mN for F_x and F_y , respectively [110].

forces lie along x-axis (peeling direction) due to the alignment of jaws, and excessive side loads (F_y) are highly unexpected. The histograms of the residual errors (Fig. 3.34.e and 3.34.f) show that the probability of errors beyond 1 mN is very low for both F_x and F_y , which have standard deviations of 0.27 mN and 0.49 mN respectively indicating a good repeatability.

Solving the system of equations given by (3.20), we were not able to identify an adequately accurate fitting to estimate the axial load. The resulting coefficient C^{ax} led to very large errors (an rms error of 8.34 mN, a mean absolute error of 6.19 mN, and a standard deviation of 3.87 mN) especially in the presence of significant transverse loads

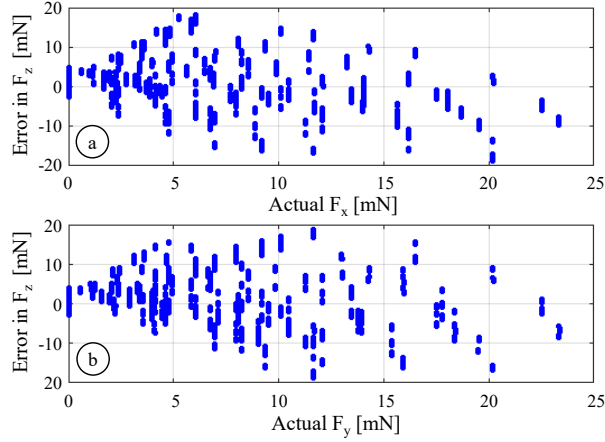


Figure 3.35: Axial force (F_z) computation error versus the concurrent transverse load along (a) x-axis and (b) y-axis based on the global linear calibration. The magnitude of errors rapidly grows when larger transverse forces are applied, deteriorating the linearity of the axial FBG [110].

in addition to axial forces. Fig. 3.35 shows that the magnitude of errors in axial force computation steeply rises with greater magnitude of transverse forces (both F_x and F_y), which suggests that the assumption of modeling the axial FBG response as a linear combination of axial and transverse load effects does not hold globally.

Local Linear Calibration

In membrane peeling, forces applied in the transverse plane are mostly along the peeling direction, which corresponds to the x-axis of our tool. Our previous membrane peeling experiments on various types of artificial phantom also support that transverse loads containing large F_y (associated with $\alpha > 30^\circ$) are not very likely in practical use of the micro-forceps [113]. In an attempt to find a more accurate linear fitting for the axial force, we first analyzed a subset of the calibration data associated with $\alpha \leq 30^\circ$. However, limiting α and hence F_y alone did not lead to any significant improvement in axial force sensing accuracy. The rms error in estimated F_z was still 7.08 mN and the mean absolute error was 5.41 mN. Next, we considered a smaller subset limiting both the pitch ($\beta \leq 15^\circ$)

and roll ($\alpha \leq 30^\circ$) angles so that both of the transverse force components were constrained ($F_x < 6.04$ mN and $F_y < 3.02$ mN), and the applied forces were dominantly axial. For this subset of 72,000 samples, it was possible to obtain

$$C^{\text{ax}} = [1.3216 \quad -0.3652 \quad -0.3717 \quad 0.7369] \text{ mN/pm}$$

which indicates an axial force resolution of about 1.32 mN. Fig. 3.36.a illustrates the resulting fit, and the distribution of residuals is shown in Figs. 3.36.c and 3.36.e. Accordingly, the errors are reduced to an rms value of 3.17 mN and a mean absolute value of 2.38 mN. The standard deviation is 3.09 mN, indicating slightly better repeatability. The improved accuracy with this reduced data set verifies our hypothesis on

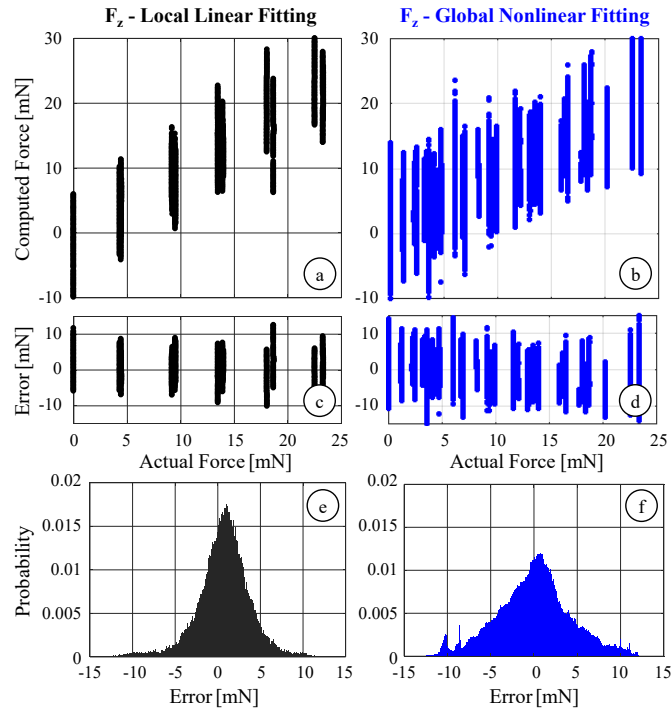


Figure 3.36: Axial force computation results for local linear calibration using samples with limited roll ($\alpha \leq 30^\circ$) and pitch ($\beta \leq 15^\circ$) angles (black), and for global nonlinear calibration (blue): (a,b) The comparison of computed values to the actual force level, (c,d) variation of error with respect to the axial force magnitude, (e,f) probability distribution of residuals (bin size = 0.1 mN). The latter provides almost the same sensing accuracy as the local fitting, but for the entire range of force directions [110].

the loss of linearity in the presence of dominant transverse loads. Yet, this method is not feasible for estimating axial forces, not only because the resulting error is still over our accuracy target (2 mN), but also because in membrane peeling a significant portion of the exerted forces are transverse rather than axial, which remains in contrast to the extremely confined workspace of this method.

Global Nonlinear Calibration

Using the entire log data of 504,000 samples, we fit a nonlinear regression model based on 2nd order Bernstein polynomials to better estimate both the transverse and axial forces. The obtained coefficient vector $C^{\text{Bernstein}}$ derives a resolution of 0.074 mN for F_x and F_y , and 1.85 mN for F_z , respectively. The accuracy in computing the transverse forces are slightly better than the linear method with an rms error of 0.15 mN for F_x and 0.25 mN for F_y . More importantly, the axial force estimation is significantly improved in comparison to the global linear fitting results. The residual error spans approximately ± 4.33 mN while the mean absolute error is 3.34 mN. Although the results displayed in Fig. 3.36 are still unsatisfactory based upon our accuracy criterion (2 mN), they show an important improvement: the nonlinear regression provides a global axial sensing accuracy similar to what could be obtained by the linear fitting only locally.

Local Nonlinear Calibration

Considering that forces associated with large F_y forces are not very probable during an actual membrane peeling operation as discussed previously, we repeated our nonlinear calibration method using a reduced dataset ($\alpha \leq 30^\circ$), without limiting F_x (0-23.35 mN) which is expectedly the dominant force component along the peeling direction but constraining F_y below 11.7 mN. This corresponds to a dataset of 252,000 samples with 84

distinct loading conditions. The regression analysis revealed a coefficient vector ($C^{\text{Bernstein}}$) providing a finer force resolution in comparison to all of the previous fittings: 0.01 mN for F_x and F_y and 0.38 mN for F_z . The resulting force estimates and associated errors are plotted in Fig. 3.37. The rms errors are 0.12, 0.07 and 1.76 mN for F_x , F_y and F_z , respectively, which are all sufficiently smaller than our initial design target (0.25 mN for transverse and 2 mN for axial forces). For the axial load, the magnitude of the residual error remains mostly within the ± 5 mN envelope across the entire force range as shown

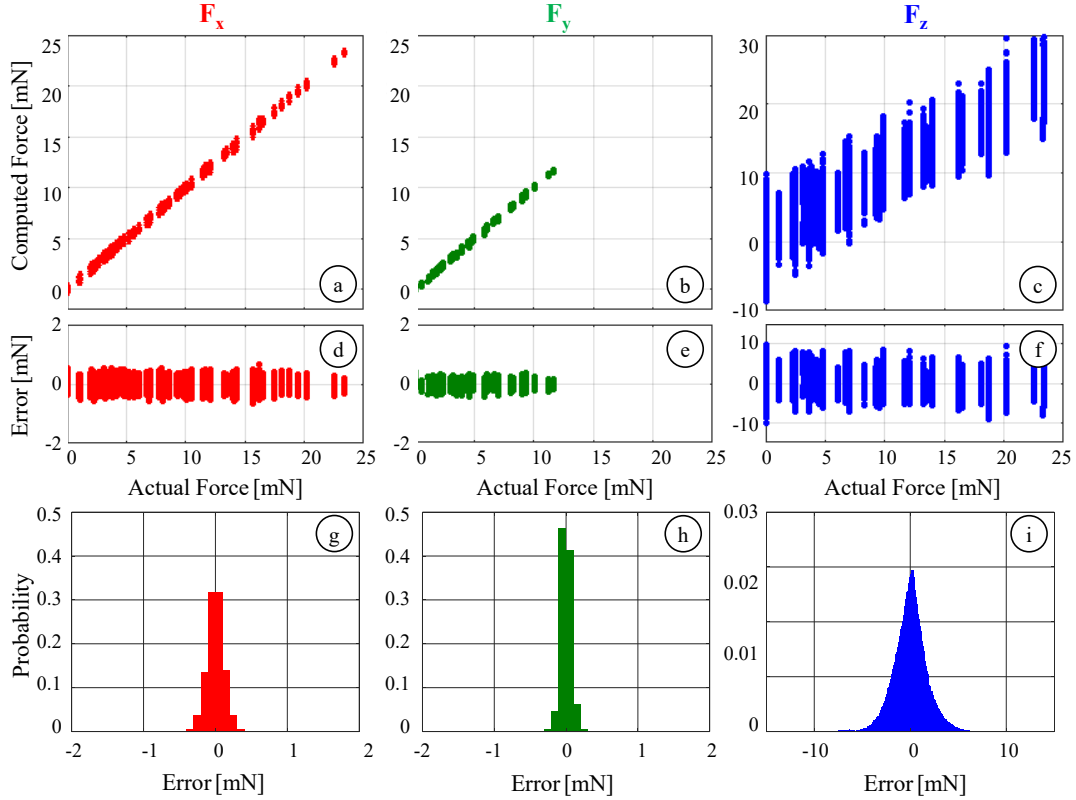


Figure 3.37: Results of local nonlinear calibration using samples with limited roll ($\alpha \leq 30^\circ$) angles for computing F_x (red), F_y (green) and F_z (blue): (a-c) The comparison of computed values to the actual force level, (d-f) variation of residuals with respect to the force magnitude, (g-i) probability distribution of residuals (bin size = 0.1 mN). By limiting the roll angle ($\alpha \leq 30^\circ$), samples with excessive F_y (> 11.7 mN), which are not very likely in an actual membrane peeling operation, were excluded from calibration. The rms errors in estimating F_x , F_y and F_z are 0.12, 0.07 and 1.76 mN respectively [110].

in Fig. 3.37.f. Fig. 3.37.g-i illustrates the probability distributions of the residuals, which show that with the local nonlinear calibration errors mostly stay under 0.5 mN for F_x and F_y , and 5 mN for F_z . The standard deviations of errors are 0.12, 0.07 and 1.76 mN respectively, which show significantly better repeatability of readings in comparison to the aforementioned calibration methods.

E. Validation Experiments

For validating the performance of our nonlinear force computation method, we took measurements at loading conditions that were not used during the calibration, still

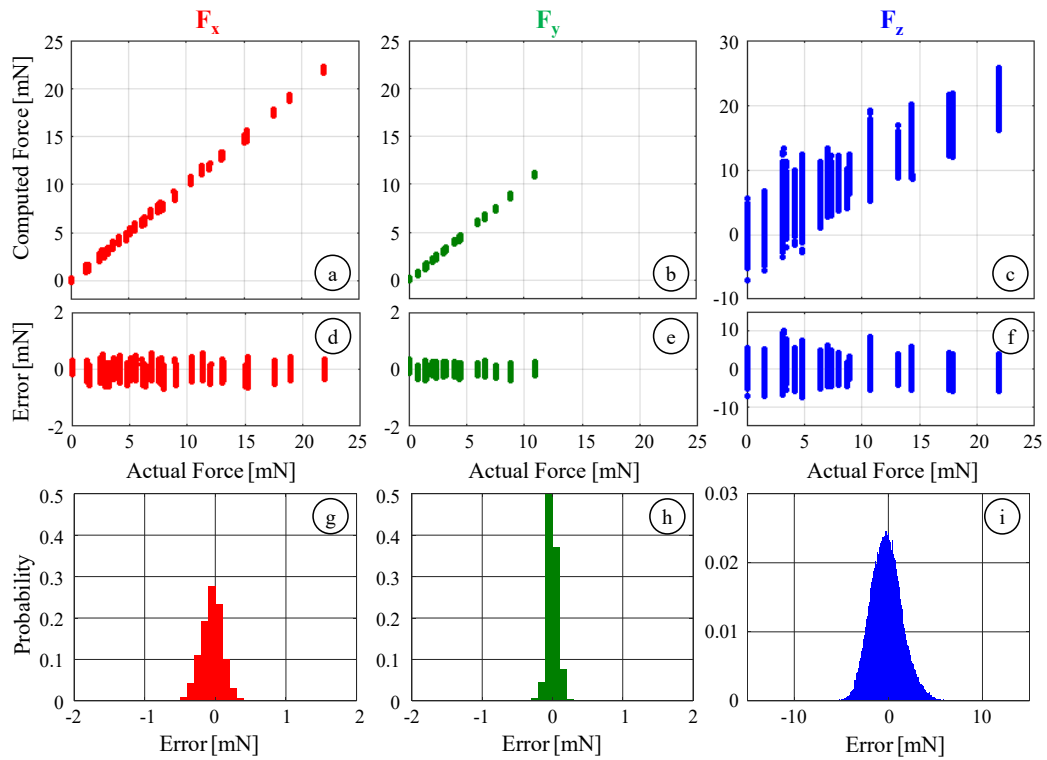


Figure 3.38: Results of the validation experiment for computing F_x (red), F_y (green) and F_z (blue): (a-c) The comparison of computed values to the actual force level, (d-f) variation of residuals with respect to the force magnitude, (g-i) probability distribution of residuals (bin size = 0.1 mN). Tested data consists of loading conditions that were not involved during calibration. The identified local nonlinear regression can still accurately predict the applied forces with rms errors of 0.16, 0.07 and 1.68 mN for F_x , F_y and F_z , respectively [110].

limiting the transverse loads to the range of interest in membrane peeling, i.e. $\alpha \leq 30^\circ$. We investigated if the identified local calibration constants could still accurately predict the applied forces. The validation experiment consisted of forces ranging from 0 mN to 23.35 mN in increments of 4.67 mN while holding the tool at 2 different roll angles ($\alpha=0^\circ, 30^\circ$) and 3 different pitch angles ($\beta=20^\circ, 40^\circ, 70^\circ$). Each case was repeated 6 times and 500 samples were collected per case. The data set was further extended by adding 15 more measurements per each roll angle at randomized pitch angles ($0^\circ-90^\circ$) and forces (0-23.35 mN), producing a total of 66 distinct loading conditions and 123,000 samples.

Using validation dataset, we observed a similar force computation performance to what was obtained with the calibration dataset (Fig. 3.38). Our locally fit nonlinear model is able to accurately predict the applied transverse forces within the considered force range, 0-25 mN for F_x and 0-11.7 mN for F_y . The rms errors are 0.16 mN and 0.07 mN for F_x and F_y , respectively. The axial forces are captured with an rms error of 1.68 mN, which is satisfactorily smaller than our design target of 2 mN. The standard deviation of errors indicates a force sensing repeatability of 0.15 mN, 0.07 mN and 1.67 mN about x, y and z axes, respectively. These results demonstrate that the 3-DOF force-sensing micro-forceps with the nonlinear force computation method can provide measurements within the desired sensitivity and accuracy.

F. Discussion

Our earlier works demonstrated that the temperature compensation method described in Section 3.2.2.3.3 provides robust transverse and axial force measurements against thermal changes for other tools [99,114]. In this work, the first set of our calibration experiments explored the thermal influence on each FBG sensor output in response to

slow and gradual ambient temperature variation, which revealed similar behavior to that observed in our previous 3-DOF force-sensing pick tool [114]. In case of sudden ambient temperature variations though, such as the instant when the tool is inserted into the eye, whether the linear correlation between the axial sensor response and the common mode of lateral sensors is valid remains controversial. In practice, this issue can be alleviated by rebiasing the force sensor to adapt to the new temperature level right after the tool is placed inside the eyeball. After this time, the expected thermal fluctuations inside the eye will be relatively small and gradual so that our thermal drift method cancelling based on common mode of lateral sensors can be used. There are several potential solutions that can improve the robustness of our force-sensing tool to thermal changes: adding a separate reference FBG [115], using two different wavelengths [116], or using different optical modes [117,118]. In the future, further exploration of these methods may lead to faster and more accurate compensation of thermal drift in our 3-DOF force-sensing micro-forceps.

In order to compute forces from the optical sensor information, we explored the use of a nonlinear fitting based on second order Bernstein polynomials. Increasing the polynomial order may potentially improve the sensing accuracy, especially in the axial direction. However, identifying a higher order polynomial without overfitting requires calibration experiments that capture the FBG sensor outputs for a finer grid of forces. Such extensive dataset is quite challenging to acquire with the presented setup. Furthermore, the manual operation of rotary stages and loading/unloading of washers to modulate the loading induced at the tool tip is prone to human error. However, using a robotic calibration approach similar to [114], it is possible to collect more samples reliably in a shorter time

and identify a more accurate higher order nonlinear force computation model.

In our calibration and validation experiments, the applied forces in the axial direction were always tensile. Therefore, the identified models do not describe the behavior for compressive loads. In addition, the final accuracy and resolution values were obtained for a limited force range of 0-25 mN with minor force component perpendicular to the peeling direction ($F_y < 11.7$ mN). Although, these may be interpreted as limitations of our approach, they are highly relevant to the actual clinical scenario. In epiretinal membrane peeling, to avoid retinal injuries, the magnitude of forces need to be maintained typically below 10 mN [62]. Also, the membrane is pulled away from the retina surface, which causes axial loads on the micro-forceps tip to be tensile if any. The exerted forces in the transverse plane follow the direction of tool motion, which means they are usually along the opening/closing direction of the jaws (x-axis of our tool). These practical facts support the constraints of our force computation model for epiretinal membrane peeling. Nevertheless, using the same experimental method, the instrument can be calibrated to the desired force domain for a different application as well.

Based on the practically relevant force ranges, using our nonlinear method showed that the rms error in axial force sensing could be lowered under 2 mN. This is a significant improvement on our previously reported results [108], and is presumably useful for limiting intra-operative forces and preventing retinal injuries in epiretinal membrane peeling. A future direction in this work is to evaluate the force-sensing performance during actual peeling tasks using *ex vivo* bovine eyes and *in vivo* animal models. In addition, for quantitative assessment of differing surgical techniques, objective evaluation of the surgical performance and accurate modeling of retinal tissues, our future work

aims to further improve the axial sensing accuracy. Some potential methods include using higher order nonlinear models for force computation, and exploring customized sensor architectures that provide better decoupling between axial and transverse forces [119].

3.3 Force-Sensing Microneedle for Retinal Vein Cannulation

3.3.1. Actuation Mechanism

Injecting t-PA into thin branch retinal veins ($\text{Ø} < 200 \text{ }\mu\text{m}$) requires the use of even thinner and sharp tipped cannulae. Targeting $\text{Ø} 100\text{-}500 \text{ }\mu\text{m}$ veins (most vessels in the retina are at most $125 \text{ }\mu\text{m}$ in diameter), we devised a motorized force-sensing microneedle with an outer diameter of $70 \text{ }\mu\text{m}$ at the tip (Fig. 3.39). This is a compact lightweight modular unit carrying all the necessary sensors (FBGs and an encoder) and a linear motor that can be independently actuated, which enables an easy integration with various types of tool

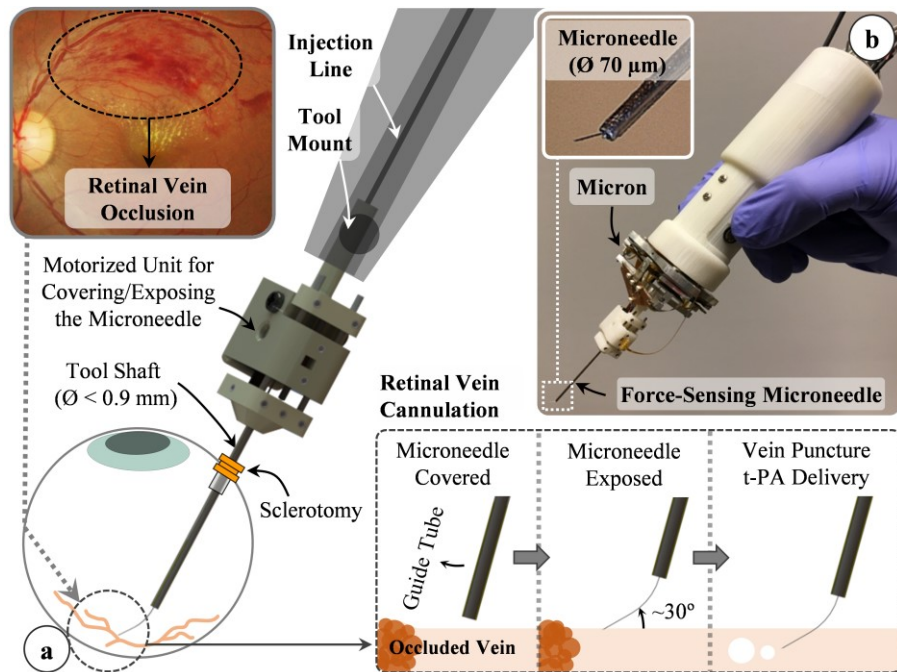


Figure 3.39: Conceptual design of our motorized force-sensing microneedle for retinal vein cannulation. The needle has a modular design that allows an easy integration with robotic devices, such as the handheld micromanipulator: Micron.

handles, either manual or robotic, without interfering with their operation.

The tool has a sharp beveled (15°) and bent (45° relative to the tool shaft) tip. If a straight and blunt tipped microneedle were used, the vein walls would be pushed towards each other severely making the already thin lumen even smaller. In addition, after piercing the vein wall, the instantaneous release of stress would cause the tissue to recoil towards the needle, which would make overshooting the target vein almost inevitable. To avoid overshoot, it is important to approach the retina at an angle, and move the needle tip almost parallel to and with minimal vertical motion into the vein. This way, the tissue will deform less and along the vein axis, so that any relative motion due to tissue relaxation after venous puncture will not force the needle tip out of the vein lumen. Based upon these factors, the optimal approach angle while cannulating the vasculature on CAM was previously explored, which revealed a range of 25° - 35° between the needle tip and vein surface [47]. Due to constraints at the sclerotomy, it is not easy to approach the retinal

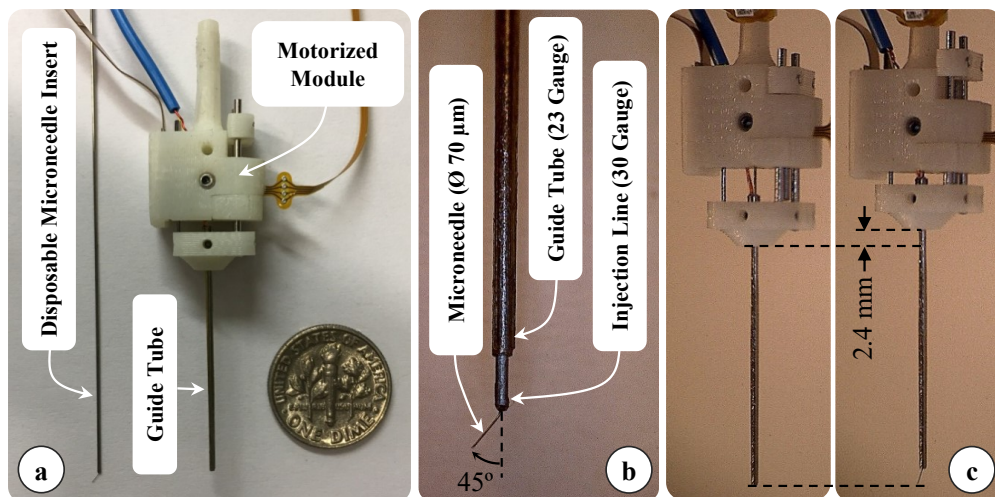


Figure 3.40: (a) Components of the design: force sensitive motorized unit, and the disposable prebent needle (b) Assembled prototype (c) Tool actuation: the microneedle is exposed by retracting the guide tube as much as 2.4 mm.

surface at this angle with a straight tool. Using a flexible prebent tip can help, however the angle between the tool axis and tool axis is an important design factor: bending the microneedle too much in order to achieve a very shallow approach angle may not only cause severe deformation of the needle while pushing it against the vein, but will also lead to excessive resistance to fluid flow inside the lumen at the bend, and may require too much pressure to inject t-PA through. Considering these limitations, the approximate pars plana position for tool insertion (3.5 mm posterior to the limbus to avoid lens or retinal injury [120]), the dimensions of the typical adult eye (the average vertical and horizontal diameters are 23 and 23.5 mm, respectively [121].), and targeting an ideal approach angle of about 30° [47], we bent the needle tip 45° relative to the tool shaft as shown in Fig. 3.40.b. The bent needle tip was bonded to a 30 Gauge stainless steel tube using medical device adhesive (Loctite 4013 Prism, Henkel, CT) to form the injection line of our tool.

Due to the bent structure of the thin needle, it is not easy to introduce the tool into the eye through a small incision ($\text{Ø} < 1 \text{ mm}$) without damaging the tip. In order to keep the sharp and prebent microneedle protected and flexed straight while passing it through the sclera, we devised a motorized module with a retractable guide tube functioning as a protective sheath. As depicted in Fig. 3.40.a and 3.40.b, the injection line (30 Gauge tube with the bent microneedle attached at its tip) is passed through a 23 Gauge guide tube and firmly anchored to the body of the module with the help of a set screw. This component is designed to be disposable since the needle tip may gradually lose its sharpness and impede venous puncture in case of consecutive cannulation attempts. By releasing the set screw, the old injection line with the dull tip can easily be replaced with a new one while preserving the rest of the module. The guide tube is fixed onto a slider mechanism driven

by a linear micro motor (Squiggle-RV-1.8, New Scale Technologies Inc., Victor, NY), so that when the motor is actuated, the guide tube moves along the tool shaft to cover or expose the needle tip. While inserting the tool into the eye and approaching the retina surface, the needle tip is flexed and held straight inside the guide tube. Upon reaching the target vessel site, retracting the guide tube deploys the bent needle tip out (Fig. 3.40.c). Fully covering or exposing the microneedle requires a travel of 2.4 mm. The selected motor supplies enough force and travel range for this task in a very small (2.8x2.8x6 mm), and light weight (0.16 grams) package. There is a bar magnet located on the side of the slider (Fig. 3.42.a). The position of the slider, and thus of the micro motor, is tracked via the magnetic position sensor (NSE-5310, ams AG, Austria) located on the side of the base. This enables closed loop position control of the motor and ensures accurate motion of the guide tube despite the potentially variable friction at the insertion port through the sclera. The parts holding the guide tube, housing the motor, anchoring the injection line to the module and the lid shielding the slider mechanism were built using 3D printed Acrylonitrile Butadiene Styrene (ABS) with a resolution of 0.254 mm. The assembled actuation unit occupies a space of 13.0 x 15.5 x 9.3 mm and weighs only about 2.9 grams. The modular design enables easy integration with robotic systems. An example application is shown in Fig. 3.41, where we attached the motorized module to Micron's tool mount. The fluid line (30 Gauge tube protruding from the back of the tool in Fig.3.41.a) was passed through the hollow center of Micron handle, and connected to a syringe with a 30 Gauge needle via a sealed polyethylene tubing (PE-10, Warner Instruments, Hamden, CT) to deliver the injection fluid. The infusion rate and amount can be controlling the syringe with a standard infusion pump (11 Pico Plus Elite, Harvard

Apparatus, Holliston, MA). The controller board of the linear actuator was located inside the tool handle. A force-sensing resistor (FSR 400, Interlink Electronics, Westlake Village, CA) was attached on the tool handle under the operator's thumb (Fig. 3.41.b), and interfaced with the micro motor controller such that the target position of the motor varies linearly with the exerted force on the resistor. Simply by releasing or squeezing the hand piece, the operator can cover or expose the microneedle, respectively.

3.3.2. Force Sensor Integration

Detection of the very fine tool-tissue interaction forces while cannulating retinal veins requires the use of a very sensitive force sensor with sub-mN resolution. In addition, the location of the force sensor is critical. Since the forces at the sclera insertion port can be

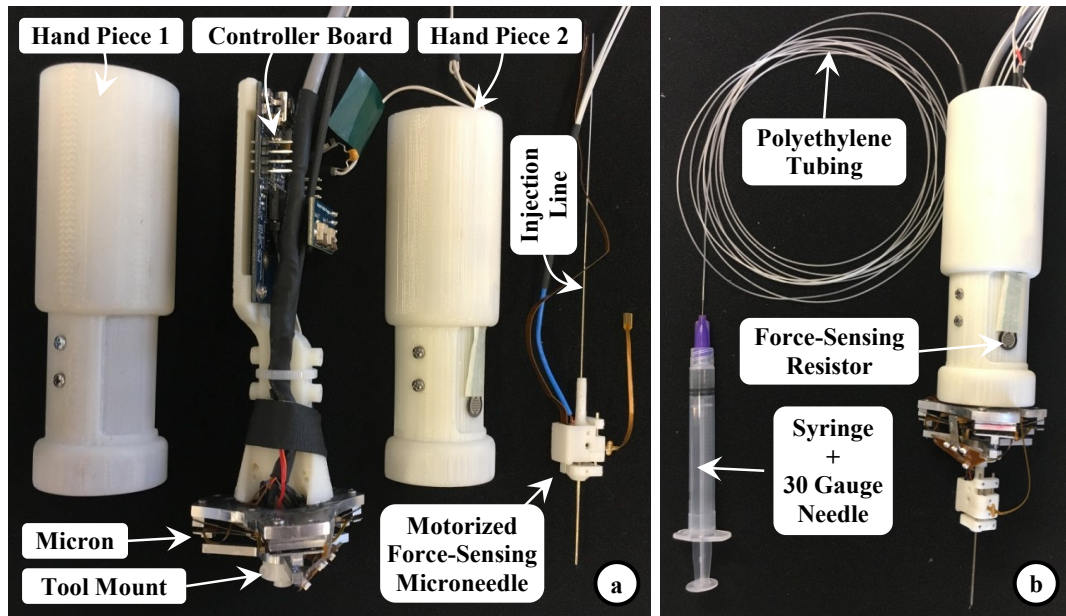


Figure 3.41: Sample integration of the motorized force-sensing microneedle with a handheld micromanipulator, Micron. (a) The controller board for the tool's motor was located on Micron's handle inside the two hand pieces. (b) A force-sensing resistor was mounted on one of the hand pieces, under the operator's thumb, to control the microneedle's actuation by squeezing or releasing the hand piece. The injection line passes through the center of the instrument and is connected to a syringe via polyethylene tubing to deliver fluid to the microneedle.

much larger than the typical cannulation forces at the tool tip, a handle mounted force sensor measuring a combination of these two forces would not be appropriate. In order to capture only the tool tip forces, the sensor needs to be located proximal to the tool apex and inside of the eye. Bringing the sensor into the eye puts strict requirements and limits the available sensors for this use. FBG strain sensors (Technica S.A., Beijing, China) with their small dimension ($\text{Ø}=80\ \mu\text{m}$), high sensitivity, biocompatibility, sterilizability, and immunity from electrostatic and electromagnetic noise satisfy these criteria.

While inserting the needle into the vein, forces induced at the needle tip will be mostly along the axis of the needle, and hence will be dominantly perpendicular to the tool shaft due to the bent tip. Previously, our team has developed several ophthalmic tools capable of sensing the transverse forces at the tool tip with a 0.25 mN resolution during other retinal procedures [99,101,102,122]. Following a similar architecture, we bonded 3 FBG sensors evenly around the guide tube using medical device adhesive (Loctite 4013 Prism, Henkel, CT) as shown in Fig. 3.42.b. This led to an overall tool shaft diameter less than 0.9 mm,

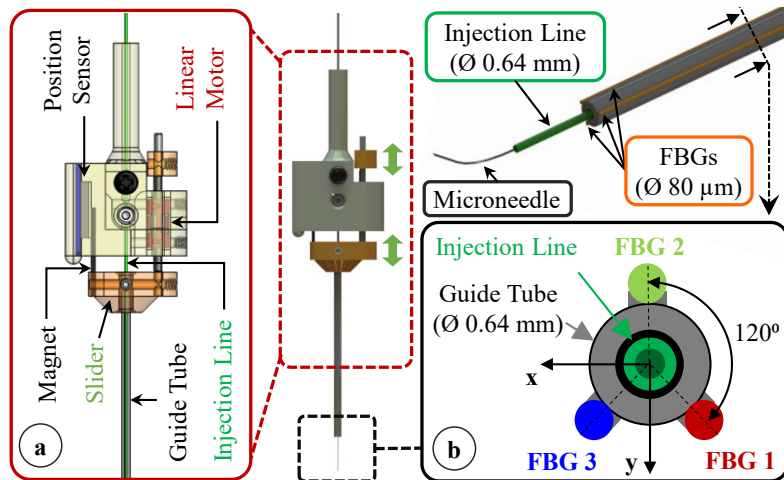


Figure 3.42: Motorized actuation of the tool for retracting the guide tube back and exposing the prebent microneedle. The inner tube of the tool shaft delivers the injection fluid, while 3 FBG sensors on the outer tube sense transverse forces on the microneedle.

which is sufficiently small for insertion through the sclera.

In order to transform the optical wavelength information from each embedded sensor to force domain, the linear model presented in Section 3.2.1.1 was used. In order to find the constant matrix K in eqn. (3.5), we performed a calibration experiment using the setup shown in Fig. 3.43.a. We mounted our force-sensing tool horizontally on a rotary stage to modulate its axial orientation (θ). A soft plastic piece carrying a wire hook was attached to the microneedle tip (Fig. 3.43.b). By hanging aluminum washers on the wire hook, varying forces (pure F_x at $\theta=0^\circ$ and pure F_y at $\theta=90^\circ$) were induced at the tool tip. The washers were weighed using a precision scale (Sartorius GC2502, Germany) which provides a resolution of 0.01 mN and a repeatability of ± 0.02 mN. The maximum test load was 20.6 mN, and each washer weighed about 1.03 mN. The Bragg wavelength of each FBG sensor was acquired using an optical sensing interrogator (sm130-700 from Micron Optics Inc., Atlanta, GA). Measurements were taken for 20 different levels of loading at each orientation. For each test condition, 1000 samples were recorded at a rate of 200 Hz.

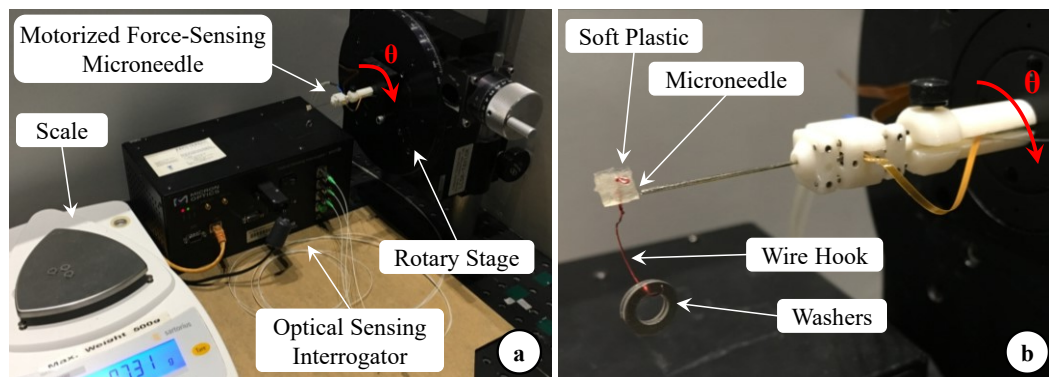


Figure 3.43: (a) Setup for calibration experiments: The force-sensing micro-needle was held horizontal and mounted on a rotary stage to modulate its axial orientation (θ). (b) The microneedle tip was inserted into a soft plastic piece carrying a wire hook. Forces were applied at the needle tip by hanging washers of known weight on the hook.

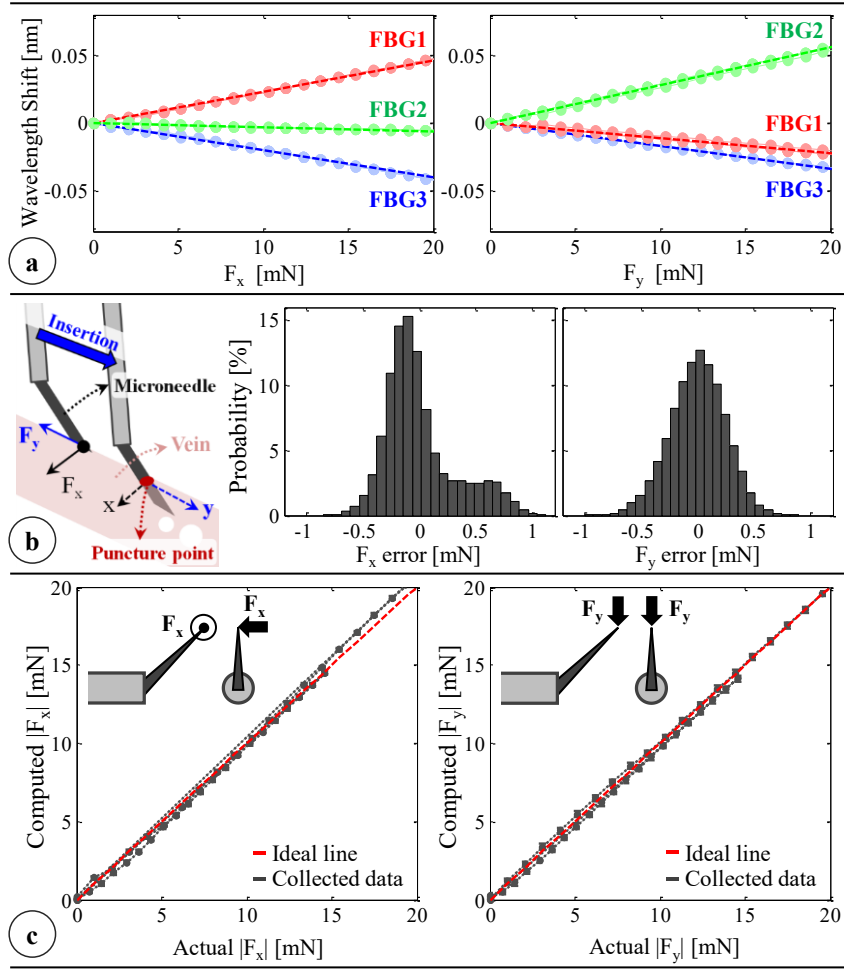


Figure 3.44: (a) Calibration results: linear response for all FBGs when the needle is loaded along x and y axes. (b) The force-sensing coordinates relative to the target vein and the histogram of residual errors in each direction. (c) Computed forces vs. the actual forces along the x and y axes.

The calibration results in Fig. 3.44.a show that all FBGs exhibit a linear reproducible behavior to forcing along both the x- and y-axis. The slope for each FBG indicates the following calibration matrix (K):

$$K = \begin{bmatrix} -0.2128 & 0.2455 & -0.0327 \\ -0.1418 & -0.0927 & 0.2346 \end{bmatrix} \text{mN/pm}$$

The wavelength resolution of our optical sensing interrogator is 1 pm. Based upon the obtained calibration matrix, this corresponds to a resolution of about 0.25 mN for both F_x

and F_y . The optical sensing interrogator has a scan rate of 1 kHz, and the time constant of the sensor is about 5 ms [104], providing a fast-enough response for accurate tracking of quick force variations in RVC. To validate sensor operation, the tool tip was loaded/unloaded repeatedly at 3 different orientations (0° , 45° and 90°). 20 different load conditions (0-20.6 mN) were tested at each orientation, and each case was repeated 6 times (3 load/unload cycles). For each test, 1000 samples were recorded at a rate of 200 Hz. When the computed forces were compared with the actual force values, the root mean square error was 0.31 mN and 0.24 mN respectively for F_x and F_y . The histograms of the residual errors (Fig. 3.44.b) show that the probability of errors beyond 0.5 mN is very low. For 0-10 mN range, computed forces match the actual values for both F_x and F_y , producing a close fit to the ideal straight line (slope=1) passing through the origin in Fig. 3.44.c. Above 10 mN, although F_y accuracy is preserved, F_x is observed to gradually deviate from the ideal line as the loading is increased. This effect can be attributed to the torque generated due to the distance between the tip of bent needle and the tool shaft center. Such error can in theory be corrected by modeling the error. However during RVC, since the needle insertion will take place mostly along the needle axis (y-axis of the tool), forces exceeding 10 mN along the x-axis are highly unexpected. Thus, the slightly bigger errors in predicting F_x at larger amplitudes is not a major concern.

3.3.3. Effect of Actuation on Force Sensor Response

In this design concept, the force sensitive elements are integrated on a functional component that moves and goes under stress during the actuation of the tool. As shown in Fig. 3.44, this causes a shift in FBG sensor readings, which produces an erroneous reading of about 2 mN in F_x and 6 mN in F_y when the guide tube is fully retracted back (motor

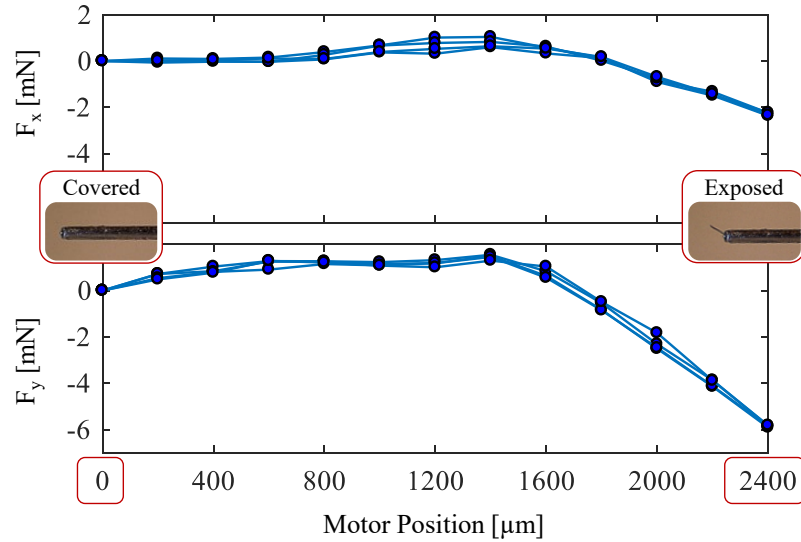


Figure 3.45: Effect of actuation on the sensed forces during 3 cycles of cover/expose cycles. Although the microneedle is not contacting any tissue, covering and exposing the microneedle shifts the force readings by about 2 mN in F_x and 6 mN in F_y with a consistent behavior. In practice, these undesired components due to actuation can be eliminated from the force readings by automatically rebiasing the FBG readouts once the motor position reaches the fully exposed position (2400 μm).

position=2.4 mm) although the needle tip is not interacting with the tissue yet. In addition, the computed calibration matrix is valid for the fully exposed configuration of the needle. The sensitivity may differ for middle positions and fully covered states, which are not relevant to the practical use of the needle. In our force computation algorithm, to get an accurate measurement of forces during cannulation, after the motor position reaches 2.4 mm and the needle is fully exposed, each FBG sensor is automatically rebiased to eliminate the actuation artifact and set a zero-force reference for the subsequent measurements. After touching the retinal surface, the interaction forces are computed relative to this baseline using the calibration matrix obtained in the previous section.

3.4 Integration with Robotic Systems

Combining force-sensing instruments with robotic assistants is a progress towards overcoming important challenges encountered during vitreoretinal surgery. Preventing

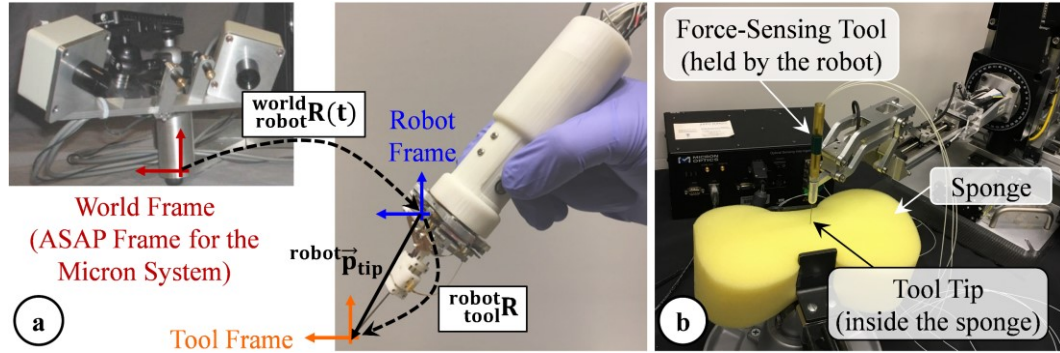


Figure 3.46: (a) Coordinate systems associated with the robotic systems and force-sensing tools. (b) Setup for finding the transformation from the robot's tool mount frame to the force-sensing tool's coordinate system for their integrated use.

involuntary movements of the operator and providing valuable information regarding tool-to-tissue interactions in real time will greatly enhance surgeon capabilities. Among the available robotic manipulators, the handheld Micron [72] runs based on the detected tool tip position in its optical tracker (ASAP) frame, which requires an accurate knowledge of the end-effector tip position relative to the robot frame located at the robot's tool mount (${}^{\text{robot}}\vec{p}_{\text{tip}}$). Similarly, while operating the Steady-Hand Eye Robot [89-94], we use the measured tool tip position and speed, for which the instrument tip position needs to be defined in the robot frame. Meanwhile the force-sensing instrument (either micro-forceps or microneedle) reports forces at the tool tip in its own coordinate system defined by the calibration of the tool (${}^{\text{tool}}\vec{F}_{\text{tip}}$). To manipulate these tools using robotic devices based upon the detected forces, the sensed tool tip position and forces need to be transformed into the same frame, such as the world frame or a phantom coordinate system. The coordinate frames and transformations associated with the operation of Micron and the Steady-Hand Eye Robot are shown in Fig. 3.46.a.

After attaching the force-sensing tool onto the robotic platform, a pivot calibration is performed, by taking multiple measurements in different poses of the force-sensing tool

while the tool tip is maintained on the same spot. The measurements are used to solve for ${}^{\text{robot}}\vec{p}_{\text{tip}}$ in a least-squares sense. This step is a one-time procedure that needs to be performed for each tool presented in Sections 3.2 and 3.3 separately. Using the computed ${}^{\text{robot}}\vec{p}_{\text{tip}}$, the tool tip position can be transformed, for instance to ASAP coordinates while using Micron as follows:

$${}^{\text{ASAP}}\vec{p}_{\text{tip}} = {}^{\text{ASAP}}R_{\text{robot}} {}^{\text{robot}}\vec{p}_{\text{tip}} + {}^{\text{ASAP}}\vec{p} \quad (3.25)$$

The force-sensing tools presented in Sections 3.2 and 3.3 output forces in their own coordinate frame, as defined during their calibration. To register the force-sensing tool to the robotic manipulator, the tip of the tool (the microneedle or the forceps jaws) is pushed into a soft sponge affixed to the table as shown in Fig. 3.46.b. Then the robotic system (the Steady-Hand Eye Robot as in Fig. 3.46.b, or the Micron system with the hand piece clamped in a vise) is commanded to move the tool tip first along its x-axis and then along its y-axis. Since the tool tip is embedded inside the elastic sponge, moving the tool will induce reaction forces on the tool shaft. The resulting forces can be used to construct the rotation matrix from the world frame (either ASAP tracker coordinates in case of Micron or world coordinates in case of the Steady-Hand Eye Robot) to the force-sensing tool coordinates (${}^{\text{world}}R_{\text{tool}}$). For this, each force vector is first negated (since the reaction forces point opposite to the direction of motion), then normalized to obtain the x and y unit vectors of the robot frame in the force sensor coordinates, which form the first two columns of ${}^{\text{world}}R_{\text{tool}}$. The third column of ${}^{\text{world}}R_{\text{tool}}$ is found via the cross product of the first two vectors. Once ${}^{\text{world}}R_{\text{tool}}$ is computed, the measured pose of the robot (${}^{\text{world}}R_{\text{robot}}$) is used to compute the rotation from the robot frame at the tool mount to the force sensor frame

$({}^{\text{robot}}_{\text{tool}}\mathbf{R})$, which completes the registration of the force-sensing tool to the robotic manipulator. While using the tool, the measured tool tip forces are transformed into world coordinates by multiplying the time-variant robot pose $({}^{\text{world}}_{\text{robot}}\mathbf{R}(t))$ – measured by the ASAP tracker while using Micron, or given by the forward kinematics of the Steady-Hand Eye Robot – with the fixed rotation from the robot frame to the force sensor frame $({}^{\text{robot}}_{\text{tool}}\mathbf{R})$ and the force sensor output $({}^{\text{tool}}\vec{\mathbf{F}})$ as follows:

$${}^{\text{world}}\vec{\mathbf{F}} = {}^{\text{world}}_{\text{robot}}\mathbf{R}(t) {}^{\text{robot}}_{\text{tool}}\mathbf{R} {}^{\text{tool}}\vec{\mathbf{F}} \quad (3.26)$$

The computed tool tip position and force information, both of which are now expressed in the same (world) frame, can be used in various ways to accomplish different goals during membrane peeling and vein cannulation procedures, as will be discussed in chapters 4 and 5.

3.5 Conclusion

In this chapter, two main categories of ophthalmic tools were presented: micro-forceps and microneedle. A key feature of these tools is the integrated force sensing at the tool tip, either in 2 dimensions (transverse forces) or in 3 dimensions (transverse and axial forces). The design challenge is to strategically embed sensors such that the tool shaft fits through a sub-millimetric incision on the sclera. This goal was accomplished by the use of thin ($\text{\O} 80 \mu\text{m}$) Fiber-grating fibers, which led to a maximum tool diameter of 20 Gauge ($\text{\O} 0.9 \text{ mm}$) and very fine force sensing capabilities (0-25 mN range within an accuracy of 0.25 mN for transverse and 2 mN for axial forces). The advantage of the presented tool architectures is that the tool-tissue interaction forces can be directly measured in real time without the adverse effect of sclerotomy contact. Methods have

been implemented to eliminate the drift from sensor readings due to ambient temperature variation and tool actuation.

In designing micro-forceps both manual and motorized tool actuation were explored. The manually actuated tools rely on a mechanical coupling between the tool handle and tool tip. They can work either handheld or in combination with the cooperatively controlled Steady-Hand Eye Robot. The motorized concept mechanically separates the tool actuation from the hand piece. The devised modular tool can be actuated independent from its site of attachment, and hence can be integrated with the handheld Micron system, or similarly other handheld or teleoperated robotic platforms, without interfering with their operation.

Our 3-DOF tools are able to capture axial forces in addition to transverse forces. Relative to transverse forces, the axial sensing is challenged by the much higher axial stiffness of the tool and thus lower sensitivity and limited wavelength resolution of the optical sensing interrogator (1 pm). In order to avoid the detrimental effect of frictional forces during tool actuation on the axial force readings, three alternative concepts were explored. The first concept proposes a customized compliant mechanism for the jaws, which was shown through simulations to provide a successful decoupling between axial and transverse forces; nevertheless, this design was not fabricated due to its manufacturing and assembly challenges. The second concept uses asymmetric jaws, which measures forces properly when held at a certain orientation relative to the peeling trajectory. The third concept attenuates the frictional actuation forces by modifying the sliding interface between jaws and the tool shaft. Validation experiments including random samples shows that this tool with the nonlinear force computation method can

predict 3-D forces with an rms error under 0.15 mN in the transverse plane and within 2 mN accuracy in the axial direction.

The force-sensing microneedle presented in this chapter enables approaching vasculature at an optimal angle with its bent tip. Using the motorized mechanism, it is possible to hold the microneedle initially straight and protected inside a guide tube while introducing the tool into the eye through the sclera. After reaching the retina surface the needle is deployed out to flex to its normally bent state. The optical fibers embedded on the guide tube track forces along the needle axis almost in real time within an accuracy of 0.25 mN.

As proof of concept instruments, the presented work in this chapter bears the drawbacks of manual assembly. Based upon the developed calibration and force computation methods the tool structure and fabrication process can further be optimized to improve the force sensing accuracy. In addition, further downsizing of tool shaft diameter to 23 Gauge with improved fabrication and assembly will deliver greater

clinical impact. Currently, the sensors and actuators in our designs add to the cost of the instrument. For this reason, the force-sensitive parts were designed to be sterilizable while the motorized actuation unit can be protected inside a drape. In the future, with mass production, the cost of these force-sensing instruments could be dramatically reduced so that they could become disposable.

The calibration procedure followed for transforming optimal readings into force information is currently based upon static measurements, where samples are acquired after the response of each sensor reaches steady-state. Investigating the dynamic response of our 2-DOF tools revealed a first order system response with a time constant of 5 ms. A similar strategy needs to be followed for the 3-DOF tools as well to evaluate their

performance in estimating rapidly changing force profiles in future experiments. Future work includes more validation experiments, both benchtop and in vivo, and exploring the potential of these conceptual tools in other microsurgeries such as vascular and cochlear implant surgeries, as well as in catheterization procedures.

Publications

1. **B. Gonenc**, P. Gehlbach, R.H. Taylor, and I. Iordachita, "3-DOF Force-Sensing Motorized Micro-Forceps for Robot-Assisted Vitreoretinal Surgery," *IEEE Sensors Journal*, vol. 17, no. 11, pp. 3526-3541, June 1, 2017.
2. **B. Gonenc** and I. Iordachita, "FBG-Based Transverse and Axial Force-Sensing Micro-Forceps for Retinal Microsurgery," *IEEE SENSORS 2016*, 2016, pp. 667-669.
3. A. Gao, **B. Gonenc**, J. Guo, H. Liu, and I. Iordachita, "3-DOF Force-Sensing Micro-Forceps for Robot-Assisted Membrane Peeling: Intrinsic Actuation Force Modeling," *IEEE RAS EMBS Int. Conf. Biomed. Robot. Biomechatron. (BioRob'16)*, 2016, pp. 489-494.
4. **B. Gonenc**, P. Gehlbach, J. Handa, R.H. Taylor, and I. Iordachita, "Force-Sensing Microneedle for Assisted Retinal Vein Cannulation," *IEEE SENSORS 2014*, 2014, pp. 698-701 - **Best Student Paper Award**.
5. **B. Gonenc**, E. Feldman, P. Gehlbach, J. Handa, R.H. Taylor, and I. Iordachita, "Towards Robot Assisted Vitreoretinal Surgery: Force-Sensing Micro-Forceps Integrated with a Handheld Micromanipulator," *IEEE Int. Conf. on Robotics and Automation (ICRA'14)*, 2014, pp. 1399-1404.
6. **B. Gonenc** and I. Iordachita, "3-DOF Force-Sensing Micro-Forceps for Vitreoretinal Surgery," *Int. Conf. of Mechanical Engineering (ICOME'13)*, Craiova, Romania, 2013.
7. **B. Gonenc**, J. Handa, P. Gehlbach, R.H. Taylor, and I. Iordachita, "Design of 3-DOF Force Sensing Micro-Forceps for Robot-Assisted Vitreoretinal Surgery," *Int. Conf. of the IEEE EMBS (EMBC'13)*, 2013, pp. 5686-5689.
8. I. Kuru, **B. Gonenc**, M. Balicki, J. Handa, P. Gehlbach, R.H. Taylor, and I. Iordachita, "Force Sensing Micro-Forceps for Robot Assisted Retinal Surgery," *Int. Conf. of the IEEE EMBS (EMBC'12)*, 2012, pp. 1401-1404.

CHAPTER 4 : FORCE-BASED ROBOTIC ASSISTANCE METHODS FOR EPIRETINAL MEMBRANE PEELING

4.1 Introduction

4.1.1. Background and Motivation

Epiretinal membrane peeling is a typical task in vitreoretinal surgery, where a very thin (micron scale) fibrous membrane adherent to the retina surface is delaminated, either by using a pick or a micro-forceps tool. To catch the membrane edge without injuring the underlying retina, very precise manipulation of the tool to the correct depth under the membrane is required. In addition, the peel needs to be completed by exerting very fine forces with a small pace of generation on the retina [62]. Application of excessive forces with abrupt changes may damage retinal vasculature [23], and lead to serious complications, such as iatrogenic retinal injury and breaks [24], vitreous hemorrhage, or subretinal hemorrhage [25,26]. The required peeling forces for a safe operation routinely lie below the surgeon's sensory threshold. Currently, the surgeons adjust their peeling rate, and therefore applied forcing, using indirect visual cues, such as changing light reflections from the deforming tissue, which requires a great concentration and significant experience.

4.1.2. Contributions

The sensitized instruments presented in Chapter 3 enable quantitative monitoring of tool-to-tissue interaction forces during the surgery. To assist surgeons in completing membrane removal without facing the complications, this chapter describes methods based on detected tool-tissue forces that will inform the operator and robotically assist in maintaining forces at a safe level, and if possible facilitate delamination to minimize the

forcing on the retina. To limit the peeling force, an auditory force-feedback mechanism will be tested on two distinct robotic platforms and a new automatic tissue release method will be developed. To further reduce the peeling force, a micro-vibratory modulation method will be explored.

Credit: Auditory force feedback algorithm was developed by Balicki et al. for the Steady-Hand Eye robot. The Micron system was originally developed by Cameron Riviere and his team at Carnegie Mellon University. Based on this infrastructure, software components were developed to implement the auditory force feedback, micro-vibratory modulation and automatic tissue release modes by Berk Gonenc. Experiments in Section 4.2.2 were carried out by Ismail Kuru and Berk Gonenc.

4.2 Auditory Force Feedback

4.2.1. Algorithm

To keep applied forces at a safe level in epiretinal membrane peeling, auditory feedback is a potential method to inform the operator of the magnitude of the interaction forces at the tool tip, which otherwise lie below human sensory thresholds [29]. Therefore, in current retinal practice, control of force is based predominantly on visual cues. During surgery, the surgeon visually monitors local surface deformation and changing light reflections to assess the stress applied to the tissue. However, during such visual sensory substitution, there is a great reliance on prior experience, secondary rather than primary tissue changes and somewhat unpredictable light reflexes. Therefore, the surgeon is left with incomplete and sometimes false data with which to make crucial surgical decisions intraoperatively.

Since tool manipulation and decision making while trying to maintain the exerted forces at a safe level relies on the real-time information received from the environment, this information needs to be presented to the surgeon in an intuitive, real time, easy to process and overlay means. It should specifically not become an additional distraction to a surgeon who is already at the point of sensory overload due to multiple competing information inputs. With this in mind, studies [123-125] have shown that visual feedback can improve surgical performance in minimally invasive surgery, whereas retinal surgeons prefer not to have additional visual cues introduced into the already demanding visual channel. Visual feedback was experimented with and found distracting by retinal surgeons, while haptic and auditory feedback have been identified as the potentially useful methods that can be directly perceived, and have minimal conflict with other human sensing channels [126].

It was previously shown by Kitagawa *et al.* that continuous real-time auditory feedback representing the applied force could be a useful cue that significantly improved human performance in complex surgery [124]. Balicki *et al.* [127] developed an auditory feedback scheme that modulates "beeps" played at different frequencies depending on the measured force magnitude at the surgical tool's tip. Cutler *et al.* [30] investigated and compared this method with another binary mode that signaled a continuous high-pitch alarm when the force exceeded the given threshold. While both modes were shown to significantly reduce the forces during membrane peeling, the auditory feedback, frequency modulated first mode revealed a more consistent force application throughout the operation.

For precise tool manipulation, when a tremor canceling robotic platform is used, such as Micron or the Steady-Hand Eye Robot, simultaneous control of tool position and force can be achieved by implementing auditory sensory substitution to work jointly with the tremor canceling control loop of the robotic device. In this section, we implement a frequency modulated auditory feedback mechanism with both the Micron and the SHER systems. After the forces at the tool tip are measured using one of the sensitized instruments described in Section 3.2, depending on the magnitude of the force, the surgeon is provided with three different tempos of audio “beeps” representing three safety zones. The borders of these zones were defined based on typical vitreoretinal operations [122]. The audio remains silent until 1 mN or greater force is measured. Between 1 mN and 3.5 mN, a constant slow beeping is emitted, which is designated to be a “safe zone”. The second zone is between 3.5mN and 7 mN. A proportionally increasing tempo is generated to indicate this “caution zone”. Beyond 7 mN is a "danger zone" for potential retinal breaks and tears, which is represented by a constant high beeping.

4.2.2. Experiment 1: Evaluation of the Steady-Hand Eye Robot with a Force-Sensing Micro-Forceps

4.2.2.1. Setup and Procedure

In order to assess the performance of our micro-forceps in robot assisted membrane peeling, we conducted four types of experiments on the setup shown in Fig. 4.1. In all tests, we used the inner shell membrane (ISM) and the chick chorioallantoic membrane (CAM) as a biological phantom since it has previously been reported to be a suitable model for vitreoretinal microsurgical instrument studies [46].

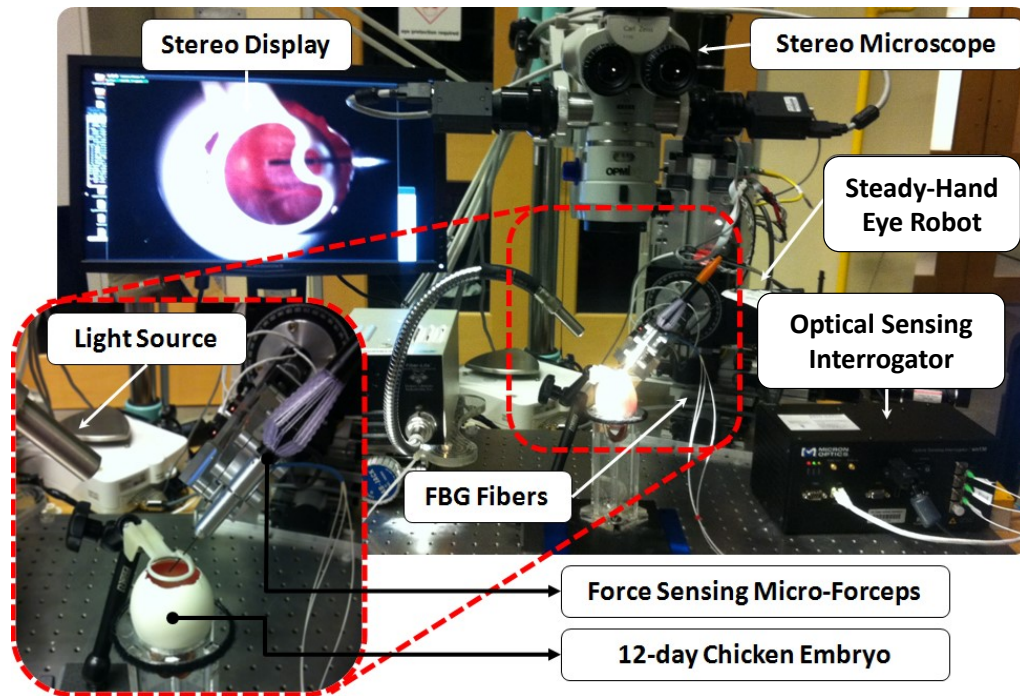


Figure 4.1: (a) Setup for membrane peeling experiments on 12-day fertilized chicken eggs using the Steady-Hand Eye Robot and a force-sensing micro-forceps.

After removing the eggshell gently, ISM of the chicken embryo becomes accessible. Attached under this thin layer is the CAM. In our experiments, the ISM simulates the ILM while the CAM serves as a phantom for the retina. The task is to peel off the ISM without breaking the CAM using the force sensing micro-forceps. In order to assist the subject, force sensor output is translated into auditory signals the frequency of which is modulated based on the magnitude of the measured force as described in Section 4.2.1. In order to assess the effect of such auditory force feedback and robotic assistance, we studied four different cases:

- (1) Freehand peeling with auditory force feedback
- (2) Robot-assisted peeling with auditory force feedback
- (3) Robot-assisted peeling with force scaling

(4) Robot-assisted peeling with auditory force feedback and force scaling

10 trials were performed for each case, and the mode of operation was changed in random order. For all cases, the 2-DOF force sensing forceps was held perpendicular to the direction of the peeling motion to minimize axial forces. The tool tip force and video were recorded. Based on the video timestamp, starting and ending points of the peeling motion were identified in the acquired data. The assessment was based on the applied forces during delaminating motion.

4.2.2.2. Results and Discussion

A typical force measurement from each of the test cases is presented in Fig. 4.2. According to Fig. 4.2.a, freehand membrane peeling forces exhibit two main types of variations during the delaminating period: (1) low frequency changes due to varying peeling speed and heterogeneous tissue structure, (2) high frequency oscillations due to hand tremor. Using the steady-hand robot, most of the hand-tremor based components were eliminated as shown in Fig. 4.2.b.

When force scaling feature of the Steady-Hand Eye Robot is activated, the force on the tool tip is multiplied by a cofactor (300x) and applied to the operator's hand, which is further described in [127]. Practically, this provides a stiffer tool manipulation in the direction of the applied force. The results presented in Fig.4.2.c indicate that force scaling feature provides enhanced stability and smoother force variations during the procedure as compared to the trials without force scaling. The fluctuations in Fig.4.2.b are attenuated upon activation of force scaling mode in Fig. 4.2.c and d. However, force scaling alone cannot keep the forces within the safe zone (below 7 mN). Fig. 4.2.d. shows that only the

combination of robot assistance, force scaling and auditory force feedback can provide relatively stable and limited forces during membrane peeling.

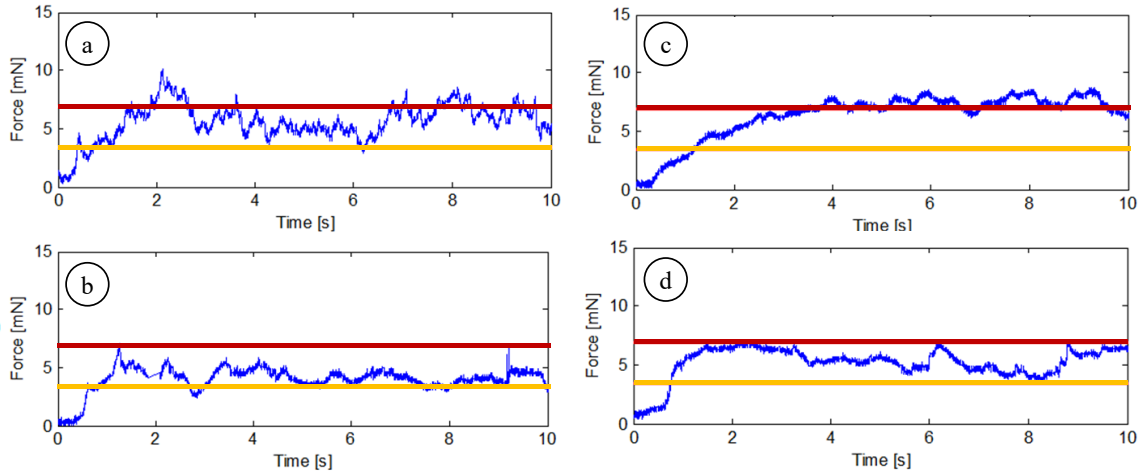


Figure 4.2: Membrane peeling forces on chicken embryo from a test sample: (a) completely unaided, (b) robot assisted with only auditory force feedback, (c) robot assisted with only force scaling, (d) robot assisted with auditory force feedback and force scaling. High frequency oscillations in delaminating forces are reduced by steady-hand robot. Force scaling provides smoother force variations. Auditory feedback (yellow line is the threshold for the caution signal and red line indicates the threshold for the danger warning) is beneficial for keeping the forces within the safe operation zone (below the red line).

4.2.3. Experiment 2: Evaluation of Micron with a Force-Sensing Hook

4.2.3.1. Setup and Procedure

To simulate membrane peeling, a series of experiments have been performed by a single novice user on the setup shown in Fig. 4.3. The tool velocity was tracked by ASAP optical sensors. In order to monitor the integrated force sensor, an optical sensing interrogator, sm130-700 from Micron Optics Inc. (Atlanta GA), was used.

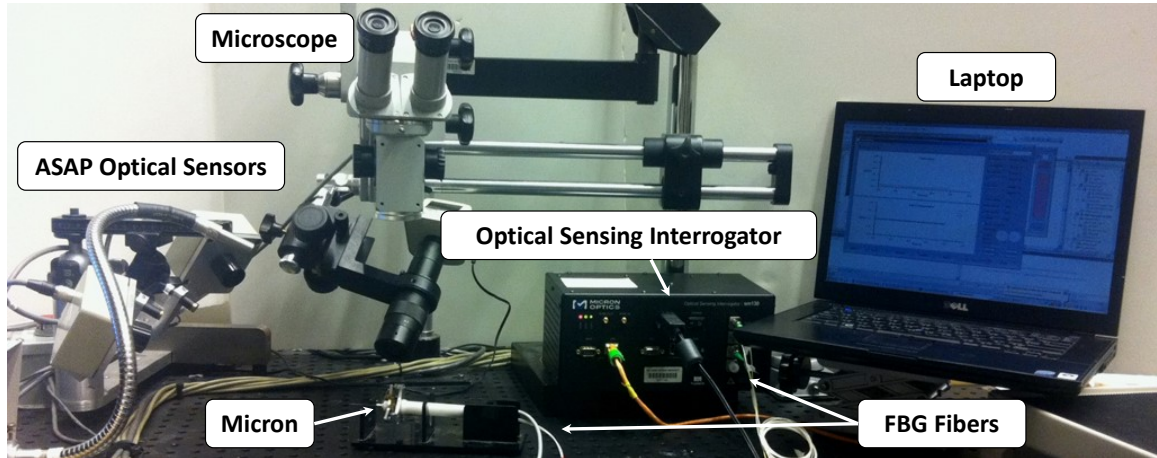


Figure 4.3: Setup for membrane peeling experiments using the Micron system with a force-sensing hook [128].

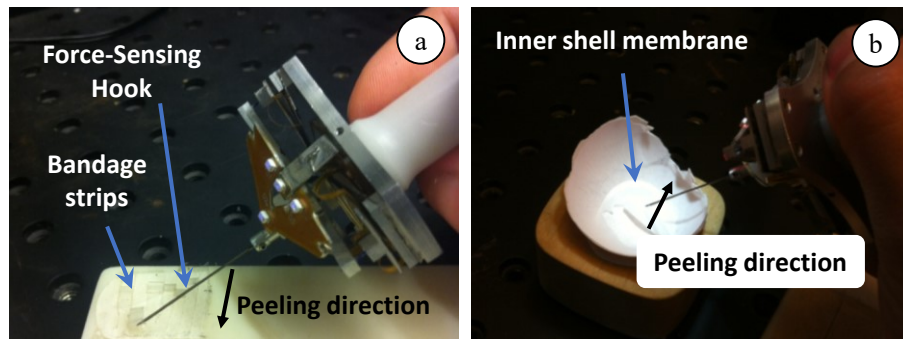


Figure 4.4: Experiments were done on two types of phantoms: (a) bandage phantom and (b) inner shell membrane of raw chicken eggs [128].

In this experiment, two sets of tests were done. The performance of a non-surgeon researcher was analyzed for different cases. The challenge in all cases was to keep the tool velocity as uniform as possible (~ 0.5 mm/s) and the delaminating forces below the danger threshold (~ 7 mN). For each phantom type, an extensive training period (~ 3 hrs) was allowed before data collection.

(1) Membrane Peeling on Bandage Phantom: Sticky tabs from 19 mm Clear Bandages (RiteAid brand) were sliced to produce strips 2 mm wide. The subject was asked to peel a 10 mm section of the strip steadily and without stopping while holding the Micron

instrument almost perpendicular to the bandage surface in order to minimize the forces along the tool axis.

(2) Membrane Peeling on Raw Chicken Eggs: The inner shell membranes of raw chicken eggs were peeled following a linear trajectory. Unlike the bandages, this phantom accounted for biological factors such as heterogeneous tissue structure and its effect on force. A single egg shell was used for each test, and it was assumed that the membrane structure did not vary significantly between eggs.

Table 4.1: Membrane Peeling Performance Test Cases

Case (n=5 trials/case)	Tremor Suppression	Force Feedback
Completely unaided	No	No
Only Micron-aided	Yes	No
Only with auditory feedback	No	Yes
Micron aided with auditory feedback	Yes	Yes

For each experiment set, four different cases were evaluated as shown in Table 4.1. Five trials were performed in random order for each of these scenarios. The tool tip force, position, speed and video were recorded. Based on the video timestamp, starting and ending points of the peeling motion were identified in the acquired data. The assessment was based on the applied forces during delaminating motion.

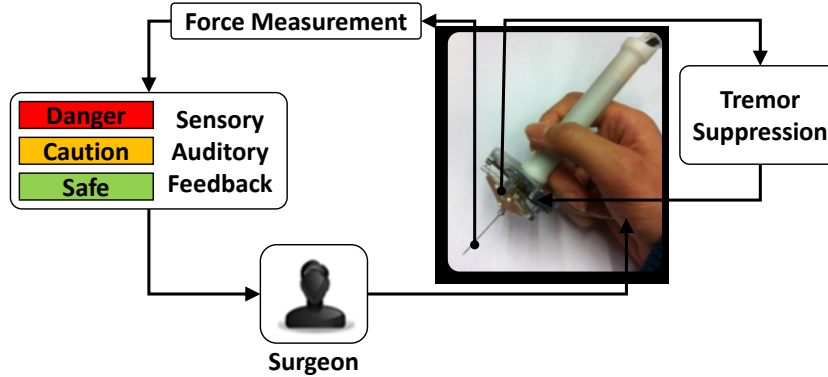


Figure 4.5: Force sensing Micron control scheme. The measured forces on the tool tip are translated into auditory signals to guide the surgeon while Micron suppresses hand-tremor in another loop [128].

4.2.3.2. Results and Discussion

4.2.3.2.1. Membrane Peeling on Bandage Phantom

In Fig. 4.6, the results of a test set on bandage phantom are presented for all cases. Accordingly, freehand membrane peeling forces exhibited two main types of variations during the delaminating period: low frequency changes due to varying peeling speed and high frequency oscillations due to hand tremor. In the absence of auditory and tremor suppression aids, peeling forces exceeding 7 mN were recorded with high frequency oscillations. Upon activation of Micron, these oscillations were significantly reduced. However, still, forces in danger zone were observed due to lack of force feedback. When auditory sensory substitution was used alone, almost all forces were kept below the safety threshold successfully, nevertheless with high frequency oscillations, which appeared both in speed and force plots. In the last case, combination of active tremor canceling together with auditory sensory substitution provided the best performance, where peeling forces were kept within the safe operation zone free of high frequency oscillations.

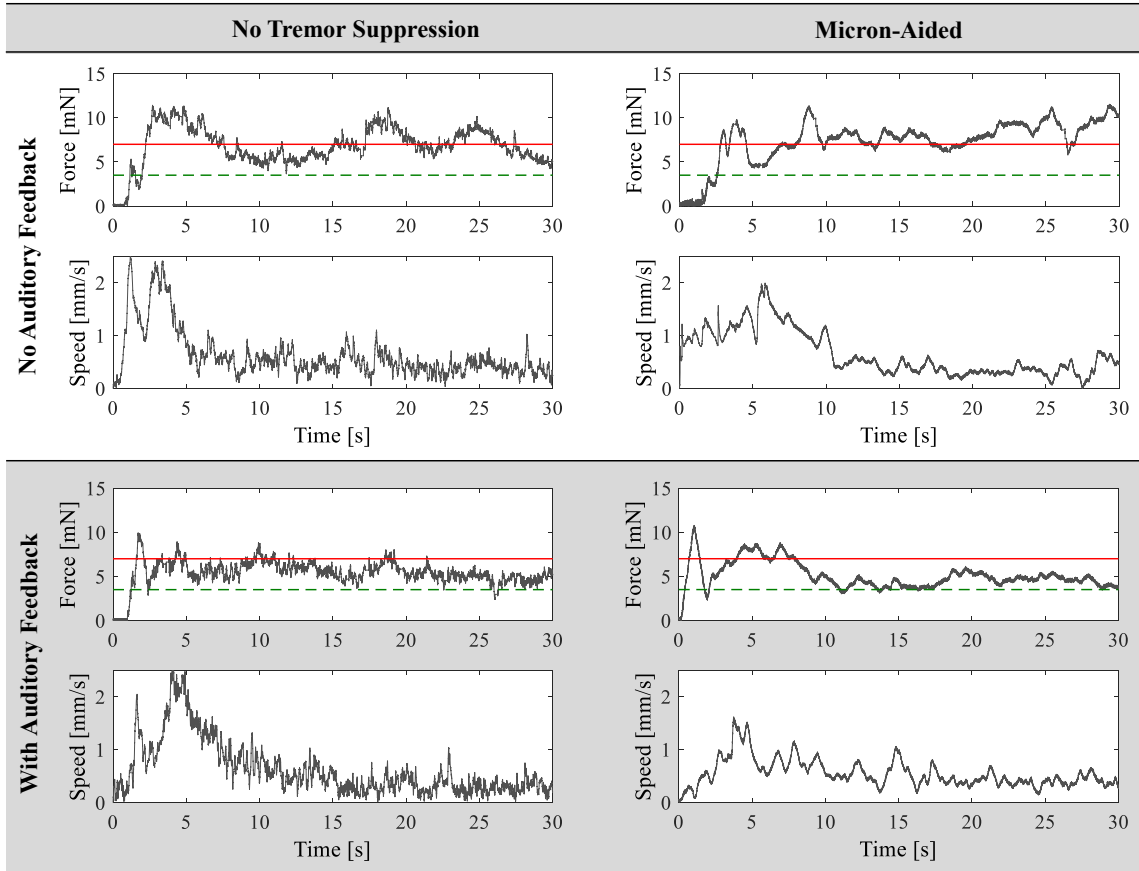


Figure 4.6: Measured membrane peeling force samples for four different cases using bandage phantom. Maximum allowable operation zone (3.5 mN - 7mN) is between the green dashed and red solid lines. High frequency oscillations in the force and speed due to hand tremor (left) are eliminated when Micron is activated (right). Without the auditory sensory substitution, the exerted forces may exceed the safety threshold shown in red (upper), whereas with the auditory feedback they are mostly maintained at a safe level (lower).

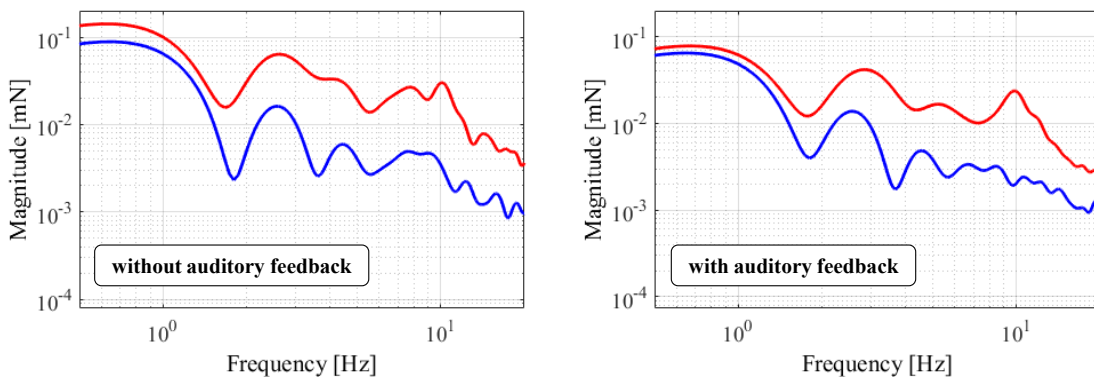


Figure 4.7: Frequency analysis of recorded forces for all 4 cases on bandage phantom: with auditory feedback (left), without auditory feedback (right), with tremor suppression (blue), and without tremor suppression (red).

Beyond 2 Hz until 20 Hz, the magnitude of forces is greatly reduced in both the absence and presence of auditory force feedback. In this range, the recorded reduction is 60%-90% with auditory sensory substitution, and 70%-90% without auditory sensory substitution as shown in Fig. 4.7.a and 4.7.b respectively.

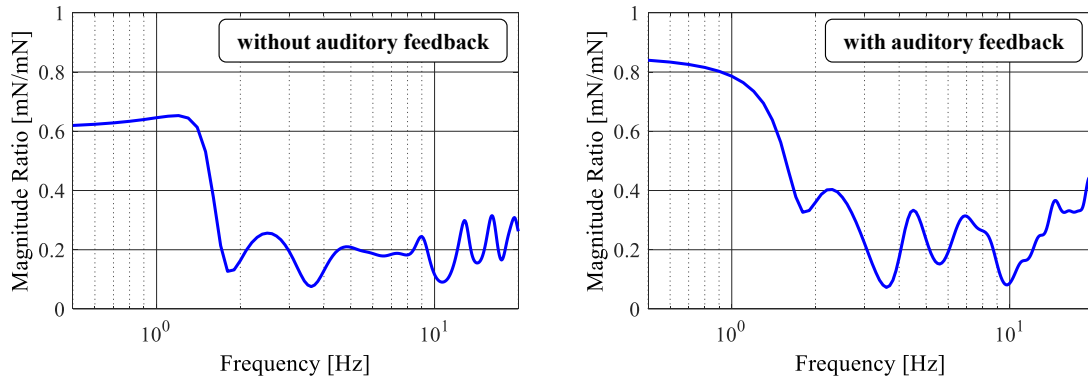


Figure 4.8: Micron aided to free-hand force magnitude ratio with respect to frequencies. Significant reduction in 2-20 Hz forces: (a) 60%-90% with auditory feedback, (b) 70%-90% without auditory feedback.

4.2.3.2.2. Membrane Peeling on Raw Chicken Eggs

Although a different phantom type is used, the results are in great agreement with bandage phantom observations as shown in Fig. 4.9. The peeling forces exhibit very similar characteristics for each of the tested cases. In free hand tests (Fig. 4.9.a), high force variations with occasional non-safe forces were observed. Micron was successful in eliminating the high frequency oscillations (Fig. 4.9.b) while auditory feedback reduced overall forces below the safety threshold (Figs. 4.9.c and 4.9.d).

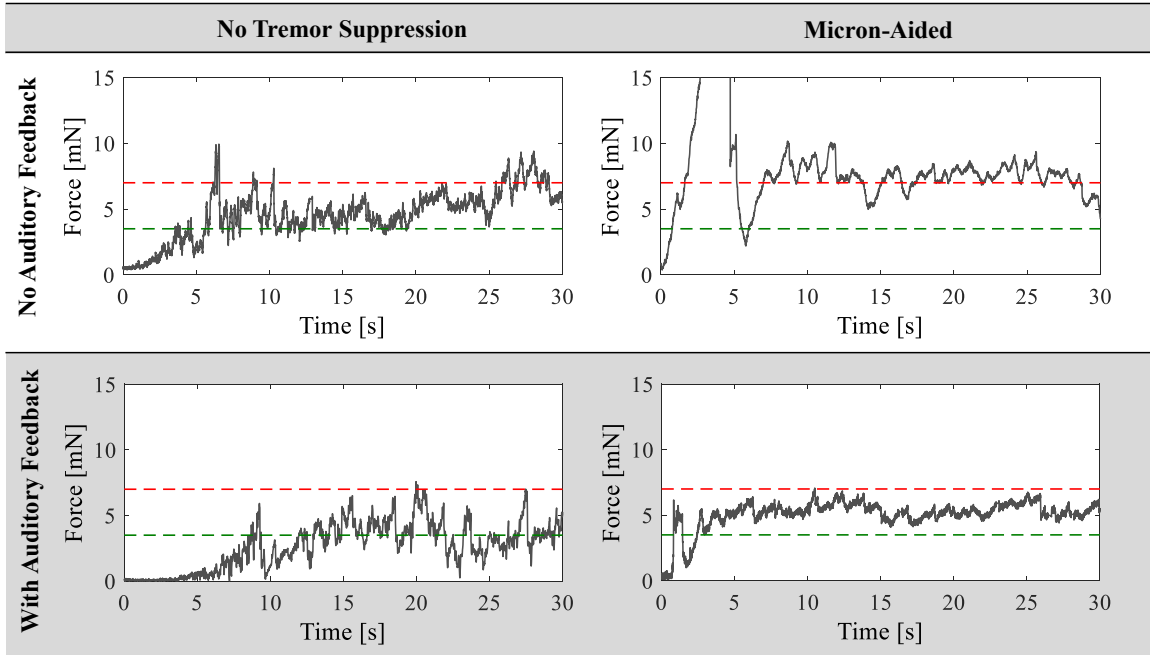


Figure 4.9: Membrane peeling forces on raw chicken eggs:(a) completely unaided, (b) only Micron aided, (c) only with auditory feedback, (d) Micron aided with auditory feedback. Oscillations in delaminating forces are highly reduced by Micron while auditory feedback could prevent application of forces above 7 mN.

Frequency analysis of forces measured in Micron-activated and Micron-deactivated cases revealed a significant reduction between 2-10 Hz, which is shown in Fig 4.10. In free-hand peeling tests (red plot in Fig. 4.10), a peak was observed again at 10 Hz, which disappeared upon activation of Micron (blue plot in Fig. 4.10). Despite the smoother tool motion with Micron's assistance, the forces still could go beyond the safety limits when no auditory guidance was provided. When Micron's tremor canceling was used together with auditory sensory substitution, the operation was accomplished within the desired zone successfully.

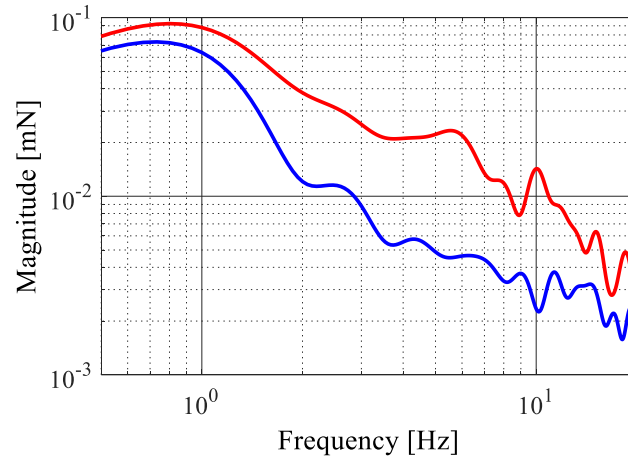


Figure 4.10: Frequency analysis of recorded forces on raw chicken eggs: with tremor suppression (blue), and without tremor suppression (red).

4.2.4. Experiment 3: Performance Comparison Between Micron versus the Steady-Hand Eye Robot

4.2.4.1. Setup and Procedure

A series of membrane peeling experiments were conducted aiming to compare the performance of the Steady-Hand Eye Robot and Micron with and without auditory force feedback. The setup for each system is presented in Fig. 4.11.a and 4.11.b, respectively. Being a table mounted system, the Steady-Hand Eye Robot occupies a larger footprint in the operation area as compared to the hand-held Micron. On the other hand, Micron requires an additional equipment, ASAP optical sensors, for tracking the tool motion. These trackers have a limited field of view, therefore while setting up the system one needs to position the trackers carefully such that the phantom falls inside the working volume of the tracker. In both systems, the applied forces are monitored by using an FBG optical sensing interrogator, sm130-700 from Micron Optics Inc. (Atlanta GA). The tests were done on two types of phantoms, which have been used in the previous experiments

in Sections 4.2.2 and 4.2.3: the bandage phantom and the inner shell membrane (ISM) of 12-day old fertilized chicken eggs.

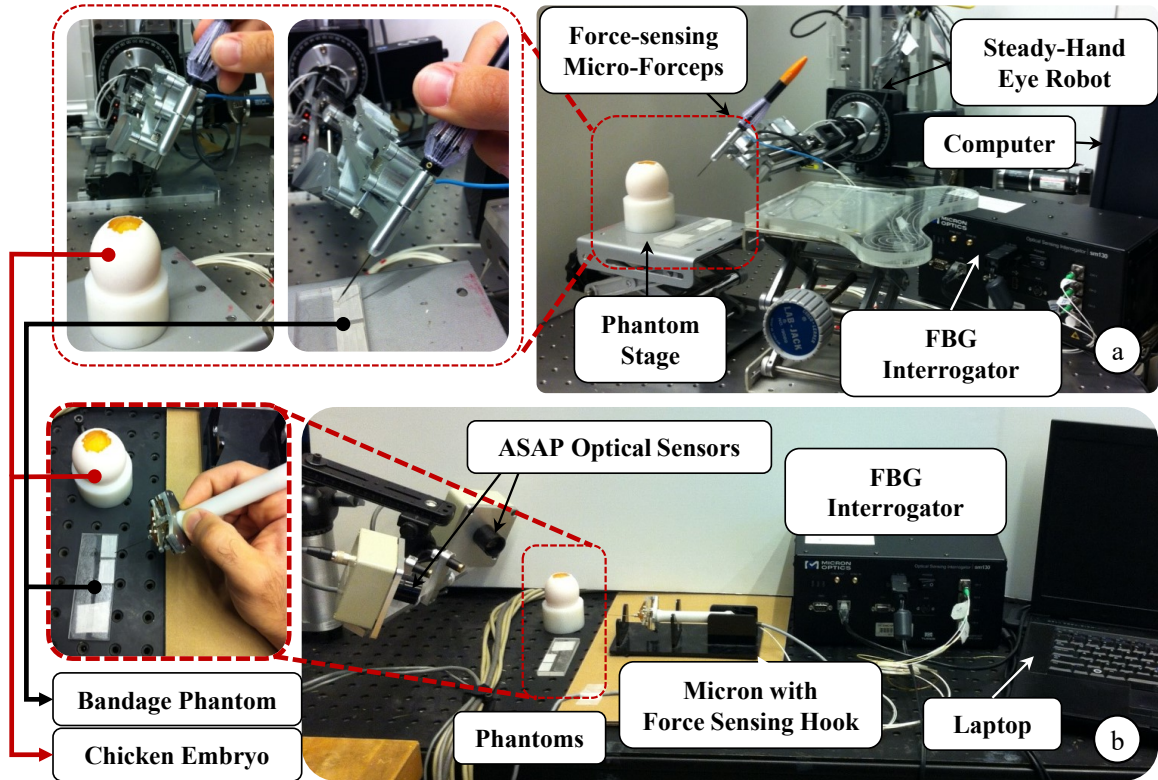


Figure 4.11: Setup for membrane peeling experiments using (a) the Steady-Hand Eye Robot with a force-sensing micro-forceps, and (b) Micron with a force-sensing hook. [129]

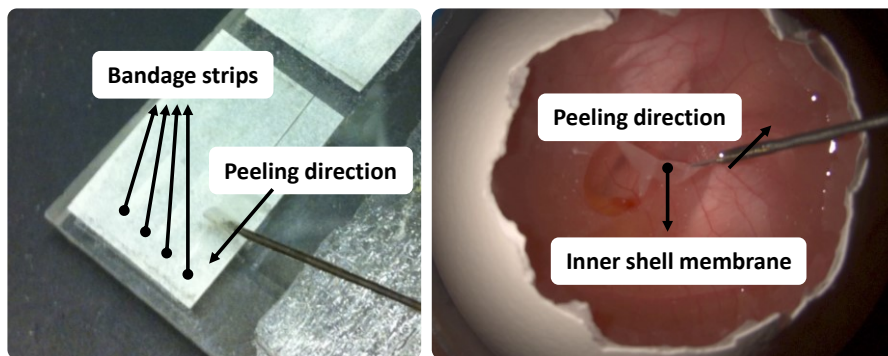


Figure 4.12: Membrane peeling procedure using bandage phantom (left) and inner shell membrane in chicken embryo (right) [129].

Bandage Phantom: This phantom has 2 mm wide strips that are produced by slicing sticky tabs from 19 mm Clear Bandages (RiteAid brand). At the end of each strip, there is

a flap for holding/grasping. Each strip can be used several times without significant change in the required force.

ISM of Chicken Embryo: The eggshell is removed gently to access the ISM chicken embryo. Under the thin ISM layer, there is chorioallantoic membrane (CAM), which serves as a good surrogate for retina. Peeling the ISM off without breaking the CAM is similar to the challenge involved in the epiretinal membrane peeling surgery.

Using these phantoms, experiments were done by a single novice non-surgeon researcher for different test cases of both systems. The studied cases are summarized in Table 4.2.

Table 4.2: Tested cases for membrane peeling with Micron or the Steady-Hand Eye Robot on the bandage phantom and ISM of fertilized chicken eggs.

Phantom	Tool	Case	Tremor Suppression	Auditory Feedback
Bandage Phantom	Hook	(1) Freehand	No	No
		(2) Only with AF	No	Yes
		(3) Micron aided with AF	Yes	Yes
	Forceps	(4) Freehand	No	No
		(5) Only with AF	No	Yes
		(6) Steady-Hand Robot aided with AF	Yes	Yes
ISM of Chicken Embryo	Hook	(7) Only with AF	No	Yes
		(8) Micron aided with AF	Yes	Yes
	Forceps	(9) Only with AF	No	Yes
		(10) Steady-Hand Robot aided with AF	Yes	Yes

Procedure on the Bandage Phantom: The subject was asked to peel a 10 mm section of the bandage strip steadily and without stopping while holding the tool perpendicular to

the peeling direction so that the task is completed with pure transverse loading on the tool tip. 3 cases were studied and 10 trials per case were conducted in random order.

Procedure on ISM of Chicken Embryo: The subject was asked to peel off the ISM without breaking into the CAM by following a linear trajectory. The tool was again held perpendicular to the peeling direction to minimize axial forces. 2 cases were studied and 2 tests were done per case. A new embryo was used for each trial and it is assumed that there is no significant difference between embryos.

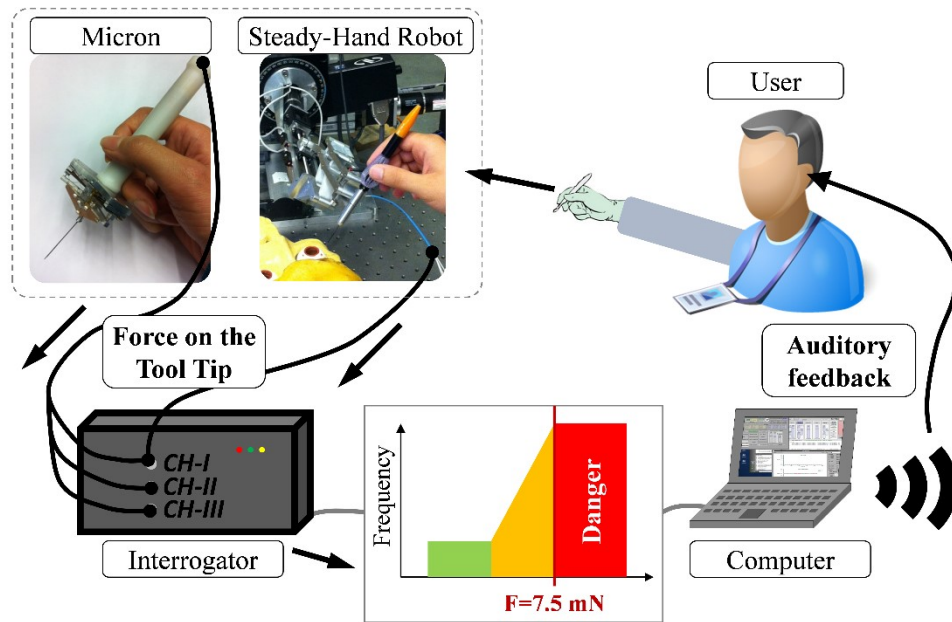


Figure 4.13: System overview with robotic assistance and integrated force sensing. Auditory feedback is provided to the user based on sensed forces at the tool tip.

For each case, an extensive training period (~3 hrs) was allowed before data collection. The challenge in all cases was to complete the peeling task by moving the tool with a uniform velocity (~0.5 mm/s) and by applying forces below the danger threshold (~7.5 mN). Robot-assisted and freehand tests were done in random order. Only in some cases, the user was provided with auditory feedback whereas force sensing was used only for data acquisition purposes in the rest. During the experiments, we recorded the tool tip

force, position, speed and video. Based on the video timestamp, the recorded data was segmented into two phases: (1) catching/lifting the membrane edge and creating a flap, (2) delaminating the membrane. The forces measured during the delaminating period after creating the flap form the basis of our performance evaluation.

4.2.4.2. Results

4.2.4.2.1. Membrane Peeling on Bandage Phantom

Measured forces on bandage phantom are shown for all trials in Fig. 4.14. Consistent characteristics were visible among the trials in each case. In freehand trials, highly oscillatory forces exceeding the safety threshold were observed. When the user was supplied with force information through auditory feedback, some of these forces could be reduced below the safety limit. In this case, although the user clearly knew the applied force, there were challenges in controlling the tool motion precisely due to physiological hand tremor. The assistance of either Micron or the Steady-Hand Eye Robot was able to eliminate this problem. Compensating for the unintentional high frequency motion, tool control of the user was greatly improved. In this case, knowing the force level through auditory feedback, the user was able to complete the task very precisely such that in the delaminating period, almost all of the forces were kept below 7.5 mN free of high frequency vibrations.

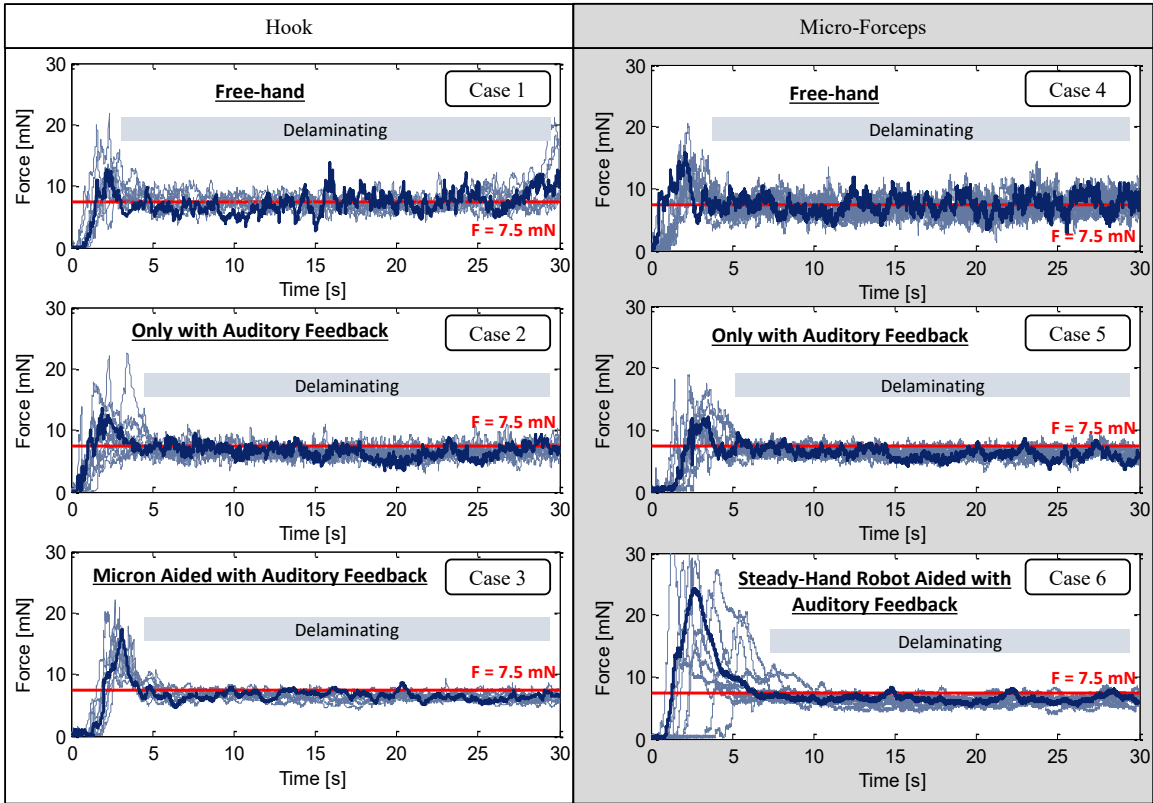


Figure 4.14: Measured peeling forces (blue) using *bandage phantom* for all trials (10 trials/case). Auditory feedback helps in keeping forces below the safety threshold (red horizontal line). Robotic assistance helps in eliminating oscillations. Additional effort and longer duration in grasping the bandage while using micro-forceps with the Steady-Hand Robot due to additional system inertia.

Despite the improvement in tool control while peeling, difficulty in initial grasping was observed at the beginning of each trial when micro-forceps were used with the Steady-Hand Eye Robot. The additional inertia introduced on the user hand makes certain maneuvers more challenging for a novice user. This extra effort can clearly be seen from the first 10 seconds of case 6 in Fig. 4.14. On the other hand, being a hand-held tool, Micron has better dexterity but a more limited workspace. The user can still perform similar maneuvers as a manual tool, but while paying attention to stay within the boundaries of the workspace. For this reason, the manipulation problem in case 6 does not exist in case 3.

The hand tremor reduction characteristics for each device can better be seen when the measured forces are analyzed in frequency domain as shown in Fig. 4.15. Accordingly, presence of auditory force feedback does not change the frequency distribution of forces very much for either the hook or the micro-forceps. However, utilizing robotic assistance has great impact on the characteristics. The bandwidth of human eye-hand feedback is usually from 0.5 Hz to 2 Hz [130]. Thus, the region below 0.5 Hz in Fig. 4.15 represents controlled actions, whereas frequencies above 2 Hz indicate the unintentional motion of the user. The postural hand tremor frequency in normal humans is at about 8-10 Hz [130]. The prominence of a peak at 10 Hz in all freehand trials is primarily due to this reason. When Micron is used, this peak is eliminated and the high frequency components (2-15 Hz) are overall reduced by 60-80%. The reduction zone for the Steady-Hand Eye Robot is slightly broader with a similar reduction ratio as compared to Micron.

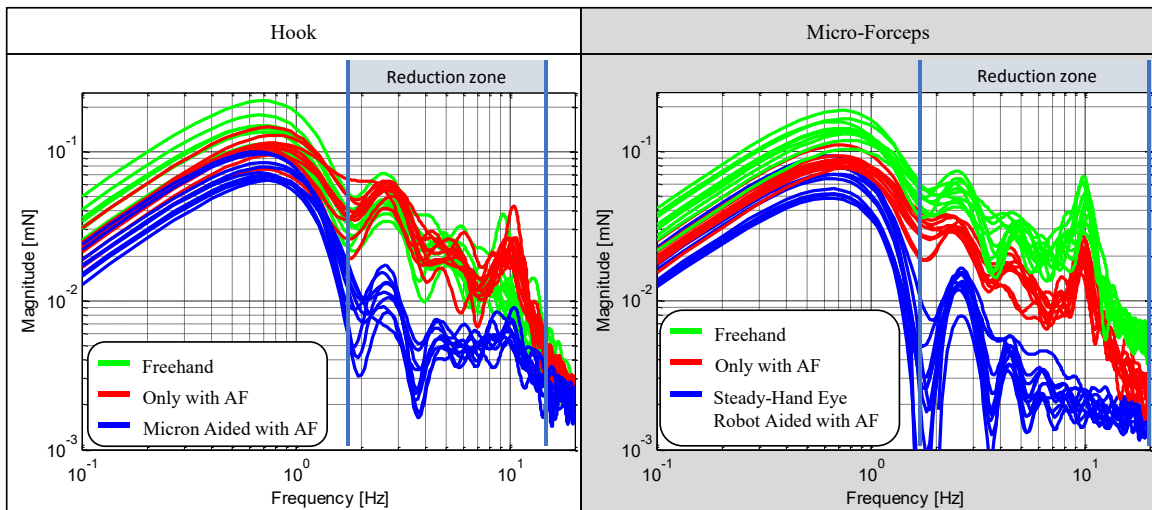


Figure 4.15: Frequency analysis on forces applied in all trials on *bandage phantom*. 60-80% reduction in 2-15 Hz oscillations by using Micron (left), Steady-Hand Eye Robot (right) [129].

4.2.4.2.2. *Membrane Peeling on ISM of Chicken Embryo*

Having proven the benefits of force sensing capability in the first part of our experiments, we did all trials in this section using auditory force feedback. The aim was to account for heterogeneous tissue properties in our comparison between Micron and the Steady-Hand Eye Robot by using a more realistic biological phantom. Consequently, we observed significantly different characteristics for each device as compared with the bandage phantom.

The measured forces for all trials are shown in Fig. 4.16. Since all tests were done under auditory feedback, most of the measured forces were maintained successfully below the safety threshold (7.5 mN). However as opposed to our bandage phantom trials, the user had to grasp the membrane and peel it several times to complete the task, which can be attributed to two main reasons: First, it is not possible to remove the whole ISM in a single linear peel. Second, the ISM is more slippery and deformable than the bandage phantom, which makes it hard to hold firmly. This fact is most apparent while using hook in cases 7 and 8 due to inability to grasp ISM with this type of tool. Micro-forceps have performed better in this respect with only 1-3 delaminating periods in cases 9 and 10.

Frequency analysis of measured forces on ISM is shown in Fig. 4.17. In all results, an increase in low frequency oscillations as compared to bandage phantom results is prominent. This is an expected result of using biological phantom with non-uniform tissue properties. By using a hook manually in case 7, high frequency oscillations were observed in Fig. 6. However, 10 Hz peak corresponding to the physiological hand tremor is not visible for this case in Fig. 4.17. This is mainly due to poor grasping and slippage of the tissue, and resulting disturbance on the force measurement. But still 40-50%

reduction in high frequency oscillations was recorded with Micron assistance. Using micro-forceps, a behavior that is similar to the results on bandage phantom is obtained. 10 Hz peak is clearly visible in manual use of micro-forceps. Utilizing Steady-Hand Robot assistance with this tool has decreased 2-15 Hz oscillations by 50-60%.

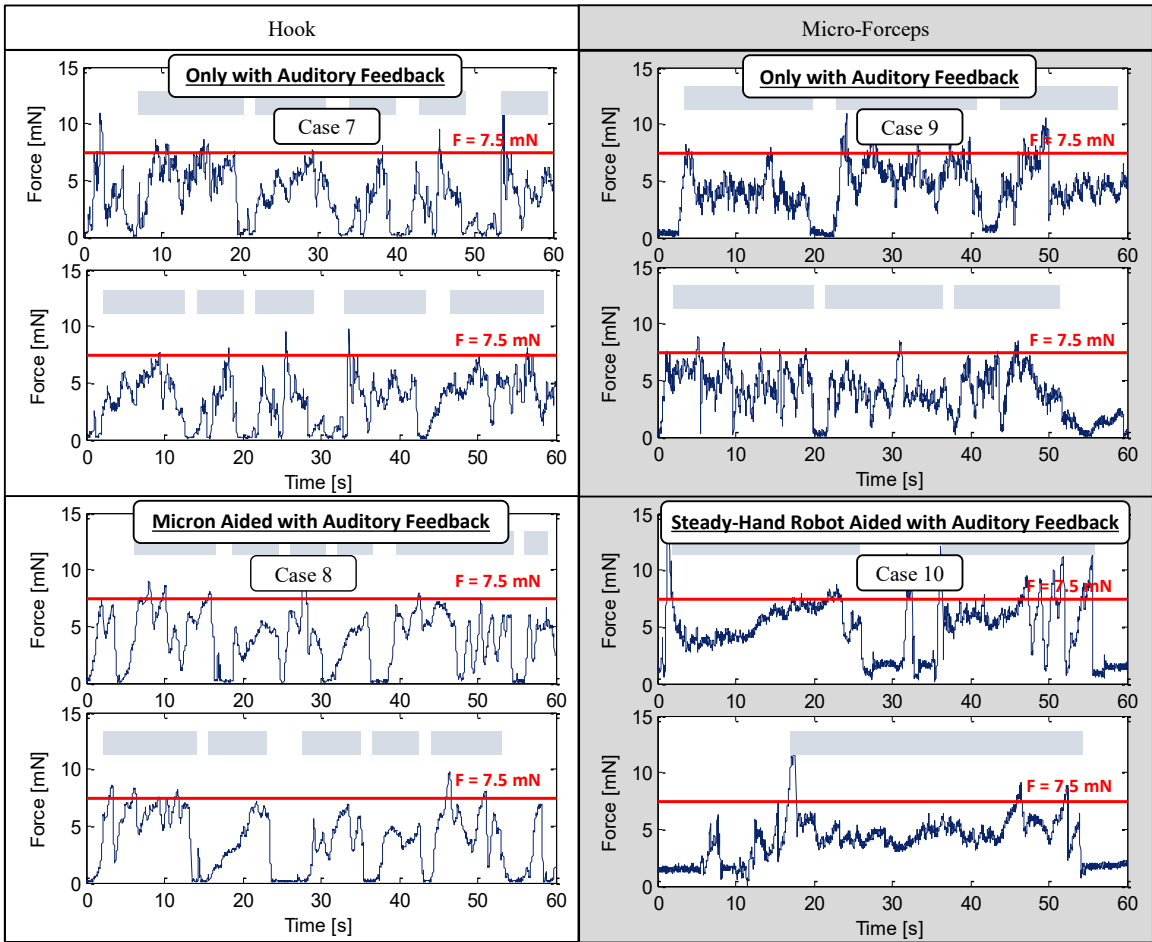


Figure 4.16: Measured peeling forces (dark blue) using *ISM of chicken embryo* for all trials (2 trials/case). Shorter multiple peeling periods (light blue rectangles) as opposed to bandage phantom trials [129].

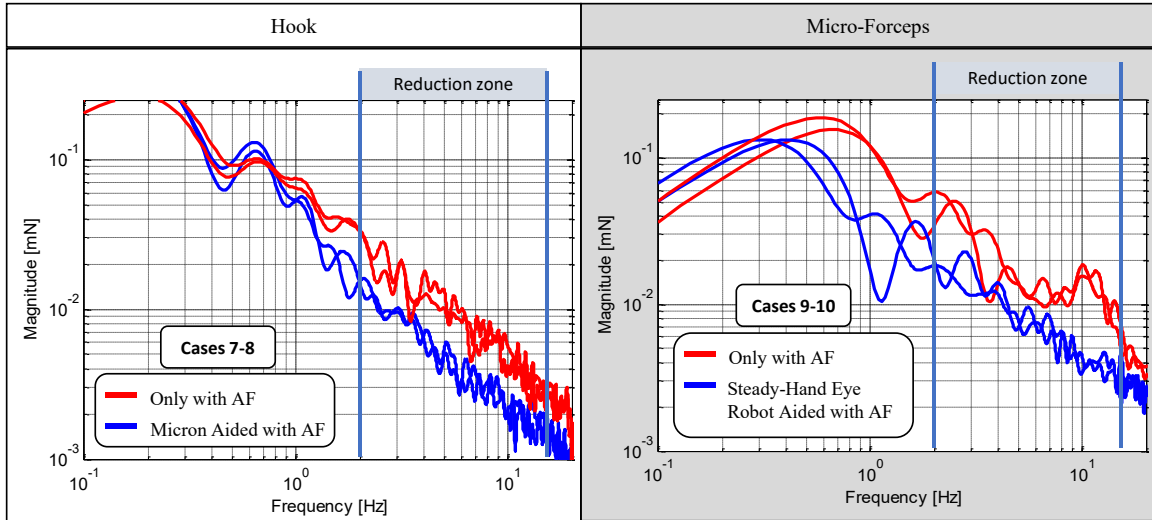


Figure 4.17: Frequency analysis on forces applied in all trials on *ISM of chicken embryo*. Reduction in 2-15 Hz oscillations: 40-50% by Micron (left), 50-60% by the Steady-Hand Eye Robot (right). 10 Hz peak corresponding to physiological hand tremor is not visible while using hook (upper) due to the inability to grasp, hence the tissue slippage [129].

4.2.4.3. Discussion

The acquired force data for each case was analyzed based on average values of five main criteria, which are summarized in Table 4.3. On the bandage phantom, using either Micron or the Steady-Hand Eye Robot have provided similar improvements, which are significant in terms of reducing the standard deviation of forces (by 63% with Micron and 60% with the Steady-Hand Eye Robot) and the danger zone percentage (4.97% with Micron and 4.26% with the Steady-Hand Eye Robot). Hence, a more consistent and safe operation was provided through the assistance of either robotic system.

In contrast to the consistent peeling environment provided by the bandage phantom, the ISM of chicken embryo exhibited non-uniform tissue properties. It was more challenging to manipulate the ISM due to these variations and its slippery deformable structure. For this reason, the success in decreasing the standard deviation was drastically reduced on ISM (by 13% with Micron and 8.9% with the Steady-Hand Eye Robot). The danger zone

percentage was already low in all trials as compared to the previous cases. Thus, the robotic assistance on ISM did not provide much benefit in terms of keeping the forces below the safety threshold. This could be either a difference between the two types of phantoms, or a matter of the user's learning curve since ISM tests were done after completion of the bandage experiments which need to be addressed in future experiments.

Table 4.3: Comparison of force and duration of unsafe forces during peeling experiments.

Phantom	Tool	Case	Max. Force [mN]	Mean Force [mN]	Standard Deviation [mN]	Duration in Danger Zone [sec]	Danger Zone Percentage [%]
Bandage Phantom	Hook	(1) Freehand	14.81	7.63	1.68	9.30 ± 3.23	46.51 ± 16.14
		(2) Only with AF	9.91	6.46	0.98	2.94 ± 1.21	14.71 ± 6.03
		(3) <u>Micron aided</u> with AF	8.65	6.38	0.62	0.99 ± 0.50	4.97 ± 2.52
	Forceps	(4) Freehand	12.11	6.85	1.59	6.60 ± 1.94	33.02 ± 9.68
		(5) Only with AF	8.96	6.20	0.79	1.25 ± 0.64	6.24 ± 3.22
		(6) <u>Steady-Hand Eye Robot aided</u> with AF	8.20	6.26	0.64	0.85 ± 0.84	4.26 ± 4.24
ISM of Chicken Embryo	Hook	(7) Only with AF	8.27	4.55	1.56	0.32 ± 0.31	0.54 ± 0.12
		(8) <u>Micron aided</u> with AF	7.58	4.81	1.35	0.44 ± 0.41	0.74 ± 0.11
	Forceps	(9) Only with AF	9.05	4.93	1.46	1.26 ± 0.91	2.11 ± 1.53
		(10) <u>Steady-Hand Eye Robot aided</u> with AF	7.96	4.87	1.33	1.11 ± 0.84	1.85 ± 1.32

4.2.5. Experiment 4: Evaluation of Micron with a Force-Sensing Micro-Forceps

4.2.5.1. Setup and Procedure

The experiment in Section 4.2.4 revealed the necessity of a micro-forceps instrument for controlled tissue manipulation with a firm grasp preventing the reduced slippage of the tissue during peeling. After replacing the force-sensing hook on the Micron with the motorized force-sensing micro-forceps introduced in Section 3.2.1.3, the peeling trials were repeated by the same subject as in the previous section using an artificial eye model,

where, instead of a flat surface, the bandage strips were attached to a curved base (\varnothing 25 mm) resembling the back of the eye. In addition, a rubber sclerotomy constraint was located approximately 9.5 mm above the bandage strips.

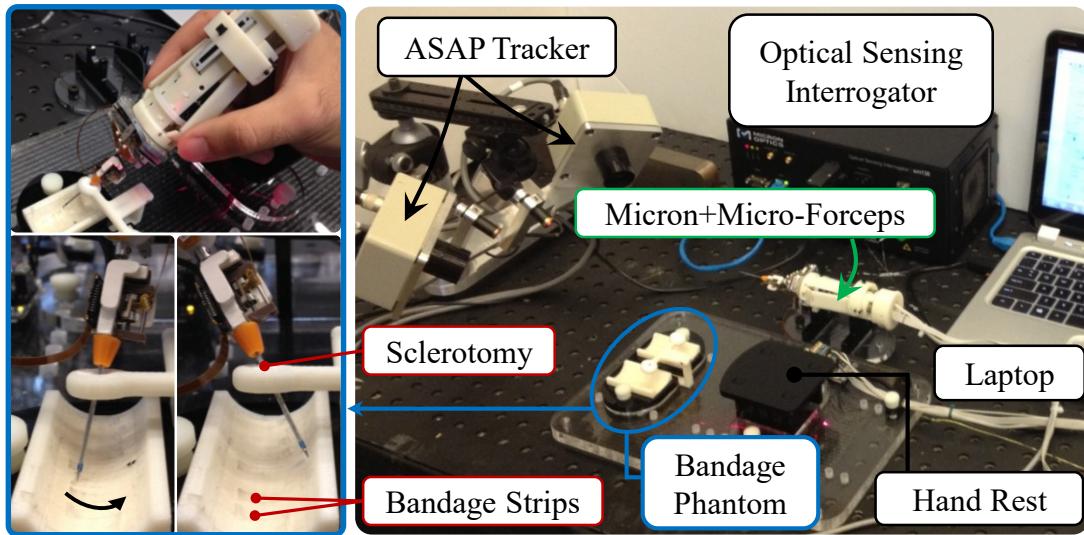


Figure 4.18: Setup for membrane peeling experiments in an artificial eye model with bandages using Micron with a force-sensing micro-forceps [102].

During the experiment, the subject was asked to (1) insert the micro-forceps tool through the sclerotomy point, (2) grasp and lift the bandage edge, and (3) peel the strip off of the plastic surface while keeping the tool velocity as uniform as possible (~ 0.5 mm/s) and the delaminating forces below the danger threshold (~ 7.5 mN) based on the provided auditory force feedback. The goal of the experiment was to identify any interference between the micro-forceps and Micron operation, and to determine whether the implemented hardware modifications affect the device's tremor canceling characteristics. For this reason, the experiments were done in two sets by turning the tremor cancellation feature on and off. Five peels were recorded per category, and the tests were performed in alternating order. Before data collection, an extensive training period (~ 1 hrs) was allowed for the subject to become accustomed to the system and phantom, and to

minimize learning curve effects in the recorded measurements. During data collection, the tool tip force and position, and micro-forceps motor position were recorded with time stamp. Based upon the micro-forceps motor position, the grasp/release instants, hence the starting/ending points of the delamination period were identified in the acquired data. The assessment was based on the applied forces and tool tip positions during this period.

4.2.5.2. Results and Discussion

Measured forces on the bandage phantom are displayed for all trials in Fig. 4.19. The starting time of the task is set at the point when the user starts closing the grasper jaws. The delaminating period begins after the forceps are closed, and the forces after this time are of interest. During the delaminating period, the exerted forces in all trials remained below the safety threshold (7.5 mN), which displays the effectiveness of the auditory force feedback and agrees with our previous results [128,129]. On the other hand, high frequency oscillations were visible when the tremor suppression feature of the system was not used. Upon activation of Micron, these oscillations were significantly reduced.

The effect of physiological hand tremor is also visible in velocity and tip position plots. In all trials, the user managed to keep the peeling speed around 0.5 mm/s as desired; however, oscillations and difficulty increased in the absence of Micron tremor aid. Fig. 4.20 shows that the tool tip in Micron-assisted trials followed a much smoother trajectory with higher positioning accuracy in comparison to the cases without tremor cancellation.

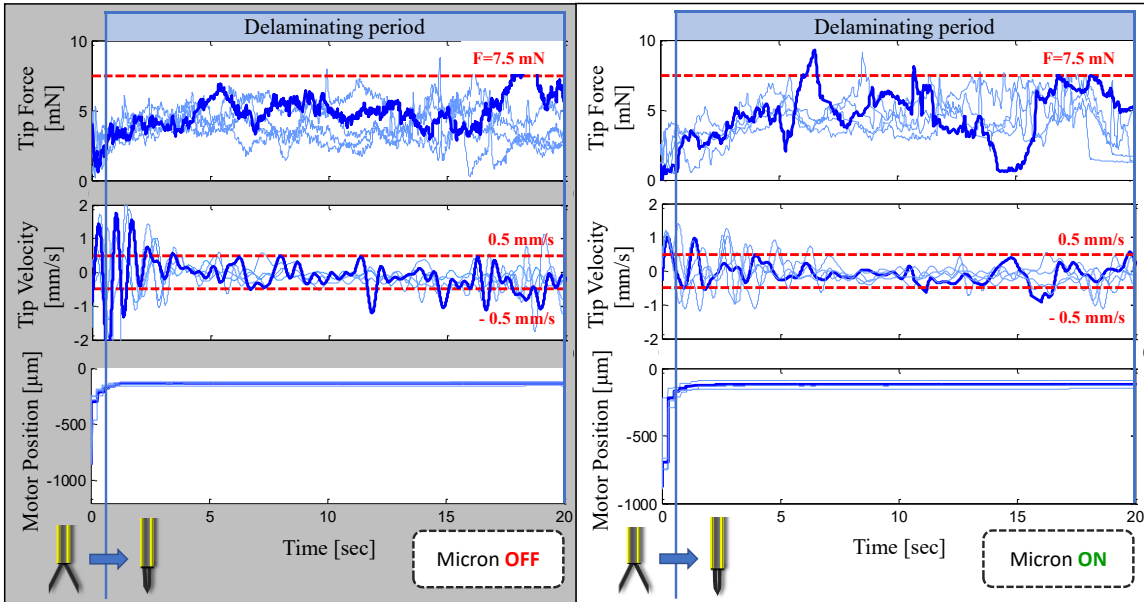


Figure 4.19: Measured peeling forces using bandage phantom for all trials (5 trials/case). One of the trials was shown in darker color to highlight the important characteristics. Auditory feedback helps in keeping forces below the safety threshold (7.5 mN). The peeling speed is kept below 0.5 mm/s successfully in all cases, but with much difficulty when Micron is off. The tremor canceling feature of Micron helps in reducing high frequency oscillations in both tip force and tip velocity [102].

To assess the tremor canceling effect of Micron in our tests, we performed frequency analyses based on both position and force measurements. The results are presented in Fig. 4.21. The bandwidth of human hand-eye feedback usually is from 0.5 Hz to 2 Hz [130]. Below 0.5 Hz, hand-eye feedback becomes effective. Thus, the regions below 0.5 Hz in these figures represent controlled actions, whereas frequencies above 2 Hz indicate the unintentional motion of the user. The postural hand tremor frequency in normal humans is approximately 8-10 Hz [130]. The prominence of a peak around 9 Hz in Micron-off trials is primarily due to the subject's hand tremor. When the tremor suppression feature is activated, this peak is eliminated and the high-frequency components (2-20 Hz) are overall reduced by 60-95% in both the tip force and tip position spectra.

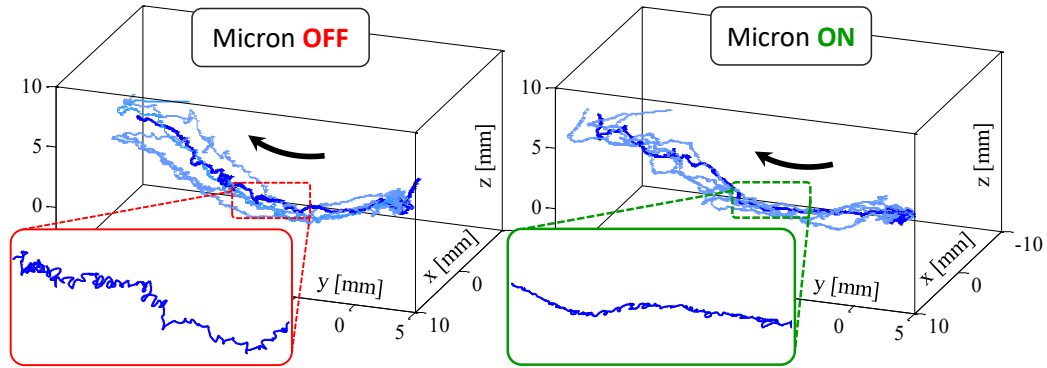


Figure 4.20: Tool tip trajectory during the delaminating period. The arrow indicates the peeling direction. Higher positioning accuracy and smoother paths are observed with Micron use. [102]

The significant reduction in the 2-20 Hz band and percentages comparable to our previous results with Micron [128,129] confirm that there is no adverse effect in tremor suppression characteristics due to the newly-introduced micro-forceps tip module. On the contrary, the forceps allow for grasping—and thus a more rigid connection between the tool tip and membrane—which now enables us to relate the characteristics of the measured forces to the tool tip dynamics. The common power spectral density traits in Fig. 4.21 strongly indicate this connection. Previously, when using the force-sensing hook, such direct comparison did not yield reliable results, especially during trials using the ISM of chick embryos as shown earlier in Fig. 4.17, due to slippage between the tool and the tissue. Furthermore, with the new forceps tip, the user can accomplish the peeling task in a single attempt, whereas a pick instrument could necessitate multiple attempts due to associated challenges in tissue manipulation. This is not only important for ease of use, but also significantly increases safety, since multiple delamination attempts intensify the risk of retinal damage.

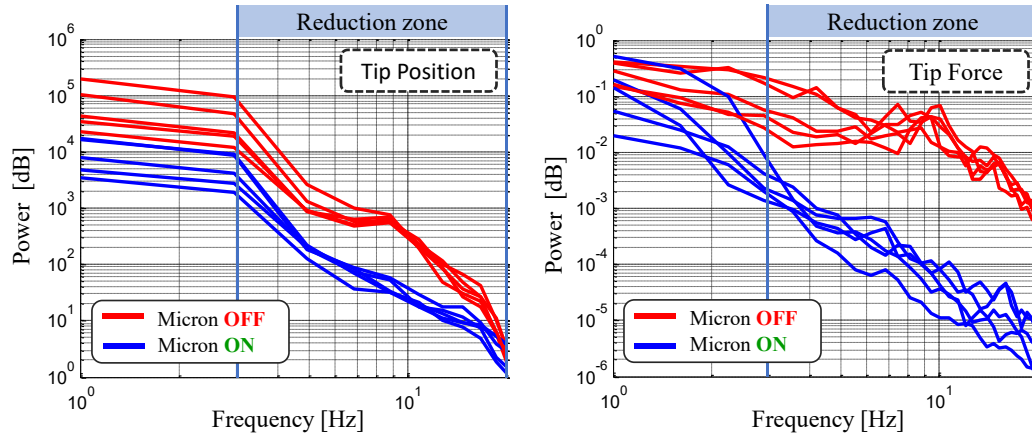


Figure 4.21: Frequency analysis on tip position and peeling forces. Highly correlated spectral density traits due to strong grasping provided by forceps use: a peak at 9 Hz due to physiological hand tremor and a 60-95% reduction in 2-20 Hz oscillations in both tip force and position spectra [102].

4.3 Micro-Vibratory Modulation

4.3.1. Algorithm

Membrane peeling is essentially a two-phase procedure. In the first phase, the surgeon needs to approach the membrane, grasp and lift it to create an edge. For this task, positioning accuracy, and thus tremor suppression is important. The second phase is the delamination of the grasped membrane, where the main concern is limiting the exerted forces on the retina rather than canceling the tremor. Although several micromanipulators were developed for assisting vitreoretinal surgery before, the focus has so far been on suppressing the hand tremor, primarily focusing on the initial phase. For assisting the second phase of this procedure, there are motivating applications in other fields, such as inserting a biopsy needle, where reciprocation of the needle was shown to facilitate the advance of the needle through tissue and penetration of the site of interest [131]. The potential impact of introducing such vibrations while delaminating membranes in vitreoretinal practice is novel.

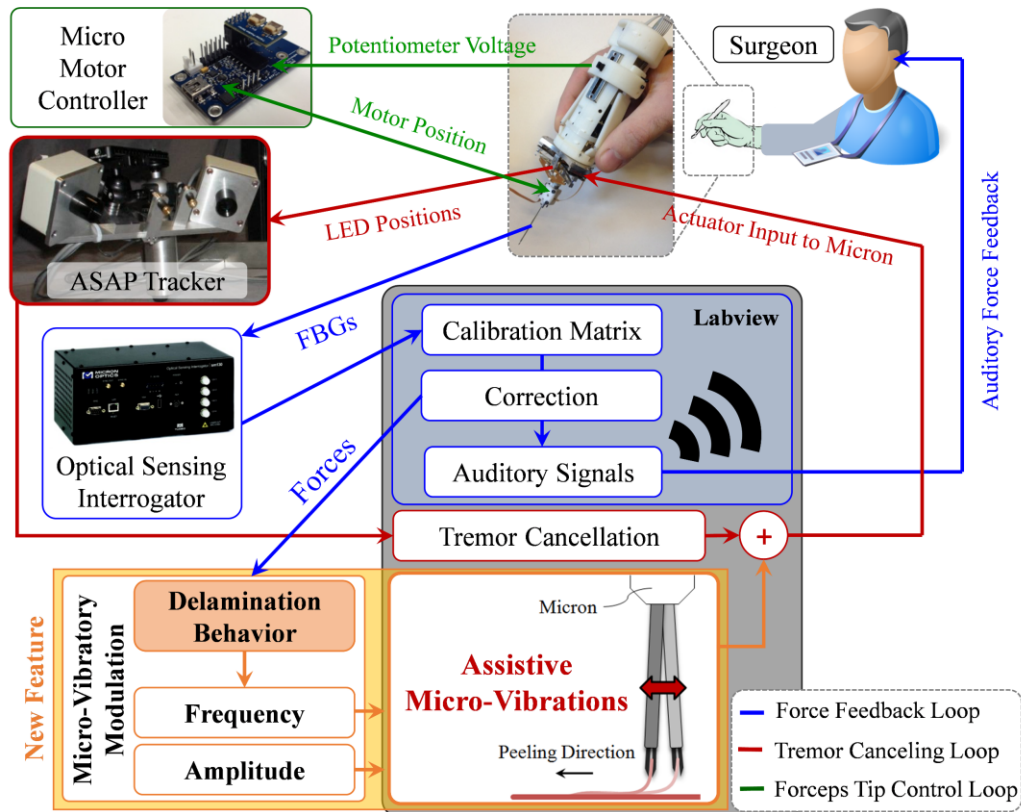


Figure 4.22: System overview. A handheld micromanipulator (Micron) was combined with a force-sensing micro-forceps to assist membrane peeling previously. A novel feature, vibrating the tool tip along the peeling direction, is added to the system to facilitate membrane delamination (shown in orange) [103].

This section aims to develop a system that (1) attenuates hand-tremor when accurate positioning is needed, (2) provides auditory force feedback to the user so that the exerted forces are kept at a safe level, and (3) pulsates the tool tip at high frequency to provide ease in delaminating membranes. An overview of such system based on the Micron system is presented in Fig. 4.22. In modulating the micro-vibrations, deciding on an optimal frequency and amplitude that will reduce the force, and updating the micro-vibration parameters adaptively in response to the changing tissue properties requires the knowledge of each parameter's individual effect on the peeling behavior, which we will investigate through experiments in the remainder of this section.

4.3.2. Experiment 1: Obtaining a faster peel with the same force

4.3.2.1. Setup and Procedure

To simulate membrane peeling, tests were done on two types of phantoms, which have previously been used in this chapter: bandage phantom, and inner shell membrane (ISM) of raw chicken eggs. Bandage phantom provides a very consistent platform, and is easy to obtain enabling ample tests. ISM of raw chicken eggs is a biological tissue exhibiting heterogeneous properties, and thus is a more realistic phantom for membrane peeling trials. However, the number of tests that can be done using ISM is limited since a single egg shell is used for each test.

The goal of the experiments was to observe the effect of controlled vibrations at various frequencies in comparison to freehand and regular tremor cancellation performances. For this reason, the tests were done in 5 sets exploring the following conditions:

(1) Freehand peeling;

(2) Micron-assisted peeling with regular tremor cancellation;

(3,4,5) Micron-assisted peeling with tremor cancellation and controlled vibrations at 10 Hz, 30 Hz, and 50 Hz.

In sets 3 to 5, sinusoidal oscillations at the specified frequency were injected to the commanded forceps tip trajectory to oscillate the tool tip back and forth along the peeling direction. The amplitude of vibrations was kept constant at 100 μm .

For each test condition, 15 trials on the bandage phantom and 5 trials on ISM were completed. The experiments were performed by a non-surgeon user by alternating the sequence of sets initially on bandage phantom, and then on ISM using the setup shown in

Fig. 4.23. In all cases, the user was provided with auditory force feedback, clearly indicating whether the applied forces are close to or beyond the safety threshold (7.5mN). The challenge was to peel the membranous layer off as quickly as possible while maintaining the peeling force below the threshold, and thus adjusting the peeling speed based on the force feedback. By fixing the exerted forces at their maximum allowable level, the corresponding peeling speed was observed to evaluate the ease of peel in each set.

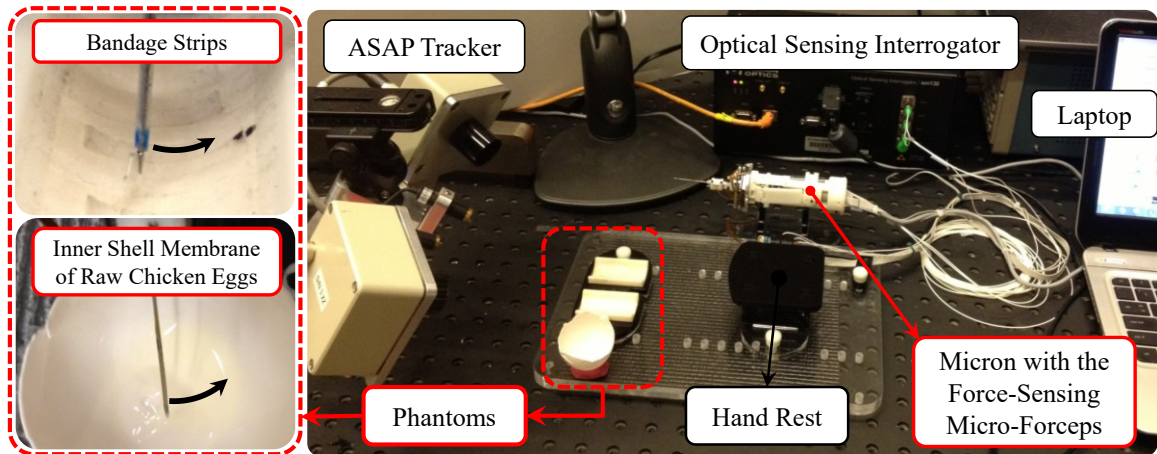


Figure 4.23: Setup for membrane peeling experiments on bandage phantom and inner shell membrane of raw chicken eggs [103].

Before data collection, an extensive training period (~1 hr) was allowed for the subject to become accustomed to the system and phantoms, and to minimize learning curve effects in the recorded measurements. For each peel, the tool tip force and position data was collected. The micro-forceps motor position was also recorded to determine the starting and ending points of the delamination phase in the recorded data. The assessment was based upon the tool tip force and position measurements during this phase. Welch's power spectral density estimate was used to verify tremor canceling and vibration behavior. The mean peeling force and speed from each set were compared using one-way

ANOVA followed by Tukey's HSD (honest significant difference) test separately for each phantom type. Statistical significance was defined as $p < 0.05$.

4.3.2.2. Results and Discussion

4.3.2.2.1. Membrane Peeling on Bandage Phantom

Sample force measurements from each test condition is shown in Fig. 4.24. With the aid of the auditory feedback, in all trials, the subject tried to maintain a mean peeling force of under 7.5 mN while the induced micro-vibrations induced oscillations in the applied force as well at about the same frequency.

To verify the accuracy of performed motion in response to the commanded frequencies, and to check the correlation between the oscillatory tip position and peeling force measurements after the grasping and lifting phase, during membrane delamination (phase II in Fig. 4.24), we performed frequency analyses. Results for 3 sample trials per set are shown in Fig. 4.25. The prominence of a peak around 10 Hz in the plots of freehand trials is primarily due to subject's hand tremor. When the tremor cancellation feature of Micron was activated, this peak was largely attenuated and the high frequency components (2-20 Hz) were overall reduced by 80-90% in both position and force spectra. This confirms that the structural modification done for transforming the micromanipulator into a micro-forceps tool, and thus the added inertia at the tip, does not adversely affect the tremor cancelling functionality of Micron. The effect of adding controlled vibrations on tool tip trajectory is clearly visible as peaks at the specified frequencies (10, 30, and 50 Hz), meaning that the low inertia of the designed micro-forceps module allows resonating the tip at high frequencies accurately within Micron's 1N force capability. The common traits between the tip position and the tip force spectra in all cases indicate a rigid connection

between the tool tip and the bandage layer provided by strong grasping of forceps, even when the tip is resonating at 50 Hz.

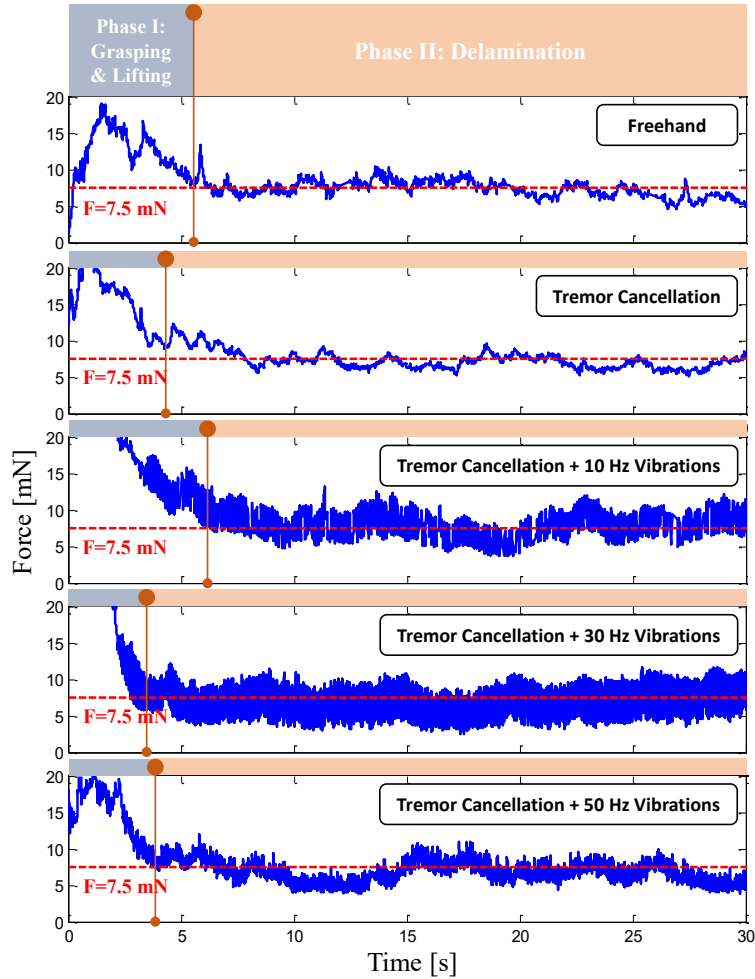


Figure 4.24: Sample force measurements while peeling off bandages with a force-sensing micro-forceps under five different conditions with varying micro-vibration frequency.

The mean peeling force and speed for each set is displayed in Table 4.4. Within each set, consistent results were obtained as indicated by the low standard deviation values due to high repeatability of tests on this type of phantom. In all sets, the mean peeling force was maintained just below the set safety threshold (7.5 mN) while trying to maximize the peeling speed as required. The variance analysis showed no significant difference in peeling forces among the sets, meaning that the bandages were peeled off by exerting

similar forces (around 7 mN) with the help of the auditory force feedback ($p=0.32$). However, there was a statistically significant difference among the mean of peeling speeds ($p<0.05$). Further analysis with Tukey's HSD revealed that the mean peeling speed significantly increased as higher frequency oscillations were introduced on the tool tip trajectory during delamination. The mean peeling speed was 0.1392 mm/s in freehand trials whereas upon pulsating the tip at 10, 30 and 50 Hz, it rose respectively to 0.1789, 0.2232 and 0.2809 mm/s. Thus, tremor cancellation combined with 50 Hz vibrations enabled significantly faster peeling as compared to all other sets ($p<0.05$), and thus provided easier delamination. There was no statistical difference in terms of peeling speed between the freehand trials and the trials with sole tremor cancellation ($p=0.21$).

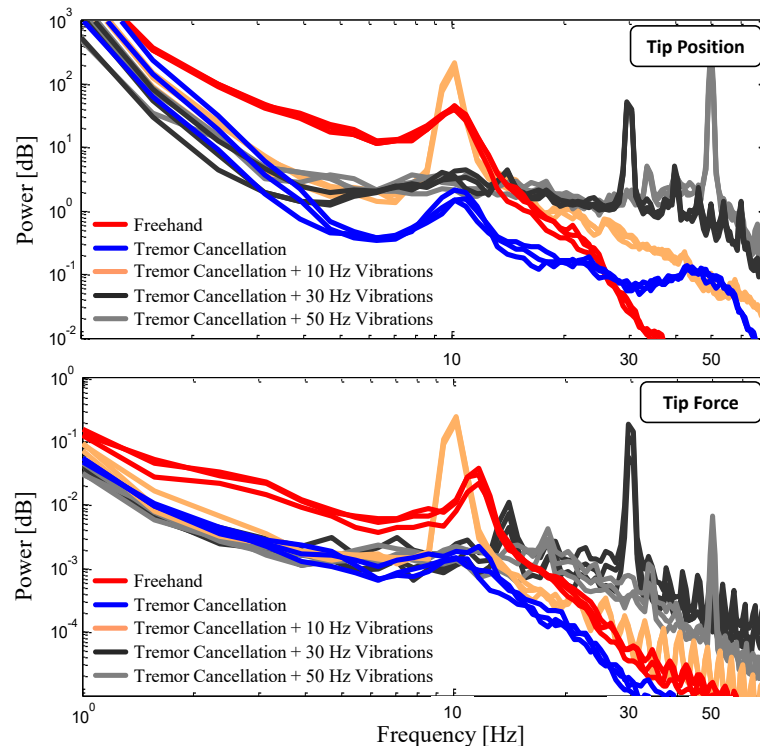


Figure 4.25: Power spectra of tip position and tip forces measured while peeling bandages (3 arbitrary trials per set are shown). Freehand trials exhibit a peak at 10 Hz due to physiological hand tremor. 80-90% reduction in 2-20 Hz oscillations and visible peaks at 10, 30, and 50 Hz at both spectra reveal success in tremor canceling, strong grasping, and accurate fast tip vibrations [103].

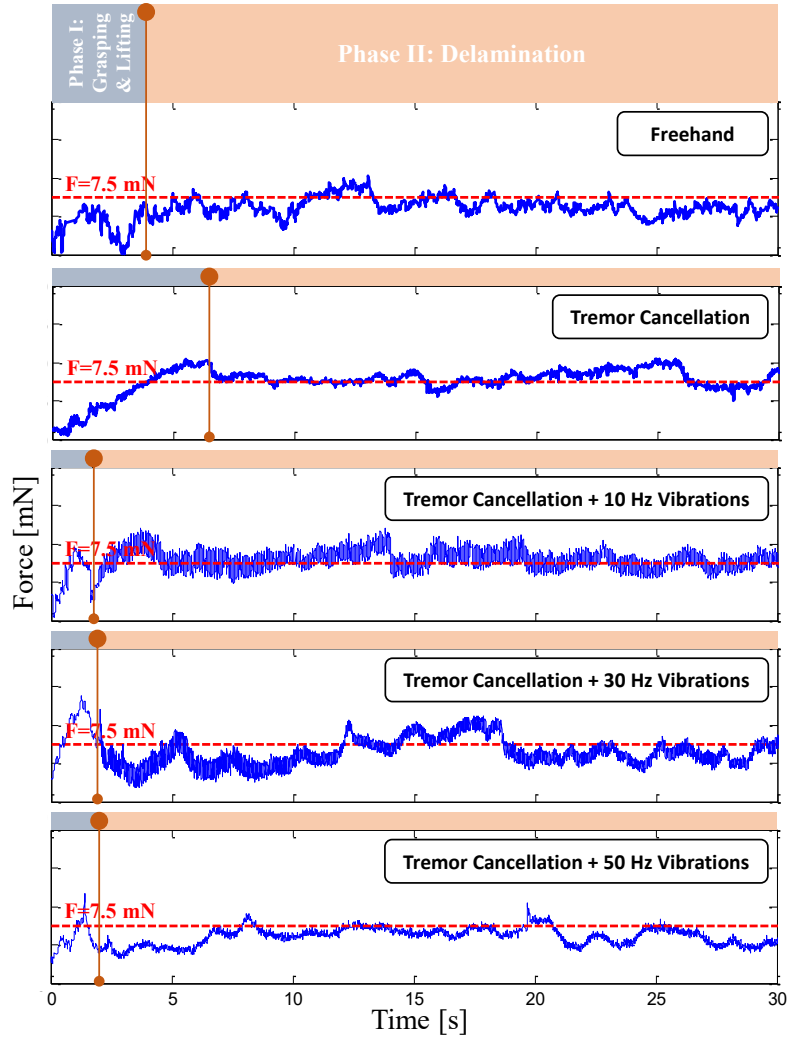


Figure 4.26: Sample force measurements while peeling off the ISM of raw chicken eggs with a force-sensing micro-forceps under five different conditions with varying micro-vibration frequency.

4.3.2.2.2. Membrane Peeling on Raw Chicken Eggs

Peeling experiments on ISM of raw chicken eggs revealed similar force profiles to those obtained for bandages for each test condition. A sample measurement from each set is presented in Fig. 4.26. The Power density spectra for the measurements during the delamination phase is shown for 3 samples per case in Fig. 4.27. Compared with the bandage trials a slightly larger amplitude variation between the sets was observed. The 10 Hz peak due to hand tremor was still clearly visible in freehand trials. By tremor

cancellation, the oscillations in 2-20 Hz band were reduced by 45-90% and 5-85% respectively in the tip position and tip force spectra.

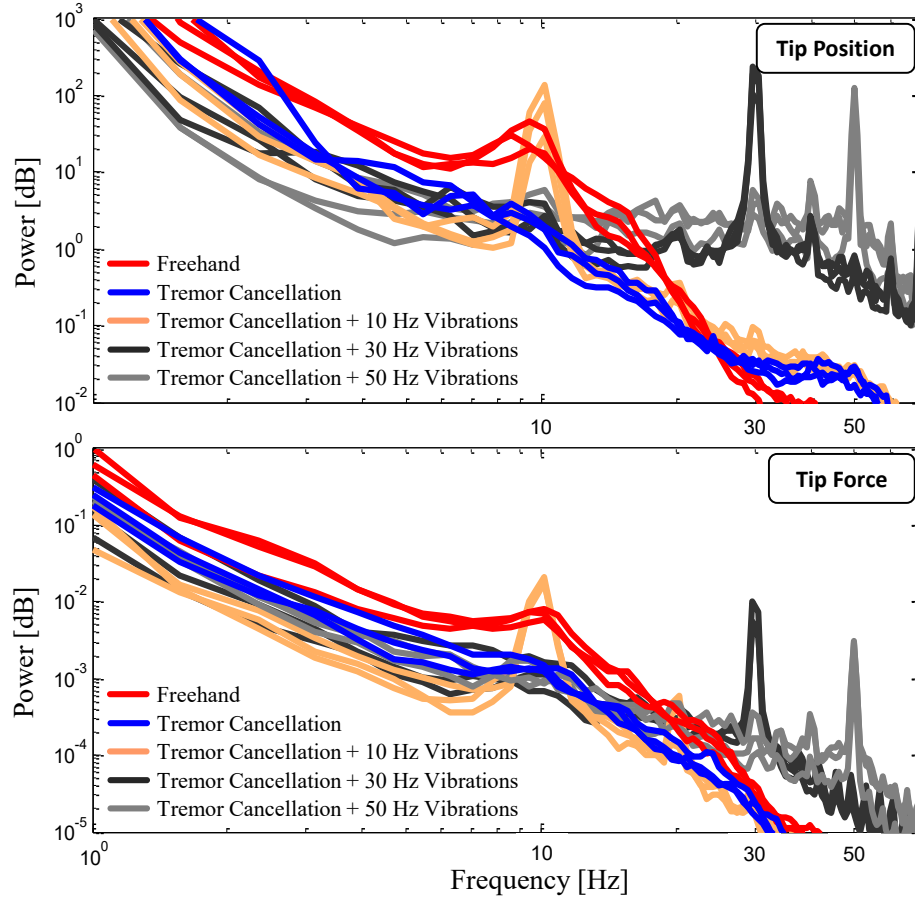


Figure 4.27: Power spectra of tip position and tip forces measured while peeling inner shell membrane of raw chicken eggs (3 arbitrary trials per set are shown). More deviation between trials as compared with bandage phantom, but the main traits were preserved: 45-90% and 5-85% reduction in 2-20 Hz band of tip position and force spectra respectively with tremor cancellation; visible peaks at 10, 30, and 50 Hz at both spectra [103].

The common properties of the position and force spectra, and the prominence of 10, 30, and 50 Hz peaks in the trials using the new "controlled vibrations mode" strongly indicate that our micro-forceps is able to provide a rigid connection between the tool and the membrane being peeled also on this biological tissue, even when resonating the tip at high frequencies. Previously, when using a pick instrument instead of a micro-forceps

tool (in Section 4.2.4), the slippage between the tool and the tissue was causing problems in manipulation of ISM, and such correlation between the tool tip dynamics and tool-to-tissue forces was not possible.

Peeling ISM of chicken eggs requires slightly larger forces than those for the bandage phantom. These forces are in fact a combination of tearing and delaminating forces in contrast to sole delaminating forces involved in bandage peeling. As shown in Table 4.4, in freehand trials, the recorded peeling forces averaged approximately 7.7 mN, which is slightly above the set threshold (7.5 mN). The corresponding mean peeling speed though is very slow (0.0868 mm/s). In these freehand trials, the user tried to stay below 7.5 mN threshold by peeling the membrane as slow as he could. This was however limited by the unintentional tool motion due to hand tremor. In addition, being a biological tissue, ISM exhibits slight variations in tissue properties within the same layer as well as between the eggs. Using ISM, it is harder to adjust peeling forces, since the exerted forces are not only related to tool tip speed, but also depend on local tissue properties. This behavior more closely simulates the real vitreoretinal practice. Due to these variations, the standard deviations in all sets were higher than those for the bandages.

The ANOVA analysis revealed that the difference in the mean peeling force among groups is not statistically significant ($p=0.47$). However, similar to the results for bandages, the tested cases significantly differ in terms of average peeling speed ($p<0.05$). Based on Tukey's HSD, controlled micro-vibrations of the tool tip provided ease in peeling, enabling faster delamination at the same force level. The mean peeling speed was 0.0868 mm/s in freehand trials whereas upon pulsating the tip at 10, 30, and 50 Hz, it

rose respectively to 0.1416, 0.1850, and 0.2948 mm/s. The difference between freehand trials and trials with sole tremor cancellation was not statistically significant ($p=0.20$).

Table 4.4: Evaluation of bandage and ISM peeling cases based on the average peeling force and speed measured during each trial.

	Experiments	Number of Trials	Peeling Forces [mN]			Peeling Speed [mm/s]		
			Mean	Std. Dev.	Median	Mean	Std. Dev.	Median
Bandages	Freehand	15	6.86	0.37	6.88	0.14	0.02	0.14
	Tremor Cancellation	15	6.78	0.29	6.79	0.15	0.02	0.15
	Tremor Cancellation + 10Hz Vibrations	15	7.05	0.35	7.02	0.18	0.02	0.18
	Tremor Cancellation + 30Hz Vibrations	15	6.94	0.32	6.86	0.22	0.05	0.21
	Tremor Cancellation + 50Hz Vibrations	15	6.92	0.44	6.97	0.28	0.06	0.27
Eggs	Freehand	5	7.71	0.70	7.91	0.09	0.02	0.08
	Tremor Cancellation	5	7.31	1.26	6.79	0.10	0.03	0.10
	Tremor Cancellation + 10Hz Vibrations	5	7.29	0.98	7.14	0.14	0.06	0.13
	Tremor Cancellation + 30Hz Vibrations	5	6.96	1.52	6.81	0.18	0.03	0.17
	Tremor Cancellation + 50Hz Vibrations	5	6.34	1.35	6.57	0.29	0.06	0.26

4.3.3. Experiment 2: Obtaining reduced forces at the same peeling rate

4.3.3.1. Setup

There are various factors affecting the forces in membrane peeling. Some of these pertain to tissue properties, such as tissue width and thickness, while some are related to the motion of the peeling instrument, such as the peeling speed. In order to isolate the influence of micro-vibrations, all other factors affecting the peeling force need to be eliminated in a very reproducible experimental setup. Using a handheld micromanipulator, it is hard to keep the peeling speed constant. To avoid peeling speed alterations during and between trials, we fixed the Micron handle to a clamp, and used a linear stage to drive phantoms relative to Micron (Fig. 4.28). The micro-forceps module was attached onto Micron for grasping the phantom before peeling. This setup is only for identifying the effect of microvibrations in membrane delamination. The practical use of our system will

eventually work based on this identified behavior, but will be handheld (not with a linear stage).

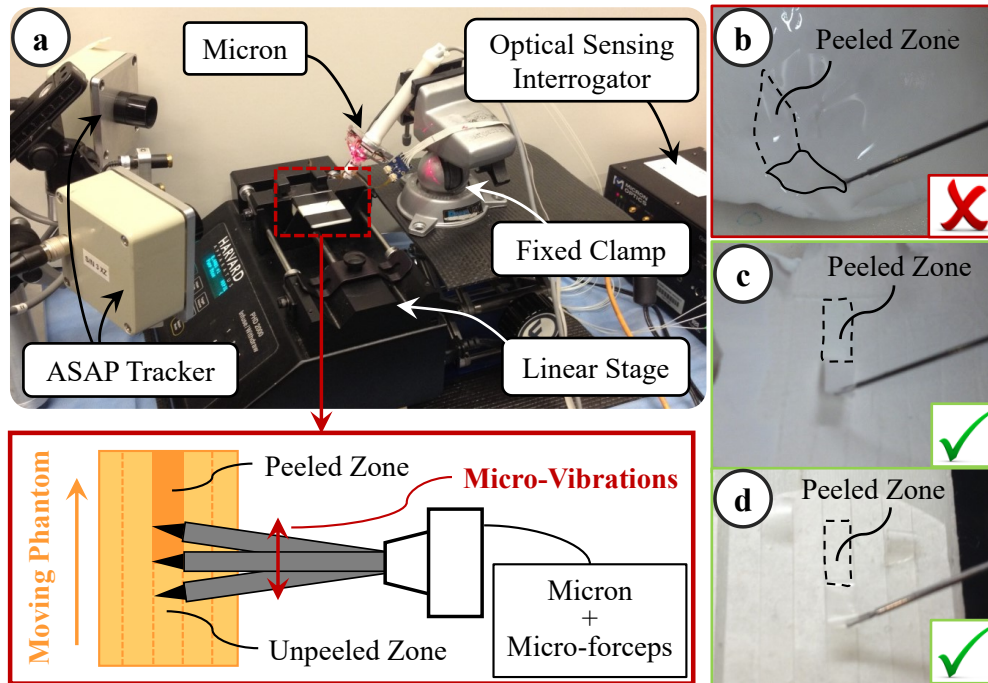


Figure 4.28: Experimental setup: (a) To ensure constant peeling speed, the phantoms were moved on a linear stage. (b) Peeling inner shell membrane of raw eggs produces triangular shaped strips, and requires both tearing and delaminating forces. Using sliced egg shell membranes (c) and bandages (d), the effect of tearing forces and varying membrane width throughout delamination were avoided [104].

To simulate epiretinal membrane, inner shell membrane (ISM) of raw chicken eggs can normally be used. However, in this phantom, the membrane routinely comes off the egg shell creating a non-uniform triangular piece of membrane if a linear peeling trajectory is followed (Fig. 4.31.b). The varying width of the peeled tissue significantly affects the forces, and the dimensions of this wedge shape varies between the phantoms. To peel consistent and constant width membrane strips, a helical trajectory needs to be followed as in [132]. However, such dexterous motion is not possible using a linear stage. Furthermore, while peeling the ISM, the measured forces stem from two main sources: (1) the tearing force between the peeled section and the surrounding membrane; (2) the

delaminating force due to the adhesion between the peeled section and the underlying shell. Of these components—for purposes of epiretinal and/or internal limiting membrane peeling—we believe the delaminating force is more critical, and needs to be reduced/limited as it is the force that is directly applied onto the delicate retinal surface. In order (1) to eliminate the tearing forces and focus purely on the delaminating forces, and (2) to fix the width of the peeled layers for consistency between trials, we used two different phantoms: sliced bandages and sliced shell membranes of raw chicken eggs.

The bandage phantom provides a consistent platform that enables ample testing with the same peeling behavior. Repeated peeling tests using a single bandage strip on the setup shown in Fig. 4.28.a revealed that the adhesion between the bandage strip and its backing decays with each peel initially (Fig. 4.29.a). However, after approximately the 10th peel, the bandage sticks back on consistently, requiring similar amount of delamination force for a prolonged time. This enables the use of each strip numerous times by brushing it back in place with its consistent level of adhesion after each peel, and provides a very repeatable platform for conducting multiple tests.

The membrane inside the raw chicken egg shell was sliced similarly using a razor (Fig. 4.28.c). Both the inner and the adherent outer shell membranes are cut together. Thus, while peeling the cut strips, both membranes need to be delaminated off the egg shell surface, which requires a larger force as compared to the removal of ISM alone. In contrast to the bandage phantom, each membrane strip can be used only once, limiting the total number of tests on this phantom. Yet, assuming that the membrane structure does not vary significantly between the eggs, this phantom provides a consistent platform for studying the effect of micro-vibrations on peeling biological tissue.

4.3.3.2. Procedure

Peeling tests on the bandage phantom were done in 2 sets, each set having a different speed setting (0.15 mm/s and 0.3 mm/s). In each set, a total of 10 operational modes were examined. In the first mode, delaminating forces during regular peeling were monitored. The remaining modes explored the effect of micro-vibrations at 3 frequencies (10, 30 and 50 Hz) and 3 amplitudes (50, 100 and 150 μm). 15 trials per mode were completed using a single bandage strip for each speed setting. Each bandage was peeled and brushed back 10 times before starting the trials, so that the adhesion between the bandage and its backing remained consistent throughout the experiments (Fig. 4.29.a). For the egg trials, the experimental conditions were limited to 1 speed setting (0.15 mm/s), 2 frequencies (30 and 50 Hz) and 2 amplitudes (100 and 150 μm). Ten shell membrane strips were peeled for each setting, and each strip was used only once.

The experiments were conducted by alternating the order of experimental modes. Each strip was peeled continuously for a 60 second period. The measured tool tip force was acquired at 1 kHz. The recorded force profile was segmented into two phases based on the recorded video as shown on the sample recordings in Fig. 4.29.b: (1) grasping and lifting of the membrane edge, (2) delamination of the membrane. For each mode of operation, the average and maximum peeling force (F_{average} and F_{peak}) during the delamination (second) phase were analyzed using one-way analysis of variance (ANOVA) followed by a t-test assuming unequal variance. Statistical significance was defined as $p < 0.05$.

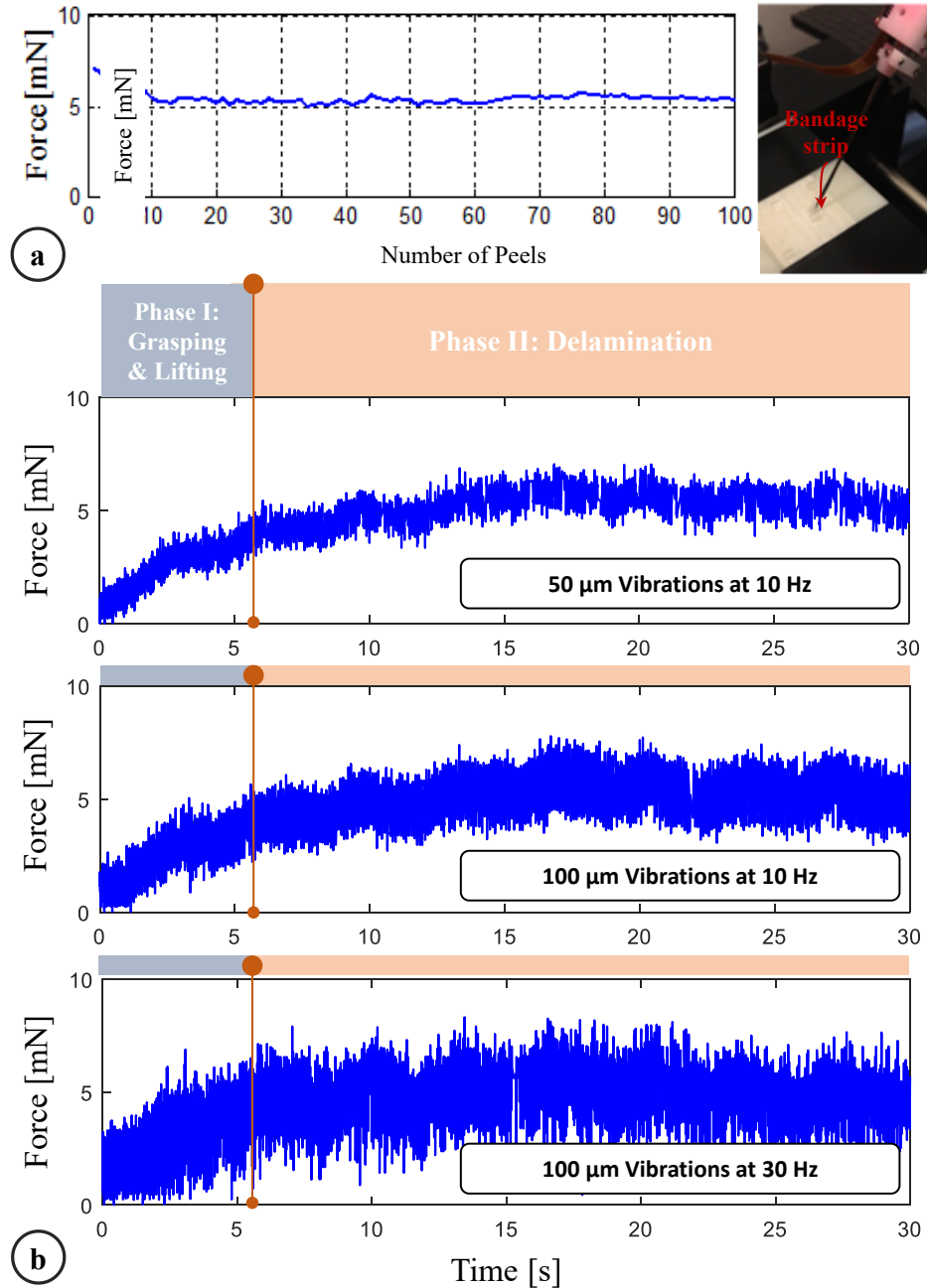


Figure 4.29: (a) A single bandage strip was peeled at constant speed (0.15 mm/s) and brushed back on several times. The required delamination force leveled off after approximately the 10th peel. (b) Sample recordings for 3 different micro-vibratory settings: Increasing the micro-vibration amplitude causes larger oscillations in force, the micro-vibration frequency correlates with the frequency of oscillations in the peeling force.

4.3.3.3. Results and Discussion

4.3.3.3.1. Frequency of Micro-Vibrations

The variation of delaminating forces with respect to micro-vibration frequency is shown in Table 4.5 and Fig. 4.30.a for both phantoms. For F_{average} , no statistically significant difference was identified between the different frequency settings with a 50 μm amplitude ($p=0.62$). F_{average} remained around 5mN and 8 mN respectively for 0.15 mm/s and 0.30 mm/s speed settings regardless of the induced micro-vibrations. However, at larger amplitudes (100 and 150 μm), the change in force was significant. In the slower speed setting, F_{average} was minimized at 30 Hz to 4.80 mN and 4.64 mN respectively for 100 μm and 150 μm vibrations ($p<0.05$). Doubling the speed changed this profile to a monotonically decreasing curve for 100 μm vibrations, but a similar concave trend with a minimum (7.19 mN) at 30 Hz appeared for 150 μm vibrations ($p<0.05$). F_{average} for shell membranes (20.2 mN) was much larger as compared to bandages (5.02 mN). Introducing micro-vibrations with increasing frequency gradually decreased this force, down to 9.02 mN at 50 Hz. The drop was statistically significant for all settings ($p<0.05$) except for 30 Hz vibrations at 100 μm ($p=0.24$). The change in F_{average} combined with the amplitude of force fluctuations due to induced vibrations affected F_{peak} as well. Peeling bandages with 10 Hz vibrations resulted in a reduced F_{peak} for the slower speed setting. Though for the faster peeling case, only 10 Hz and 50 μm vibrations produced this result. In most cases—excluding the slower peeling tests with 150 μm vibrations— F_{peak} gradually rose as the frequency was increased ($p<0.05$).

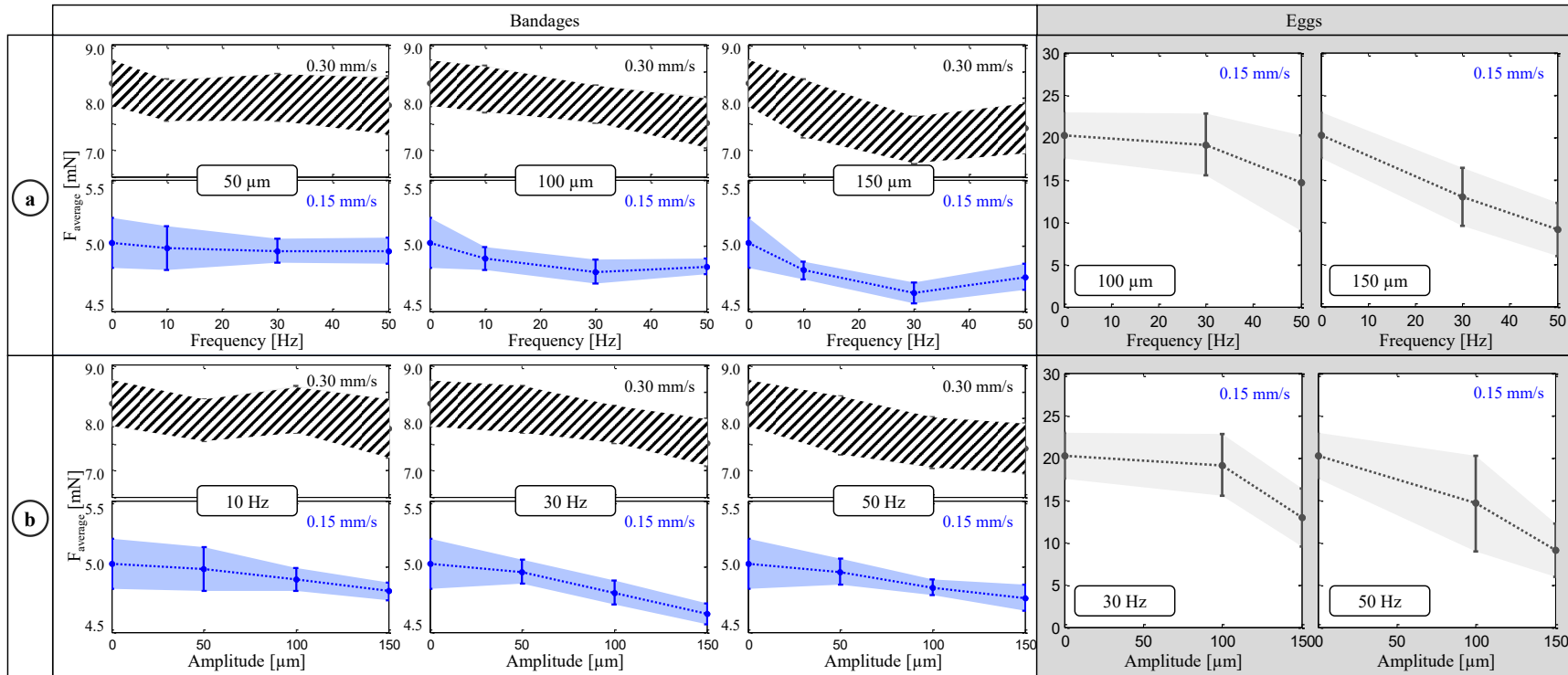
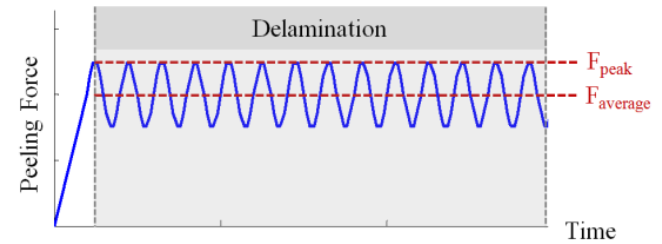


Figure 4.30: Variation of average peeling force (F_{average}) with respect to the (a) frequency and (b) amplitude of micro-vibrations. Dotted lines represent the mean, and the shaded region is ± 1 standard deviation. Inducing micro-vibrations at an "optimal" frequency among the tested cases—at 30 Hz for bandages, and at 50 Hz for the egg shell membranes within the tested frequency interval—minimized F_{average} . The force-frequency trend varied depending upon the peeling speed (0.15 mm/s in blue vs. 0.30 mm/s in striped grey) as seen from bandage peeling with 100 μm vibrations. Increasing the amplitude of micro-vibrations lowered F_{average} in most cases, except for bandage peeling with 50 and 100 μm vibrations at 10 Hz.

Table 4.5: Mean and standard deviation of the measured average and peak peeling force for each micro-vibration setting.

	Number of Trials	Amplitude	Peeling Speed = 0.15 mm/s				Peeling Speed = 0.30 mm/s				
			$f = 0 \text{ Hz}$	$f = 10 \text{ Hz}$	$f = 30 \text{ Hz}$	$f = 50 \text{ Hz}$	$f = 0 \text{ Hz}$	$f = 10 \text{ Hz}$	$f = 30 \text{ Hz}$	$f = 50 \text{ Hz}$	
Bandages	15	50 μm	F_{average} [mN]	4.98 \pm 0.17	4.96 \pm 0.09	4.96 \pm 0.10	7.96 \pm 0.40	8.01 \pm 0.44	7.86 \pm 0.56		
	15	100 μm		5.02 \pm 0.19	4.90 \pm 0.09	4.80 \pm 0.09	4.84 \pm 0.06	8.28 \pm 0.44	8.17 \pm 0.44	7.88 \pm 0.35	7.53 \pm 0.48
	15	150 μm		4.81 \pm 0.07	4.64 \pm 0.08	4.76 \pm 0.10	7.80 \pm 0.55	7.19 \pm 0.45	7.42 \pm 0.47		
	15	50 μm	F_{peak} [mN]	6.07 \pm 0.15	6.13 \pm 0.21	6.25 \pm 0.25	10.57 \pm 1.46	11.53 \pm 1.69	12.04 \pm 1.51		
	15	100 μm		6.32 \pm 0.28	6.05 \pm 0.14	7.00 \pm 0.26	7.91 \pm 0.39	10.86 \pm 1.61	11.48 \pm 1.62	14.30 \pm 1.93	15.17 \pm 2.26
	15	150 μm		6.24 \pm 0.30	8.12 \pm 0.34	8.09 \pm 0.42	11.49 \pm 1.19	14.92 \pm 2.05	17.98 \pm 3.06		
Eggs	10	100 μm	F_{average} [mN]	20.24 \pm 2.75	—	19.14 \pm 3.64	14.58 \pm 5.65				
	10	150 μm		—	12.92 \pm 3.39	9.02 \pm 3.16					
	10	100 μm	F_{peak} [mN]	25.07 \pm 3.47	—	28.46 \pm 5.04	27.06 \pm 7.72				
	10	150 μm		—	23.92 \pm 4.01	22.91 \pm 4.88					



4.3.3.3.2. Amplitude of Micro-Vibrations

The effect of vibration amplitude on F_{average} is shown in Fig. 4.30.b. On bandages, introducing 50 and 100 μm vibrations did not change F_{average} significantly at 10 Hz ($p=0.13$). However, when keeping the frequency at 10 Hz, and increasing the amplitude to 150 μm , the force for both speed settings was lowered ($p<0.05$). At 30 Hz and 50 Hz, a common trend was observed in both bandages and eggs: F_{average} monotonically decreased with larger amplitude. This decay was more significant in shell membrane and faster (0.30 mm/s) bandage peeling trials. Despite the inverse relation between the vibration amplitude and F_{average} , the cost of using larger vibrations is increased force fluctuation, which may in fact result in larger F_{peak} (Table 4.5). This trend can clearly be seen in slower (0.15 mm/s) bandage peeling trials (Fig. 4.31). At 10 Hz trials, no significant change in F_{peak} can be observed since the reduction in F_{average} was greater than the amount of force fluctuation even for 150 μm oscillations. However, at 30 and 50 Hz, as the vibration amplitude is increased, the drop in F_{average} fails to compensate for the resulting force fluctuation, producing a larger F_{peak} . This implies that the amplitude of micro-

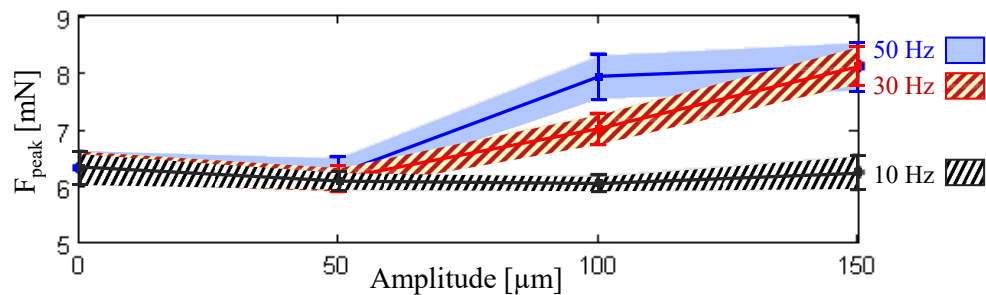


Figure 4.31: Variation of maximum peeling force (F_{peak}) with respect to micro-vibration amplitude at different frequencies while peeling bandages with 0.15 mm/s speed. Solid lines represent the mean, and the shaded region is ± 1 standard deviation. Above 10 Hz, the peak force increased with greater micro-vibration amplitude due to larger fluctuations in force.

vibrations cannot simply be maximized to reduce F_{average} , but rather requires careful tuning to produce a smaller F_{average} while keeping F_{peak} below dangerous levels.

4.4 Automatic Tissue Release

Motorized and sensitized architecture of the micro-forceps enables control of the grasping action based on the detected peeling forces. This functionality can be used as a safety precaution to automatically release the grasped tissue in case the detected tool-tissue interaction forces reach a critical level to effectively prevent deleterious force transfer to the delicate anatomy, and prevent retinal injuries during vitreoretinal procedures.

The motorized grasping action can normally be controlled via a touch sensor or a linear potentiometer located on the robotic or manual tool handle: the distance between the grasper tips are linearly proportional to the sensed pressure by the touch sensor, and the proportionality constant can be adjusted to accommodate user's comfort as shown earlier in Section 3.2.1.3. In a peeling procedure, using a micro-forceps tool rather than a hook provides a firm grasp of the membrane for a more controlled manipulation without slippage. However, this also leads to a more rigid tool-tissue coupling and hence a direct correlation between tool tip motion and the exerted forces on the retina. In addition, the adhesion between the membrane and the retina can vary locally. Adapting to the nonuniform tissue properties throughout the peeling process and maintaining the applied forces below injurious levels is not trivial. In case rapidly increasing forces are detected at a critical level, opening the forceps and releasing the grasped membrane can be an effective and simple solution to prevent direct transfer of excessive forces and hence damage to the retina. For proper operation, though, the knowledge of critical force levels

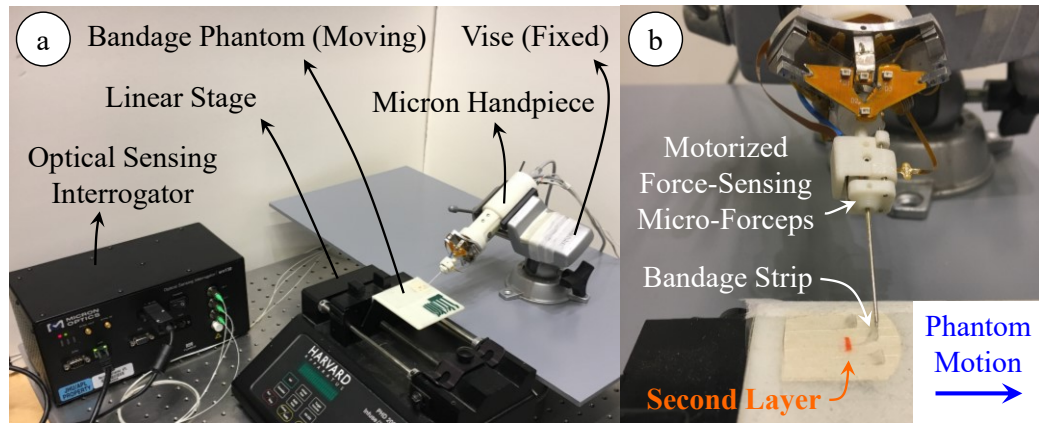


Figure 4.32: Experimental setup for testing the automatic tissue release feature. (a) Micron with the motorized force-sensing micro-forceps was held fixed in a vise while the phantom platform with attached bandages was mounted on a linear stage. (b) A bandage strip on the phantom was grasped using the micro-forceps, and the phantom was driven relative to the tool by actuating the linear stage to perform the peel at constant speed. To simulate nonuniform tissue properties, a second layer (shown in orange) was attached onto the bandage strip after about the 5th mm.

causing retinal injuries is needed, which has not been studied in human eyes yet, mainly due to the lack of force-sensitive functional instruments in vitreoretinal practice until this time. Earlier experiments using animal models reported that retinal injuries (hyaloid detachment and retinal tear) are associated with forces beyond 7.5 mN [29]. Taking this as a reference, we programmed our micro-forceps to automatically open and release the grasped tissue if the detected tissue manipulation forces reach 7.5 mN.

We tested our automatic tissue release feature by peeling a nonuniform bandage strip using our motorized force-sensing micro-forceps from Section 3.2.1. In the setup shown in Fig. 4.32.a, the force-sensing tool is attached to the Micron, and Micron is held stationary clamped in a vise. The bandage phantom is placed on a linear stage to be driven relative to the micro-forceps at a fixed speed. In our experiments, we adjusted the speed of the linear stage to have a peeling rate of 0.15 mm/s, which is within the range encountered in an actual ERM peeling procedure. The total length of the bandage strip

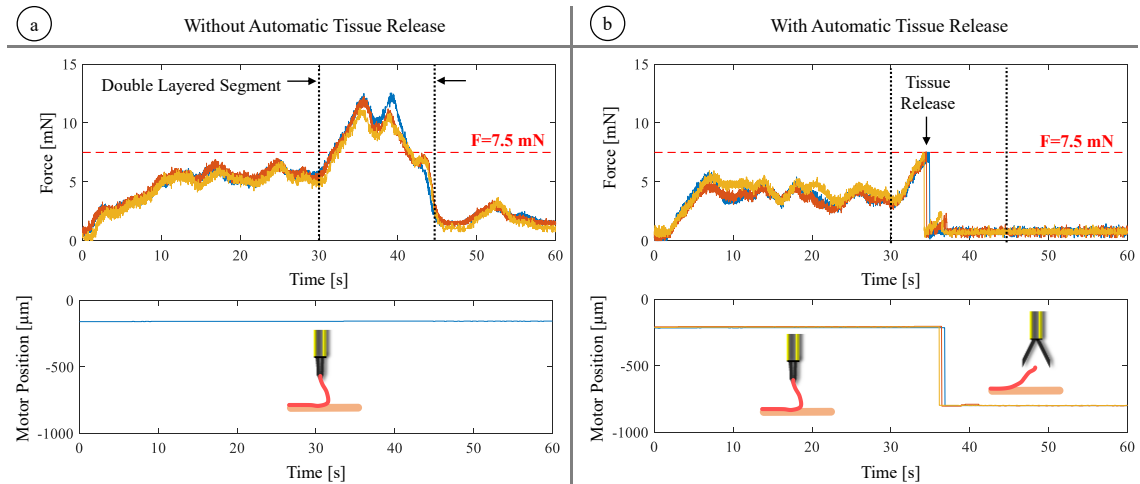


Figure 4.33: Sensed forces while peeling off a bandage strip at a constant rate (a) without and (b) with the automatic tissue release feature. With the automatic tissue release, after reaching the double layered segment of the phantom, when the force reaches a critical level (dashed red line at 7.5 mN), the forceps jaws are quickly opened (motor position=800 μm) to release the tissue and prevent excessive forces.

was approximately 9 mm taking around 60 seconds per peel. However, to introduce inhomogeneity to peeling properties, after about the 5th mm, an extra second layer (about 2.5 mm long, marked in orange in Fig. 4.32.b) was attached onto the bandage strip, leading to a local change in peeling behavior and emulating a stickier region in case of a real ERM peeling. Experiments were performed in 2 sets, each set consisting of 3 trials, the first set using the default force-sensing mode and the second set using the automatic tissue release mode of our micro-forceps. Results in Fig. 4.33 show that all 3 trials in each set output similar performance, indicating a high repeatability of the experiment. Without the auto-release feature, the detected forces rapidly increase and go beyond the safe level right after reaching the double layered portion of the phantom. When the automatic tissue release mode is used, as soon as the force reaches the critical value (7.5 mN), the jaws are opened by quickly retracting the forceps motor and releasing the

bandage. The peel could not be completed in a single grasp in this case, but the transfer of forces beyond the safety threshold has been successfully avoided.

The automatic tissue release mode, may increase the overall operation time, as the operator will need to approach the membrane to grasp it again and attempt to peel slower each time the tissue is released. Nevertheless, this will ensure the completion of the peel without any forces beyond the set safety threshold. Figs. 4.34.a and 4.34.b demonstrate the results from two peeling tests on the same bandage phantom, with and without the automatic release feature, respectively. Different from the previous trials, in this experiment, the phantom was maintained fixed while the micro-forceps tool was moved by hand to approach, grasp and peel off the bandage. During the first trial, the user was provided with auditory feedback to help maintain the forces below 7.5 mN manually as detailed in Section 4.2. Despite the effort, forces exceeding 7.5 mN still appear in Fig. 4.34.a. When the automatic release feature was used, the forceps let go of the bandage as soon as the applied force reached 7.5 mN threshold, which happened 8 times in total, mostly while peeling off the double layered sticky segment of the phantom. After each release, the bandage had to be grasped again to continue the peel. This caused a slight delay, leading to a task completion of 141.96 seconds in comparison to 106.30 seconds with the default auditory force feedback mode. However, the applied forces were successfully maintained below the safety threshold, 7.5 mN, throughout the peel as shown in Fig. 4.34.b.

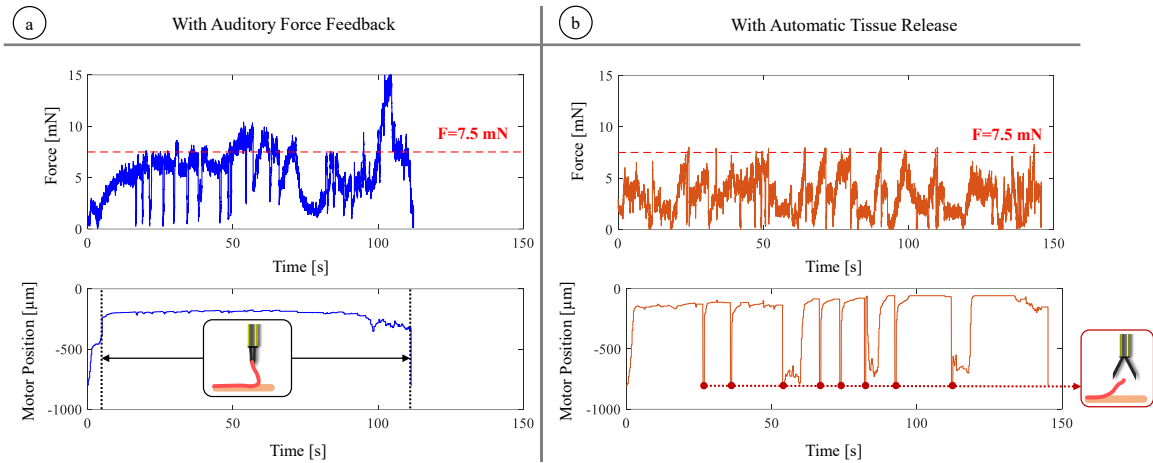


Figure 4.34: Forces measured while peeling the bandage (a) with auditory force feedback and (b) with the automatic tissue release feature. With the auditory feedback, it's challenging to adapt to the changing phantom properties and peel off the double-layered segment of the bandage while keeping the applied force below the safety threshold (dashed red line at 7.5 mN). The automatic tissue release mode prevents forces above the threshold, but may lead to longer task completion time since the tissue may need to be regrasped multiple times. In this sample trial, 8 releases were recorded during the peel, which are marked as red dots (micro-forceps' motor position = 800 μm).

4.5 Conclusion

This chapter reported the use of force-sensing tools integrated with two distinct robotic platforms, Micron and the Steady-Hand Eye Robot, under various assistance modes to limit applied forces during membrane peeling. First contribution of this chapter is the implementation and evaluation of an auditory force feedback mechanism, where the measured forces were mapped into audio signals to inform the operators, and let them adjust their maneuvers and the peeling rate to keep the peeling forces at a safe level. When combined with the tremor canceling feature of the robotic platforms, and therefore improved precision and control in tool tip motion, experiments using phantoms (bandage phantom and ISM of chicken embryo) showed that forces could be maintained mostly below a predefined danger level. A performance comparison study between Micron and the Steady-Hand Eye Robot with force-sensing tools was performed, where systems

provided similar tremor reduction and force limiting success. Use of micro-forceps on either robotic platform provided a more controlled manipulation of the tissue with a firm grasp and therefore less slippage, which led to a stronger correlation between tool tip velocity and applied forcing. The results of our single-user studies in this chapter are encouraging and provide the basis for a multi-user study in order to assess the influence of various system parameters, and inspect the existence of optimal values for different tasks. Performance analyses with both surgeon and non-surgeon users can provide a more extensive comparison between the two systems also accounting for ergonomics, feasibility, workflow, and the learning curves.

The second contribution of this chapter is a micro-vibratory modulation method which makes use of the firm grasping capability of micro-forceps. Through experiments on different types of membranes (bandages and ISM of chicken eggs), it was shown that vibrating the tool tip along the peeling trajectory could facilitate membrane delamination at a material dependent optimal frequency and amplitude, and reduce the mean peeling force. The interaction between the main parameters that influence membrane peeling forces: membrane properties, peeling speed, micro-vibration amplitude and frequency were described in this chapter, however the viscoelastic mechanisms behind these findings have yet to be fully explored. Based upon the identified behavior, an adaptive control scheme can be implemented for optimal selection and real-time update of the micro-vibration parameters to minimize delamination forces. Before this method can be proposed as a clinically feasible assistance option, the effect of micro-vibrations on underlying retinal tissues also needs to be critically examined via experiments on live tissues and in animal models.

The third contribution of this chapter is an automatic tissue release mode that demonstrates a potential benefit of motorizing and sensitizing the micro-forceps. Experiments have demonstrated that automatically opening the jaws (when the sensed forces reach a certain level) and quickly releasing the tissue can effectively keep the forces below a predefined threshold. Although it will require multiple grasp attempts to catch the membrane edge and complete the peel, which may increase the overall operation time, the automatic tissue release feature may be beneficial especially in case of highly nonuniform adhesion properties (and sudden variations) across the membrane, where the operator is challenged by dynamically adjusting the peel rate. Yet, the method's feasibility needs to be assessed through peeling experiments using inhomogeneous phantoms and biological membranes.

Publications

1. **B. Gonenc** and I. Iordachita, "Safe Tissue Manipulation in Retinal Microsurgery via Motorized Instruments with Force Sensing," *IEEE SENSORS 2017* – submitted.
2. A. Gupta, S. Singh, **B. Gonenc**, M. Kobilarov, and I. Iordachita, "Toward Sclera-Force-Based Robotic Assistance for Safe Micromanipulation in Vitreoretinal Surgery," *IEEE SENSORS 2017* – submitted.
3. **B. Gonenc**, P. Gehlbach, R.H. Taylor, and I. Iordachita, "Effects of Micro-Vibratory Modulation during Robot-Assisted Membrane Peeling," *IEEE/RSJ Int. Conf. on Intelligent Robots and Systems (IROS'15)*, 2015, pp. 3811-3816.
4. A. Gupta, **B. Gonenc**, M. Balicki, K. Olds, J. Handa, P. Gehlbach, R.H. Taylor, and I. Iordachita, "Human Eye Phantom for Developing Computer and Robot-Assisted Epiretinal Membrane Peeling," *Int. Conf. of the IEEE EMBS (EMBC'14)*, 2014, pp. 6864-6867.
5. **B. Gonenc**, P. Gehlbach, J. Handa, R.H. Taylor, and I. Iordachita, "Motorized Force-Sensing Micro-Forceps with Tremor Cancelling and Controlled Micro-Vibrations for Easier Membrane Peeling," *IEEE RAS EMBS Int. Conf. Biomed. Robot. Biomechatron. (BioRob'14)*, 2014, pp. 244-251.
6. **B. Gonenc**, J. Handa, P. Gehlbach, R.H. Taylor, and I. Iordachita, "A Comparative Study for Robot Assisted Vitreoretinal Surgery: Micron vs. the Steady-Hand Robot," *IEEE Int. Conf. on Robotics and Automation (ICRA'13)*, 2013, pp. 4832-4837.

7. **B. Gonenc**, M. Balicki, J. Handa, P. Gehlbach, C.N. Riviere, R.H. Taylor, and I. Iordachita, "Preliminary Evaluation of a Micro-Force Sensing Handheld Robot for Vitreoretinal Surgery," *IEEE/RSJ Int. Conf. on Intelligent Robots and Systems (IROS'12)*, 2012, pp. 4125-4130.

CHAPTER 5 : FORCE-BASED ROBOTIC ASSISTANCE METHODS FOR RETINAL VEIN CANNULATION

5.1 Introduction

5.1.1. Background and Motivation

Retinal vein cannulation is a demanding procedure proposed to treat retinal vein occlusion by direct therapeutic agent delivery methods. After the cannula is brought onto the occluded vein, it is pushed against the vein wall to pierce through. During this phase of the procedure, identifying the moment of venous puncture is critical to stop needle penetration in a timely manner – right after piercing through the superficial vessel wall and before piercing through the inferior vessel – to avoid double puncturing the vein. In addition, after the cannula is placed inside the vein, any unintentional movement, not only the higher frequency tremulous components but also the lower frequency drift in tool position, needs to be counteracted to maintain the cannula in place for a longer period with minimal trauma to the vasculature until the infusion is completed.

The physiological hand tremor of the vitreoretinal surgeon, which is comparable in amplitude to the size of retinal veins, it is hard to accurately aim especially the thin branch retinal veins, and to maintain the cannula within the lumen after piercing the vein throughout the infusion time. In addition, in contrast to conventional venipuncture, the forces in cannulating retinal veins are associated with much smaller forces, which makes the event of puncture almost imperceptible to the operator. Challenges in identifying the moment of venous puncture, achieving cannulation and maintaining cannulation during drug delivery currently limit the feasibility of the procedure. In this chapter, we respond to these problems with assistive systems combining robotic manipulators, either Micron or

the Steady-Hand Eye Robot, with a force-sensing microneedle. The aim is to precisely detect the moment of venous puncture and maintain the cannula securely inside the vein following venous puncture until drug delivery is completed.

5.1.2. Contributions

Contributions of this chapter are threefold. By fusing the measured forces at the microneedle tip with the available position information from the robotic manipulators, a novel method will be developed to capture the instant of venous puncture quickly and reliably despite the variable tissue behavior [133]. Second, a new “position-holding control mode” will be presented, which adds onto the default “tremor-canceling mode” of the robotic systems to fixate needle inside the vein after the event of venous puncture [134]. These are to the best of our knowledge, the first assistive RVC systems that can detect venous puncture and act automatically. Third, evaluation studies using phantoms will be conducted to demonstrate the improvement in the total time the needle could be maintained stably inside of the vein, the decrease involuntary movement of the cannula after the puncture, and compare the performance of two distinct robotic platforms.

***Credit:** Software for the venous puncture detection and automatic position holding were developed by Berk Gonenc. Experiments were carried out by Berk Gonenc, veterinary surgeon Jeremy Chae, and vitreoretinal surgeon Peter Gehlbach.*

5.2 Venous Puncture Detection

5.2.1 Force-Based Method

5.2.1.1. Algorithm

In earlier needle puncture studies using rabbit ear veins [51] and CAM of fertilized chicken eggs [52], a characteristic force behavior was reported. After the needle tip touches the tissue surface, the tool-tissue interaction force gradually rises until a sharp drop signaling the entrance of the needle tip into the vein. Our first method aims to quickly identify this instant by continually checking the time derivative of forces measured by the sensitized microneedle. For this, a custom LabVIEW program was developed. During the operation, first, the wavelength information from each FBG channel is collected and processed at 1 kHz and transmitted over TCP/IP to the LabVIEW environment. Using the calibration matrix, the transverse force at the tool tip is obtained. Then, the time derivative of tip force is computed and passed through a second-order low-pass filter. The optimal filter parameters (cutoff frequency and damping coefficient) are tuned based on measured force profiles in [52] so that the sharp oscillations due to measurement noise is filtered properly and the sharp drop in force is easily detectable with minimal delay (within 60 ms). When the filtered derivative of force turns negative ($d|\vec{F}_{\text{needle}}|/dt < 0$), or falls below a certain threshold value (P) that distinguishes venipuncture from tool retraction ($d|\vec{F}_{\text{needle}}|/dt < P$), a puncture is reported by this algorithm, right after which the operator can be warned via an auditory signal or helped with a robotic assistance method to halt needle advancement and maintain its position fixed.

5.2.1.2. Experiments

To assess the feasibility of our force-based puncture detection method, vein cannulation experiments were performed on the setup shown in Fig. 5.1.a by a non-surgeon subject with no prior experience. To simulate the retina and its vasculature, CAM of 12-day-old chicken embryos (Fig. 5.1.b) were used due to their similar anatomical features and histological properties [46]. The force-sensing microneedle was mounted on Micron, and the embedded LEDs on its handle were used for accurate tool tip tracking with the ASAP tracker [135]. The hand piece of Micron was fixed on a linear stage for driving the microneedle at constant speed into the target vein.

Before starting the experiment, the eggshell was partially removed to access the inner shell membrane (ISM). Then, the ISM was carefully peeled off using fine forceps to remove any variability in tests due to ISM thickness, and directly expose CAM. The target vessels on CAM were chosen to be within 100-140 μm in diameter using a fine fiber ($\text{\O} 125 \mu\text{m}$) for reference. After identifying the target, the microneedle was aimed and driven toward the target vessel using the linear stage at two different speed settings in alternating sequence: 0.3 mm/s and 0.5 mm/s. For each speed setting, 8 trials were performed. The task in each trial was to cannulate a small vessel and inject air into it using an infusion pump (11 Pico Plus Elite, Harvard Apparatus, Holliston, MA). The tip forces were monitored and an alarm sound was provided by the system upon sensing a puncture event. After hearing the alarm sound, the linear stage was stopped by the operator, and air injection was started. The success of vessel puncture and thus of the implemented force feedback mechanism, was assessed based on the observation of air bubbles flowing inside of the vessel as shown in Fig. 5.1.c.

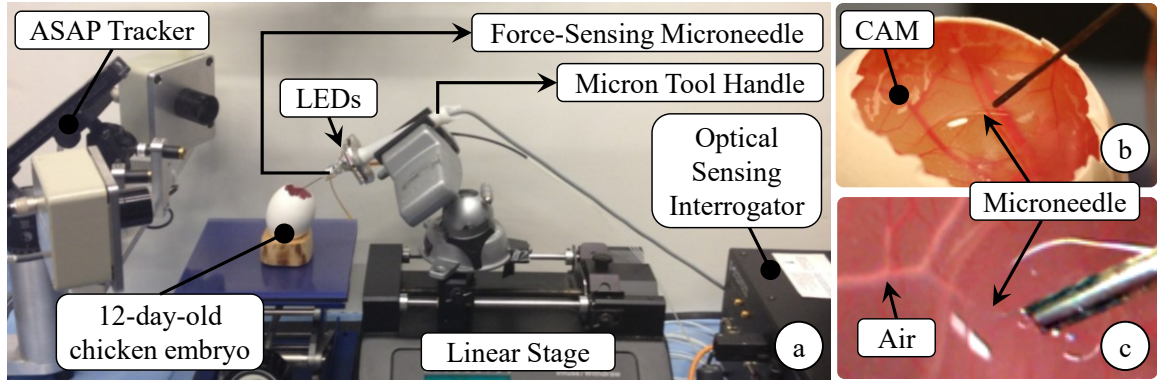


Figure 5.1: (a) Setup for vein cannulation experiments on CAM of 12-day fertilized chicken eggs. (b) Using a linear stage, the force-sensing microneedle was driven into the target vein on CAM at constant speed while its position was recorded by the ASAP tracker. (c) After vein puncture is detected, air injection was started. The success of cannulation was assessed based on the observation of air bubbles inside the vein.

5.2.1.3. Results and Discussion

Typical results for each speed level are shown in Fig. 5.2.a. In all trials, after the microneedle touched the CAM surface, a gradually rising force, thus a positive force gradient was observed. At the end of phase (a), the microneedle entered the vessel, which caused a sharp drop in the force and a sudden negative gradient triggering the auditory feedback mechanism. After the alarm sound, the stage was stopped manually and the needle was held in place during phase (b) while the operator started air injection to verify successful cannulation. During this time, the force at the tool tip remained at the same level. Then, the needle was retracted back while smaller forces in the opposite direction were measured at the tool tip.

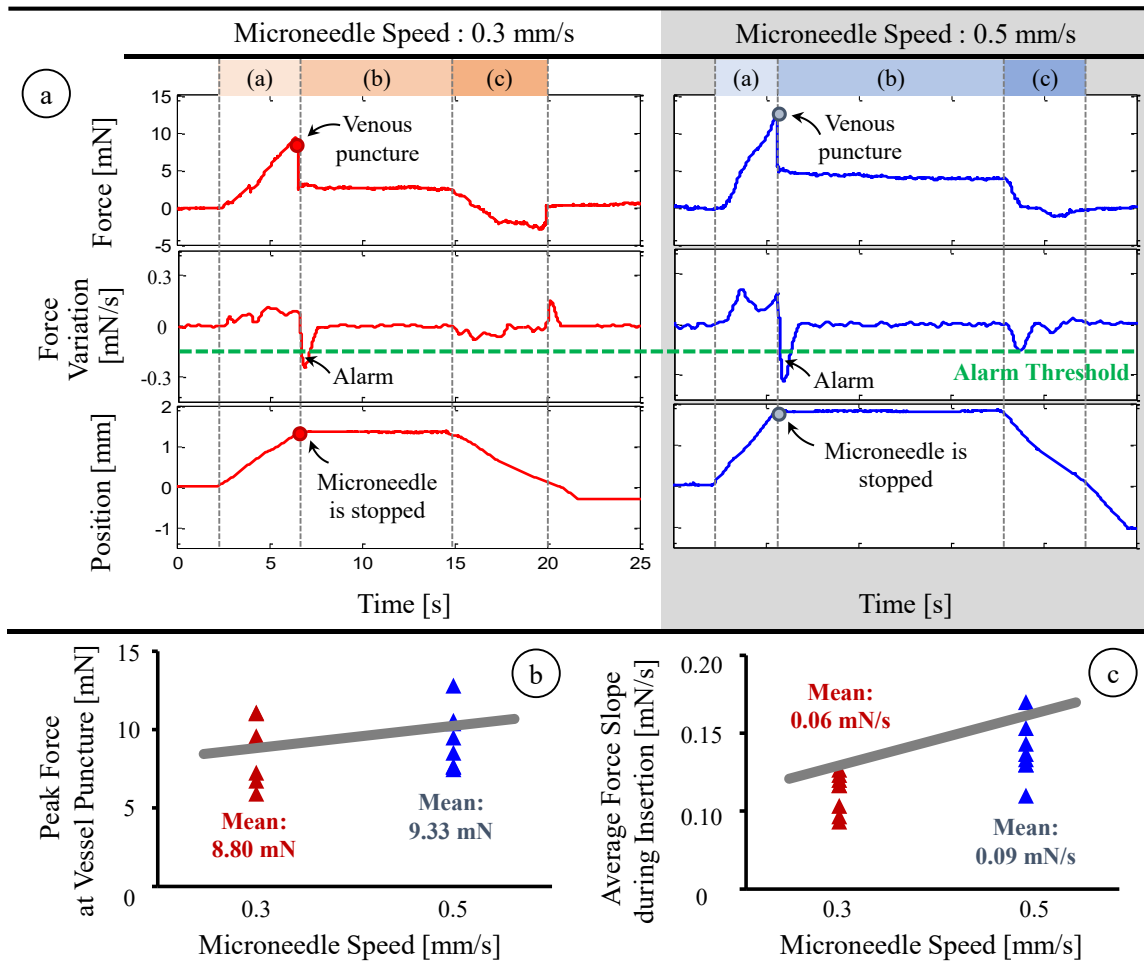


Figure 5.2: (a) A representative cannulation trial from each speed setting. The sharp drop in force signifies vessel puncture and generates an alarm to warn the operator. (b,c) Force statistics for 8 trials per speed setting.

Regardless of the speed setting, successful cannulation was achieved in all trials. Although the overall force trend remained the same, statistical analyses of all trials revealed the effect of linear stage speed on the observed force variation and peak force values. As shown in Fig. 5b, the mean rate of change in force during phase (a) was higher in 0.5 mm/s setting (0.0027 mN/s) than the 0.3 mm/s setting (0.0019 mN/s) ($p=0.0043$). The mean peak force also increased with higher insertion speed (Fig. 5c), yet this was not a statistically significant difference ($p=0.588$). In both Fig. 5b and 5c, the variation

among the tests within each speed setting is mainly due to minor differences between embryos and selected vessel diameters.

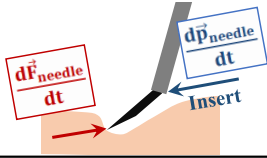
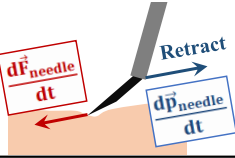
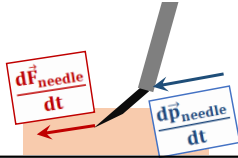
5.2.2. Force-and-Position-Based Method:

5.2.2.1. Algorithm

The previous study showed the feasibility of identifying the instant of venous puncture based on solely the time derivative of measured forces, and alerting the operator via auditory feedback. In testing our force-based method, the microneedle was driven into the target vein using a linear stage, which provided a unidirectional continuous needle motion at a fixed speed. In this case, checking only the time derivative of force was found to be sufficient since any force drop during the needle insertion could easily be related to a puncture event. Using a linear stage to drive the microneedle though, does not provide the necessary dexterity required while working inside a real eye. In cannulating retinal veins, either manipulating the tool by hand either manually or with the aid of a robotic micromanipulator, it is difficult to guarantee a constant insertion speed. As shown in Table 5.1, while pushing the needle against the vein wall, moving the tool slightly slower or retracting it before the venipuncture can cause a decline in the force magnitude ($|\vec{F}_{\text{needle}}|$), which can be misinterpreted still as a puncture event if the sensing system is checking only the sign of the exerted force's time derivative ($d|\vec{F}_{\text{needle}}|/dt < 0$). To distinguish a venous puncture from retraction events, a threshold value (P) needs to be specified such that only a sufficiently sharp drop in force ($d|\vec{F}_{\text{needle}}|/dt < P$) will be reported as a venous puncture. Identifying a proper threshold though requires careful tuning [48,136] and may differ depending on the local mechanistic properties of the

inhomogeneous retinal tissue as well as the operator's skill level. On the contrary, keeping track of both the force and position of the tool tip can give a more generalized and reliable prediction of the venous puncture without having to worry about the force derivative threshold.

Table 5.1: Variation of tool tip force and position before and at the instant of puncture.

Before Puncture		At the Instant of Puncture
$\frac{d \vec{F}_{\text{needle}} }{dt} > 0$	$\frac{d \vec{F}_{\text{needle}} }{dt} < 0$	$\frac{d \vec{F}_{\text{needle}} }{dt} < P$
$\frac{d\vec{F}_{\text{needle}}}{dt} \cdot \frac{d\vec{p}_{\text{needle}}}{dt} < 0$	$\frac{d\vec{F}_{\text{needle}}}{dt} \cdot \frac{d\vec{p}_{\text{needle}}}{dt} < 0$	$\frac{d\vec{F}_{\text{needle}}}{dt} \cdot \frac{d\vec{p}_{\text{needle}}}{dt} > 0$
		

Venous puncture is an event associated with a sharp drop in force while the needle is moving into the vein, which distinguishes it from a retraction event where the needle is moved away from the tissue. After the needle tip touches the vein wall, pushing it in will gradually deform the tissue and generate an increasing force at the needle tip. In contrast, retracting the needle backward will relax the tissue and therefore decrease the interaction force. Therefore, as long as the vein is not pierced, the law of action-reaction requires that the time derivative of the sensed tool tip force ($d\vec{F}_{\text{needle}}/dt$) and the velocity of the tool tip ($d\vec{p}_{\text{needle}}/dt$) always oppose directions; hence, the inner product of these two vectors is normally negative. Upon piercing the vein, however, this rule is reversed as the force variation vector ($d\vec{F}_{\text{needle}}/dt$) instantly flips its orientation and points in the same direction as the velocity vector. Therefore, the venous puncture can be detected by continually checking the sign of the inner product of the force variation and velocity

vectors, which will spike up to some positive value at the instant of venous puncture ($d\vec{F}_{\text{needle}}/dt \cdot d\vec{p}_{\text{needle}}/dt > 0$). Since our microneedle is bent 45° relative to the tool shaft, the insertion will induce mostly transverse (negligible axial) forces at the tool tip. Thus, although the force sensing properties of the microneedle are limited to only two dimensions (F_{needle}^x and F_{needle}^y), puncture of the vein can still be captured effectively by taking $dF_{\text{needle}}^z/dt = 0$.

5.2.2.2. Experiments

The setup shown in Fig. 5.3 was designed to replicate the main challenges of RVC, and as a very consistent platform to enable extensive testing. To simulate the retina and its vasculature, CAM is an anatomically similar model in both scale and the composition of structure and morphology [46]. However, using CAM, the number of trials for each test case remains limited, and it is hard to guarantee phantom consistency throughout the trials due to slight differences in the size of cannulated veins, and the anatomical variation between the eggs. To simulate the vein wall with consistent mechanical behavior, we created an artificial phantom with a thin membranous layer by stretching a vinyl layer (analogous to the polydimethyl siloxane sheet used in [68]) onto an acrylic insert with laser cut slots. The channels (1 mm wide) were cut much larger than the typical diameter of retinal veins to leave room for membrane deformation and unintentional drift of the operator's hand without letting the needle tip contact the acrylic surface, and were made small enough to create support for the vinyl membrane's surface tension.

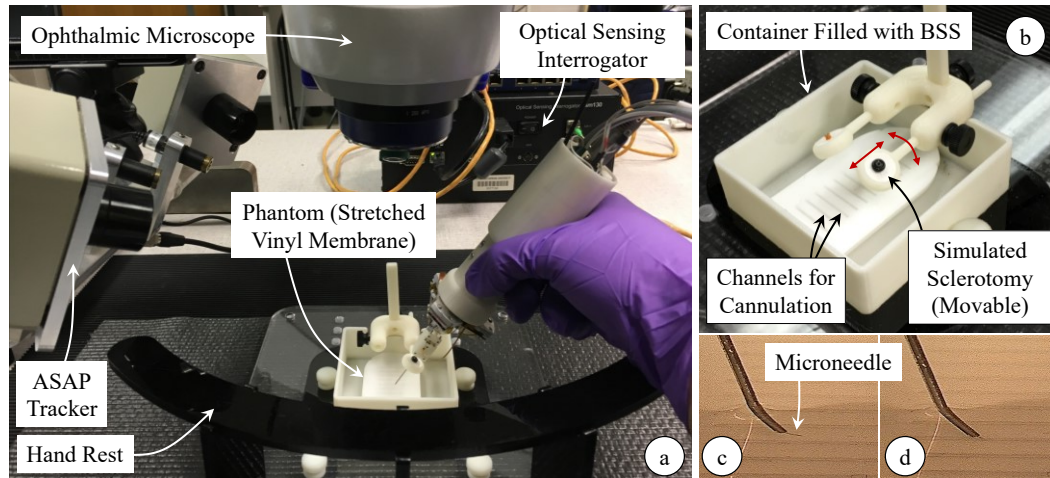


Figure 5.3: Experimental setup for cannulation experiments using an artificial phantom. (a) Stretched vinyl membranes simulating the vein walls were punctured using the force-sensing micro-needle under an ophthalmic microscope. (b) An acrylic insert with channels (1mm wide) was used to tension the vinyl layer. The phantom was placed inside a container filled with balanced salt solution (BSS). To approach the channels on the phantom, the needle was inserted through the trocar on the movable (as shown with red arrows) sclerotomy port. A digital microscope was used to monitor the operational area from the side and assess the moment of puncture: (c) before puncture, (d) after puncture.

Previous studies showed that the applied force while cannulating retinal veins can range anywhere from 5 mN to 35 mN depending on the angle of approach, the needle tip bevel, and the vein size [52]. The width of the acrylic insert in our phantom determines how stretched the vinyl membrane is, which affects the force required to pierce the membrane. The dimensions in the current setup produces a tension such that the piercing force varies within 5-15 mN. Fig. 5.4 shows the measured forces during 10 consecutive punctures at different locations on the phantom. Accordingly, the peak force (min: 7.72 mN, max: 13.48 mN) and rate of force drop at the instant of piercing the membrane (min: -35.21 mN/s, max: -8.73 mN/s) vary. The difference between punctures can be attributed to the slight discrepancies in the local surface tension of the membrane, variations in approach angle and insertion speed.

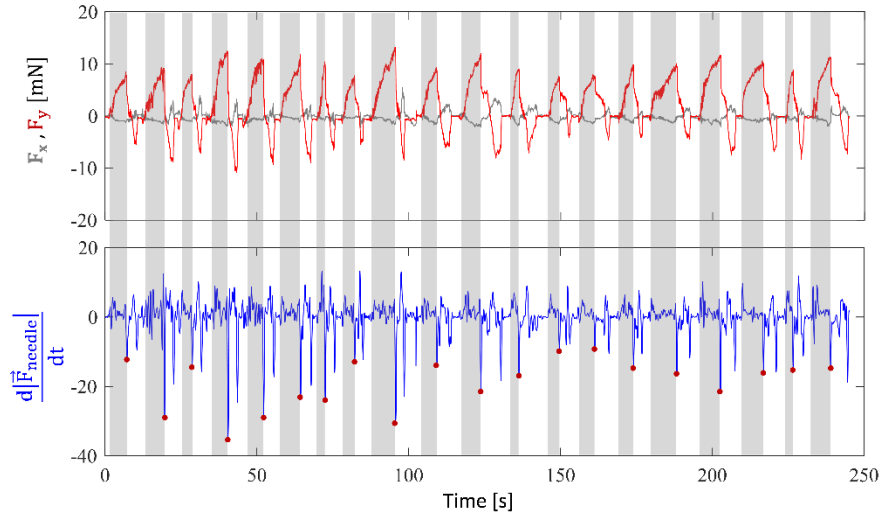


Figure 5.4: Measured forces during 20 consecutive punctures on the stretched vinyl membrane phantom. Grey zones correspond to the needle insertion phase while the white regions are for the retraction of the needle after puncture. During the insertion phase, most of the forces are along the needle axis (y-axis of the tool), with minor side load ($F_x < 5$ mN). The peak force before puncture ranges from 7.72 mN to 13.48 mN as the stretch of the phantom was adjusted targeting a range of 8-15 mN. The rate of force drop at the instant of piercing the membrane (marked with red dots in the lower plot) vary with a minimum of -35.21 mN/s and maximum of -8.73 mN/s for this set of trials.

The phantom was placed inside a container, which was filled with balanced salt solution (BSS) to emulate the aqueous environment inside the eye after vitrectomy. A white silicone port (fabricated as outlined in [113]) was mounted above the phantom to simulate the sclera. To reach the phantom surface, the needle is first passed through the trocar on the silicone port. Analogous to the movable eyeball while manipulating the tools during surgery, the silicone port is not a hard constraint but can be rotated and translated as shown in Fig. 5.3.b. Experiments were performed under an ophthalmic microscope (OPMI Lumera, Zeiss), providing only the top view of the phantoms. For analysis of collected data, a side view of the operation side (Fig. 5.3.c-d) was recorded using a digital microscope (USB2-Micro-200X, Plugable Technologies).

Using the force-sensing microneedle in combination with a handheld micromanipulator (Micron), the phantom was punctured several times at different locations. The experiment

was performed by 2 subjects with differing skill and experience: (1) a non-surgeon with 5 years of experience on the robotic system but with no prior cannulation experience, (2) an ophthalmology fellow with moderate cannulation experience and 2 hours of training on the robotic system. To prevent significant performance degradation in time due to fatigue, tests were completed in 3 periods, each period involving a total of 8 trials, with a 10-minute break between the periods. Similar to the procedural flow in RVC, the task in experiments was to puncture the vinyl membrane by moving the microneedle almost entirely laterally (in the direction the needle tip is pointing), and as slowly as possible without retracting the instrument before the puncture. After piercing the membrane – as observed from the side view of the operation site monitored by the digital microscope – the users were informed via auditory feedback, after which they tried to maintain the needle fixed for the following 45 seconds. Since each puncture causes the membrane to lose its tension locally, every new trial was done at a sufficiently distant location from the previous puncture point.

During the experiments, the Bragg wavelength of each FBG sensor was acquired using an optical sensing interrogator (sm130-700, Micron Optics Inc., Atlanta, GA) and the tool-tissue interaction forces were computed at 1 kHz. Similarly, the needle tip position was monitored using the ASAP tracker of the Micron system at 1 kHz. After completing the trials, the exact timing of each puncture was identified from the video recorded by the side-view digital microscope. The recorded forces and tool tip position were used to test the feasibility of the force-and-position-based puncture detection method, and compare its performance to the force-based technique.

5.2.2.3. Results and Discussion

As shown in Fig. 5.4 earlier, the rate of force drop upon piercing the membrane can vary significantly between trials even for the same user, depending on the local surface tension of the membrane, the insertion speed of the needle and the approach angle between the needle tip and membrane surface. In addition, there may be differences between the users. This makes it quite challenging to define a generalized threshold for detecting every puncture using the force-based method.

The recorded force characteristics for each user and the performance of the developed puncture detection methods are summarized in Table 5.2. In addition, sample measurements from each user are presented in Fig. 5.5. The exerted forces by the first user involve force drops ranging from -119.10 mN/s to -49.23 mN/s. On the other hand, the second user's data reveals a wider range from -141.20 mN/s to -19.67 mN/s. Using the force-based method from the previous section, if the first subject's data is taken as the basis for puncture detection ($d|\vec{F}_{\text{needle}}|/dt = -49.23 \text{ mN/s}$, the black dashed line in Fig. 5.5), then the first user's all punctures can be accurately identified with only 2 trials involving a faulty detection after the actual puncture (false positives), which can be attributed to the involuntary movements and resulting force oscillations while trying to maintain the needle inside the membrane after the puncture. Despite the good results for the first user, this threshold is not appropriate for the second user's performance as one third of the punctures, which have softer force drops, will be missed. The trial shown in Fig. 5.5.b exemplifies this issue, where the puncture leads to a force drop of $d|\vec{F}_{\text{needle}}|/dt = -45.51 \text{ mN/s}$, and the threshold indicated by the dashed black line ($d|\vec{F}_{\text{needle}}|/dt = -49.23 \text{ mN/s}$) does not intersect the force variation profile failing to

detect the puncture. To remedy, if the threshold is set to a higher value ($d|\vec{F}_{\text{needle}}|/dt = -19.67 \text{ mN/s}$), then all punctures for both users can be accurately sensed. Though among the 24 trials, in 3 of the trials in the second user's performance, due to a momentary retraction of the needle before the actual puncture, the force profile follows a fluctuating trend rather than a steady rise, causing a faster force drop than the threshold value. This causes the force-based method with the elevated threshold to misinterpret these instances as puncture events. The sample trial shown in Fig. 5.5.b illustrates one such case, where the blue dashed threshold ($d|\vec{F}_{\text{needle}}|/dt = -19.67 \text{ mN/s}$) intersects the force profile before the actual puncture due to the momentary retraction of the needle as evident from the trajectory plots. The retraction causes a force drop of $d|\vec{F}_{\text{needle}}|/dt = -36.76 \text{ mN/s}$, which is under -19.67 mN/s and hence reported as a puncture by the force-based method. In addition, the elevated threshold triggers several false positives due to involuntary tool motion and rapidly fluctuating forces after the puncture for both users (in %83 of the trials for the first user, and %63 of the trials for the second user).

In contrast to the force-based method, monitoring the inner product of force variation and tool tip velocity gives a much clearer image, and helps with distinguishing between needle retraction and puncture events. As shown in the sample data for each user in Fig. 5.5, the puncture leads to sharp positive peak in the product. Although the value of this peak can vary between users and trials, since the rest of variations in force and position lead to negative oscillations, the puncture, as the only prominent positive peak, remains very clear. As a result, using the force-and-position-based method, all punctures can be precisely detected for both users without any false positives before the actual puncture. This method performs satisfactorily as long as the filtered force and velocity information

accurately describe the tool-tissue interactions. On the contrary, in the presence of rapid changes the method can still lead to erroneous detection of punctures. After the actual puncture, while trying to compensate the user's drift and maintain the needle fixed in place, the micromanipulator can run out of its workspace (limited to 0.5 mm along each axis), which leaves no range to cancel user's hand tremor. In this case, due to the tremulous tool motion and the complicated interactions while the tip is inside the membrane, the method will fail and report several faulty punctures. In terms of the faulty detections after the puncture, the force-based method with the lower threshold seems to have the best performance (Table 5.2), though it has the risk of failing to detect the actual puncture – only %67 of the actual punctures were detected for the second user. The force-and-position-based method can identify all the actual punctures for both users, and meanwhile provides much less frequent false detection after the puncture (46% and 50% of trials for users 1 and 2 respectively) in comparison to what the force-based method with the elevated threshold causes (83% and 63% of trials for users 1 and 2 respectively). The rate of false detections after the puncture These false positives can presumably be avoided by tuning the parameters of the low-pass filters on the velocity and force signals. However, this is not preferable as it would also induce a delay in predicting the actual puncture, and since for practical purposes, identifying the initial puncture precisely in a timely manner is of utmost importance. Without any false positives before the actual puncture and with a full detection rate of the actual puncture, the force-and-position based method has shown feasibility in predicting the instant of puncture quickly (within 90 ms) with less dependence on local mechanical properties of the phantom and the user's performance.

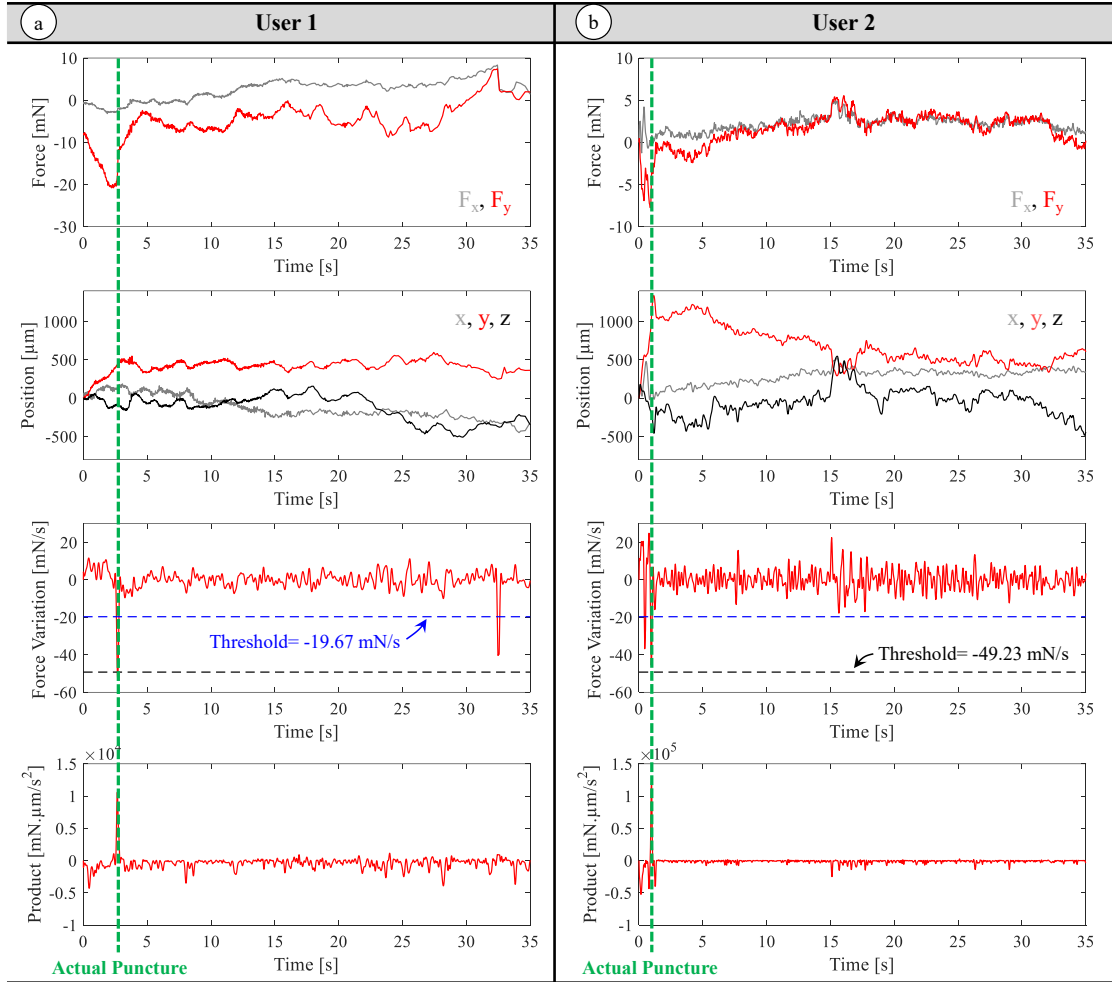


Figure 5.5: Measurements from a sample trial for each user: needle tip force (F_x in grey, F_y in red), needle tip position (x in grey, y in red, z in black), the variation of force ($d|\vec{F}_{\text{needle}}|/dt$) and the inner product of tool velocity and variation of force ($d\vec{F}_{\text{needle}}/dt \cdot d\vec{p}_{\text{needle}}/dt$). The timing of the actual puncture in each trial is marked with a green dashed line. (a) Data for the first user: The elevated threshold (the dashed blue line at $d|\vec{F}_{\text{needle}}|/dt = -19.67$ mN/s) may intersect the time derivative of force multiple times, and may trigger faulty detections after the actual puncture. (b) Data for the second user: The low threshold (the dashed black line at $d|\vec{F}_{\text{needle}}|/dt = -49.63$ mN/s) fails to intersect the force variation curve while the elevated threshold intersects it twice, leading to a faulty detection before the actual puncture using the force-based method. In both trials, the inner product of the force variation and tool velocity clearly displays the instant of actual puncture with a prominent positive peak. The force-and-position-based method, relying on the inner product value, is able to distinguish the event of puncture.

Table 5.2: Puncture detection rates with the force-based versus the force-and-position-based methods for two users with differing skill and experience (n=24 trials per user).

Puncture Criterion	Force-Based Method						Force-and-Position-Based Method		
	$\frac{d \vec{F}_{\text{needle}} }{dt} < -49.23 \text{ mN/s}$			$\frac{d \vec{F}_{\text{needle}} }{dt} < -19.67 \text{ mN/s}$			$\frac{d\vec{F}_{\text{needle}}}{dt} \cdot \frac{d\vec{p}_{\text{needle}}}{dt} > 0$		
	Detected the Actual Puncture	False Detection Before Puncture	False Detection After Puncture	Detected the Actual Puncture	False Detection Before Puncture	False Detection After Puncture	Detected the Actual Puncture	False Detection Before Puncture	False Detection After Puncture
User 1	100%	0%	8%	100%	0%	83%	100%	0%	46%
User 2	67%	0%	17%	88%	13%	63%	100%	0%	50%

5.3 Automatic Position Holding

Following venous puncture, the operator needs to maintain the needle tip inside the vein throughout the infusion. This can take up to 2 minutes or even longer [20]. Given the fragility and small size of retinal veins, the physiological hand tremor and unintentional drift of user's hand during the manual operation, it is very challenging to quickly stop needle insertion right after venous puncture is detected and hold it fixed for a prolonged injection. Robotic assistants can attenuate high-frequency components of involuntary motion, such as surgeon's physiological hand tremor, which is beneficial for accurately positioning the needle tip on the target vein before puncture. However, they remain insufficient for identifying the instant of venous puncture or eliminating the low-frequency drift of the cannula after the puncture. To promote longer intravenous stability of the cannula for a longer period, this section uses the force-and-position-based puncture detection method from Section 5.2 and focuses on altering the operation modes of both Micron and the Steady-Hand Eye Robot (SHER) as shown in Table 5.3.

5.3.1 Algorithm

Micron normally operates in "Tremor Canceling Mode" (TCM), which attenuates physiological hand tremor by continually tracking the tool handle motion via its ASAP trackers, filtering it to compute a goal position for the tool tip, and using its actuators to

counteract the tremulous components of motion. This is a beneficial feature that enables a stable and safer approach to the target vein. Once the needle pierces the vein ($d\vec{F}_{\text{needle}}/dt \cdot d\vec{p}_{\text{needle}}/dt > 0$), the goal of operation changes into fixating the needle at the detected puncture position. This can be accomplished by switching Micron's operation mode to a "Position Holding Mode" (PHM) as soon as a puncture is sensed, so that the goal position is constantly set to the position detected at the instant of puncture (Fig. 5.6). In this mode of operation, even if the user unintentionally moves the Micron handle, Micron deflects its tip to actively compensate any (both high and low frequency) motion so that the tip is held fixed right at the puncture point. This active position holding mode is functional within the limits of Micron's actuators (within a sphere of ~ 0.5 mm radius). Deviating from the puncture point beyond these limits will saturate the actuators, and thus may not be compensated. The operator still maintains the gross positioning control while Micron makes fine adjustments to fixate the tool tip. In this way, Micron actuation can be overridden if needed, in case the needle needs to be quickly removed from the tissue.

On the other hand, SHER normally operates in a "Cooperative Control Mode" (CCM), where the robot complies proportional to the user forcing. Upon venous puncture, the mode can be altered into a PHM similar to Micron by setting the controller admittance gain to zero ($K=0$) so that the needle is held fixed (unless the operator wants to disable the mode via a foot pedal, which was implemented as a safety measure). On both systems, when the PHM is activated, the user is informed of the venous puncture via auditory feedback to signal the right time to start injecting the medicine.

Table 5.3: Operation mode regulation for Micron and the Steady-Hand Eye Robot (SHER).

Condition	Puncture?	Operation Mode
$\frac{d\vec{F}_{needle}}{dt} \cdot \frac{d\vec{p}_{needle}}{dt} \leq 0$	No	Tremor Canceling Mode (Micron) Cooperative-Control Mode (SHER)
$\frac{d\vec{F}_{needle}}{dt} \cdot \frac{d\vec{p}_{needle}}{dt} > 0$	Yes	Position Holding Mode

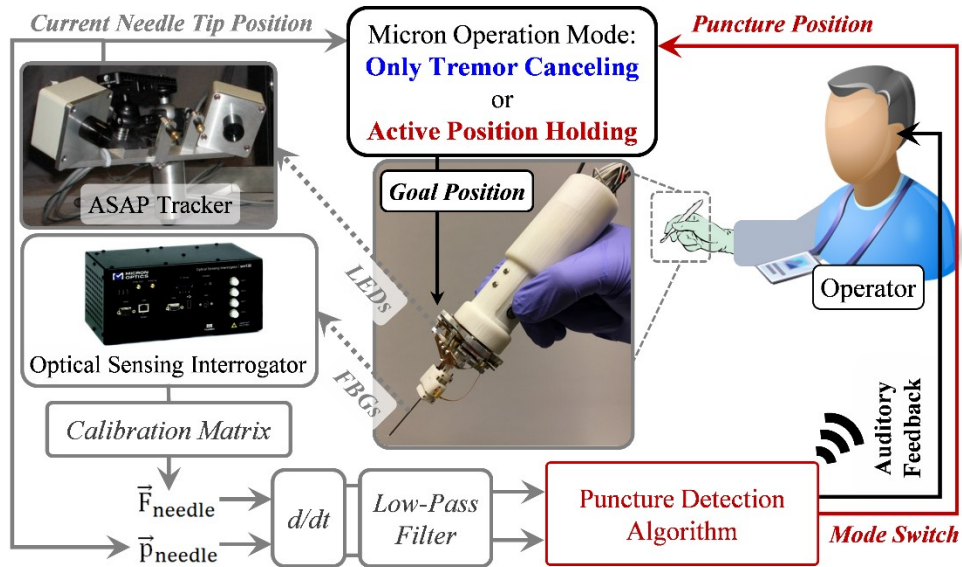


Figure 5.6: The control scheme of the integrated system for Micron. The time derivative of needle position and force are computed and filtered. The inner product of the two turns positive at the event of vein puncture. When puncture is detected (1) the operator is informed with an alarm sound, and (2) Micron operation mode is switched from default "only tremor canceling" to "active position holding".

5.3.2. Experiment 1: A Multi-User System Evaluation

5.3.2.1. Setup and Procedure

We performed an experimental study to quantify the effects of our system on operator performance during simulated cannulation trials using the setup shown in Fig. 5.7. The experimental procedures involving human subjects described in this section were approved by the Institutional Review Board.

To emulate the retinal vasculature, the artificial phantom previously described in Section 5.2.2. was used. The experiments were performed by 3 subjects with differing level of skill and experience: (1) a non-surgeon user with 5 years of experience on the robotic system but with no prior cannulation experience, (2) an ophthalmology fellow with moderate cannulation experience and 2 hours of training on the robotic system, and (3) an expert vitreoretinal surgeon with 1 hour of training on the robotic system. The task in each experiment was to approach the phantom submerged in the BSS solution, and puncture the vinyl membrane by moving the microneedle almost entirely laterally, in the direction the needle tip is pointing, and hold the needle fixed for 45 seconds after the event of puncture.

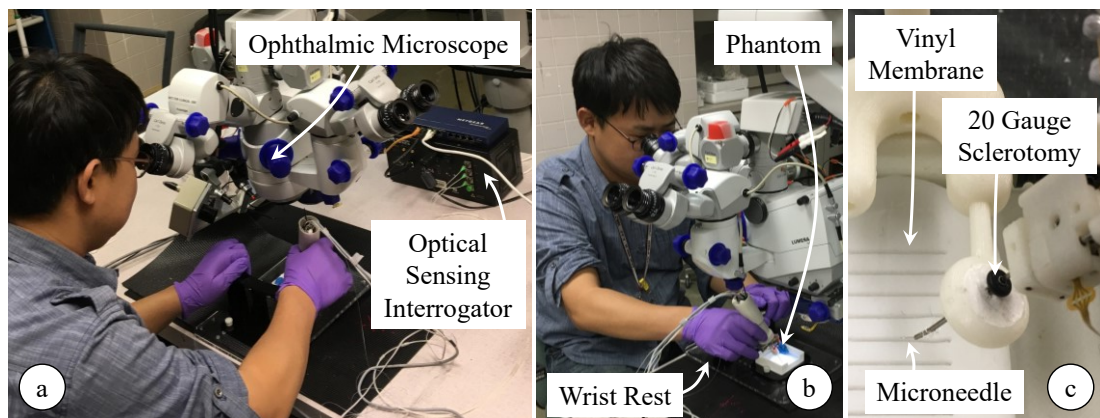


Figure 5.7: Experimental setup. (a) An ophthalmic microscope was used to monitor the operation site, and the optical sensing interrogator acquired the readings from the force-sensing microneedle. (b) Trials were done on the vinyl phantom submerged in BSS. (c) The experimental task was to approach the vinyl membrane inserting the force-sensing micro-needle through the sclerotomy port, puncture it which is detected by the force-and position-based method, and maintain it fixed during the following 45 seconds.

Two cases were experimented by altering the operation mode of Micron: (1) only tremor canceling mode (TCM), and (2) automatic position holding mode (PHM). In either case, the force-and-position-based puncture detection method from Section 5.2.2 was used, and the operator was informed upon the puncture via auditory feedback. The needle trajectory after this instant was recorded for analysis. To prevent significant performance

degradation in time due to fatigue, tests were completed in 3 periods, each period involving a total of 8 trials (4 trials per case), with a 10-minute break between the periods. During the trials, Micron mode was altered between TCM and PHM in random order. Since each puncture on the phantom causes the membrane to lose its tension locally, every new trial was done at a sufficiently distant location from the previous puncture. Performance assessment was based upon the recorded deviation from the point of puncture. Analyses were done using one-way analysis of variance (ANOVA) followed by a t-test assuming unequal variance. Statistical significance was defined as $p < 0.05$.

5.3.2.2. Results and Discussion

Sample measurements from trials with TCM and with PHM for the first subject are shown in Fig. 5.8. In these trials, after the microneedle touches the membrane surface (the simulated vein wall), a gradual rise in force is observed. Most of the forces are exerted along the y-axis (all the measured x-axis forces remain under 5 mN) since the insertion is performed by moving the tool mostly laterally along the needle axis (y-axis) (Fig. 5b). In both trials, the puncture is detected based on the sharp positive peak in the inner product of needle velocity and force variation vectors (Fig. 5.8.c). Throughout the 45-second period following this instant, the difference in tool tip travel between TCM and PHM trials is clearly visible in Fig. 5.8.b. In TCM, all components of the position vector fluctuate, especially the z-component due to operator's poor depth perception with the provided 2D microscope view. Using PHM, the tool motion after the puncture is significantly lowered. The reduced deviation from the puncture point with PHM can clearly be seen in Fig. 5.8.d, which includes the needle tip trajectories recorded during 3 sample trials of each operation mode for the first user.

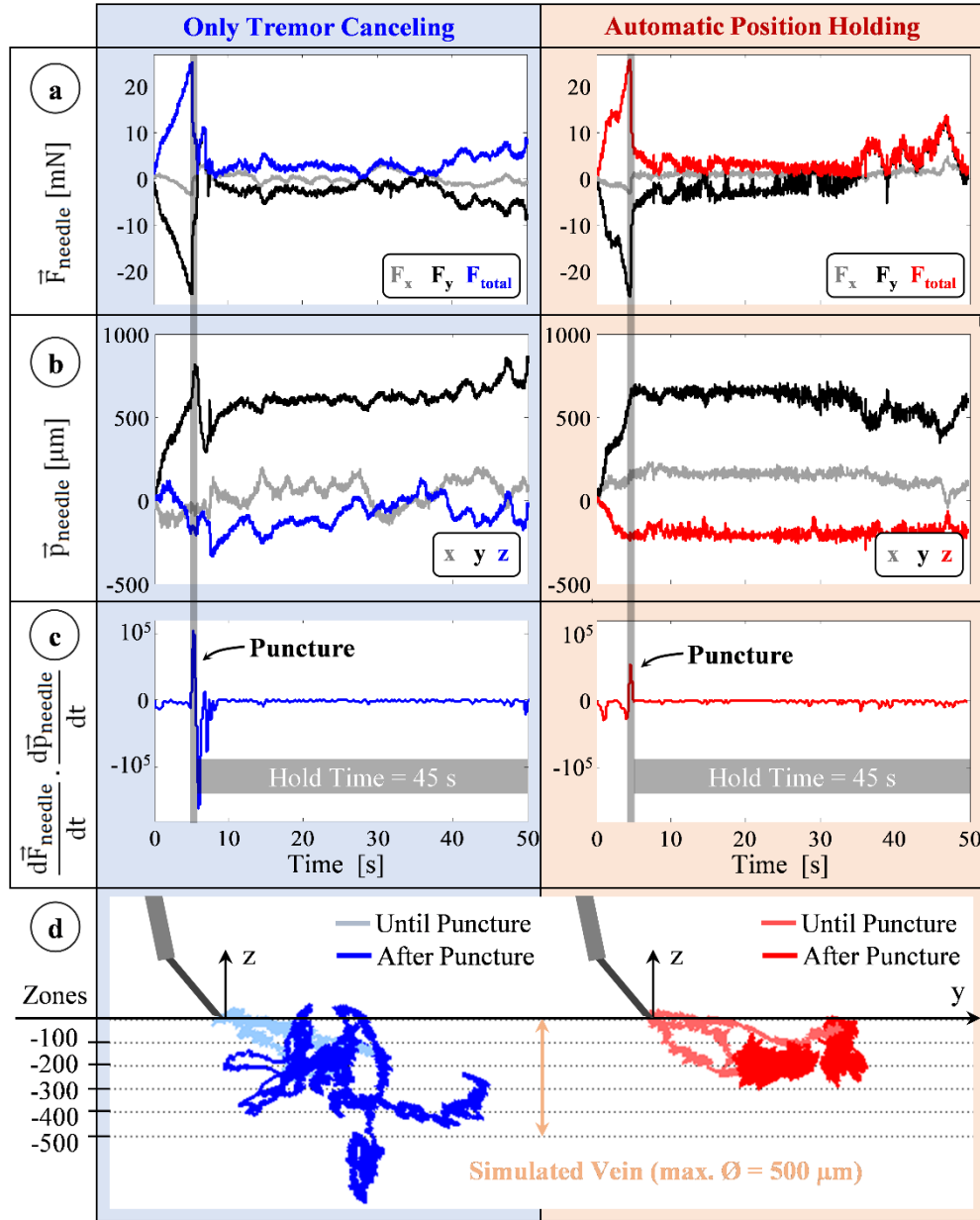


Figure 5.8: Typical measurements taken during trials of the first user using the tremor canceling (blue) and automatic position holding (red) features of the system. (a) Forces on the needle: mostly along the y-axis with a gradual rise during insertion and a sharp drop at the instant of puncture. (b) Position of the needle remains fixed with the position holding mode in contrast to the fluctuations with only tremor canceling. (c) The event of puncture: a positive peak in the inner product of needle velocity and force variation vectors. (d) Recorded needle tip trajectories for 3 representative trials of each mode. Position holding mode significantly reduced tool tip deviation from the puncture point.

The characteristics observed at the instant of puncture during the 24 trials for each user are summarized in Table 5.4. Accordingly, the puncture forces for all users lie mostly

within the range that the phantom was developed for (5-15 mN), as detailed in Section 5.2.2.2. The mean value of the puncture force did not vary depending on the mode of operation (TCM or PHM), revealing no statistically significant difference ($p=0.83$) between the mechanical behavior of membranes used in either test case. Furthermore, no statistically significant difference could be identified between the mean puncture forces of the three users ($p=0.12$). The forces for the first user ($F = 10.46 \pm 1.70$ mN), with extensive training on both the robotic system and the phantom, show the lowest deviation throughout the trials. Similar consistency is also observed in the surgeon's (user 3) performance ($F = 8.74 \pm 1.70$ mN). The rate of force drop associated with the event of puncture differs significantly among the users (-49.48 ± 15.75 mN/s for user 1, -67.47 ± 34.35 mN/s for user 2, -51.37 ± 16.06 mN/s for user 3, and $p=0.019$). Therefore, to detect puncture, the force-based method would require separate tuning for each user. Using the force-and-position based method, the instant of puncture, which produced a clearly visible positive spike ($8.75 \times 10^3 - 7.21 \times 10^5$ mN. μ m/s²) in the normally negative inner product of tool velocity and force variation, was detected precisely in all trials.

Table 5.4: Force characteristics associated with the instant of puncture for three different users (n=24 trials/user).

	$ \vec{F}_{\text{needle}} $				$\frac{d \vec{F}_{\text{needle}} }{dt}$ [mN/s]				$\frac{d\vec{F}_{\text{needle}}}{dt} \cdot \frac{d\vec{p}_{\text{needle}}}{dt}$ [mN. μ m/s ²]			
	MEAN	STD.	MIN.	MAX.	MEAN	STD.	MIN.	MAX.	MEAN	STD.	MIN.	MAX.
User 1	10.46	1.70	7.68	12.09	-49.48	15.75	-78.31	-26.14	7.08×10^4	4.18×10^4	1.53×10^4	1.34×10^5
User 2	11.66	6.90	4.55	22.45	-67.47	34.35	-141.20	-19.67	2.07×10^5	1.61×10^5	8.75×10^3	7.21×10^5
User 3	8.74	1.70	6.51	13.02	-51.37	16.06	-89.21	-29.83	8.17×10^4	4.53×10^4	2.62×10^4	1.69×10^5

To assess the ability to maintain cannulation in veins of different sizes, using the measured tool tip position throughout the entire hold period (45 seconds), we computed the time spent inside five different zones of varying distance from the puncture point

(Fig. 5.8.d). The size of each zone was chosen to represent a vein diameter, and was decided based upon the typical sizes of retinal vasculature (\varnothing 100-500 μm). In RVC, since both the vasculature and the microneedle are elastic, going beyond the borders of these zones does not necessarily mean that the needle will get out of the vein; instead, the needle will flex and the tissue will deform to some extent. The deviation from the puncture point, therefore, is a measure of the trauma that would have been induced on the vasculature in a clinical scenario. The results in Fig. 5.9 show that, compared with the TCM trials, using the PHM enabled all the users to maintain the tip within each zone for a significantly longer period ($p < 0.05$). For instance, for the first user, who is the most experienced subject in using Micron and the phantom, the average time that the tip was maintained within a 100 μm distance from the puncture point was measured to be only 5.41 seconds with TCM; and in none of the 12 TCM trials could this duration exceed 40 seconds. In contrast, upon using PHM, the mean time was raised to 13.27 seconds, with 2 trials reaching a hold time over 40 seconds. Similar performance improvement with PHM was observed in the 200 and 300 μm zones. For the 400 and 500 μm zones, in terms of the average time maintained inside, no statistically significant difference between TCM and PHM could be identified for the first user ($p = 0.07$ for 400 μm , $p = 0.26$ for 500 μm). However, even for the 500 μm zone, where the performance of TCM and PHM is closest, the number of trials with successful "in-zone" hold time over 40 seconds was still 50% greater in PHM than TCM.

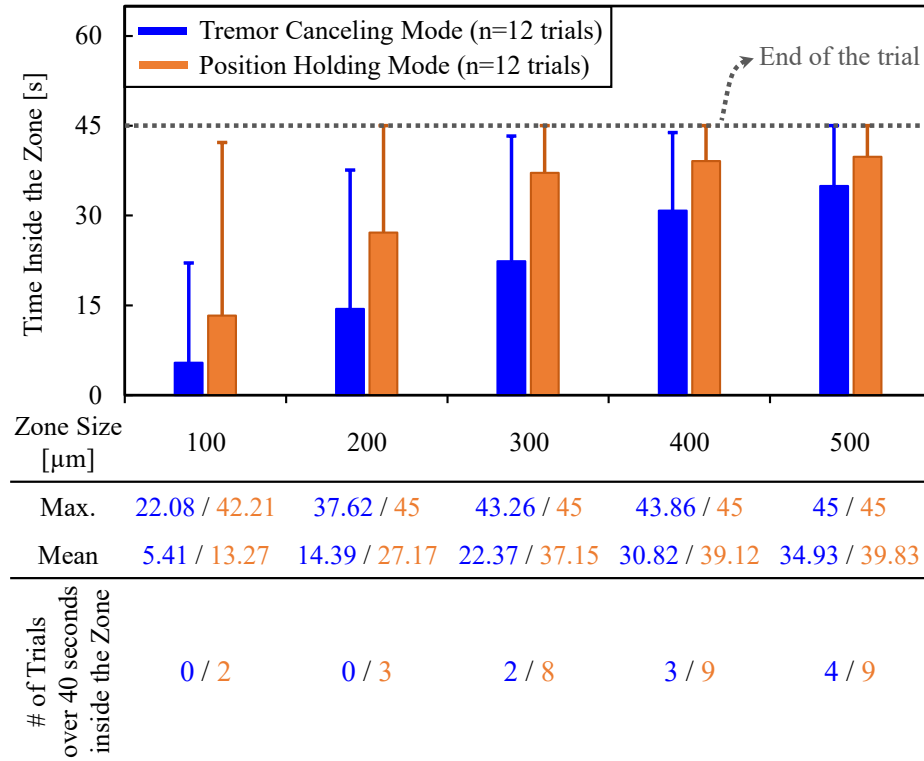


Figure 5.9: The total time that the needle tip was maintained inside various sizes of zones around the puncture point using the TCM (in blue) versus the PHM (in orange) features. The solid bars show the mean, and the error bars represent the maximum values. The active position holding helps in maintaining the needle tip inside the vein for a significantly longer time, especially for veins smaller than 300 μm.

The length of stay within each zone for all users with the TCM versus the PHM are compared in Fig. 5.10. In contrast to the first user, the limited training that both user 2 (ophthalmology fellow) and user 3 (vitreo-retinal surgeon) received on the robotic system is a factor affecting their performance. Despite that, with TCM, the third user could still maintain the needle inside the smallest zone (100 μm) for the longest time (8.47 seconds on the average) among others. As the zone size increases, the average time spent inside the zone grows for all users, following a different trend for each – with almost a constant rate for user 1, and with increasing rates for users 2 and 3. Nevertheless, the durations measured for all users, especially within the smaller zones, are far from being feasible to

do prolonged infusions in RVC. When PHM is used, the average time spent in each zone is significantly improved for all subjects ($p < 0.05$). This shows that the PHM is helpful in keeping the needle close to the point of puncture for longer periods. For instance, user 3 could maintain the needle within 300 μm around the point of puncture for an average of only 14.43 seconds with the TCM, whereas with the aid of PHM this period was almost doubled up to an average of 27.92 seconds. For the largest zone (500 μm), all subjects exhibited almost identical performance using the PHM; the surgeon's average time inside the zone (44.19 seconds) equaled almost the full test period.

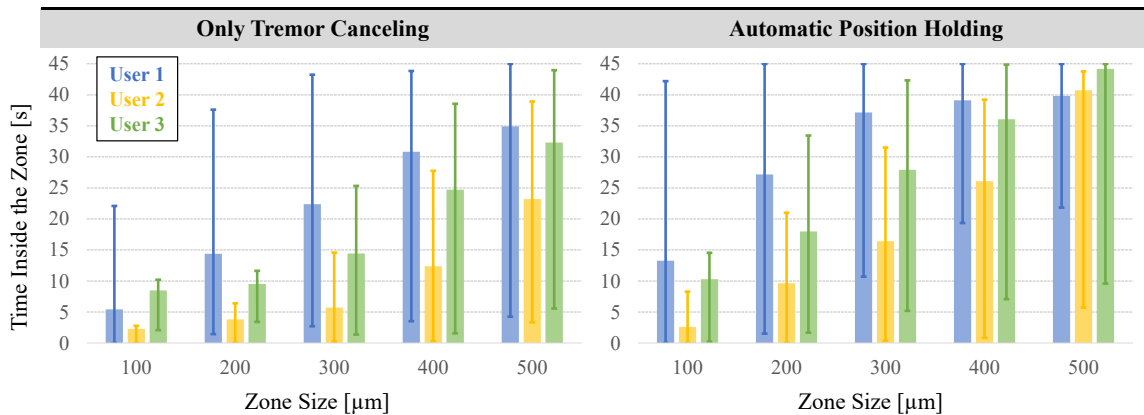


Figure 5.10: The performance of each user in maintaining the needle around the point of puncture (zone size=distance from the puncture point). User 1 is a non-surgeon with extensive experience on the robotic system. Users 2 and 3 are, respectively, an ophthalmology fellow and an expert vitreoretinal surgeon with some training on the robotic system. The solid bars show the mean, and the error bars represent the maximum and minimum values. The automatic position holding mode aids in maintaining the needle close to the puncture point for a longer period for all users.

If the length of stay in each zone is analyzed with respect to the total length of the hold period, a significant improvement is observed for all users as shown in Fig. 5.11. The ideal line in these plots corresponds to keeping the needle inside the zone for the full hold period. For the smallest zone, user 3 among the other subjects is closest to reaching this goal with the TCM (shown in blue). Using the PHM (shown in orange), the improved

performance of user 1, is brought up to a similar level, while for user 2, TCM remains ineffective in bringing the tip within 100 μm from the puncture point. This can be attributed to the limited motion range of the micromanipulator – Micron can correct erroneous movement up to 500 μm along each axis while user 2 movements average over 700 μm , which will be analyzed in detail as a second performance metric. For bigger zones, the plots with PHM are above the plots with TCM, closer to the ideal line; using PHM all users can hold the needle within 500 μm from the puncture point during almost the entire hold period.

Our second performance metric is based on the range of needle tip motion after the puncture—which needs to be minimized to reduce trauma—as a function of the hold time. For this, we analyzed the tip deviation during the first 15, 30 and 45 seconds after the puncture for each user. The results are shown in Fig. 5.12. Accordingly, an almost linear rise is observed in the maximum and mean deviation from the puncture point as the needle is held for longer periods for all users. This rise was inevitable, regardless of whether TCM or PHM was used. Nevertheless, for all hold times, when PHM was used, both the mean and the maximum distance from the puncture point was significantly lowered for all users ($p < 0.05$). In case of a 15-second hold time for instance, the mean deviation from the puncture point for the first subject was reduced by more than 65% (from 276.18 μm to 90.34 μm). The decay was similar for the 30 and 45-second hold periods. The mean deviation from the puncture point during a 45-second hold exceeded 350 μm with the TCM, whereas the PHM lowered it to below 200 μm for user 1. Similarly, for the second and third users, the mean drift after the puncture was reduced from 854.98 μm to 553.06 μm and from 812.06 μm to 412.32 μm , respectively. These

results show that the automatic position holding is an essential feature that can potentially enable the cannulation of smaller veins, and provide an extended period of intravenous cannula stability, and thereby allow sustained periods of drug delivery at tolerable pressures.

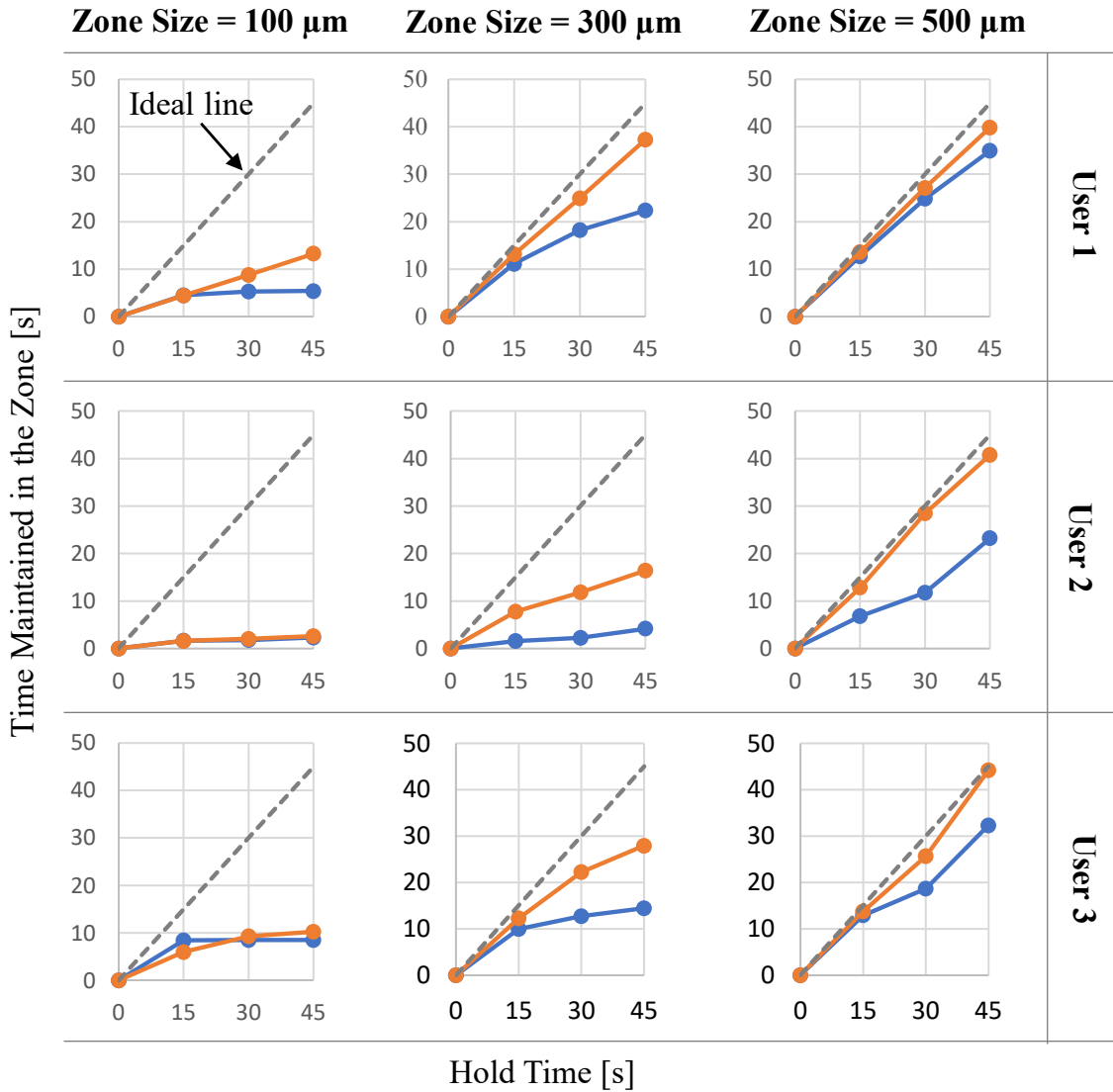


Figure 5.11: The variation of time that the needle is maintained in different zones as a function of the hold duration for each user using the TCM (blue) vs. the PHM (orange). The ideal line (dashed grey) corresponds to keeping the needle inside the zone throughout the entire hold period. The performance of each user is closer to the ideal line when the PHM is used.

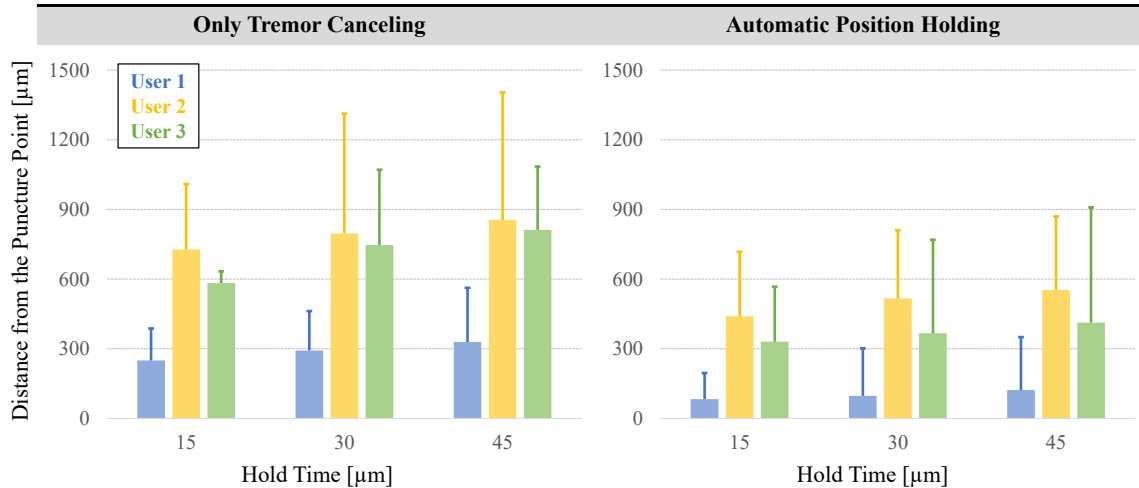


Figure 5.12: Deviation from the puncture point vs. the hold time for each user. The solid bars show the mean distance from the puncture point, and the error bars represent the maximum values. A longer hold time causes the needle to move away from the puncture point more. The automatic position holding mode significantly helps in keeping the needle tip proximal to the puncture point.

5.3.3. Experiment 2: A Performance Comparison Between Micron and the Steady-Hand Eye Robot

5.3.3.1. Setup and Procedure

We performed a series of cannulation experiments to comparatively evaluate the performance of Micron and SHER with the developed microneedle, puncture detection method and automatic position holding features using the setups shown in Fig. 5.13.a and 5.13.b respectively. The experimental procedures involving human subjects described in this section were approved by the Institutional Review Board.

To closely replicate the vein cannulation procedure *in vitro*, we developed an artificial phantom platform similar to the one used in sections 5.2.2.2 and 5.3.2.1, which is an acrylic plate with 18 circular holes covered by a thin, uniformly stretched vinyl layer emulating the retinal vein walls. The diameter of the holes on the plate is 2.5 mm, small enough to create the support for the vinyl membrane’s tension while leaving sufficient

space for the user to perform several cannulations. The phantom was fixed on a light pad to clearly visualize the membrane under a digital microscope. The microscope view was displayed on a monitor providing only the top view of the phantom.

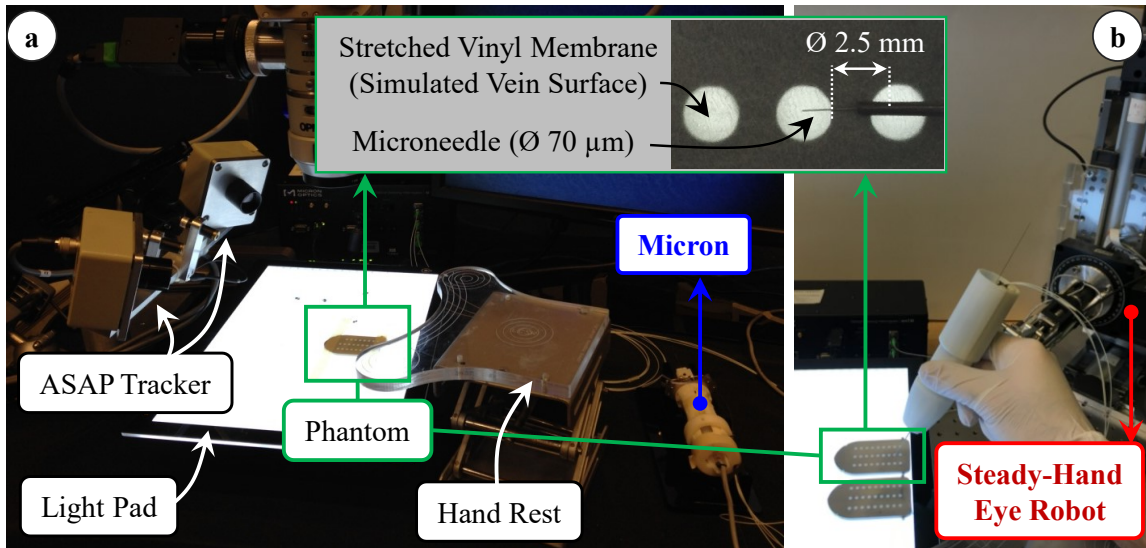


Figure 5.13: The experimental setup for evaluating the performance of (a) Micron and (b) SHER on an artificial phantom. Stretched vinyl membranes, simulating the vein walls, were punctured open-sky using the force-sensing microneedle.

Tests were done by a non-surgeon subject with no prior cannulation experience, but with extensive training on both Micron and SHER systems. The task in each trial was to puncture the vinyl membrane by moving the microneedle almost entirely laterally, in the direction the needle tip is pointing, and hold the needle fixed for 45 seconds after the event of puncture.

Using Micron, two cases were experimented: only TCM, and with PHM. On SHER side, three cases were explored: only CCM with low gains ($K=2$ mm/N.s), only CCM with high gains ($K=20$ mm/N.s), and with PHM. 12 trials were completed for each case. In order to prevent significant performance degradation in time due to fatigue, tests were completed in 3 periods, each period involving a total of 8 trials for Micron and 12 trials for SHER (4

trials per case), with a 10-minute break between the periods. During the trials, the operation mode was altered in random order for either robotic system. To preserve the membrane's surface tension at a similar level between trials, a new hole on the phantom was used for each trial.

A detailed performance assessment on Micron trials was reported earlier in the previous section. In this experimental study, the focus is more on the evaluation of the SHER system and comparison of its performance with our earlier findings on Micron. We assess the performance based upon the recorded deviation from the point of puncture, which would be highly correlated to the trauma on the cannulated vasculature in a clinical scenario. Analyses are done by a t-test assuming unequal variance. Statistical significance is based on $p < 0.05$.

5.3.3.2. Results and Discussion

Typical measurements taken from a representative trial for each test case is shown in Figs. 5.14 and 5.15. Until the puncture, the force is observed to rise gradually as a common trend between the two figures. What is different though is the variations after the puncture. In Fig. 5.14, the position measurements fluctuate when the default mode of each robotic system is used. Using the developed position holding feature, as shown in Fig. 5.15, leads to less movement after the puncture. For performance comparison, between the different operation modes and robotic platforms, we evaluated the range of deviation from the puncture point as a function of the hold time, analyzing the acquired needle tip position data during the first 15, 30 and 45 seconds after the puncture.

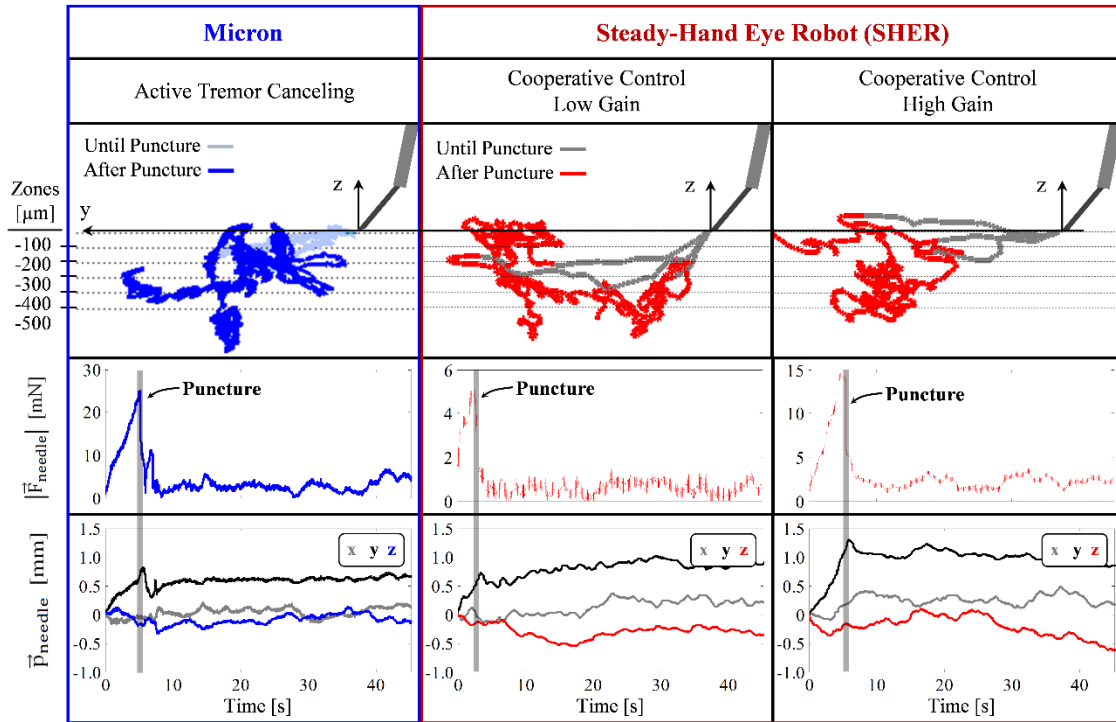


Figure 5.14: Sample measurements from the trials using the default modes of two robotic platforms: Active tremor canceling mode of Micron (blue), and cooperative control of SHER (red). Large deviations from the puncture point are observed in both systems. Modulating the controller gains on the SHER system does not lead to a significant improvement in terms of reducing the needle movement after the puncture.

5.3.3.2.1. CCM Gain Modulation for SHER

In CCM of SHER, using higher controller gains is beneficial in manipulating the tool faster, saves operational time and results in less fatigue on the operator's hand. On the other hand, using low controller gains provides a slower and safer motion if the tool tip is moving close to critical anatomical features, which is important while approaching the target vein. After the needle tip punctures the simulated vein wall, results in Fig. 5.16.a show that with the low controller gains, the deviation from the puncture point is $459.50 \pm 181.54 \mu\text{m}$ during the first 15 seconds. This rises to $668.54 \pm 252.69 \mu\text{m}$ for the full experiment period of 45 seconds. When the controller gains are increased, resulting in a more freely moving system similar to a handheld tool, slightly less deviation,

341.95±75.04 μm, is observed for the first 15 seconds ($p<0.05$). However, for 45 seconds of hold time, the deviation rises to 625.16±280.07 μm, revealing no statistically significant difference from the low gain case ($p=0.4$). Therefore, modulating the controller gain does not produce a significant reduction in the involuntary needle motion after the puncture, especially for longer hold periods.

5.3.3.2.2. CCM vs. PHM for SHER

Shown in Fig. 5.16.b is the comparison between the deviation obtained with regular CCM and with PHM. The force-based puncture detection and motion locking in PHM significantly reduces the motion after puncture, from 625.16±280.07 μm to 9.68±4.18 μm for the full experiment period of 45 seconds. In contrast to the gradually increasing deviation in time with CCM, the performance with PHM is not affected from the hold time, maintaining it fixed at the same level ($p<0.05$).

5.3.3.2.3. Performance Comparison: Micron vs. SHER

When the two robotic systems are used in their regular operational modes, namely TCM for Micron and CCM for SHER, the performance difference observed in the initial 15 seconds is not statistically significant ($p=0.10$). However, as shown in Fig. 5.16.c, for longer hold times, slightly more deviation from the puncture point is observed with SHER (489.76±189.78 μm for 30 s and 625.16±280.07 μm for 45 s) than with Micron (328.86±134.19 μm for 30 s and 367.32±113.57 μm for 45 s) ($p<0.05$). Upon using PHM on both systems (Fig. 5.16.d), an opposite trend is obtained with the SHER providing significantly less deviation regardless of the hold time ($p<0.05$). Micron can attenuate the undesired motion after puncture by more than 65% (from 276.18 μm to 90.34 μm in case of a 15-second hold time for instance). However, due to its small workspace, the range of

motion it can compensate is limited (± 0.5 mm). If the tool is moved beyond this range after the puncture, the actuators will saturate and fail in fixing the needle tip position. This is why almost a linear rise in the average deviation is observed for Micron as the needle is held for longer periods (Fig. 5.16.d). On the other hand, SHER can stop the needle motion right after the puncture and lock the position without any saturation issues. This results in an almost 95% reduction in the deviation for all hold periods as compared to regular CCM (from $75.04 \mu\text{m}$ to $4.17 \mu\text{m}$ during a 15-second hold time).

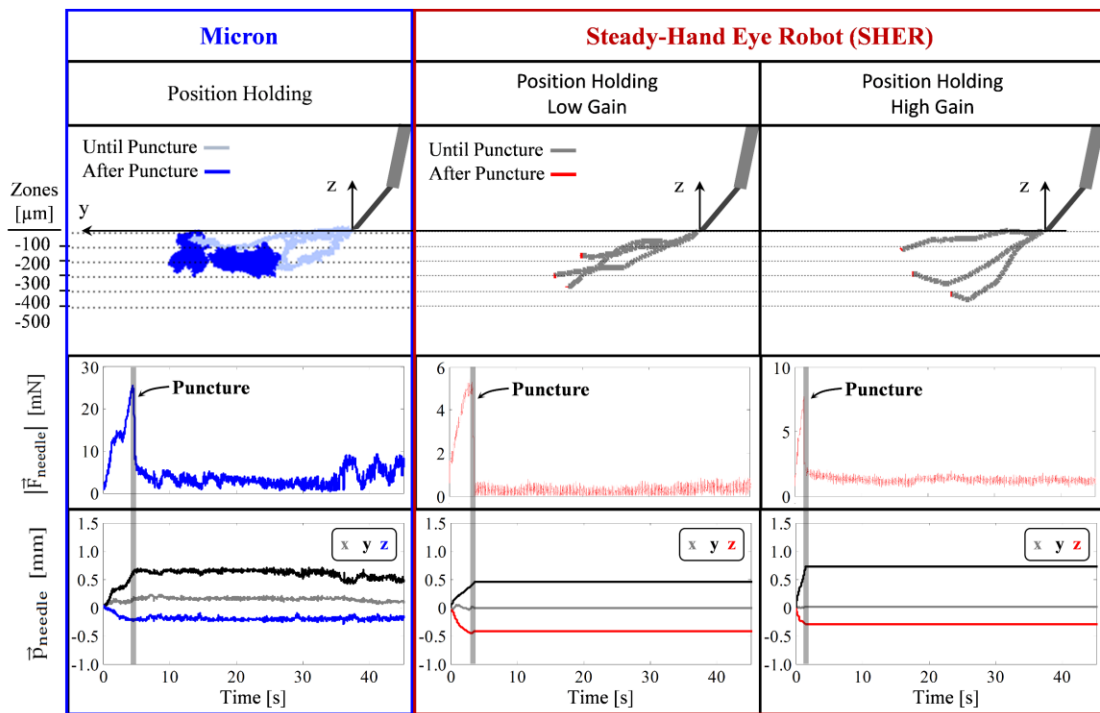


Figure 5.15: Sample measurements from the trials using the automatic position holding modes of two robotic platforms: Micron (blue) and SHER (red). Deviations from the puncture point are significantly reduced with Micron, and almost eliminated with SHER. Modulating the controller gains on the SHER system does not change the performance.

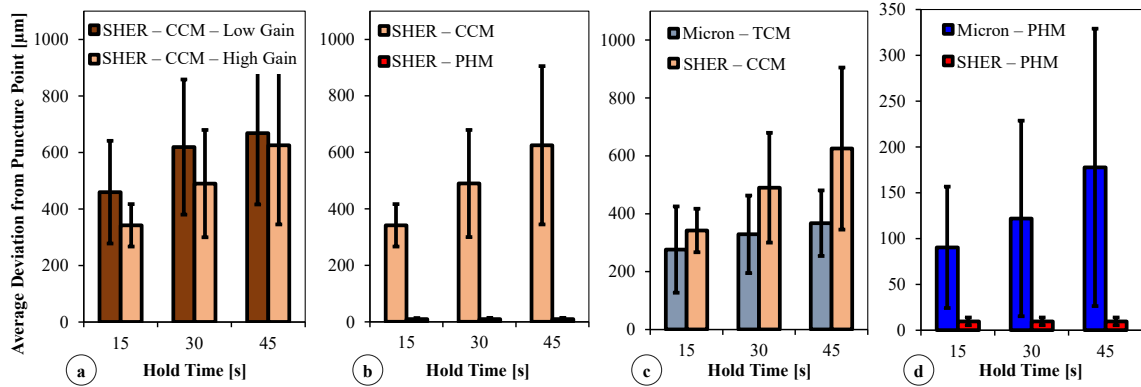


Figure 5.16: Experimental results: Average deviation from the puncture point during the initial 15, 30 and 45 seconds after the puncture. The solid bars represent the mean, and the error bars show ± 1 standard deviation. (a) Changing the controller admittance gain of SHER does not create a statistically significant difference. (b) Activating the force-based puncture detection and PHM significantly reduces the deviation. (c) When Micron and SHER are used in their normal operating modes, TCM and CCM respectively, slightly larger deviation is observed in SHER trials. (d) When Micron and SHER are used with puncture detection and PHM, SHER system fixates the needle position better since Micron has a smaller workspace and its actuators may saturate.

5.4 Conclusion

Retinal vein cannulation (RVC) is a demanding procedure, and its feasibility is currently limited by the challenges in identifying the moment of venous puncture, achieving cannulation and maintaining cannulation during drug delivery. In this chapter, we responded to these problems using the force-sensing microneedle developed in Chapter 3 in combination with robotic manipulators, Micron and the Steady-Hand Eye Robot, to help the operator detect the instant of puncture, and maintain cannulation for a longer period by holding the microneedle fixed inside the vein.

To identify the instant of venous puncture, two methods were explored. The first method based on the time derivative of only the tool tip forces required careful tuning of a threshold value that distinguishes the puncture from other force drops for each user. The second method which made use of both the tool tip force and position information together, and monitored the inner product of force variation and tool velocity vectors,

revealed a more reliable prediction of the puncture without requiring the adjustment of any user-dependent parameters.

The second contribution of this chapter is an automatic position holding feature which was developed to switch from a sole tremor canceling operation to a full motion cancellation. After identifying the venous puncture, the robotic system, either Micron or SHER, is commanded to hold the cannula fixed at the detected puncture position. Using an artificial phantom, we conducted a multi-user study with subjects from three different levels of skill and experience evaluating the performance of Micron system with and without this new feature. Results showed that the developed puncture detection algorithm combined with active positive holding can maintain the needle tip inside the vein for a much longer time especially for smaller veins, and that it significantly attenuates the tool motion in the vein following venipuncture and cannulation.

The third contribution of the chapter is a performance comparison study between two robotic systems for retinal vein cannulation, Micron and SHER, with or without the aid of puncture detection and automatic position holding features. Micron is a compact handheld system that feels more like a standard surgical instrument. However, it provides a limited workspace. If the motion artifact is beyond a certain level, the actuators saturate and the device cannot fully compensate the undesired motion to hold the cannula fixed. The SHER system does not have this saturation issue, but it has a larger footprint than the Micron system and exerts a higher resistance force on the user's hand. The sensitivity and feel of this robot can be altered by modulating the gains on the cooperative controller. Our experiments have shown however that modulating the admittance control gain of SHER alone is not a very effective solution for preventing the undesired tool motion after

venous puncture. Nevertheless, after using puncture detection and automatic position holding, the deviation from the puncture point was significantly reduced, by 65% with Micron, and by 95% with SHER representing a potential advantage over freehand for both.

The evaluation studies presented in this chapter is based upon a fixed phantom position, and are limited to the very consistent mechanical behavior of an artificial phantom. A performance evaluation integrating the effect of variability in tissue properties using in vivo models in the future may reveal more distinguishing results between the two robotic platforms, and may lead to greater difference in the performance of novice and expert operators. In a real clinical scenario, after venous puncture, the cannula needs to be maintained fixed relative to the tissue. Therefore, it is essential to account for potential movement of the tissue. Force information from the sensitized cannula may be used to detect relative movements and stabilize the cannula relative to the vasculature. Alternatively, optical coherence tomography guidance can be used after integrating an additional imaging fiber on the sensitized cannula to track and fixate tool-tissue distance after the venous puncture, which are some of the potential future directions to pursue in this branch.

Publications

1. H. Zhang, **B. Gonenc**, and I. Iordachita, "Admittance Control for Robot-Assisted Retinal Vein Micro-Cannulation under Human-Robot Collaborative Mode," *Int. Conf. on Control, Automation and Systems*, 2017 – submitted.
2. **B. Gonenc**, N. Tran, P. Gehlbach, R.H. Taylor, and I. Iordachita, "Robot-Assisted Retinal Vein Cannulation with Force-Based Puncture Detection: Micron vs. the Steady-Hand Eye Robot," *Int. Conf. of the IEEE EMBS (EMBC'16)*, 2016, pp. 5107-5111.

3. **B. Gonenc**, N. Tran, C.N. Riviere, P. Gehlbach, R.H. Taylor, and I. Iordachita, "Force-Based Puncture Detection and Active Position Holding for Assisted Retinal Vein Cannulation," *Int. Conf. on Multisensor Fusion and Integration for Intelligent Systems (MFI'15)*, 2015, pp. 322-327 - **Best Paper Award**.

CHAPTER 6 : CONCLUSIONS

In vitreoretinal procedures, a very fine manipulation on delicate tissues is required. Given the physiological hand tremor of the operator and very limited tactile perception of tool-tissue interactions, surgical task performance is constrained by natural human capabilities, and relies on the advanced surgical skills and experience of the surgeon. Previous chapters introduced novel force-sensing instruments that quantify tool-tissue interaction forces, methods that combine these tools with distinct robotic platforms to achieve motion guidance and force feedback, and demonstrated their performance for membrane peeling and retinal vein cannulation tasks. In this Chapter, the technical achievements and contribution of this dissertation are summarized along with some discussion of future research directions.

6.1 Summary and Recapitulation of Contributions

Chapter 1 introduced the clinical problems in vitreoretinal surgery focusing on two distinct procedures. First is epiretinal membrane peeling, which is the most common vitreoretinal operation. The tissue manipulation forces in this procedure are mostly imperceptible to the surgeon, and depending on the applied forcing on the retina, serious complications may arise. In addition, physiological hand tremor limits the precision while manipulating the surgical tool close to the retina. The second procedure is retinal vein cannulation, which is not a routinely performed procedure currently due to three main challenges. To cannulate a small retinal vein, a properly small cannula is required that is clearly visible under the microscope and that will endure forces without breaking during the procedure. The second challenge is to insert the cannula to the correct depth, in other words halting needle insertion at the correct time without overshooting the vein although

detecting the instant of venous puncture quickly is very difficult. The third challenge is to maintain intravenous stability after puncture and hold the needle fixed in place for several minutes until the infusion is completed.

Chapter 2 reviewed the related work on force sensing in microsurgery and robotic systems for ophthalmology with different control approaches. These studies showed the significance of force sensing and force feedback in medical robotics. However, none of them were suited to sense forces in the vitreoretinal surgery. Consequently, the prior robotic platforms could not incorporate tool-tissue interaction forces and provide the required assistance during membrane peeling and retinal vein cannulation procedures.

Chapter 3 presented two main categories of ophthalmic tools with integrated force sensing at the tool tip. The force sensing was provided by several optical fibers, fiber Bragg grating strain sensors, lying along and inside the tool shaft of these instruments. The first category consisted of micro-forceps that enabled delamination of membranes with a firm grasp while providing a real-time measurement of the peeling forces. Various architectures were developed for measuring only the transverse forces in 2 dimensions (2-DOF tools) or all forces in 3 dimensions (3-DOF tools). A linear model was used to compute forces for 2-DOF tools. For the 3-DOF tools, a second-order Bernstein polynomial model was applied to describe the nonlinear behavior of sensors. The second category of tools in this chapter was a force-sensing microneedle for retinal vein cannulation. This instrument had a prebent tip (\varnothing 70 μm) for approaching the retinal vasculature at an optimal angle, which can be straightened while inserting through the sclera via an actuation mechanism. Various concepts were presented for actuating the tool manually and using the force-sensing tool handheld or for actuating the tool via a

motor in a modular compact form factor that can be easily attached onto robotic platforms as an end-effector. An experimental calibration approach was followed for each instrument to transform fiber Bragg readings to force measurements. The tools demonstrated very fine force-sensing capability within an accuracy of 0.25 mN and 2 mN in transverse and axial directions, respectively.

Contributions: (1) novel force-sensing micro-forceps tools for membrane peeling via motorized actuation mechanisms and sensor configurations to capture 3 dimensional forces at the tool tip; (2) a novel force-sensing microneedle for retinal vein cannulation.

Chapter 4 introduced three distinct methods to provide a precise motion and to limit applied forces in membrane peeling. Based on measurements from the force-sensing tools, an auditory feedback mechanism was implemented on two distinct robotic platforms: the cooperatively-controlled Steady-Hand Eye Robot and the handheld Micron. The performance of each system was comparatively evaluated, which revealed that force feedback combined with either system for tremor canceling and precise tool manipulation could effectively help in maintaining forces below a preset threshold. By introducing micro-vibrations along the peeling trajectory at an optimal amplitude and frequency, the mean peeling force could be attenuated. Using the motorized tools, the tissue could be automatically released in case excessive forces are sensed to prevent their transfer to the retina.

Contributions: (1) a comparative evaluation of auditory force feedback on two distinct robotic systems with force-sensing tools; (2) a novel micro-vibratory modulation method that facilitates membrane delamination and hence reduces the peeling force; (3) an

automatic tissue release mode that makes use of the motorized actuation of the new tools developed in Chapter 3 and helps limiting the peeling force.

Chapter 5 presented a novel puncture detection method for assisting retinal vein cannulation based on the force measurements from the force-sensing microneedle and the tracked tool tip position. The method could precisely identify the moment of venous puncture. Combining the force-sensing microneedle with two robotic systems, the Steady-Hand Eye Robot and Micron, a position holding feature was developed that aimed to cancel not only the hand tremor but also the drift of the operator to maintain the needle fixed inside the vein after the venous puncture. Experiments revealed significantly reduced motion and improved ability to maintain the needle closer to the point of puncture for a longer period on both systems.

Contributions: (1) a novel method that reliably predicts the instant of venous puncture based on both the measured tool-tissue interaction force and the tracked tool tip position; (2) a robotic fixation method for holding the needle inside the vein after the venous puncture; (3) an evaluation study comparing the performance using two distinct robotic platforms.

In summary, the force-sensing instruments combined with robotic assistance methods presented in this dissertation demonstrated their potential to provide enhanced information and feedback to the surgeon, to enable precise interactions with patients – hence, a safer and easier operation – to improve and expand the capabilities of vitreoretinal surgery.

6.2 Future Directions

Currently in vitreoretinal practice, no quantitative record or feedback on the tool-tissue interactions is available yet. The performance in surgical manipulations is limited by the natural human capabilities and is highly dependent on the surgeon's skills and experience. This dissertation demonstrated the ability to monitor tool-tissue interactions through force-sensing ophthalmic instruments and the ability to assist surgical interactions for enhanced safety via robotic assistance. The presented technology enables the precise measurement and control of tool-tissue interaction forces during surgery, which forms the foundation for a better understanding of tissue behavior during key surgical tasks, integrated assistive systems for safer and easier procedures, and substantial changes in clinical care enabling new and potentially more effective treatment methods.

The technology presented in this dissertation has been evaluated using artificial phantoms or ex-vivo models. The developed force-sensing instruments and the accompanying robotic platforms are yet in prototype stage, which need further efforts to address various aspects (safety, cost and clinical workflow) and translate into clinical use. First, more developmental effort and extensive validation studies using animal models are required to assure the safety of both the hardware and the software [137-139]. Another important parameter for the translation of the developed device to clinical practice is their cost-effectiveness. Sensitized instruments and robotic platforms introduce not only additional equipment cost to the operating room, but also may increase the cost of surgery by adding onto the duration and complexity of procedures. To compensate for this and promote acceptance by clinicians, demonstration of enhanced surgical capabilities, and evaluation of the longer-term benefits, such as reduced hospital stays due to safer procedures with

less complications or application of new more effective treatment methods, are important. The new sensitized robotic equipment and their method of use should also well integrate in the surgical workflow. Since operating rooms are already quite busy and cluttered, any additional system to be introduced into this environment needs to be ergonomic, easy to use, and minimally obtrusive. For instance, the force-sensing tools developed in this work carry three to four fiber optic sensors, each of which has a separate connector that needs to be plugged into an external additional equipment, an optical sensing interrogator, in a specific order. Furthermore, depending on the tool used (micro-forceps or microneedle) selection of the correct set of calibration parameters is required before starting the operation. This is currently an inconvenient procedure, though can be addressed in commercial products by possible improvements, for instance by using a single fiber optic connector and an automatic tool parameter loading method with RFID.

Besides translation to clinical use, there are several future research directions that will advance the smart instrumentation and robotic guidance methods in vitreoretinal surgery. Force-sensing tools enable detection of the very small tool-tissue interaction forces, bringing the sense of feel to the operation. In a parallel branch, instruments with integrated imaging fibers have been developed for retinal microsurgery based on optical coherence tomography (OCT) [78]. These tools, via their integrated OCT fibers, can see what the surgeon cannot visualize through the microscope: the layers of an underneath the retina. Based on this feature, they can effectively detect the distance between the tool tip and the retinal layers, and guide the instrument to a specific layer for targeted drug delivery (which may enable safe cannulation of retinal vein and/or delivery of stem cells into the retina and gene therapies), or maintain a desired offset from delicate layers to

prevent injuries by actively compensating operator's involuntary movements. In the future, fusion of these technologies can lead to smart instruments that can both sense and see, which will have great significance not only for intra-operative assistance to the surgeon but also for characterizing the mechanical behavior of retinal tissues. Based on the force and tissue motion sensing capabilities, force maps of retinal tissues can be generated, characterizing tissue deformation with corresponding forces. While a single force map represents individual tissue characteristics, a large collection of force maps can form a library of surgical manipulations and tissue interactions. This library can be used for surgical planning, monitoring, evaluation, developing virtual reality based platforms for faster and better training of new surgeons, and even studying new surgical methods that lessen trauma and increase the therapeutic effect. As we progress through these continuous improvements of robotic actuation, sensing and vision, new standards will be set in health care.

BIBLIOGRAPHY

- [1] J. H. Kempen, B. J. O'Colmain, M. C. Leske, S. M. Haffner, R. Klein, S. E. Moss, H. R. Taylor, and R. F. Hamman, "The prevalence of diabetic retinopathy among adults in the United States," *Arch Ophthalmol*, vol. 122, no. 4, pp. 552-563, 2004.
- [2] X. Zhang, J. B. Saaddine, C. F. Chou, M. F. Cotch, Y. J. Cheng, L. S. Geiss, E. W. Gregg, A. L. Albright, B. Klein and R. Klein, "Prevalence of diabetic retinopathy in the United States," *JAMA*, vol. 304, no. 6, pp. 649-656, 2010.
- [3] J. B. Saaddine, A. A. Honeycutt, K. V. Narayan, X. Zhang, R. Klein, and J. P. Boyle, "Projection of diabetic retinopathy and other major eye diseases among people with diabetes mellitus," *Arch Ophthalmol*, vol. 126, no. 12, pp. 1740-1747, 2008.
- [4] S. Sharma S, T. H. Mahmoud, and S. M. Hariprasad, "Surgical management of proliferative diabetic retinopathy," *Ophthalmic Surg Lasers Imaging Retin*, vol. 45, no. 3, pp. 188-193, 2014.
- [5] S. Chang, E. M. Gregory-Roberts, S. Park, K. Laud, S. D. Smith, and Q. V. Hoang, "Double peeling during vitrectomy for macular pucker: the Charles L. Schepens Lecture," *JAMA Ophthalmol*, vol. 131, no. 4, pp. 525-530, 2013.
- [6] C. H. Ng, N. Cheung, J. J. Wang, A. Islam, E. K. Klein, R. Klein, and T. Y. Wong, "Prevalence and risk factors for epiretinal membranes in a multi-ethnic United States population," *Ophthalmology*, vol. 118, no. 4, pp. 694-699, 2011.
- [7] U. C. Christensen. "Value of internal limiting membrane peeling in surgery for idiopathic macular hole and the correlation between function and retinal morphology," *Acta Ophthalmol*, vol 87, pp. 1-23, 2009.
- [8] B. Rahmani, J. M. Tielsch, J. Katz, J. Gottsch, H. Quigle, J. Javitt, and A. Sommer, "The cause-specific prevalence of visual impairment in an urban population. The Baltimore Eye Survey," *Ophthalmology*, vol. 103, no. 11, pp. 1721-1726, 1996.
- [9] Gillis K. Medicare Physician Payment Schedule Services for 2001 - A Summary of Claims Data. In: *Physician Marketplace Report*. Chicago: American Medical Association, 2003.
- [10] S. Rogers, R. L. McIntosh, N. Cheung, L. Lim, J. J. Wang, P. Mitchell, J. W. Kowalski, H. Nguyen, and T. Y. Wong, "The prevalence of retinal vein occlusion: Pooled data from population studies from the United States, Europe, Asia, and Australia," *Ophthalmology*, vol. 117, no. 2, pp. 313-19.e1, Feb. 2010.
- [11] Klein R, Moss SE, Meuer SM, Klein BEK. The 15-year cumulative incidence of retinal vein occlusion: the beaver dam eye study. *Arch Ophthalmol* 2008; 126:513±518. doi: 10.1001/archoph.126.4.513 PMID: 18413521
- [12] Natural history and clinical management of central retinal vein occlusion. The Central Vein Occlusion Study Group. *Arch Ophthalmol*, vol. 115, pp. 486-491, Oct. 1997.

- [13] T.Y. Wong, and I.U. Scott, "Retinal Vein Occlusion, " N Engl J Med , vol. 363, pp. 2135-2144, 2010.
- [14] S.S. Hayreh, "Retinal vein occlusion," Indian J Ophthalmol, vol. 42, no. 3, pp. 109-132, 1994.
- [15] Inagaki K, Ohkoshi K, Ohde S, Deshpande GA, Ebihara N, Murakami A. Subthreshold micropulse photocoagulation for persistent macular edema secondary to branch retinal vein occlusion including best-corrected visual acuity greater than 20/40. J Ophthalmol 2014; 2014:251257. doi: 10.1155/2014/ 251257 PMID: 25276413
- [16] Glacet-Bernard A, Atassi M, Fardeau C, Romanet JP, Tonini M, Contrath J, *et al.* Hemodilution therapy using automated erythrocytapheresis in central retinal vein occlusion: results of a multicenter randomized controlled study. Graefe Arch Clin Exp Ophthalmol 2011; 249:505±512.
- [17] Garcia-Arumi J, Boixadera A, Martinez-Castillo V, Montolio M, Verdugo A, Corcostegui B. Radial optic neurotomy in central retinal vein occlusion: Comparison of outcome in younger vs older patients. Am J Ophthalmol 2007; 143:134±140.e133. PMID: 17113557
- [18] Kumagai K, Furukawa M, Ogino N, Uemura A, Larson E. Long-term outcomes of vitrectomy with or without arteriovenous sheathotomy in branch retinal vein occlusion. Retina 2007; 27:49±54. PMID: 17218915
- [19] Moisseiev E, Goldstein M, Waisbourd M, Barak A, Lowenstein A. Long-term evaluation of patients treated with dexamethaxone intravitreal implant for macular edema due to retinal vein occlusion. Eye 2013; 27:65±71. doi: 10.1038/eye.2012.226 PMID: 23154502
- [20] J.N. Weiss, and L.A. Bynoe, "Injection of tissue plasminogen activator into a branch retinal vein in eyes with central vein occlusion," Ophthalmology, vol. 108(12), pp. 2249-2257, July 2001.
- [21] de Smet MD, Stassen JM, Meenink TCM, *et al.* Release of experimental retinal vein occlusions by direct intraluminal injection of ocriplasmin British Journal of Ophthalmology 2016;100:1742-1746.
- [22] S. Hamid, S.A. Mirza, and I. Shokh, "Branch retinal vein occlusion," J Ayub Med Coll Abbottabad, vol. 20, no. 2, pp. 128-132, June 2008.
- [23] M. K. Tsilimbaris, E. S. Lit, D. J. D'Amico, "Retinal microvascular surgery: A feasibility study," Invest Ophthalmol Vis Sci, vol. 45(6), pp. 1963-1968, Jun. 2004.
- [24] R. N. Sjaarda, B. M. Glaser, J. T. Thompson, R. P. Murphy, and A. Hanham, "Distribution of iatrogenic retinal breaks in macular hole surgery," Ophthalmology, vol. 102:9, pp. 1387-1392, Sep. 1995.
- [25] A. Kwok, D. Leung, C. Hon, and D. Lam, "Vision threatening vitreous hemorrhage after internal limiting membrane peeling in macular surgeries," Br J Ophthalmol, vol. 86, no. 1449-1450, 2002.

- [26] K. Nakata, M. Ohji, Y. Ikuno, S. Kusaka, F. Gomi, and Y. Tano. "Sub-retinal hemorrhage during internal limiting membrane peeling for a macular hole," *Graefe's Arch Clin Exp Ophthalmol*, vol. 241, no. 582-584, 2003.
- [27] H. S. Tan, S. Y. Lesnik, M. Mura, and M. D. de Smet, "Enhanced internal search for iatrogenic retinal breaks in 20-gauge macular surgery," *Br J Ophthalmol*, vol. 94, no. 11, pp. 1490-1502, 2010.
- [28] H. S. Tan, M. Mura, and M. D. de Smet, "Iatrogenic retinal breaks in 25-gauge macular surgery," *Am J Ophthalmol.*, vol 148, no. 3, pp. 427-430, 2009.
- [29] P. K. Gupta, P. S. Jensen, and J. E. de, "Surgical forces and tactile perception during retinal microsurgery," *Lect Notes Comput Sci*, vol. 1679, no. 1218-1225, 1999.
- [30] N. Cutler, M. Balicki, M. Finkelstein, J. Wang, P. Gehlbach, J. McGready, I. Iordachita, R. Taylor, and J. T. Handa, "Auditory force feedback substitution improves surgical precision during simulated ophthalmic surgery," *Investigative Ophthalmol. Visual Sci.*, vol. 54, no. 2, pp. 1316-24, 2013.
- [31] M. K. Tsilimbaris, E. S. Lit, and D. J. D'Amico, "Retinal microvascular surgery: A feasibility study," *Invest. Ophthalmol. Vis. Sci.*, vol. 45, no. 6, pp. 1963-1968, June 2004.
- [32] J. N. Weiss, "Apparatus and method for cannulating retinal blood vessels," U.S. Patent 6 402 734 B1, June 11, 2002.
- [33] M. R. Glucksberg, R. Dunn, and C. P. Giebs, "In vivo micropuncture of retinal vessels," *Graefe's Archive for Clinical and Experimental Ophthalmology*, vol. 231, no. 7, pp. 405-407, July 1993.
- [34] Bynoe LA, Weiss JN. Retinal endovascular surgery and intravitreal triamcinolone acetonide for central vein occlusion in young adults. *Am J Ophthalmol*. 2003;135:382-384.
- [35] Bynoe LA, Hutchins RK, Lazarus HS, Friedberg MA. Retinal endovascular surgery for central retinal vein occlusion: initial experience of four surgeons. *Retina*. 2005;25:625-632.
- [36] Feltgen N, Junker B, Agostini H, Hansen LL. Retinal endovascular lysis in ischemic central retinal vein occlusion: one-year results of a pilot study. *Ophthalmology*. 2007;114:716-723.
- [37] Feltgen N, Agostini H, Auw-Haedrich C, Hansen LL. Histopathological findings after retinal endovascular lysis in central retinal vein occlusion. *Br J Ophthalmol*. 2007;91:558-559. 22.
- [38] Yamamoto T, Kamei M, Sakaguchi H, et al. Comparison of surgical treatments for central retinal vein occlusion; RON vs. cannulation of tissue plasminogen activator into the retinal vein. *Retina*. 2009;29:1167-1174. 23.
- [39] Suzuki Y, Matsushashi H, Nakazawa M. In vivo retinal vascular cannulation in rabbits. *Graefes Arch Clin Exp Ophthalmol*. 2003;241:585-588.

- [40] Pournaras CJ, Petropoulos IK, Pournaras JAC, Stangos AN, Gilodi N & Rungger-Brandle E (2012): The rationale of retinal endovascular fibrinolysis in the treatment of retinal vein occlusion: from experimental data to clinical application. *Retina* 32: 1566–1573.
- [41] Marc D. de Smet , Thijs C. M. Meenink, Tom Janssens, Valerie Vanheukelom, Gerrit J. L. Naus, Maarten J. Beelen, Caroline Meers, Bart Jonckx, Jean-Marie Stassen, Robotic Assisted Cannulation of Occluded Retinal Veins, September 27, 2016 <http://dx.doi.org/10.1371/journal.pone.0162037>
- [42] Willekens, K., Gijbels, A., Schoevaerds, L., Esteveny, L., Janssens, T., Jonckx, B., Feyen, J. H. M., Meers, C., Reynaerts, D., Vander Poorten, E. and Stalmans, P. (2017), Robot-assisted retinal vein cannulation in an in vivo porcine retinal vein occlusion model. *Acta Ophthalmol.* doi:10.1111/aos.13358
- [43] K. Kadonosono, A. Arakawa, S. Yamane, E. Uchio, and Y. Yanagi, “An experimental study of retinal endovascular surgery with a fabricated needle,” *Invest. Ophthalmol. Vis. Sci.*, vol. 52, no. 8, pp. 5790-5793, July 2011.
- [44] Asami T, Kaneko H, Miyake K, et al. An Endovascular Cannulation Needle with an Internal Wire for the Fragmentation of Thrombi in Retinal Vein Occlusion. *Translational Vision Science & Technology.* 2016;5(5):9. doi:10.1167/tvst.5.5.9.
- [45] K. Kadonosono, S. Yamane, A. Arakawa, M. Inoue, T. Yamakawa, E. Uchio, Y. Yanagi, and S. Amano, “Endovascular cannulation with a microneedle for central retinal vein occlusion,” *JAMA Ophthalmol*, vol. 131, no. 6, pp. 783-786, June 2013.
- [46] T. Leng, J.M. Miller, K.V. Bilbao, D.V. Palanker, P. Huie, and M.S. Blumenkranz, “The chick chorioallantoic membrane as a model tissue for surgical retinal research and simulation,” *Retina*, vol. 24:3, pp. 427-434, Jun. 2004.
- [47] W. Wei, C. Popplewell, S. Chang, H. F. Fine, N. Simaan, “Enabling technology for microvascular stenting in ophthalmic surgery,” *Journal of Medical Devices*, vol. 4, no. 1, Mar. 2010.
- [48] A. Gijbels, E.B. Vander Poorten, P. Stalmans, D. Reynaerts, “Development and Experimental Validation of a Force Sensing Needle for Robotically Assisted Retinal Vein Cannulations,” in *Proc. IEEE Int. Conf. on Robotics and Automation*, Seattle, 2015, pp. 2270-2276.
- [49] B. Gonenc, P. Gehlbach, J. Handa, R.H. Taylor, and I. Iordachita, “Force-Sensing Microneedle for Assisted Retinal Vein Cannulation,” in *Proc. IEEE SENSORS 2014*, 2014, pp. 698-701.
- [50] S. P. N. Singh and C. N. Riviere, “Physiological tremor amplitude during retinal microsurgery,” in *Proc. IEEE 28th Annu. Northeast Bioeng. Conf.*, Philadelphia, 2002, pp. 171-172.
- [51] H. Saito, and T. Togawa, “Detection of needle puncture to blood vessel using puncture force measurement,” *Med. Biol. Eng. Comput.*, vol.43, no. 2, pp. 240-244, Mar. 2005.

- [52] O. Ergeneman, J. Pokki, V. Pocepcova, H. Hall, J. J. Abbott, and B. J. Nelson, "Characterization of puncture forces for retinal vein cannulation," *J. Med. Dev.*, vol. 5, no.4, pp. 044504, Dec. 2011.
- [53] Menciassi, A., Eisinberg, A., Scalari, G., Anticoli, C., Carrozza, M., and Dario, P., - Force feedback-based microinstrument for measuring tissue properties and pulse in microsurgery, IEEE International Conf. on Robotics and Automation, 0-7803-6576-3, Pisa,2001.
- [54] Zhang, X., - Silicon microsurgery-force sensor based on diffractive optical MEMS encoders, *Sensor Review*, 24(1), 2004.
- [55] Peirs, J., Clijnen, J., Reynaerts, D., Van Brussel, H., Herijgers, P., Corteville, B., and Boone, S., - A micro optical force sensor for force feedback during minimally invasive robotic surgery, *Sensors and Actuators A: Physical*, 115(2-3), 2004.
- [56] P. Puangmali, H. Liu, L. D. Seneviratne, P. Dasgupta, and K. Althoefer, "Miniature 3-Axis distal force sensor for minimally invasive surgical palpation," *IEEE/ASME Trans. Mechatron.*, vol. 17, no. 4, pp. 646–656, 2012.
- [57] Seibold, U., Kubler, B., and Hirzinger, G., - Prototype of instrument for minimally invasive surgery with 6-axis force sensing capability, IEEE International Conf. on Robotics and Automation, 2005.
- [58] B. Bell, S. Stankowski, B. Moser, V. Oliva, C. Stieger, L.-P. Nolte, M. Caversaccio, and S. Weber, "Integrating optical fiber force sensors into microforceps for ORL microsurgery," in *Proc. IEEE Eng. Med. Biol. Soc. Conf.*, 2010, vol. 2010, pp. 1848–1851.
- [59] Gwang Min Gu, Yong Kyun Shin, Jina Son, Jung Kim, Design and characterization of a photo-sensor based force measurement unit (FMU), *Sensors and Actuators A: Physical*, Volume 182, August 2012, pp. 49-56.
- [60] S. Kyeong *et al.*, "A hand-held micro surgical device for contact force regulation against involuntary movements," *2015 37th Annual International Conference of the IEEE Engineering in Medicine and Biology Society (EMBC)*, Milan, 2015, pp. 869-872.
- [61] K. Zareinia *et al.*, "A Force-Sensing Bipolar Forceps to Quantify Tool–Tissue Interaction Forces in Microsurgery," in *IEEE/ASME Transactions on Mechatronics*, vol. 21, no. 5, pp. 2365-2377, Oct. 2016.
- [62] S. Sunshine, M. Balicki, X. He, K. Olds, J. U. Kang, P. Gehlbach, R. Taylor, I. Iordachita, and J. T. Handa, "A force-sensing microsurgical instrument that detects forces below human tactile sensation," *Retina (Philadelphia, Pa.)*, vol. 33, no. 1, pp. 200–206, Jan. 2013.
- [63] P. J. Berkelman, L. L. Whitcomb, R. H. Taylor, and P. Jensen, "A miniature microsurgical instrument tip force sensor for enhanced force feedback during robot-assisted manipulation," *IEEE Trans. Robotics and Automation*, vol. 19, no. 5, pp. 917–921, Oct. 2003.

- [64] A. S. Jagtap and C. N. Riviere, "Applied force during vitreoretinal microsurgery with handheld instruments," in Proc. IEEE Eng. Med. Biol. Soc., 2004, vol. 4, no. 1, pp. 2771–2773.
- [65] R. Channa, I. Iordachita, and J.T. Handa, "Robotic Vitreoretinal Surgery," Retina, doi: 10.1097/IAE.0000000000001398.
- [66] P.S. Jensen, K.W. Grace, R. Attariwala, J.E. Colgate, and M.R. Glucksberg, "Toward robot-assisted vascular in the retina," Graefes Arch Clin Exp Ophthalmol, vol. 235, no. 11, pp. 696-701, Nov. 1997.
- [67] W. Wei, C. Popplewell, S. Chang, H.F. Fine, N. Simaan, "Enabling technology for microvascular stenting in ophthalmic surgery," Journal of Medical Devices, vol. 4, no. 1, Mar. 2010.
- [68] S. Tanaka *et al.*, "Quantitative assessment of manual and robotic microcannulation for eye surgery using new eye model," Int J Med Robotics Comput Assist Surg, Apr. 2014.
- [69] Thijs Meenink, Gerrit Naus, Marc de Smet, Maarten Beelen, Maarten Steinbuch; Robot assistance for micrometer precision in vitreoretinal surgery. Invest. Ophthalmol. Vis. Sci. 2013;54(15):5808.
- [70] I. Fleming, M. Balicki, J. Koo, I. Iordachita, B. Mitchell, J. Handa, G. Hager, and R. Taylor, "Cooperative robot assistant for retinal microsurgery," Med. Image Comput. Comput. Assist. Interv., vol. 5242, 2008, pp. 543-550.
- [71] A. Gijbels, N. Wouters, P. Stalmans, H. Van Brussel, D. Reynaerts, and E. Vander Poorten, "Design and realisation of a novel robotic manipulator for retinal surgery," in Proc. IEEE Int. Conf. on Intelligent Robots and Systems, Tokyo, 2013, pp. 3598-3603.
- [72] B.C. Becker, S. Yang, R.A. MacLachlan, and C.N. Riviere, "Towards vision-based control of a handheld micromanipulator for retinal cannulation in an eyeball phantom," in Proc. 4th IEEE RAS EMBS Int. Conf. Biomed. Robot. Biomechatron., 2012, pp. 44-49.
- [73] W.T. Latt, U.X. Tan, C.Y. Shee, and W.T. Ang, "A compact handheld active physiological tremor compensation instrument," in Proc. IEEE/Amer.Soc. Mech. Eng. Int. Conf. Adv. Intell. Mechatronics, 2009, pp. 711–716.
- [74] C.J. Payne, K. Kwok; and G. Yang, "An ungrounded hand-held surgical device incorporating active constraints with force-feedback," in Proc. IEEE Int. Conf. on Intelligent Robots and Systems (IROS '13), 2013, pp.2559-2565.
- [75] D. Chang, G. M. Gu, and J. Kim, "Design of a novel tremor suppression device using a linear delta manipulator for micromanipulation," in Proc. IEEE Int. Conf. on Intelligent Robots and Systems (IROS '13), 2013, pp.413-418.
- [76] A. Saxena and R.V. Patel, "An active handheld device for compensation of physiological tremor using an ionic polymer metallic composite actuator," in Proc. IEEE Int. Conf. on Intelligent Robots and Systems (IROS '13), 2013, pp.4275-4280.

- [77] S. Kyeong *et al.*, "A hand-held micro surgical device for contact force regulation against involuntary movements," *2015 37th Annual International Conference of the IEEE Engineering in Medicine and Biology Society (EMBC)*, Milan, 2015, pp. 869-872.
- [78] Cheon, G. W., Lee, P., Gonenc, B., Gehlbach, P. L., & Kang, J. U. (2016). Active depth-guiding handheld micro-forceps for membranectomy based on CP-SSOCT. In *Optical Fibers and Sensors for Medical Diagnostics and Treatment Applications XVI*.(Vol. 9702). [97020C] SPIE. DOI: 10.1117/12.2212715
- [79] <http://www.ox.ac.uk/news/2016-09-12-world-first-robot-eye-operation>, last accessed on 05/15/2017.
- [80] <https://www.kuleuven.be/english/news/2017/surgical-eye-robot-performs-precision-injection-in-patient-with-retinal-vein-occlusion>, last accessed on 05/15/2017.
- [81] C. N. Riviere, W. T. Ang, and P. K. Khosla, "Toward active tremor canceling in handheld microsurgical instruments," *IEEE Transactions on Robotics and Automation*, vol. 19, no. 5, pp. 793–800, 2003.
- [82] R. A. Maclachlan, B. C. Becker, J. C. Tabar, G. W. Podnar, L. A. Lobes, and C. N. Riviere, "Micron: an actively stabilized handheld tool for microsurgery," *IEEE Transactions on Robotics*, vol. 28, no. 1, pp. 195–212, 2012.
- [83] B. C. Becker, S. Voros, R. a. MacLachlan, G. D. Hager, and C. N. Riviere, "Active guidance of a handheld micromanipulator using visual servoing," *IEEE International Conference on Robotics and Automation*, pp. 339–344, 2009.
- [84] B. C. Becker, R. a. MacLachlan, G. D. Hager, and C. N. Riviere, "Handheld micromanipulation with vision-based virtual fixtures," *IEEE International Conference on Robotics and Automation*, pp. 4127–4132, 2011.
- [85] S. Yang, M. Balicki, R. a. MacLachlan, X. Liu, J. U. Kang, R. H. Taylor, and C. N. Riviere, "Optical coherence tomography scanning with a handheld vitreoretinal micromanipulator," in *International Conference of the IEEE Engineering in Medicine and Biology Society*, 2012, pp. 948–951.
- [86] G. Stetten, B. Wu, R. Klatzky, J. Galeotti, M. Siegel, R. Lee, F. Mah, A. Eller, J. Schuman, and R. Hollis, "Hand-held force magnifier for surgical instruments," in *International Conference on Information Processing in Computer-Assisted Interventions*, vol. LNCS 6689, 2011, pp. 90–100.
- [87] C. Payne, H. Rafii-Tari, H. Marcus, and G. Yang, "Hand-held microsurgical forceps with force-feedback for micromanipulation," *IEEE International Conference on Robotics and Automation*, pp. 284–289, 2014.
- [88] C. Song, D. Y. Park, P. L. Gehlbach, S. J. Park, and J. U. Kang, "Fiber-optic OCT sensor guided "SMART" micro-forceps for microsurgery," *Biomedical Optics Express*, vol. 4, no. 7, pp. 1045–1050, 2013.
- [89] R. Taylor, P. Jensen, L. Whitcomb, A. Barnes, R. Kumar, D. Stoianovici, P. Gupta, Z. Wang, E. DeJuan, and L. Kavoussi, "A Steady-Hand Robotic System

- for Microsurgical Augmentation,” *The International Journal of Robotics Research*, vol. 18, no. 12, pp. 1201–1210, 1999.
- [90] R. Kumar, P. Berkelman, P. Gupta, A. Barnes, P. Jensen, L. Whitcomb, and R. Taylor, “Preliminary experiments in cooperative human/robot force control for robot assisted microsurgical manipulation,” in *IEEE International Conference on Robotics and Automation*, 2000, pp. 610–617.
- [91] B. Mitchell, J. Koo, I. Iordachita, P. Kazanzides, A. Kapoor, J. Handa, G. Hager, and R. Taylor, “Development and application of a new steady-hand manipulator for retinal surgery,” in *IEEE International Conference on Robotics and Automation*, 2007, pp. 623–629.
- [92] I. Fleming, M. Balicki, J. Koo, I. Iordachita, B. Mitchell, J. Handa, G. Hager, and R. Taylor, “Cooperative robot assistant for retinal microsurgery,” in *International Conference on Medical Image Computing and Computer-Assisted Intervention*, vol. 11, no. Pt 2. Springer, Jan. 2008, pp. 543–550.
- [93] A. Uneri, M. A. Balicki, J. Handa, P. Gehlbach, R. H. Taylor, and I. Iordachita, “New Steady-Hand Eye Robot with micro-force sensing for vitreoretinal surgery,” in *IEEE International Conference on Biomedical Robotics and Biomechatronics*, 2010, pp. 814–819.
- [94] X. He, D. Roppenecker, D. Gierlach, M. Balicki, K. Olds, P. Gehlbach, J. Handa, R. Taylor, and I. Iordachita, “Toward clinically applicable steady-hand eye robot for vitreoretinal surgery,” in *ASME 2012 International Mechanical Engineering Congress and Exposition*, vol. 2, 2012, pp. 145–153.
- [95] A. Othonos and K. Kalli, *Fiber Bragg Gratings: Fundamentals and Applications in Telecommunications and Sensing*. Artech House, 1999.
- [96] S. Ambastha, S. Umesh, S. Dabir, and S. Asokan, “Spinal needle force monitoring during lumbar puncture using fiber bragg grating force device,” *Journal of Biomedical Optics*, vol. 21(11): 117002, Nov. 2016.
- [97] D. Tosi, E. G. Macchi, M. Gallati, G. Braschi, A. Cigada, S. Poeggel, G. Leen, and E. Lewis, “Monitoring of radiofrequency thermal ablation in liver tissue through fibre Bragg grating sensors array,” *Electron. Lett.*, vol. 50, no. 14, pp. 981-983, 2014.
- [98] S. Sefati, F. Alambeigi, R. Murphy, I. Iordachita, and M. Armand, "FBG-Based Large Deflection Shape Sensing of a Continuum Manipulator: Manufacturing Optimization," in *Proc. International Conference of the IEEE SENSORS (SENSORS'16)*, 2016, pp. 1511-1513.
- [99] I. Iordachita, Z. Sun, M. Balicki, J. Kang, S. Phee, J. Handa, P. Gehlbach, and R. Taylor, “A sub-millimetric, 0.25 mn resolution fully integrated fiber-optic force-sensing tool for retinal microsurgery,” *International Journal of Computer Assisted Radiology and Surgery*, vol. 4, pp. 383–390, Jun. 2009.
- [100] S. Charles, “Techniques and tools for dissection of epiretinal membranes,” *Graefe’s Archive for Clinical and Experimental Ophthalmology*, vol. 241:5, pp. 347-352, May 2003.

- [101] I. Kuru, B. Gonenc, M. Balicki, J. Handa, P. Gehlbach, R. H. Taylor, and I. Iordachita, "Force Sensing Micro-Forceps for Robot Assisted Retinal Surgery," in Proc. International Conference of the IEEE EMBS (EMBC '12), 2012, pp. 1401-1404.
- [102] B. Gonenc, E. Feldman, P. Gehlbach, J. Handa, R. H. Taylor, and I. Iordachita, "Towards Robot-Assisted Vitreoretinal Surgery: Force-Sensing Micro-Forceps Integrated with a Handheld Micromanipulator," in Proc. IEEE Int. Conf. on Robotics and Automation (ICRA'14), 2014, pp. 1399-1404.
- [103] B. Gonenc, P. Gehlbach, J. Handa, R. H. Taylor, and I. Iordachita, "Motorized Force-Sensing Micro-Forceps with Tremor Cancelling and Controlled Micro-Vibrations for Easier Membrane Peeling," in Proc. IEEE RAS EMBS Int. Conf. Biomed. Robot. Biomechatron. (BioRob'14), 2014, pp. 244-251.
- [104] B. Gonenc, P. Gehlbach, R.H. Taylor, I. Iordachita, "Effects of Micro-Vibratory Modulation during Robot-Assisted Membrane Peeling," in IEEE/RSJ Int. Conf. on Intelligent Robots and Systems (IROS'15), Hamburg, Germany, 2015, pp. 3811-3816.
- [105] B. Gonenc, J. Handa, P. Gehlbach, R. H. Taylor, and I. Iordachita, "Design of 3-DOF Force Sensing Micro-Forceps for Robot Assisted Vitreoretinal Surgery," in Proc. International Conference of the IEEE EMBS (EMBC'13), 2013, pp. 5686-5689.
- [106] B. Gonenc and I. Iordachita, "3-DOF Force-Sensing Micro-Forceps for Vitreoretinal Surgery," Int. Conf. of Mechanical Engineering (ICOME'13), Craiova, Romania, 2013.
- [107] O. Sigmund, - Design of Multiphysics Actuators Using Topology Optimization - Part I: One-material Structures, Computer Methods in Applied Mechanics and Engineering, Vol. 190 (49-50), 2001.
- [108] B. Gonenc and I. Iordachita, "FBG-Based Transverse and Axial Force-Sensing Micro-Forceps for Retinal Microsurgery," in Proc. IEEE SENSORS 2016, 2016, pp. 667-669.
- [109] F. Gerald, Curves and Surfaces for Computer Aided Geometric Design, 4th ed. New York, NY, USA: Academic, 1996.
- [110] B. Gonenc, A. Chamani, J. Handa, P. Gehlbach, R. H. Taylor and I. Iordachita, "3-DOF Force-Sensing Motorized Micro-Forceps for Robot-Assisted Vitreoretinal Surgery," in *IEEE Sensors Journal*, vol. 17, no. 11, pp. 3526-3541, Jun1, 1 2017.
- [111] Matthew D. McCawley, "Trocar cannula device with retention feature," U.S. Patent 8 062 260, Nov, 22, 2011.
- [112] A. Gao, B. Gonenc, J. Guo, H. Liu, and I. Iordachita, "3-DOF Force-Sensing Micro-Forceps for Robot-Assisted Membrane Peeling: Intrinsic Actuation Force Modeling," IEEE RAS EMBS Int. Conf. Biomed. Robot. Biomechatron. (BioRob'16), 2016, pp. 489-494.

- [113] A. Gupta, B. Gonenc, M. Balicki, K. Olds, J. Handa, P. Gehlbach, R. H. Taylor, and I. Iordachita, "Human Eye Phantom for Developing Computer and Robot-Assisted Epiretinal Membrane Peeling," in Proc. International Conference of the IEEE EMBS (EMBC'14), 2014, pp. 6864-6867.
- [114] X. He, J. Handa, P. Gehlbach, R. Taylor, and I. Iordachita, "A submillimeter 3-dof force sensing instrument with integrated fiber bragg grating for retinal microsurgery," IEEE Transactions on Biomedical Engineering, vol. 61, no. 2, pp. 522-534, 2014.
- [115] Kersey A, Berkoff T, Morey W. Fiber-optic Bragg grating strain sensor with drift-compensated high-resolution interferometric wavelength-shift detection. Optics letters. 1993;18(1):72-4. [PubMed]
- [116] Xu M, Dong L, Reekie L. Temperature-independent strain sensor using a chirped Bragg grating in a tapered optical fibre. Electronics Letters. 1995;31(10):823-825.
- [117] James S, Dockney M, Tatam R. Simultaneous independent temperature and strain measurement using in-fibre bragg grating sensors. Electronics Letters. 1996;32(12):1133-1134.
- [118] Xu M, Archambault JL, Reekie L, Dakin JP. Discrimination between strain and temperature effects using dual-wavelength fibre grating sensors. Electronics Letters. 1994;30(13):1085-1087.
- [119] A. A. G. Abushagur, A. A. A. Bakar, M. S. Dzulkefly Bin Zan and N. Arsad, "A Novel Technique Employing Tapered Fiber Bragg Grating to Solve the Axial/Transverse Forces Crosstalk in Microsurgical Instruments," in IEEE Sensors Journal, vol. 16, no. 21, pp. 7671-7680, Nov.1, 2016.
- [120] G. Peyman, S. Meffert, F. Chou, and M. Conway, Vitreoretinal Surgical Techniques. Taylor & Francis, 2000.
- [121] R. J. Last, Ed., Wolff's Anatomy of the Eye and Orbit. Including the Central Connections, Developments, and Comparative Anatomy of the Visual Apparatus, 6th ed. W. B. Saunders, 1968.
- [122] X. He, M.A. Balicki, J.U. Kang, P.L. Gehlbach, J.T. Handa, R.H. Taylor, and I.I. Iordachita, "Force sensing micro-forceps with integrated fiber bragg grating for vitreoretinal surgery," in Proc. Of SPIE, vol. 8218, pp. 82180W 1-7, Feb. 2012.
- [123] Okamura and A.M., "Methods for haptic feedback in teleoperated robot-assisted surgery," Industrial Robot: An International Journal, vol. 31, no. 6, pp. 499-508, 2004.
- [124] M. Kitagawa, D. Dokko, A. M. Okamura, and D. D. Yuh, "Effect of sensory substitution on suture-manipulation forces for robotic surgical systems." The Journal of Thoracic and Cardiovascular Surgery, vol. 129, no. 1, pp. 151-8, 2005.
- [125] C. E. Reiley, T. Akinbiyi, D. Burschka, D. C. Chang, A. M. Okamura, and D. D. Yuh, "Effects of visual force feedback on robot-assisted surgical task

- performance,” *Journal of Thoracic and Cardiovascular Surgery*, vol. 135, no. 1, pp. 196–202, 2008.
- [126] M. Balicki, “Augmentation of human skill in microsurgery,” Ph.D. dissertation, Johns Hopkins University, 2014.
- [127] M. Balicki, A. Uneri, I. Iordachita, J. Handa, P. Gehlbach, and R. Taylor, “Micro-force sensing in robot assisted membrane peeling for vitreoretinal surgery,” in *International Conference on Medical Image Computing and Computer Assisted Intervention*, vol. 13, 2010, pp. 303–310.
- [128] B. Gonenc, M. A. Balicki, J. Handa, P. Gehlbach, C. N. Riviere, R. H. Taylor, and I. Iordachita, “Preliminary evaluation of a micro-force sensing handheld robot for vitreoretinal surgery,” in *Proc. IEEE Int. Conf. on Intelligent Robots and Systems (IROS’12)*, 2012, pp. 4125-4130.
- [129] B. Gonenc, J. Handa, P. Gehlbach, R. H. Taylor, and I. Iordachita, “A Comparative Study for Robot Assisted Vitreoretinal Surgery: Micron vs. the Steady-Hand Robot,” in *Proc. IEEE Int. Conf. on Robotics and Automation (ICRA’13)*, 2013, pp. 4832-4837.
- [130] R. N. Stiles, “Mechanical and neural feedback factors in postural hand tremor of normal subjects,” *J. Neurophysiol.*, vol. 44, pp. 40-59, July 1980.
- [131] J. Damadian, “Method of conducting a needle biopsy procedure,” U.S. Patent 6 702 761, Mar, 6, 2001.
- [132] A. Almony, E. Nudleman, G. K. Shah, K. J. Blinder, D. B. Elliott, R. A. Mittra, and A. Tewari, “Techniques, rationale, and outcomes of internal limiting membrane peeling,” *Retina (Philadelphia, Pa.)*, vol. 32, no. 5, pp. 877–891, May 2012.
- [133] B. Gonenc, N. Tran, C.N. Riviere, P. Gehlbach, R.H. Taylor, and I. Iordachita, "Force-Based Puncture Detection and Active Position Holding for Assisted Retinal Vein Cannulation," in *Proc. Int. Conf. on Multisensor Fusion and Integration for Intelligent Systems (MFI'15)*, San Diego, USA, 2015, pp. 322-327.
- [134] B. Gonenc, N. Tran, P. Gehlbach, R.H. Taylor, and I. Iordachita, "Robot-Assisted Retinal Vein Cannulation with Force-Based Puncture Detection: Micron vs. the Steady-Hand Eye Robot," in *Proc. International Conference of the IEEE EMBS (EMBC’16)*, 2016, pp. 5107-5111.
- [135] R. A. MacLachlan, C. N. Riviere, “High-speed microscale optical tracking using digital frequency-domain multiplexing,” *IEEE Trans. Instrumentation and Measurement*, vol. 58, no. 9, pp. 1991-2001, June 2009.
- [136] A. Gijbels, K. Willekens, L. Esteveny, P. Stalmans, D. Reynaerts and E. B. Vander Poorten, "Towards a clinically applicable robotic assistance system for retinal vein cannulation," 2016 6th IEEE International Conference on Biomedical Robotics and Biomechatronics (BioRob), Singapore, 2016, pp. 284-291.
- [137] R. Taylor, H. Paul, P. Kazanzides, B. Mittelstadt, W. Hanson, J. Zuhars, B. Williamson, B. Musits, E. Glassman, and W. Bargar, “Taming the bull: safety in a

precise surgical robot,” in International Conference on Advanced Robotics, 1991, pp. 865–870.

- [138] P. Kazanzides, “Safety design for medical robots,” IEEE Engineering in Medicine and Biology Society Conference, pp. 7208–7211, 2009.
- [139] M. Y. Jung, “State-based safety of component-based medical and surgical robot systems,” Ph.D. dissertation, Johns Hopkins University, 2015.

VITA

Berk Gonenc received his B.S. degree in Mechanical Engineering from Middle East Technical University in 2009, and M.S. degree in Mechanical Engineering from Washington State University Vancouver in 2011. During his M.S. studies, he focused on the development of haptic interfaces for simulation of medical procedures and development of smart actuators for use on these interfaces. He joined the Advanced Medical Instrumentation and Robotics Research Laboratory (AMIRO) and the Laboratory for Computational Sensing and Robotics (LCSR) in Johns Hopkins University in 2011. He received his M.S.E. degree in Mechanical Engineering from Johns Hopkins University in 2014. Working in an interdisciplinary team his work at JHU focused on the development of smart surgical instruments, robotic mechanisms, and novel control methods for assisting retinal microsurgery. He will start work at Verb Surgical in July 2017.

APPENDIX

Technical Drawings and Software

The technical drawings of the force-sensing tools developed in Chapter 3 and the experimental setup used in Chapters 4 and 5 are accessible at:

\\win.ad.jhu.edu\cloud\lcsr-ciis\bgonenc1\TechnicalDrawings

The LabVIEW software developed for the operational modes presented in Chapters 4 and 5 are available at:

\\win.ad.jhu.edu\cloud\lcsr-ciis\bgonenc1\Software

List of Publications and Presentations

Refereed Journal Articles

- J1. **B. Gonenc**, P. Gehlbach, R.H. Taylor, and I. Iordachita, "3-DOF Force-Sensing Motorized Micro-Forceps for Robot-Assisted Vitreoretinal Surgery," *IEEE Sensors Journal*, vol. 17, no. 11, pp. 3526-3541, June 1, 2017.
- J2. G.W. Cheon, **B. Gonenc**, R.H. Taylor, P.L. Gehlbach, and J.U. Kang, "Motorized Micro-Forceps with Active Motion Guidance based on Common-Path SSOCT for Epiretinal Membranectomy," *IEEE Transactions on Mechatronics - in review*.
- J3. M. Li, G. Li, **B. Gonenc**, and I. Iordachita, "Toward Human-Controlled, Real-Time Shape Sensing Based Flexible Needle Steering for MRI-Guided Percutaneous Therapies," *The International Journal of Medical Robotics and Computer Assisted Surgery*, doi: 10.1002/rcs.1762, 2016.
- J4. **B. Gonenc** and H. Gurocak, "Haptic Interface with Hybrid Actuator for Virtual Tissue Cutting," *ASME Computing and Information Science in Engineering*, vol. 16, no. 3, pp. 031002-031002-8, 2016.
- J5. S.S. Gurbani, P. Wilkening, M. Zhao, **B. Gonenc**, G.W. Cheon, I.I. Iordachita, W. Chien, R.H. Taylor, J.K. Niparko, J.U. Kang, "Robot-Assisted Three Dimensional Registration for Cochlear Implant Surgery Using a Common-Path Swept-Source Optical Coherence Tomography Probe," *Journal of Biomedical Optics*, vol. 19, no. 5, pp. 057004/1-8, 2014.
- J6. M.S. Alkan, H. Gurocak, and **B. Gonenc**, "Linear Magnetorheological Brake with Serpentine Flux Path as a High Force and Low Off-State Friction Actuator for Haptics," *Journal of Intelligent Material Systems and Structures*, vol. 24, no. 14, pp. 1699-1713, 2013.
- J7. O.G. Erol, **B. Gonenc**, D. Senkal, S. Alkan, and H. Gurocak, "Magnetic Induction Control with Embedded Sensor for Elimination of Hysteresis in Magnetorheological Brakes," *Journal of Intelligent Material Systems and Structures*, vol. 23, no. 4, pp. 427-440, 2012.
- J8. **B. Gonenc** and H. Gurocak, "Virtual Needle Insertion with Haptic Feedback Using a Hybrid Actuator with DC Servomotor and MR-Brake with Hall-Effect Sensor," *Mechatronics*, vol. 22, no. 8, pp. 1161-1176, 2012.
- J9. **B. Gonenc** and H. Gurocak, "Blending Algorithm for Position Control with a Hybrid Actuator Made of DC Servomotor and Brake," *Industrial Robot: an International Journal*, vol. 38, no. 5, pp. 492-499, 2011.

Refereed Conference Proceedings

- C1. **B. Gonenc** and I. Iordachita, "Safe Tissue Manipulation in Retinal Microsurgery via Motorized Instruments with Force Sensing," *IEEE SENSORS 2017* – submitted.

- C2. A. Gupta, S. Singh, **B. Gonenc**, M. Kobilarov, and I. Iordachita, "Toward Sclera-Force-Based Robotic Assistance for Safe Micromanipulation in Vitreoretinal Surgery," *IEEE SENSORS 2017* – submitted.
- C3. H. Zhang, **B. Gonenc**, and I. Iordachita, "Admittance Control for Robot-Assisted Retinal Vein Micro-Cannulation under Human-Robot Collaborative Mode," *Int. Conf. on Control, Automation and Systems*, 2017 – submitted.
- C4. S. Chen, **B. Gonenc**, M. Li, D.Y. Song, E.C. Burdette, I. Iordachita, and P. Kazanzides, "Needle Release Mechanism Enabling Multiple Insertions with an Ultrasound-guided Prostate Brachytherapy Robot," *Int. Conf. of the IEEE EMBS (EMBC'17)*, 2017 – accepted.
- C5. J. Song, **B. Gonenc**, J. Guo, and I. Iordachita, "Intraocular Snake Integrated with the Steady-Hand Eye Robot for Assisted Retinal Microsurgery," *IEEE Int. Conf. on Robotics and Automation (ICRA'17)*, 2017, pp. 6724-6729.
- C6. **B. Gonenc** and I. Iordachita, "FBG-Based Transverse and Axial Force-Sensing Micro-Forceps for Retinal Microsurgery," *IEEE SENSORS 2016*, 2016, pp. 667-669.
- C7. **B. Gonenc**, N. Tran, P. Gehlbach, R.H. Taylor, and I. Iordachita, "Robot-Assisted Retinal Vein Cannulation with Force-Based Puncture Detection: Micron vs. the Steady-Hand Eye Robot," *Int. Conf. of the IEEE EMBS (EMBC'16)*, 2016, pp. 5107-5111.
- C8. A. Gao, **B. Gonenc**, J. Guo, H. Liu, and I. Iordachita, "3-DOF Force-Sensing Micro-Forceps for Robot-Assisted Membrane Peeling: Intrinsic Actuation Force Modeling," *IEEE RAS EMBS Int. Conf. Biomed. Robot. Biomechatron. (BioRob'16)*, 2016, pp. 489-494.
- C9. G.W. Cheon, P. Lee, **B. Gonenc**, P.L. Gehlbach, J.U. Kang, "Active Depth-guiding Handheld Micro-Forceps for Membranectomy based on CP-SSOCT," *Proc. SPIE 9702, Optical Fibers and Sensors for Medical Diagnostics and Treatment Applications XVI*, 2016, doi:10.1117/12.2212715.
- C10. K. Kim, M. Li, **B. Gonenc**, W. Shang, S. Eslami, and I. Iordachita, "Design of an MRI-Compatible Modularized Needle Driver for In-Bore MRI-Guided Prostate Interventions" *Int. Conf. on Control, Automation and Systems*, 2015, pp. 1520-1525.
- C11. **B. Gonenc**, P. Gehlbach, R.H. Taylor, and I. Iordachita, "Effects of Micro-Vibratory Modulation during Robot-Assisted Membrane Peeling," *IEEE/RSJ Int. Conf. on Intelligent Robots and Systems (IROS'15)*, 2015, pp. 3811-3816.
- C12. **B. Gonenc**, N. Tran, C.N. Riviere, P. Gehlbach, R.H. Taylor, and I. Iordachita, "Force-Based Puncture Detection and Active Position Holding for Assisted Retinal Vein Cannulation," *Int. Conf. on Multisensor Fusion and Integration for Intelligent Systems (MFI'15)*, 2015, pp. 322-327 - **Best Paper Award**.
- C13. **B. Gonenc**, M. Li, K. Kim, W. Shang, and I. Iordachita, "Development of an MRI-Compatible Needle Driver for In-Bore Prostate Biopsy," *IEEE 17th Int Conf. on Advanced Robotics (ICAR'15)*, 2015, pp. 130-136.
- C14. **B. Gonenc** and H. Gurocak, "Haptic Interface with Hybrid Actuator for Virtual Tissue Cutting," *ASME IDETC/CIE 2015*, pp. V01BT02A054, 8 pages.

- C15.B. Gonenc**, P. Gehlbach, J. Handa, R.H. Taylor, and I. Iordachita, "Force-Sensing Microneedle for Assisted Retinal Vein Cannulation," *IEEE SENSORS 2014*, 2014, pp. 698-701 - *Best Student Paper Award*.
- C16.A. Gupta**, **B. Gonenc**, M. Balicki, K. Olds, J. Handa, P. Gehlbach, R.H. Taylor, and I. Iordachita, "Human Eye Phantom for Developing Computer and Robot-Assisted Epiretinal Membrane Peeling," *Int. Conf. of the IEEE EMBS (EMBC'14)*, 2014, pp. 6864-6867.
- C17.P. Wilkening**, W. Chien, **B. Gonenc**, J. Niparko, J.U. Kang, I. Iordachita, and R.H. Taylor, "Evaluation of Virtual Fixtures for Robot-Assisted Cochlear Implant Insertion," *IEEE RAS EMBS Int. Conf. Biomed. Robot. Biomechatron. (BioRob'14)*, 2014, pp. 332-338.
- C18.B. Gonenc**, P. Gehlbach, J. Handa, R.H. Taylor, and I. Iordachita, "Motorized Force-Sensing Micro-Forceps with Tremor Cancelling and Controlled Micro-Vibrations for Easier Membrane Peeling," *IEEE RAS EMBS Int. Conf. Biomed. Robot. Biomechatron. (BioRob'14)*, 2014, pp. 244-251.
- C19.B. Gonenc**, E. Feldman, P. Gehlbach, J. Handa, R.H. Taylor, and I. Iordachita, "Towards Robot Assisted Vitreoretinal Surgery: Force-Sensing Micro-Forceps Integrated with a Handheld Micromanipulator," *IEEE Int. Conf. on Robotics and Automation (ICRA'14)*, 2014, pp. 1399-1404.
- C20.B. Gonenc** and I. Iordachita, "3-DOF Force-Sensing Micro-Forceps for Vitreoretinal Surgery," *Int. Conf. of Mechanical Engineering (ICOME'13)*, Craiova, Romania, 2013.
- C21.B. Gonenc**, J. Handa, P. Gehlbach, R.H. Taylor, and I. Iordachita, "Design of 3-DOF Force Sensing Micro-Forceps for Robot-Assisted Vitreoretinal Surgery," *Int. Conf. of the IEEE EMBS (EMBC'13)*, 2013, pp. 5686-5689.
- C22.B. Gonenc**, J. Handa, P. Gehlbach, R.H. Taylor, and I. Iordachita, "A Comparative Study for Robot Assisted Vitreoretinal Surgery: Micron vs. the Steady-Hand Robot," *IEEE Int. Conf. on Robotics and Automation (ICRA'13)*, 2013, pp. 4832-4837.
- C23.B. Gonenc**, M. Balicki, J. Handa, P. Gehlbach, C.N. Riviere, R.H. Taylor, and I. Iordachita, "Preliminary Evaluation of a Micro-Force Sensing Handheld Robot for Vitreoretinal Surgery," *IEEE/RSJ Int. Conf. on Intelligent Robots and Systems (IROS'12)*, 2012, pp. 4125-4130.
- C24.I. Kuru**, **B. Gonenc**, M. Balicki, J. Handa, P. Gehlbach, R.H. Taylor, and I. Iordachita, "Force Sensing Micro-Forceps for Robot Assisted Retinal Surgery," *Int. Conf. of the IEEE EMBS (EMBC'12)*, 2012, pp. 1401-1404.
- C25.B. Gonenc** and H. Gurocak, "Haptic Interface with Hybrid Actuator for Virtual Needle Insertion and Tissue Cutting," *IEEE Haptics Symposium*, 2012, pp. 451-455.
- C26.O.G. Erol**, H. Gurocak, and **B. Gonenc**, "Design Optimization Method for MR-Brake Actuators", *ASME 2011 International Mechanical Engineering Congress & Exposition*, 2011, pp. 1257-1263.
- C27.B. Gonenc** and H. Gurocak, "Force Control with Hybrid Actuator for Virtual Needle Insertion," *IEEE World Haptics Conference*, 2011, pp. 173-177.

Papers in Preparation

1. **B. Gonenc**, P. Gehlbach, R.H. Taylor, and I. Iordachita, "Micro-Vibratory Modulation for Reduced Forces during Membrane Peeling in Robot-Assisted Retinal Microsurgery," - *in preparation*.
2. **B. Gonenc**, P. Gehlbach, R.H. Taylor, and I. Iordachita, "Towards Robot-Assisted Retinal Vein Cannulation: A Force-Sensing Microneedle Integrated with a Handheld Micromanipulator," - *in preparation*.
3. **B. Gonenc**, P. Gehlbach, R.H. Taylor, and I. Iordachita, "A comparative Study for Robot-Assisted Retinal Vein Cannulation: Micron vs. the Steady-Hand Eye Robot," - *in preparation*.

Patents

- P1. Hakan GUROCAK, Doruk SENKAL, and **Berk GONENC**, "MAGNETORHEOLOGICAL DEVICES AND ASSOCIATED METHODS OF CONTROL," Patent No. US 9,093,214, issued July 28, 2015.
- P2. **Berk GONENC**, Iulian IORDACHITA, Russell TAYLOR, Cameron RIVIERE, "MICROMANIPULATION SYSTEMS AND METHODS," US 2016/0030240 A1, published Feb 4, 2016.

Presentations

Invited Lectures

- 2017 1. OCT-Guided Systems for Robotic Assistance in Retinal Microsurgery, Workshop: The future of Optical Coherence Tomography (OCT) in Ophthalmic Surgery, Technical University of Munich, Germany, 06/06/2017.
2. Force-Based Robotic Control for Medical Applications, Departmental Seminar, University of Nebraska Lincoln, USA, 03/13/2017.
3. Force-Based Robotic Control for Medical Applications, Departmental Seminar, Vanderbilt University, USA, 02/23/2017.
4. Force-Based Robotic Control for Medical Applications, Departmental Seminar, Worcester Polytechnic Institute, USA, 02/17/2017.
5. Force-Based Robotic Control for Medical Applications, Departmental Seminar, Southern Illinois University Edwardsville, USA, 02/20/2017.
6. Robotic Assistance with Force Sensing in Medical Applications, Departmental Seminar, Lawrence Technological University, USA, 01/20/2017.
- 2016 7. Force Sensing for Robotic Assistance in Retinal Microsurgery, LCSR Seminar Series, Johns Hopkins University, USA, 03/30/2016.
- 2015 8. Robotic Assistance with Force Sensing in Retinal Microsurgery, Daegu Gyeongbuk Institute of Science & Technology, South Korea, 11/17/2015.

Conference Lectures

- 2017 **1.** Intraocular Snake Integrated with the Steady-Hand Eye Robot for Assisted Retinal Microsurgery, ICRA 2017, 05/29-06/03.
- 2016 **2.** FBG-Based Transverse and Axial Force-Sensing Micro-Forceps for Retinal Microsurgery, SENSORS 2016, 10/30-11/02.
- 2015 **3.** Effects of Micro-Vibratory Modulation during Robot-Assisted Membrane Peeling, IROS 2015, 09/28-10/02.
- 4.** Force-Based Puncture Detection and Active Position Holding for Assisted Retinal Vein Cannulation, MFI, 09/14-09/16.
- 5.** Haptic Interface with Hybrid Actuator for Virtual Tissue Cutting, ASME IDETC/CIE 2015, 08/02-08/05.
- 6.** Development of an MRI-Compatible Needle Driver for In-Bore Prostate Biopsy, ICAR 2015, 07/27-07/31.
- 2014 **7.** Force-Sensing Microneedle for Assisted Retinal Vein Cannulation, SENSORS 2014, 11/02-11/05.
- 8.** Towards Robot Assisted Vitreoretinal Surgery: Force-Sensing Micro-Forceps Integrated with a Handheld Micromanipulator, ICRA 2014, 05/31-06/07.
- 2013 **9.** Design of 3-DOF Force Sensing Micro-Forceps for Robot-Assisted Vitreoretinal Surgery, EMBC 2013, 07/03-07/07.
- 10.** A Comparative Study for Robot Assisted Vitreoretinal Surgery: Micron vs. the Steady-Hand Robot, ICRA, 05/06-05/10.
- 2012 **11.** Preliminary Evaluation of a Micro-Force Sensing Handheld Robot for Vitreoretinal Surgery, IROS 2012, 10/07-10/12.
- 12.** Force Sensing Micro-Forceps for Robot Assisted Retinal Surgery, EMBC 2012, 08/28-09/01.